

---

Theses and Dissertations

---

Fall 2013

# Kinetic evaluation of the inhibition and reactivation of human acetylcholinesterase

Alexander Morris Lodge  
*University of Iowa*

Copyright 2013 Alexander M. Lodge

This dissertation is available at Iowa Research Online: <http://ir.uiowa.edu/etd/5018>

---

## Recommended Citation

Lodge, Alexander Morris. "Kinetic evaluation of the inhibition and reactivation of human acetylcholinesterase." PhD (Doctor of Philosophy) thesis, University of Iowa, 2013.  
<http://ir.uiowa.edu/etd/5018>.

---

Follow this and additional works at: <http://ir.uiowa.edu/etd>

 Part of the [Chemistry Commons](#)

KINETIC EVALUATION OF THE INHIBITION AND  
REACTIVATION OF HUMAN ACETYLCHOLINESTERASE

by

Alexander Morris Lodge

A thesis submitted in partial fulfillment of the  
requirements for the Doctor of  
Philosophy degree in Chemistry in  
the Graduate College of  
The University of Iowa

December 2013

Thesis Supervisor: Professor Daniel M. Quinn

Copyright by  
ALEXANDER MORRIS LODGE  
2013  
All Rights Reserved

Graduate College  
The University of Iowa  
Iowa City, Iowa

CERTIFICATE OF APPROVAL

---

PH.D. THESIS

---

This is to certify that the Ph.D. thesis of

Alexander Morris Lodge

has been approved by the Examining Committee for the thesis requirement for the Doctor of Philosophy degree in Chemistry at the December 2013 graduation.

Thesis Committee: \_\_\_\_\_  
Dan Quinn, Thesis Supervisor

\_\_\_\_\_  
Gregory Friestad

\_\_\_\_\_  
Chris Pigge

\_\_\_\_\_  
Lei Geng

\_\_\_\_\_  
Charles Brenner

To the most loving and fun family in the whole wide world, especially my mother Ms. Sherron Lodge, who has supported me in this very long journey.

...If you can dream--and not make dreams your master;  
If you can think--and not make thoughts your aim;  
    If you can meet with Triumph and Disaster  
    and treat those two imposters just the same;  
If you can bear to hear the truth you've spoken  
    twisted by knaves to make a trap for fools,  
Or watch the things you gave your life to, broken,  
And stoop and build'em up with worn out tools:  
    ...If you can fill the unforgiving minute,  
    With sixty seconds of distance run,  
    Yours is the Earth and everything that's in it,  
And—which is more—you'll be a Man, my son!

Rudyard Kipling, *IF*

## ACKNOWLEDGEMENTS

I would like to thank God, for the many blessings that he has given me and for giving me the resolve to complete this very long journey. God has blessed me with loving family and friends who have stuck by me and supported me unconditionally.

I truly have to thank my family. We have been through so many things and I would not have made it to this point without them. Through the ups and downs, good and bad, they have been there all the way. There are no words great enough to define the amount of love, dedication, and support they have given to me; especially my mom, sister, and brother—Sherron, Hilaria, and Clarence. Also my grandparents, Sherman and Florence Newton, who raised seven grandchildren and were parents to a second generation of children.

Very special thanks to some of the greatest friends ever, better known as “the Crew”. We all came to Iowa with doctoral dreams, and I am glad to be the next in line to realize that. My life in Iowa would probably have been miserable without these people, so thank you for your unconditional support.

Thanks to the Department of Chemistry and Dr. Dan Quinn, my research advisor.

Thanks to all who have been part of and supported my journey thus far.

## ABSTRACT

The essential role that acetylcholinesterase (AChE) plays in terminating the action potential triggered by ACh's pre-synaptic release is recognized by its astounding catalytic turnover rate, ca.  $k_{cat}/K_m = 10^8 \text{ M}^{-1} \text{ s}^{-1}$ . AChE's adeptness at rapid hydrolysis of choline esters is largely attributed to the enzyme's two step mechanism of action initiated by acylation of the enzyme and a subsequent deacylation step. Understanding the inhibition of AChE plays an essential role in both organophosphate (OP) nerve agent poisoning as well as developing new drug treatments for neurological disorders.

Novel sarin and soman analogues were prepared that all bear a fluorescent leaving group (R = 4-methylumbelliferyl, 4-trifluoromethylumbelliferyl, or N-methylquinolinium) to produce non-volatile inhibitors that all show irreversible inhibition for *h*AChE. Bimolecular inhibition rate constants ( $k_i/K_I = 10^3$  to  $10^7 \text{ M}^{-1} \text{ min}^{-1}$  range) were determined by stop-time and continuous assays, where the quarternized N-methylquinolinium sarin analogue showed the highest inhibitory potency. 4-methylumbelliferyl functionalized sarin and soman analogues were assayed for rate of aging kinetics. *Tert*-butoxy substituted OP analogue aged faster,  $^{aging}t_{1/2} = 75 \text{ min}$  at  $27^\circ\text{C}$ , than its isopropoxy and methoxy counterparts ( $^{aging}t_{1/2} = 660 \text{ min}$  and 9 days, respectively).

AChE exposed to an OP nerve agent undergoes rapid and irreversible inhibition in which acute exposure can be fatal. A secondary intermolecular process called aging can occur to completely deaden enzymatic activity which is unrecoverable by conventional methods. The synthesized OP analogue of sarin, (R,R' = 4-methylumbelliferyl, isopropoxy) was utilized in the development of a bioassay procedure to evaluate the



ability of novel alkylating or acylating AChE ligands to reactivate aged-AChE, termed the “resurrection” assay. Several families of compounds designed to alkylate or acylate a phosphonic oxyanion adduct of aged-AChE were screened for inhibition of apo *hAChE* and reactivation of aged-*hAChE* character. To date, no recovery of aged-AChE was observed following treatment with alkylating agents and evaluation in the “resurrection” assay.

Novel  $\beta$ -lactam and 6-fluoro-2-methoxy pyridinium compounds were evaluated as time dependent inhibitors of *hAChE*. Each inhibitor showed time-dependent inhibition of *hAChE* ( $IC_{50} = 24\text{-}150\ \mu\text{M}$ ). For the  $\beta$ -lactam family of inhibitors, inhibition was characterized as competitive and supported by computational docking and reaction modeling. Additional evaluation of hydrolytic stability and spontaneous reactivation of *hAChE* activity provided useful insight on observed biphasic inhibitory behavior for the  $\beta$ -lactam inhibitors. 6-fluoro-2-methoxy pyridinium showed reversible inhibition followed by a proposed nucleophilic aromatic substitution ( $S_NAr$ ) mechanism. Irreversible inhibition was characterized for 6-fluoro-2-methoxy pyridinium via stop-time and dose response assay ( $k_i/K_i = 6.6 \times 10^4\ \text{M}^{-1}\ \text{min}^{-1}$  and  $IC_{50} = 63\ \mu\text{M}$ ). Evaluation of initial rates to resolve Michaelis-Menten kinetic parameters showed non-competitive mode of inhibition, suggests slow nucleophilic attack by the active site serine supporting the  $S_NAr$  mechanism.

Additionally, several [2.2] paracyclophane compounds were evaluated as potential inhibitors of AChE. Neutral and quaternized [2.2] paracyclophanes (pCp) showed moderate, reversible inhibitory character ( $IC_{50} = 10^{-5}\text{-}10^{-6}\ \text{M}$  range) for *hAChE*. Evaluation of quaternized pCp, tetrakis(4-(tetra-N-methylpyridinium)cyclobutyl)

paracyclophane iodide, showed non-linear, non-competitive inhibition. Further evaluation as a peripheral active site inhibitor was confirmed with inhibition evaluation using the slow hydrolyzing substrate, *p*-nitrophenyl acetate.

## TABLE OF CONTENTS

LIST OF TABLES	xi
LIST OF FIGURES	xiii
LIST OF SCHEMES	xxii
CHAPTER 1: INTRODUCTION	1
Acetylcholinesterase: Structure and Function	1
Kinetic Behavior of Acetylcholinesterase	9
Inhibition of Acetylcholinesterase	15
Objectives of Study	22
CHAPTER 2: SYNTHESIS AND KINETIC EVALUATION OF ORGANOPHOSPHONATE INHIBITORS OF ACETYLCHOLINESTERASE	23
Chemical Mechanism and Significance	23
Objectives of Study	34
Materials and Methods	35
Synthesis of Non-volatile Sarin and Soman Analogues	35
Enzyme Kinetic Analysis	36
Results and Discussion	41
Conclusion	57
CHAPTER 3: KINETIC EVALUATION FOR THE REACTIVATION OF AGED HUMAN ACETYLCHOLINESTERASE BY NOVEL ALKYLATING AGENTS	59
Chemical Mechanism and Significance	59
Objectives of Study	64
Materials and Methods	72
IC <sub>50</sub> Determination of Resurrecting Agents	72
Resurrection Assay Procedure	73
Results and Discussion	75
Conclusion	93
CHAPTER 4: KINETIC EVALUATION OF N-METHYL PYRIDINIUM β-LACTAM INHIBITORS OF HUMAN ACETYLCHOLINESTERASE	94
Chemical Mechanism and Significance	94
Materials and Methods	95
Synthesis of β-Lactam Inhibitors	95

Hydrolytic Stability of Inhibitors	96
Enzyme Assay Procedures and Kinetic Analysis	98
IC <sub>50</sub> Determination	99
Continuous Assay (Kinetic InhibitionRate)	100
Determination of Inhibition Mode	101
Results and Discussion	102
Conclusion	115
CHAPTER 5: KINETIC EVALUATION OF 6-FLUORO-2-METHOXY N-METHYL PYRIDINIUM INHIBITOR OF HUMAN ACETYLCHOLINESTERASE	116
Chemical Mechanism and Significance	116
Objective of Study	117
Materials and Methods	117
Synthesis of <b>R10</b>	117
Enzyme Assay Procedures and Kinetic Analysis	121
Results and Discussion	125
Conclusion	135
CHAPTER 6: KINETIC EVALUATION OF PARACYLCOPHANE INHIBITORS OF HUMAN ACETYLCHOLINESTERASE	137
Chemical Mechanism and Significance	137
Objective of Study	139
Materials and General Method	139
Results and Discussion	143
Conclusion	156
APPENDIX A: SUPPORTING INFORMATION FOR ORGANOPHOSPHONATE INHIBITORS	158
Synthetic Procedure	158
Materials and General Methods	158
Orgnaophosphonate Inhibitors	159
APPENDIX B: SUPPORTING INFORMATION FOR RESURRECTION ASSAY	176
Materials and General Methods	176
IC <sub>50</sub> Determinations for Resurrecting Agents	177
Methoxy Methyl Pyridiniums	178
2-PAM Analogues	188
Pyridinium β-Lactams	191
Additional Aromatic Alkylating Compounds	194
Mono/Bis-Pyridinium Gorge-Spanning Compounds	195

Aricept Core/Pyridinium Gorge-Spanning Compounds	199
Sharpless Core/Pyridinium Gorge-Spanning Compounds	199
4-methylumbelliferyl/Pyridinium Gorge-Spanning Compounds	202
Dimethyl Sulfonium Compounds	205
2-PAM, R13, and R15 Resurrection Assay Procedure	208
 APPENDIX C: SUPPORTING MATERIALS FOR $\beta$ -LACTAM INHIBITORS	 215
Materials and General Methods	215
Inhibitor Structure	216
Supporting Information for Hydrolytic Stability	217
Supporting Information for IC <sub>50</sub> Determination	220
Supporting Information for Continuous Assays	223
Supporting Information for Reactivation Assay	231
Computational Docking and Molecular Modeling Procedure	233
 REFERENCES	 237

## LIST OF TABLES

Table 2.1	Bimolecular rate constants from the pseudo first-order rate constants ( $k_{\text{obs}}$ ) and the OP inhibitor ( <b>2A-2F</b> ) concentration, ( $k_{\text{obs}}/[\text{OP}]$ , $\text{M}^{-1} \text{min}^{-1}$ ) at 27°C	48
Table 2.2	Second-order bimolecular rate constants (defined by Eq. 2.6 where $K_I \gg [\text{I}]$ such that $k_{\text{obs}} = \frac{k_i}{K_I} [\text{I}]$ ) from continuous assays for Sarin analogue inhibitors <b>2A</b> , <b>2D</b> , and <b>2F</b> at 27°C	54
Table 2.3	First-order rate constants for aging of <i>hAChE</i> -OP adduct formed from inhibition by inhibitors <b>2A-2C</b>	56
Table 3.1	Resurrection assay data for <b>R1-R18</b> (methoxy N-methyl pyridiniums)	78
Table 3.2	Resurrection assay data for <b>R19-R23</b> (2-PAM analogues)	81
Table 3.3	Resurrection assay data for <b>R24-R29</b> (pyridinium $\beta$ -Lactams)	82
Table 3.4	Resurrection assay data for <b>R30-R35</b> (Other aromatic alkylating compounds)	83
Table 3.5	Resurrection assay data for <b>R36-R46</b> (gorge-spanning methoxy N-methyl pyridiniums)	84
Table 3.6	Resurrection assay data for <b>R47-R50</b> (Aricept core/pyridinium gorge-spanners)	86
Table 3.7	Resurrection assay data for <b>R51-R59</b> (Sharpless core/pyridinium gorge-spanners)	87
Table 3.8	Resurrection assay data for <b>R60-R70</b> (umbelliferyl/pyridinium gorge-spanners)	88
Table 3.9	Resurrection assay data for <b>R71-R77</b> (dimethyl sulfonium compounds)	90
Table 4.1	Absorbance maxima for inhibitors <b>R24-R28</b> , corresponding hydrolysis products for each inhibitor, $\Delta A$ values, and $\lambda_{\Delta\epsilon}$ values	105
Table 4.2	$\text{IC}_{50}$ values for inhibitors <b>R24-28</b> over 24 hour incubation period	106
Table 4.3	Summary of Kinetic Data for $\beta$ -lactam inhibitors <b>R24-28</b>	108

Table 4.4	Computed Enthalpies (kcal/mol) of Formation, Activation, and Reaction for Modeled Acylation Reactions	112
Table 5.1	IC <sub>50</sub> values for inhibitors <b>R10</b> over 7.5 hour incubation period	126
Table 6.1	IC <sub>50</sub> values for inhibitors <b>6A</b> and <b>6B</b>	147
Table C1	Bimolecular rate constants for inhibitors <b>R24</b> , <b>R26-27</b> from biphasic fit to equation Eq. 4.6	228
Table C2	Comparison of the computed ligand docking results and experimental inhibitor dissociation constants	235

## LIST OF FIGURES

Figure 1.1	Pathway of ACh signal nerve-nerve transmission in the central nervous system	4
Figure 1.2	Structure and process summary of ACh triggered action potential across the neuromuscular junction	5
Figure 1.3	AChE catalytic mechanism of action	6
Figure 1.4	Model of the active site structure of <i>hAChE</i> bound to ACh	7
Figure 1.5	Active-site gorge schematic for <i>TcAChE</i> highlighting sub-binding sites and catalytic active site (esteratic site)	8
Figure 1.6	Mechanism of action for AChE hydrolysis of acetyl-L <sub>3</sub> -thiocholine substrates. Secondary kinetic isotope effects were measured to identify rate-limiting steps in the enzyme mechanism	13
Figure 1.7	Inhibitors of human acetylcholinesterase ( <i>hAChE</i> ) and drug treatments for Alzheimer's Disease	17
Figure 1.8	Mechanism of action for the inhibition, oxime reactivation, and aging of AChE by OP nerve agent	19
Figure 1.9	Chemical structures of well-known organophosphorus nerve agents and oxime antidotes	21
Figure 2.1	Chemical structures of well-known organophosphorus nerve agents and oxime antidotes	26
Figure 2.2	AChE catalytic mechanism of action	27
Figure 2.3	Mechanism of action for the inhibition, oxime reactivation, and aging of AChE by OP nerve agent	28
Figure 2.4	3D crystal structure of aged-AChE adduct ( <i>TcAChE</i> ) with 2-PAM bound in the catalytic active site	31
Figure 2.5	Chemical structures for OP inhibitors (Sarin and Soman) and OP analogues <b>2A-2F</b>	37
Figure 2.6	Stop-time assay plot for <b>2A</b> (1 $\mu$ M) for pseudo first-order rate constant Determination	43



Figure 2.7	Stop-time assay plot for <b>2B</b> (1 $\mu\text{M}$ ) for pseudo first-order rate constant determination	44
Figure 2.8	Stop-time assay plot for <b>2C</b> (10 $\mu\text{M}$ ) for pseudo first-order rate constant determination	45
Figure 2.9	Stop-time assay plot for <b>2D</b> (1 $\mu\text{M}$ ) for pseudo first-order rate constant determination	46
Figure 2.10	Stop-time assay plot for <b>2F</b> (10 nM) for pseudo first-order rate constant determination	47
Figure 2.11	Full time course for sarin analogue inhibitor <b>2A</b> (2 $\mu\text{M}$ ) fit to Eq. 2.5 followed by Ellman method (26) ( $\lambda = 412 \text{ nm}$ )	50
Figure 2.12	Second-order plot of $k_{\text{obs}}$ ( $\text{min}^{-1}$ , pseudo-first order rate constat) as a function of inhibitor <b>2A</b> concentration (Eq. 2.6)	51
Figure 2.13	Second-order plot of $k_{\text{obs}}$ ( $\text{min}^{-1}$ , pseudo-first order rate constat) as a function of inhibitor <b>2D</b> concentration (Eq. 2.6)	52
Figure 2.14	Second-order plot of $k_{\text{obs}}$ ( $\text{min}^{-1}$ , pseudo-first order rate constat) as a function of inhibitor <b>2F</b> concentration (Eq. 2.6)	53
Figure 2.15	First-order plot of the recovered OP inhibited <i>h</i> AChE activity as a function of time	55
Figure 3.1	Mechanism of action for the inhibition, oxime reactivation, and aging of AChE by OP nerve agent	66
Figure 3.2	3D crystal structure of aged-AChE adduct ( <i>Tc</i> AChE) with 2-PAM bound in the catalytic active site	67
Figure 3.3	Chemical structures for OP inhibitors (Sarin and Soman) and OP analogues <b>2A-2F</b>	68
Figure 3.4	Mechanism of action for OP inhibition, reactivation, aging, and proposed resurrection of AChE	69
Figure 3.5	Reaction scheme and mechanism for model methyl transfer reaction and scheme for aged-AChE resurrection	70
Figure 3.6	Structure of resurrecting compounds	71
Figure 3.7	Roadmap for “resurrection” assay procedure	76

Figure 3.8	Plot of recovered aged- <i>h</i> AChE activity by treatment with oximes 2-PAM and <b>R13</b> at 5 x $K_i^{app}$ concentrations	92
Figure 4.1	Full time course for $\beta$ -lactam inhibitor <b>R24</b> (R=H, 400 $\mu$ M) fit to Eq. 4.6	107
Figure 4.2	Michaelis-Menten plot for inhibitor <b>R24</b> (0-341 $\mu$ M) fit to Eq. 4.10	109
Figure 4.3	Double reciprocal plot of the inverse initial rate ( $v_i^{-1}$ , min mA <sup>-1</sup> ) versus the inverse ATCh concentration ( $\mu$ M <sup>-1</sup> ). Slopes were calculated from $V_{max}$ and $K_m$ values generated from data fit to equation 4.10.	110
Figure 4.4	Three-dimensional plot of initial rate ( $v_i$ , mA/min), versus ATCh concentration (50-300 $\mu$ M), and inhibitor <b>R24</b> concentration (0-341 $\mu$ M) fit to Eq. 4.12	111
Figure 5.1	AChE catalytic mechanism of action	118
Figure 5.2	General mechanism for $S_NAr$ and proposed AChE inhibition mechanism by $S_NAr$	119
Figure 5.3	Plot of $K_i^{app}$ ( $\mu$ M) as a function of time (min) fit to $K_i^{app} = K_{i,\infty}^{app} + (K_{i,0}^{app} - K_{i,\infty}^{app})e^{-kt}$ where $K_{i,0}^{app} \equiv$ the observed inhibitor dissociation constant at $t = 0$ , $K_{i,\infty}^{app} \equiv$ the observed inhibitor dissociation constant at $t = \infty$ , $k \equiv$ the inhibition rate constant, and $t \equiv$ time (min)	127
Figure 5.4	Plot of pseudo first-order rate of inhibition for <b>R10</b> (30-600 $\mu$ M) as defined by equations 5.4 ( $[I] = 1.25e-4$ M to $2.5e-4$ M) and 5.5 ( $[I] = 3.125e-5$ M to $6.25e-5$ M) respectively	129
Figure 5.5	Second-order plot of $k_{obs}$ as a function of <b>R10</b> concentration from stop-time assays (Eq. 5.10)	130
Figure 5.6	Michaelis-Menten plots of $v_i$ (mA/min) versus ATCh concentration ( $\mu$ M) for various concentrations of inhibitor <b>R10</b> , Eq. 5.6	131
Figure 5.7	Double-reciprocal plot of the inverse initial rate ( $v_i^{-1}$ , min mA <sup>-1</sup> ) versus the inverse of ATCh concentration ( $\mu$ M <sup>-1</sup> ) for various concentrations of inhibitor <b>R10</b> , Eq. 5.7	132
Figure 5.8	Three-dimensional plot of initial rate ( $v_i$ , mA/min) versus the substrate concentration (ATCh, 0-400 $\mu$ M) and inhibitor <b>R10</b> concentration, Eq. 5.8	133

Figure 5.9	Recovered <i>h</i> AChE activity for inhibition by <b>R10</b> following separation of excess inhibitor, Eq. 5.9	134
Figure 6.1	Chemical structures of donepezil, donepezil's parent compound, and novel paracyclophane AChE inhibitors <b>6A</b> and <b>6B</b>	138
Figure 6.2	Michaelis-Menten plot of $v_i$ (mA/min) versus ATCh concentration ( $\mu\text{M}$ ) for various concentrations of inhibitor <b>6B</b> (0-8 $\mu\text{M}$ )	146
Figure 6.3	Double-reciprocal plot of the inverse initial rate ( $v_i^{-1}$ , $\text{min mA}^{-1}$ ) versus the inverse of ATCh concentration ( $\mu\text{M}^{-1}$ ) for various concentrations of inhibitor <b>6B</b> (0-8 $\mu\text{M}$ )	147
Figure 6.4	Slope replot from Lineweaver-Burk analysis of the slopes versus inhibitor <b>6B</b> concentration (0-8 $\mu\text{M}$ ) and described as the $\text{slope } (m) = \frac{K_m}{v_{max}} + \frac{K_m}{v_{max}K_I} [I]$	148
Figure 6.5	Three-dimensional plot of initial rate ( $v_i$ , mA/min) versus the substrate concentration (ATCh, 0-400 $\mu\text{M}$ ) and inhibitor <b>6B</b> concentration (0-8 $\mu\text{M}$ )	149
Figure 6.6	Michaelis-Menten plot of $v_i$ (mA/min) versus p-NPA concentration ( $\mu\text{M}$ ) for various concentrations of inhibitor <b>6B</b> (0-6.4 $\mu\text{M}$ )	151
Figure 6.7	Double-reciprocal plot of the inverse initial rate ( $v_i^{-1}$ ( $\text{min mA}^{-1}$ ) versus the inverse of p-NPA concentration ( $\mu\text{M}^{-1}$ ) for various concentrations of inhibitor <b>6B</b> (0-6.4 $\mu\text{M}$ )	152
Figure 6.8	Three-dimensional plot of initial rate ( $v_i$ , mA/min) versus the substrate concentration (ATCh, 0-400 $\mu\text{M}$ ) and inhibitor <b>6B</b> concentration (0-8 $\mu\text{M}$ )	153
Figure 6.9	Time course plots of absorbance versus time(s) for various concentrations of inhibitor <b>6B</b> (0-16 $\mu\text{M}$ )	154
Figure 6.10	Non-linear plot for noncompetitive inhibition of first-order rate ( $k_i$ , $\text{s}^{-1}$ ) versus concentration of inhibitor <b>6B</b> (0-16 $\mu\text{M}$ )	155
Figure A1	500 MHz $^1\text{H}$ NMR Spectrum in $\text{CDCl}_3$ of <b>2A</b>	164
Figure A2	125 MHz $^{13}\text{C}$ NMR Spectrum in $\text{CDCl}_3$ of <b>2A</b>	164
Figure A3	100 MHz $^{31}\text{P}$ NMR Spectrum in $\text{CDCl}_3$ of <b>2A</b>	165

Figure A4	400 MHz $^1\text{H}$ NMR Spectrum in $\text{CDCl}_3$ of <b>2B</b>	166
Figure A5	100 MHz $^{13}\text{C}$ NMR Spectrum in $\text{CDCl}_3$ of <b>2B</b>	166
Figure A6	80 MHz $^{31}\text{P}$ NMR Spectrum in $\text{CDCl}_3$ of <b>2B</b>	167
Figure A7	500 MHz $^1\text{H}$ NMR Spectrum in $\text{CDCl}_3$ of <b>2C</b>	168
Figure A8	125 MHz $^{13}\text{C}$ NMR Spectrum in $\text{CDCl}_3$ of <b>2C</b>	168
Figure A9	100 MHz $^{31}\text{P}$ NMR Spectrum in $\text{CDCl}_3$ of <b>2C</b>	169
Figure A10	500 MHz $^1\text{H}$ NMR Spectrum in $\text{CDCl}_3$ of <b>2D</b>	170
Figure A11	125 MHz $^{13}\text{C}$ NMR Spectrum in $\text{CDCl}_3$ of <b>2D</b>	170
Figure A12	100 MHz $^{31}\text{P}$ NMR Spectrum in $\text{CDCl}_3$ of <b>2D</b>	171
Figure A13	470 MHz $^{19}\text{F}$ NMR Spectrum in $\text{CDCl}_3$ of <b>2D</b>	171
Figure A14	400 MHz $^1\text{H}$ NMR Spectrum in $\text{CDCl}_3$ of <b>2E</b>	172
Figure A15	100 MHz $^{13}\text{C}$ NMR Spectrum in $\text{CDCl}_3$ of <b>2E</b>	172
Figure A16	80 MHz $^{31}\text{P}$ NMR Spectrum in $\text{CDCl}_3$ of <b>2E</b>	173
Figure A17	500 MHz $^1\text{H}$ NMR Spectrum in $\text{CDCl}_3$ of <b>2F</b>	174
Figure A18	125 MHz $^{13}\text{C}$ NMR Spectrum in $\text{CDCl}_3$ of <b>2F</b>	174
Figure A19	100 MHz $^{19}\text{F}$ NMR Spectrum in $\text{CDCl}_3$ of <b>2F</b>	175
Figure B1	Dose Response plot for <b>R1</b> (3-100 $\mu\text{M}$ )	179
Figure B2	Dose Response Plot for <b>R2</b> (3-100 $\mu\text{M}$ )	179
Figure B3	Dose Response plot for <b>R3</b> (3-100 $\mu\text{M}$ )	180
Figure B4	Dose Response plot for <b>R4</b> (3-100 $\mu\text{M}$ )	180
Figure B5	Dose Response plot for <b>R5</b> (3-100 $\mu\text{M}$ )	181
Figure B6	Dose Response plot for <b>R6</b> (3-100 $\mu\text{M}$ )	181
Figure B7	Dose Response plot for <b>R7</b> (3-100 $\mu\text{M}$ )	182

Figure B8	Dose Response plot for <b>R8</b> (3-100 $\mu$ M)	182
Figure B9	Dose Response plot for <b>R9</b> (3-100 $\mu$ M)	183
Figure B10	Dose Response plot for <b>R10</b> (3-100 $\mu$ M)	183
Figure B11	Dose Response plot for <b>R11</b> (3-100 $\mu$ M)	184
Figure B12	Dose Response plot for <b>R12</b> (3-100 $\mu$ M)	184
Figure B13	Dose Response plot for <b>R13</b> (3-100 $\mu$ M)	185
Figure B14	Dose Response plot for <b>R14</b> (2 $\mu$ M-1 mM)	185
Figure B15	Dose Response plot for <b>R15</b> (2 $\mu$ M-1 mM)	186
Figure B16	Dose Response plot for <b>R16</b> (2 $\mu$ M-1 mM)	186
Figure B17	Dose Response plot for <b>R17</b> (2 $\mu$ M-1 mM)	187
Figure B18	Dose Response plot for <b>R18</b> (2 $\mu$ M- 1 mM)	187
Figure B19	Dose Response plot for <b>R19</b> (3-100 $\mu$ M)	188
Figure B20	Dose Response plot for <b>R20</b> (3-100 $\mu$ M)	189
Figure B21	Dose Response plot for <b>R21</b> (0.2-100 $\mu$ M)	189
Figure B22	Dose Response plot <b>R22</b> (2 $\mu$ M-1 mM)	190
Figure B23	Dose Response plot for <b>R24</b> (3-100 $\mu$ M)	191
Figure B24	Dose Response plot for <b>R25</b> (0.2-100 $\mu$ M)	191
Figure B25	Dose Response plot for <b>R26</b> (0.2-100 $\mu$ M)	192
Figure B26	Dose Response plot for <b>R27</b> (0.2-100 $\mu$ M)	192
Figure B27	Dose Response plot for <b>R28</b> (0.2-100 $\mu$ M)	193
Figure B28	Dose Response plot for <b>R29</b> (0.2-100 $\mu$ M)	193
Figure B29	Dose Response plot for <b>R30</b> (3-100 $\mu$ M)	194
Figure B30	Dose Response plot for <b>R31</b> (3-100 $\mu$ M)	194

Figure B31	Dose Response plot for <b>R32</b> (0.2-100 $\mu$ M)	195
Figure B32	Dose Response plot for <b>R41</b> (0.2-100 $\mu$ M)	196
Figure B33	Dose Response plot for <b>R42</b> (0.2-100 $\mu$ M)	196
Figure B34	Dose Response plot for <b>R43</b> (2 $\mu$ M-1 mM)	197
Figure B35	Dose Response plot for <b>R44</b> (0.2-100 $\mu$ M)	197
Figure B36	Dose Response plot for <b>R45</b> (0.2-100 $\mu$ M)	198
Figure B37	Dose Response plot for <b>R51</b> (1 nM-100 $\mu$ M)	200
Figure B38	Dose Response plot for <b>R53</b> (20 nM-10 $\mu$ M)	200
Figure B39	Dose Response plot for <b>R54</b> (10 pM-10 $\mu$ M)	201
Figure B40	Dose Response plot for <b>R55</b> (100 pM-10 $\mu$ M)	201
Figure B41	Dose Response plot for <b>R56</b> (1 nM-10 $\mu$ M)	202
Figure B42	Dose Response plot for <b>R67</b> (51 nM-1 mM)	203
Figure B43	Dose Response plot for <b>R68</b> (51 nM-1 mM)	203
Figure B44	Dose Response plot for <b>R69</b> (51 nM-1 mM)	204
Figure B45	Dose Response plot for <b>R70</b> (51 nM-1 mM)	204
Figure B46	Dose Response plot for <b>R71</b> (4 $\mu$ M-2.5 mM)	205
Figure B47	Dose Response plot for <b>R72</b> (51 nM-1 mM)	205
Figure B48	Dose Response plot <b>R73</b> (51 nM-1 mM)	206
Figure B49	Dose Response plot <b>R74</b> (51 nM-1 mM)	206
Figure B50	Dose Response plot for <b>R75</b> (51 nM-1 mM)	207
Figure B51	Dose Response plot for <b>R76</b> (51 nM-1 mM)	207
Figure B52	Dose Response plot for <b>R77</b> (51 nM-1 mM)	208
Figure B53	Plot of apparent recovered aged- <i>hAChE</i> activity	

	by oxime substituted resurrecting agents <b>R13</b> and <b>R15</b> as a function time (h)	209
Figure B54	Plot of apparent recovered aged- <i>hAChE</i> activity as a function of time for resurrecting agent <b>R13</b> at varied concentrations (177 $\mu\text{M}$ -1.8 mM)	210
Figure B55	Plot of apparent recovered aged- <i>hAChE</i> activity as a function of time for resurrecting agent <b>R15</b> at varied concentrations (110 $\mu\text{M}$ -1.1 mM)	211
Figure B56	Plot of apparent recovered aged- <i>hAChE</i> activity with second dosing of resurrecting agents <b>R13</b> (885 $\mu\text{M}$ ) and <b>R15</b> (550 $\mu\text{M}$ )	212
Figure B57	Plot of apparent recovered aged- <i>hAChE</i> activity of resurrecting agent <b>R13</b> with parallel assay of 2-PAM	213
Figure C1	UV spectrum (250 nm-350 nm) for inhibitor <b>R24</b>	217
Figure C2	UV spectrum (250 nm-350 nm) for inhibitor <b>R25</b>	217
Figure C3	UV spectrum (250 nm-350 nm) for inhibitor <b>R26</b>	218
Figure C4	UV spectrum (250 nm-350 nm) for inhibitor <b>R27</b>	218
Figure C5	UV spectrum (250 nm-350 nm) for inhibitor <b>R28</b>	219
Figure C6	Dose Response plots for <b>R24</b> (30 $\mu\text{M}$ -1 mM)	220
Figure C7	Dose Response plots for <b>R25</b> (8-250 $\mu\text{M}$ )	220
Figure C8	Dose Response plots for <b>R26</b> (30 $\mu\text{M}$ -1 mM)	221
Figure C9	Dose Response plots for <b>R27</b> (30 $\mu\text{M}$ -1 mM)	221
Figure C10	Dose Response plots for <b>R28</b> (30 $\mu\text{M}$ -1 mM)	222
Figure C11	Truncated continuous assay time course for $\beta$ -lactam inhibitor <b>R25</b> (200 $\mu\text{M}$ ) fit to Eq. 4.7	223
Figure C12	Continuous assay time course for $\beta$ -lactam inhibitor <b>R28</b> fit to Eq. 4.8	223
Figure C13	Second-order rate constant plot of $k_{\text{obs}}$ ( $\text{min}^{-1}$ ) versus <b>R24</b> concentration, Eq. C1	224

Figure C14	Second-order rate constant plot of $k_{\text{obs}}$ ( $\text{min}^{-1}$ ) versus <b>R25</b> concentration, Eq. C1	225
Figure C15	Second-order rate constant plot of $k_{\text{obs}}$ ( $\text{min}^{-1}$ ) versus <b>R26</b> concentration, Eq. C1	226
Figure C16	Second-order rate constant plot of $k_{\text{obs}}$ ( $\text{min}^{-1}$ ) versus <b>R27</b> concentration, Eq. C1	227
Figure C17	Dixon plot of $v$ (Abs/min) versus inhibitor <b>R24</b> concentration (100 $\mu\text{M}$ -1 mM) fit to Eq. 4.9	229
Figure C18	Dixon plot of $v$ (Abs/min) versus inhibitor <b>R26</b> concentration (100 $\mu\text{M}$ -1 mM) fit to Eq. 4.9	229
Figure C19	Dixon plot of $v$ (Abs/min) versus inhibitor <b>R27</b> concentration (100 $\mu\text{M}$ -1 mM) fit to Eq. 4.9	230
Figure C20	Dixon plot of $v$ (Abs/min) versus inhibitor <b>R28</b> concentration (100 $\mu\text{M}$ -1 mM) fit to Eq. 4.9	230
Figure C21	Percent of spontaneously recovered <i>hAChE</i> activity after inhibition with inhibitor <b>R24</b>	232
Figure C22	Docking poses for each of the $\beta$ -lactam ligands under investigation in their respective lowest energy pose in the docking analysis	236



## LIST OF SCHEMES

Scheme 1.1	General reaction scheme for AChE catalyzed hydrolysis of choline esters	10
Scheme 1.2	AChE catalyzed hydrolysis of choline esters reaction scheme accounting for substrate inhibition	14
Scheme 2.1	Reaction scheme for oxime reactivation of OP inhibited AChE	29
Scheme 2.2	Proposed mechanism of aging for AChE-OP adduct	30
Scheme 2.3	Stepwise approach to kinetically evaluate recovery of aged-AChE activity	34
Scheme 2.4	General reaction scheme for preparation of sarin and soman OP analogues	35
Scheme 3.1	General mechanism of aging for AChE-OP adduct	61
Scheme 3.2	Concept for resurrection of an aged-AChE adduct	62
Scheme 3.3	Stepwise approach to kinetically evaluate recovery of aged-AChE activity	65
Scheme 4.1	Synthesis of Inhibitors <b>R24-R28</b> , (R = H, 5-F, 3-F, 5-CF <sub>3</sub> , or 4-N(Me) <sub>2</sub> )	96
Scheme 4.2	Mechanism corresponding to the reactions that were modeled computationally ( $\beta$ -Lactam 1 $\equiv$ <b>R24</b> )	113
Scheme 5.1	Synthesis of Inhibitors <b>R10</b>	120
Scheme 6.1	Reaction scheme for non-linear, non-competitive inhibition of <i>h</i> AChE	144

## CHAPTER 1: INTRODUCTION

### Acetylcholinesterase: Structure and Function

Acetylcholinesterase (acetylcholine acetylhydrolase, EC 3.1.1.7; abbreviated herein AChE) is one of the most catalytically efficient enzymes known to man. This powerful serine hydrolase is a subfamily of the cholinesterase enzymes, which are classified as being either AChE or butyrylcholinesterase (1). These subfamilies are distinguished by their substrate specificities and sensitivity to certain inhibitor types (2). AChE's primary function is to catalyze the hydrolytic decomposition of the neurotransmitter acetylcholine (ACh). More specifically, AChE operates in both the central and peripheral nervous systems to regulate impulse transmission triggered by the release of ACh at neuronal synapses (3). Regulation occurs near post-synaptic neuronal ACh receptors in the central nervous system and nicotinic ACh receptors at the neuromuscular junction following release across nerve-nerve or neuromuscular synapses (4, 5), (Fig. 1.1 and 1.2).

The essential role that AChE plays in terminating the action potential triggered by ACh's pre-synaptic release is recognized by its astounding bimolecular catalytic rate constant, ca.  $k_{cat}/K_m = 10^8 \text{ M}^{-1} \text{ s}^{-1}$  (5). AChE's adeptness at rapid hydrolysis of choline esters is largely attributed to the enzyme's two step mechanism of action initiated by acylation of the enzyme and a subsequent deacylation step (Fig. 1.3). Understanding AChE's catalytic mechanism requires a look into its structural composition, principally the enzyme's catalytic active site (esteratic site or catalytic triad) and allosteric sites.

Elucidation of *Torpedo californica* AChE's (*TcAChE*) amino acid sequence and X-ray crystal structure provided the first in-depth insight into AChE's kinetic behavior. This revealed the AChE catalytic active-site serine residue which lies near the base of a narrow gorge leading deep into the enzyme's center some 20 Å from its surface (6,7). The AChE active site consists of a catalytic triad of glutamate, histidine, and serine which work in concert for the general acid/base catalyzed hydrolysis of ACh (Fig. 1.3 and 1.4). Acetylation of the active-site serine residue completes the first mechanistic phase to generate the acylenzyme, which is then hydrolyzed by a conserved water molecule leading to substrate turnover and deacylation to restore the enzyme to its unbound state (4, 8). *Human* AChE's (*hAChE*) crystal structure showed similar structural composition and conservation of amino acid residues lining the catalytic gorge.

Structural analysis of AChE reveals sub-binding sites near the mouth of the catalytic gorge and in proximity of the enzyme's active site (Fig. 1.5). An anionic site bearing residues tryptophan, phenylalanine, and tyrosine interact with the quaternary ammonium group of ACh (9). On either side of the catalytic triad lies an acyl binding pocket and an oxyanion hole. Both the acyl binding pocket and oxyanion hole work to position ACh which helps to expedite nucleophilic attack of its carbonyl carbon by the active site serine hydroxyl group.

An additional allosteric binding site near the entrance of the AChE catalytic gorge is known as the peripheral anionic site (PAS) lying 14 Å from the enzyme's active-site. Of all the sub-binding sites of AChE, the PAS has long been suspected to play a critical role in initiating the enzyme's catalytic process and contributing to its inhibitory susceptibility (10). The PAS, which is comprised of two tyrosines, tryptophan, and

aspartate residues, functions as an additional binding site for the quaternary ammonium moiety of ACh and has been linked to the substrate inhibition compartment experienced at higher substrate concentrations (11). More so, the PAS has been implicated as a binding site for many non-competitive inhibitors of AChE in which the AChE catalytic rate is restricted due to electrostatic and steric blockade of substrate and product movement within the catalytic gorge (12).

Inhibitors binding specifically to the PAS inhibit via blockade or by affecting the structural conformation of the enzyme's catalytic triad. Discovery of the amino acid residues that comprise the catalytic triad and sub-binding sites was determined through various mutagenesis studies. To explicate the residues of *hAChE*'s active-site (Ser203, His447, Glu334), alanine was used to displace each of the integral residues yielding fully inactivated enzyme (13). Further substitutions of catalytic triad residues produced little to no activity towards substrate hydrolysis.

Delineation of the residues lining the catalytic gorge involved numerous AChE mutagens, particularly those substituting amino acid residues of the PAS. Such investigations accounted for effects on kinetic activity and binding affinity and along with molecular modeling provided topographic insights of the PAS (14). Site specific inhibitors, such as propidium, offer use of fluorescence detection in mutagenesis studies to further identify amino acid residues comprising the PAS and confirm structural features that contribute to AChE catalytic efficiency. AChE's PAS plays a critical role in substrate hydrolysis due to allosteric variations that can either aid in substrate access to the active site or inhibit enzyme activity due to PAS binding (14, 15, 16, 17).

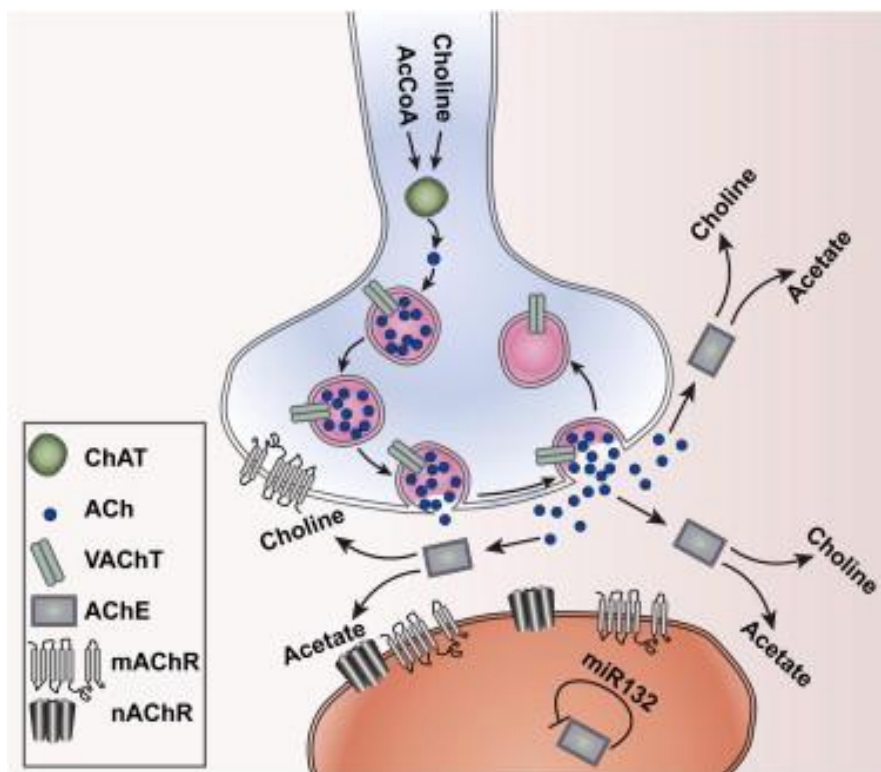


**Figure 1.1:** Pathway of ACh signal nerve-nerve transmission in the central nervous system

**Source:** Ofek, K.; and Soreq, H. *Chem. Biol. Interact.*, **2013**, 203, 113-119

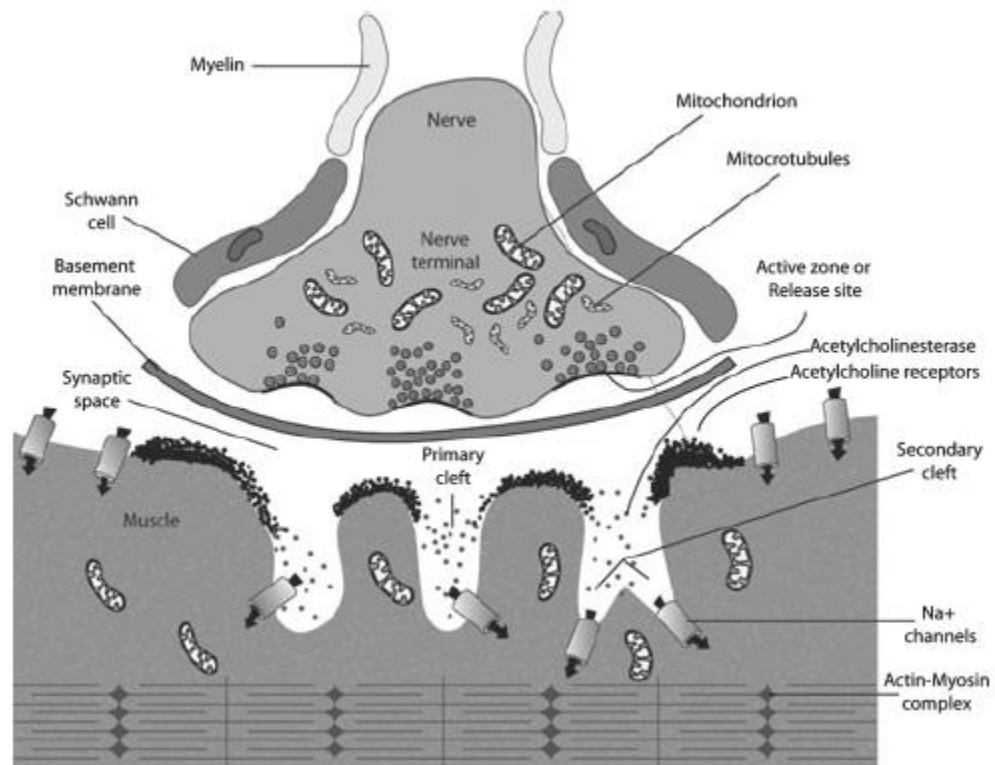


**Figure 1.2:** Structure and process summary of ACh triggered action potential across the neuromuscular junction.

Source: Martyn, J.A.J. et al., *Anaesthesia*, 2009,

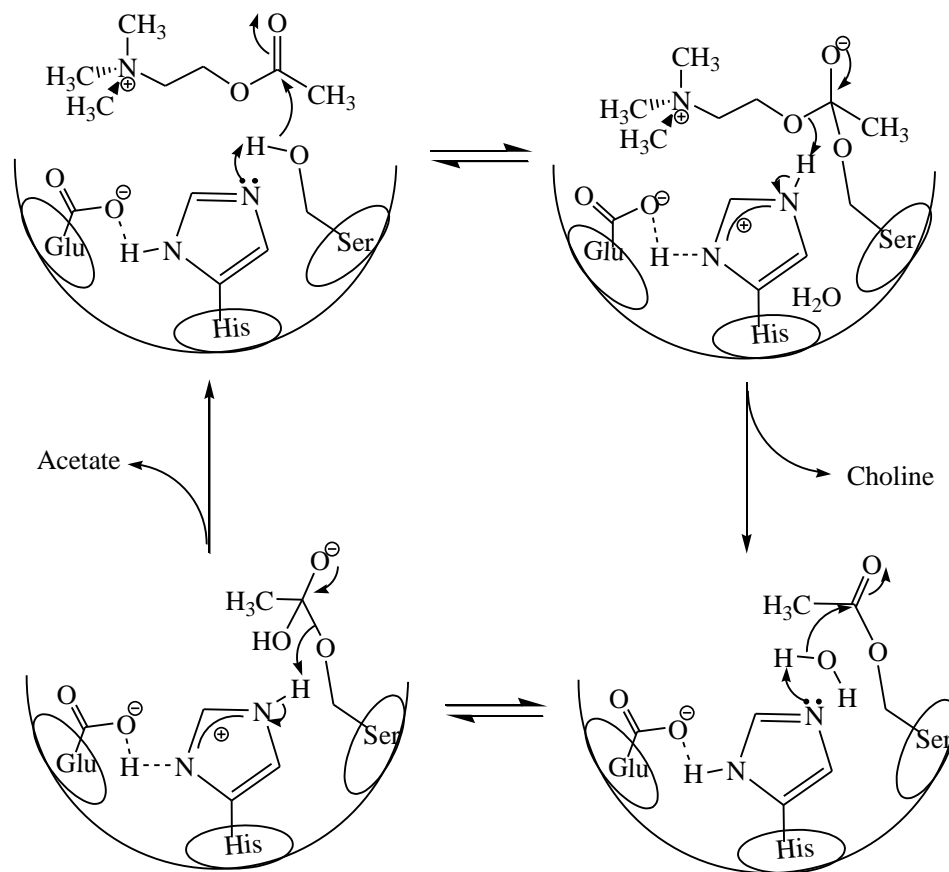


**Figure 1.3:** AChE catalytic mechanism of action.

**Source:** Delfino, R.T.; Ribeiro, T.S.; Figueroa-Villar, J.D. *J. Braz. Chem. Soc.*, **2009**, 20, 407-429

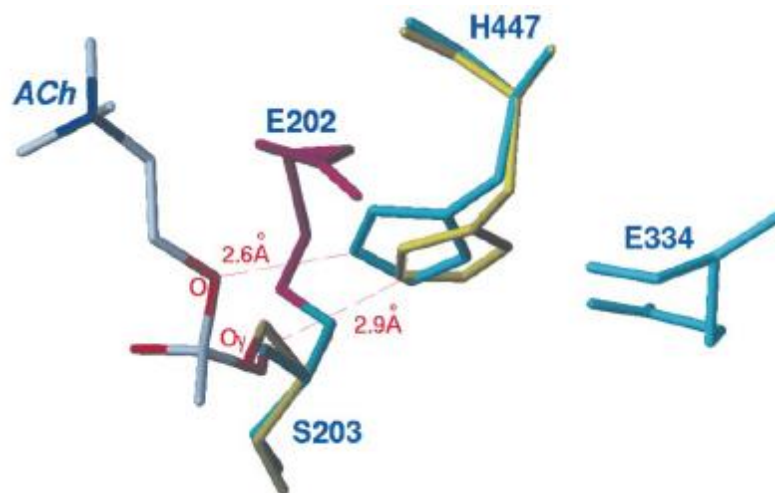


**Figure 1.4:** Model of the active site structure of *hAChE* bound to ACh

---

**Source:** Kryger, G. et al. *Acta Cryst. D*, **2000**, 56, 1385-1394



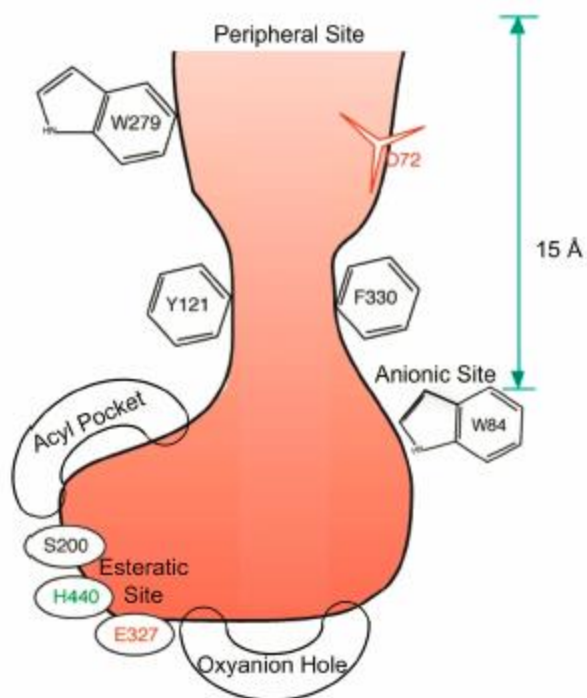


**Figure 1.5:** Active-site gorge schematic for *TcAChE* highlighting sub-binding sites and catalytic active site (esteratic site).

---

**Source:** Dvir, H. et al. *Chem. Biol. Interact.*, **2010**, 187, 10-22

AChE is expressed in cells that have non-cholinergic functions within the mammalian body. Investigations into AChE's non-cholinergic activities have revealed subtle differences in structural conformation due to cell location, origin, and physiological function (18). This is evidenced by varied polymorphisms that differ in both soluble and membrane bound forms of the AChE enzyme (19). One well studied secondary function of AChE reports trypsin-like protease behavior (20). An additional non-cholinergic function of AChE is related to its PAS, where it has been linked to the production and deposit of  $\beta$ -amyloid plaques in Alzheimer's disease (AD) sufferers (21).

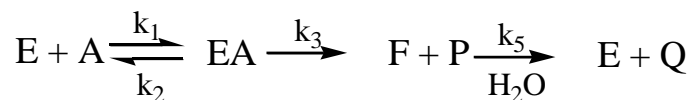
The structure of AChE attributes greatly to its powerful catalytic activity. This quality paired with a voluminous number of substrates metabolized by AChE makes it very susceptible to inhibition. Inhibition of AChE has effects that are useful in the treatment of neurodegenerative diseases including AD. Contrarily, AChE is a target of powerful nerve agents, organophosphates (OP), for which acute exposure can be fatal (22). AChE's utility in both central and peripheral neurological functions makes its inhibition by OPs an area of great concern.

#### Kinetic Behavior of Acetylcholinesterase

Cholinesterases are characterized by the voluminous number of substrates, which include aryl esters, selenoesters, carbamates, analogues of ACh, and various other substrate families (3). Given its promiscuous nature, AChE's catalytic range of substrates is overshadowed by the astounding catalytic rate of ACh hydrolysis ( $k_{\text{cat}} = 10^4 \text{ s}^{-1}$ ) which provides a  $10^{13}$  fold increase over spontaneous ester hydrolysis (23).

Scheme 1.1 represents the simplest chemical equation for AChE catalyzed hydrolysis of a choline ester substrate. ACh hydrolysis is preceded by reversible

substrate binding, which is followed through to the first irreversible step to form the acylenzyme and subsequent deacylation.



**Scheme 1.1:** General reaction scheme for AChE catalyzed hydrolysis of choline esters (23).

In Scheme 1.1, E is free enzyme, A is free substrate, EA is the Michaelis complex, F is the acylenzyme intermediate, and P & Q represent choline and acetate products. The bimolecular rate constant ( $k_{cat}/K_m \equiv k_E$ ) is represented by Eq. 1.1:

$$k_E \equiv \frac{k_{cat}}{K_m} = \frac{V_{max}}{K_m[E]_T} = \frac{k_1 k_3}{k_2 + k_3}$$

**Equation 1.1:** Kinetic expression for the bimolecular rate constant derived from Scheme 1.1.  $k_E \equiv$  bimolecular rate constant;  $k_{cat} \equiv$  catalytic turnover number;  $V_{max} \equiv$  maximum velocity;  $K_m \equiv$  Michaelis constant;  $[E]_T \equiv$  total enzyme concentration

where  $k_1$  is the microscopic second-order rate constant for the substrate binding step and  $k_3$  is the microscopic first-order rate constant for the chemical step to form the acylenzyme intermediate (acylation step) (23). As depicted in Fig. 1.3, substrate binding is followed by the formation of a tetrahedral intermediate which is then followed by release of choline product and formation of the acylenzyme. Formation of a second tetrahedral intermediate is effected by nucleophilic attack by water, and subsequent deacylation releases acetate and regenerates free enzyme.

As demarcated in Scheme 1.1,  $k_{cat}$  and  $K_m$  are represented by Eqs. 1.2 and 1.3 respectively (1):

$$k_{cat} = \frac{k_3 k_5}{k_3 + k_5}$$

**Equation 1.2:** Kinetic expression of the rate constant for catalytic turnover ( $k_{cat}$ ) of ACh to product by AChE following reaction Scheme 1.1

$$K_m = \frac{k_2 + k_3}{k_1} \times \frac{k_5}{k_3 + k_5}$$

**Equation 1.3:** Kinetic expression for the Michaelis constant ( $K_m$ ) derived from Scheme 1.1

We can derive the Michaelis-Menten equation (Eq. 1.4) using the kinetic variables defined by the preceding equations.

$$V_i = \frac{V_{max}[A]}{K_m + [A]}$$

**Equation 1.4:** Michaelis-Menten equation, where  $V_i \equiv$  initial velocity,  $V_{max} \equiv$  maximum velocity which is further defined by  $V_{max} = k_{cat}[E]_T$ ,  $K_m \equiv$  Michaelis constant,  $[A] \equiv$  substrate concentration, and  $[E]_T \equiv$  total enzyme concentration

The observed efficiency of AChE's catalysis and corresponding kinetic variables innately diminish the rate-limiting effects of transition state formation experienced in the enzyme's mechanism (23). Kinetic complexity for AChE arises in terms of clearly identifying the mechanistic phenomena affecting hydrolysis rate. Such limitations are attributed to diffusion rate to the enzyme's active site (reversible step,  $k_1$ ), acylation (first catalytic step,  $k_3$ ), or deacylation (second catalytic step,  $k_5$ ).

Kinetic isotope effect (KIE) studies have assigned an observed secondary isotope effect for AChE wherewith rate-limitations are described for reversible and catalytic

steps (23, 24). KIE studies confirm prior research reports that AChE deviates from standard Michaelis-Menten kinetic behavior and experiences substrate inhibition (1, 3, 23, 24, 25). This singularity distinguishes AChE from its subfamily counterpart butyrylcholinesterase, for which activation is observed at high substrate concentrations.

ACh's thiol ester analogue, acetylthiocholine (ATCh), is often utilized in kinetic studies and is the substrate of choice in the standard Ellman kinetic assay method (26). Isotopic analogues of ATCh are used in KIE studies to pinpoint idiosyncrasies of the AChE mechanism of action. Secondary KIE studies reveal the deacylating step to be rate-limiting at high substrate concentrations for *hAChE* and *Drosophila melanogaster* AChE (*DmAChE*). The secondary KIE converts from an inverse KIE (on  $k_{cat}/K_m$ ) to a normal KIE (catalytic step,  $k_{cat}$ ) with increased substrate concentration, suggesting that the rate-limiting step is linked to a conversion from the second tetrahedral intermediate to the final hydrolysis product ( $sp^3$  to  $sp^2$  hybridization, Fig. 1.6) (24). Therefore, it is inferred that product accumulation occurs to attribute to the rate-limiting deacylation step.

Understanding these mechanistic complexities helps to expand the general reaction scheme for AChE catalyzed hydrolysis. At low substrate concentrations, AChE catalyzed hydrolysis follows traditional Michaelis-Menten kinetics as derived from Scheme 1.1. One key feature of the AChE enzyme structure is the presence of an allosteric binding site (PAS), which is implicated in playing a key role in the observed substrate inhibition. Uniquely, binding of substrate at low concentrations to the PAS has been proven to accelerate AChE catalyzed hydrolysis. This was proven through molecular modeling studies that indicated increased association rate constants in the case

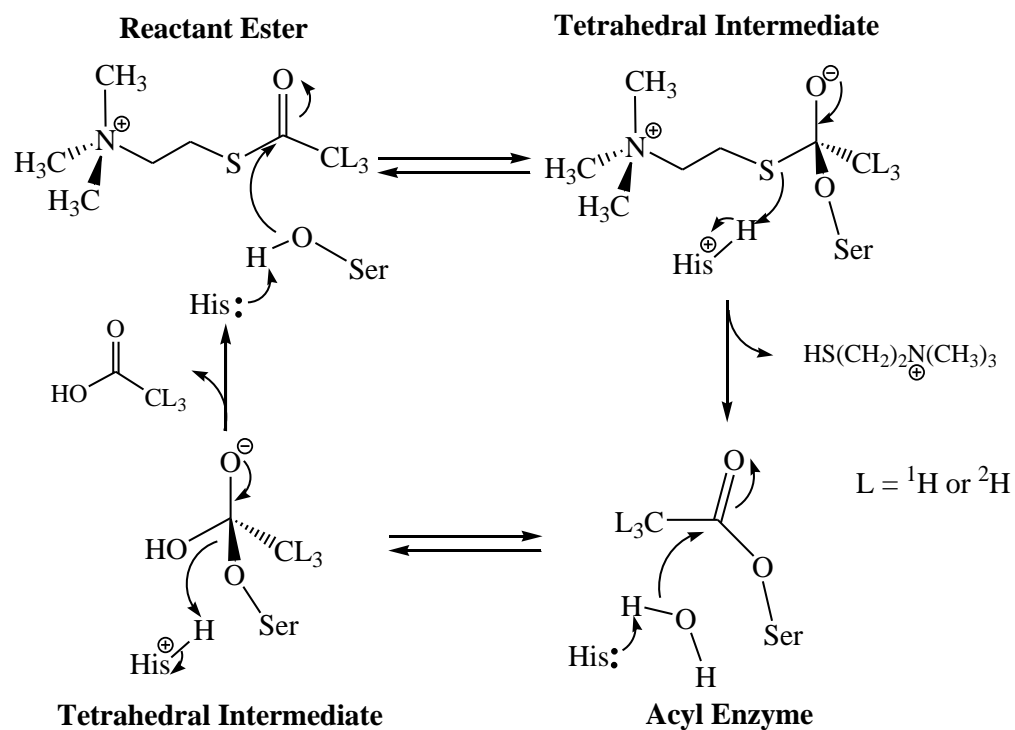
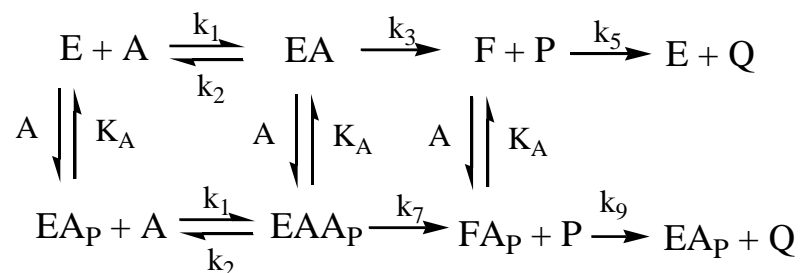


**Figure 1.6:** Mechanism of action for AChE hydrolysis of acetyl-L<sub>3</sub>-thiocholine substrates. Secondary kinetic isotope effects were measured to identify rate-limiting steps in the enzyme's mechanism.

**Source:** Tormos, J.R.; Wiley, K.L.; Wang, Y.; Fournier, D.; Masson, P.; Nachon, F.; and Quinn, D.M. *J. Am. Chem. Soc.*, **2010**, 132, 17751-17759

of cationic substrates (27). It has been proposed that substrate binding to the PAS induces a change in active site conformation leading to increased activity.



E ≡ free enzyme; A ≡ free substrate; EA ≡ Michaelis complex; F ≡ acylenzyme intermediate; EAA<sub>P</sub> ≡ ternary complex with PAS bound substrate; FA<sub>P</sub> ≡ acylenzyme-substrate complex; EA<sub>P</sub> ≡ PAS bound enzyme-substrate complex; P ≡ choline product; Q ≡ acetate product

**Scheme 1.2:** AChE catalyzed hydrolysis of choline esters reaction scheme accounting for substrate inhibition.

The bottom half of Scheme 1.2 expounds on the AChE catalytic reaction at high substrate concentrations, where excess substrate binds to the PAS. Here substrate binds reversibly to the peripheral site throughout each reversible and catalytic step until consecutive hydrolysis products are released (28). Substrate is also noted to bind to the PAS for all forms of the enzyme, which include the Michaelis complex and acylenzyme intermediate forms. The steric blockade model is largely associated with this observed substrate inhibition, but whether this is the sole cause of inhibition raises many questions. Decreases in substrate association and product dissociation rates allude to a more complex inhibitory model. PAS bound substrate at high concentrations not only blocks product release and substrate migration to the active site, but it effectively slows deacylation rate. Deacylation rate is thought to be slowed as a result of substrate

blocking nucleophilic attack of water in the enzymes active site (27, 28, 29). This is further supported by KIE and kinetic inhibition studies showing deacylation as the rate-limiting step (24, 27).

### Inhibition of Acetylcholinesterase

Acetylcholinesterase (AChE) plays an integral part in regulating impulse transmission of the neurotransmitter ACh. As previously described, AChE's catalytic efficiency is powered by the binding of substrate to an active site serine residue lying at the bottom of a 20 Å deep catalytic gorge. Substrate access to the enzyme's esteratic site experiences allosteric regulation by binding to a peripheral anionic site. It has also been well established that AChE deviates from standard Michaelis-Menten kinetics at high substrate concentrations and undergoes substrate inhibition (26, 27, 28, 29).

Additionally, AChE has been proven to function in cholinergic and non-cholinergic capacities (18). Inhibition of AChE has been profiled through kinetic studies, changes in inhibitor properties post AChE binding, mutagenesis studies, and analysis of inhibitor bound AChE X-ray crystal structures, to name a few. In general, AChE inhibitors are classified as active site (competitive) or PAS (non-competitive) inhibitors.

Inhibition of AChE is a particular research area of interest for various reasons. Its inhibition is notably targeted in the treatment of neurological disorders or by toxic chemical warfare nerve agents. In the case of the former, AChE inhibition helps to lessen the extent of ACh regulation in order to increase neurological or neuromuscular activity. AChE inhibition is targeted in the treatment of myasthenia gravis, glaucoma, and Alzheimer's Disease (AD) (30, 31, 32). Treatment of myasthenia gravis and glaucoma target AChE near nicotinic-ACh receptors lining neuromuscular junctions, where AChE



inhibition serves to increase binding at ACh receptors. For Alzheimer's Disease (AD) treatment, AChE inhibition targets the cholinergic pathway of nerve-nerve impulse transmission in the central nervous system. AD is a progressive neurodegenerative disorder originating in the basal forebrain and is projected to result in the death of more than 450,000 sufferers in the United States alone, making it the 6<sup>th</sup> leading cause of death world-wide (32).

Pinpointing a specific pathogenesis for AD has been challenging, however, the progression of the disease is attributed to the formation of  $\beta$ -amyloid plaques and tau fibrils which serves to disrupt several neuronal pathways (33). The most prominent symptoms of AD are acute dementia and an overall deterioration of cognitive function. Because of the pronounced cognitive effects on AD sufferers, 4 of the 5 current AD drug treatments target the cholinergic pathway (AChE inhibition) (34). Fig. 1.7 shows several examples of AChE inhibitors used for AD drug treatment (35). AChE has also been speculated to play a key role in the acceleration of  $\beta$ -amyloid plaque deposits in the brain (21,36). This particular non-cholinergic function is linked to the enzyme's PAS, where site-specific mutagenesis proved to have a significant effect on  $\beta$ -amyloid production.

One of the first AChE inhibitors approved for AD treatment was the reversible inhibitor tacrine, however its very negative side effects proved to be less favorable for long-term use (37). Two of the current and more widely used AChE inhibitors, rivastigmine (Exelon<sup>®</sup>) and donepezil (Aricept<sup>®</sup>), are competitive and noncompetitive inhibitors respectively (38). Rivastigmine carbamoylates the AChE esteratic site and hydrolyzes significantly slowly. In the case of the reversible inhibitor donepezil, it

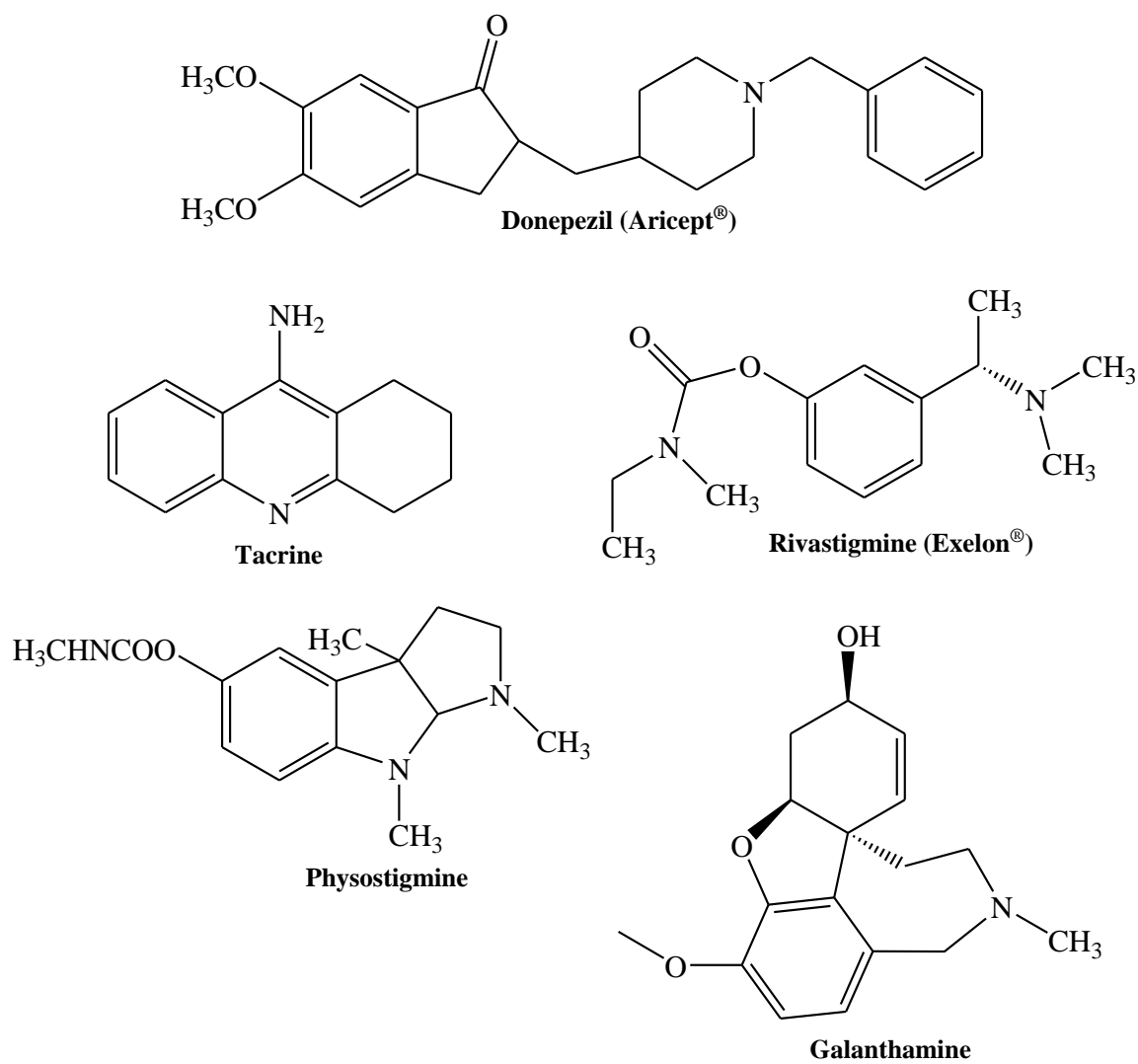


**Figure 1.7:** Inhibitors of human acetylcholinesterase (*hAChE*) and drug treatments for Alzheimer's Disease.

provides a unique inhibitory profile in that its structure extends from the AChE peripheral site down to the bottom of the catalytic gorge (39). The indanone core of donepezil binds to the enzyme's PAS, while its piperidine unit and benzyl tail interact with residues lining the gorge extending to the enzyme's acyl binding pocket. Donepezil's potency ( $IC_{50} = \sim 5 \text{ nM}$ ) is attributed to this "gorge-spanning" character such that its inhibition is characterized as mixed and not purely non-competitive.

The opposing spectrum of AChE inhibition involves that of highly toxic organophosphate chemical warfare agents (CWA). CWAs have had documented use since early civilization, for which dangerous organophosphorus (OP) agents were developed throughout the World War II era. Stockpiles of these lethal OPs, estimated to be over 25,000 tons in the United States alone, pose a major threat to communities worldwide (40). Ease of synthesis creates an added threat of OP use by domestic and international terrorists, as evidenced by their use in the Tokyo subway attacks and against Kurdish civilians by Iraqi soldiers (41). A good number of OPs serve as pesticides, for which human exposure causes 200,000 deaths annually.

These nefarious nerve agents are differentiated from other CWAs as they specifically attack the active-site of AChE and are exceptionally potent. OP's acute toxicity is afforded to its ability to covalently bind rapidly to the active site serine of AChE, where it also binds irreversibly. The structural composition of OPs contribute greatly to their potency as well, which is comprised of a phosphorous (V) center bearing a terminal oxygen, two alkoxy substituents, and an alkyl substituent (42).

Fig. 1.8 depicts the mechanism of action for OP inhibition of AChE. The initial catalytic process for OP inhibition is similar to that of the native hydrolysis reaction with ACh.

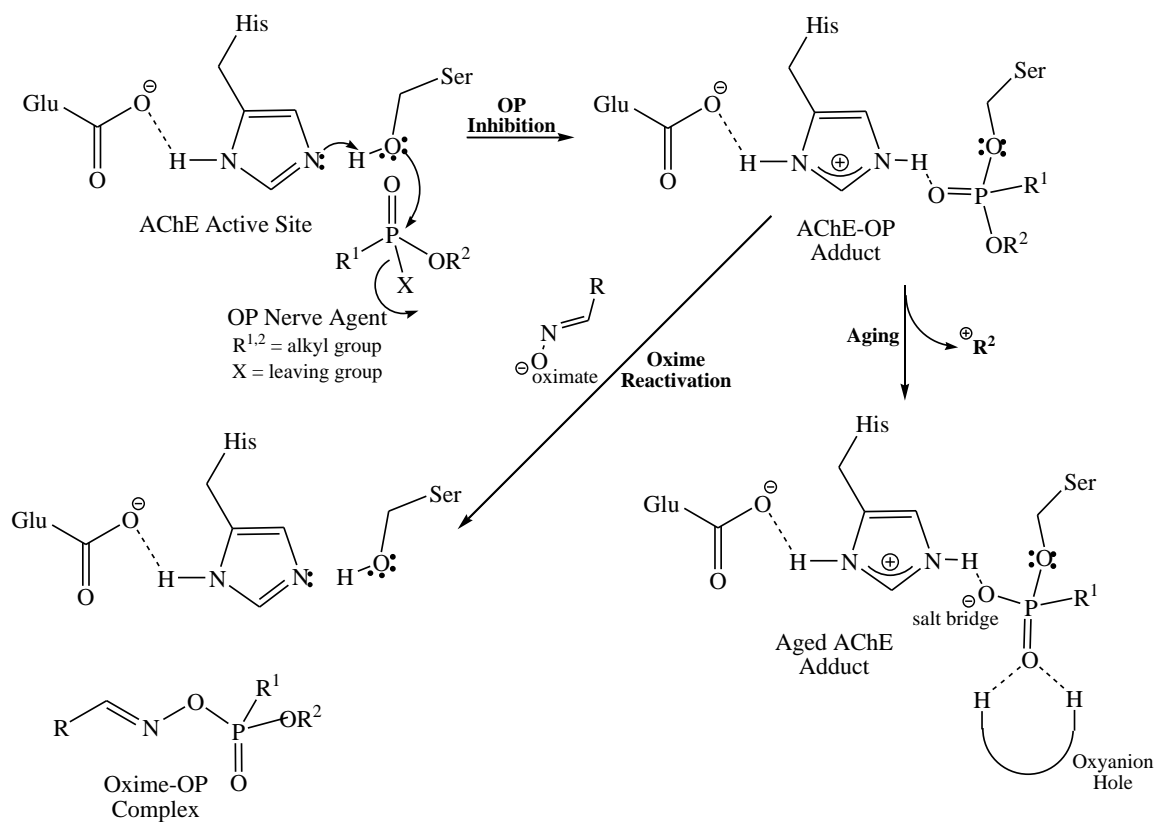


**Figure 1.8:** Mechanism of action for the inhibition, oxime reactivation, and aging of AChE by OP nerve agent

Nucleophilic attack by the esteratic site serine residue on the OP phosphorous center leads to the formation of a phosphorylated AChE adduct (AChE-OP adduct) resembling the tetrahedral intermediate of ACh hydrolysis (3). OP inactivated AChE results in loss of enzymatic activity, terminating its ability to regulate ACh levels at neuronal synapses. If untreated upon exposure (even at sub-lethal doses), ACh accumulation occurs that results in the saturation and subsequent overstimulation of nicotinic ACh receptors in the neuromuscular junction. Seizures, paralysis, and muscle fasciculation ensue due to this hyper-stimulation and can ultimately lead to death.

Once the OP-AChE adduct is formed, the enzyme can undergo reactivation by nucleophilic attack by water or an oxime reactivator to generate the free enzyme. Depending on the structure of the OP, spontaneous hydrolysis occurs very slowly or not at all making treatment with an oxime nucleophile the most effective means to recover AChE activity. Oxime reactivators (i.e. 2-PAM, Fig. 1.9) are part of an antidotal cocktail administered along with diazepam and atropine, delivered by a spring-loaded syringe following OP exposure (41, 42, 43). A secondary pathway termed “aging” can occur simultaneously in which the alkoxy substituent undergoes intramolecular dealkylation to form an AChE bound phosphoryl anion in the enzyme’s active site. The aged-AChE adduct is stabilized through H-bonding interactions to form a salt bridge between the phosphoryl oxyanion and the protonated nitrogen of the active site histidine. Treatment with oxime nucleophiles of an aged-AChE adduct is rendered ineffective because nucleophilic attack is prevented (41).

Although oxime use is effective in treating exposure to most nerve agents, there has been little advancement to current oxime treatment protocols since their initial

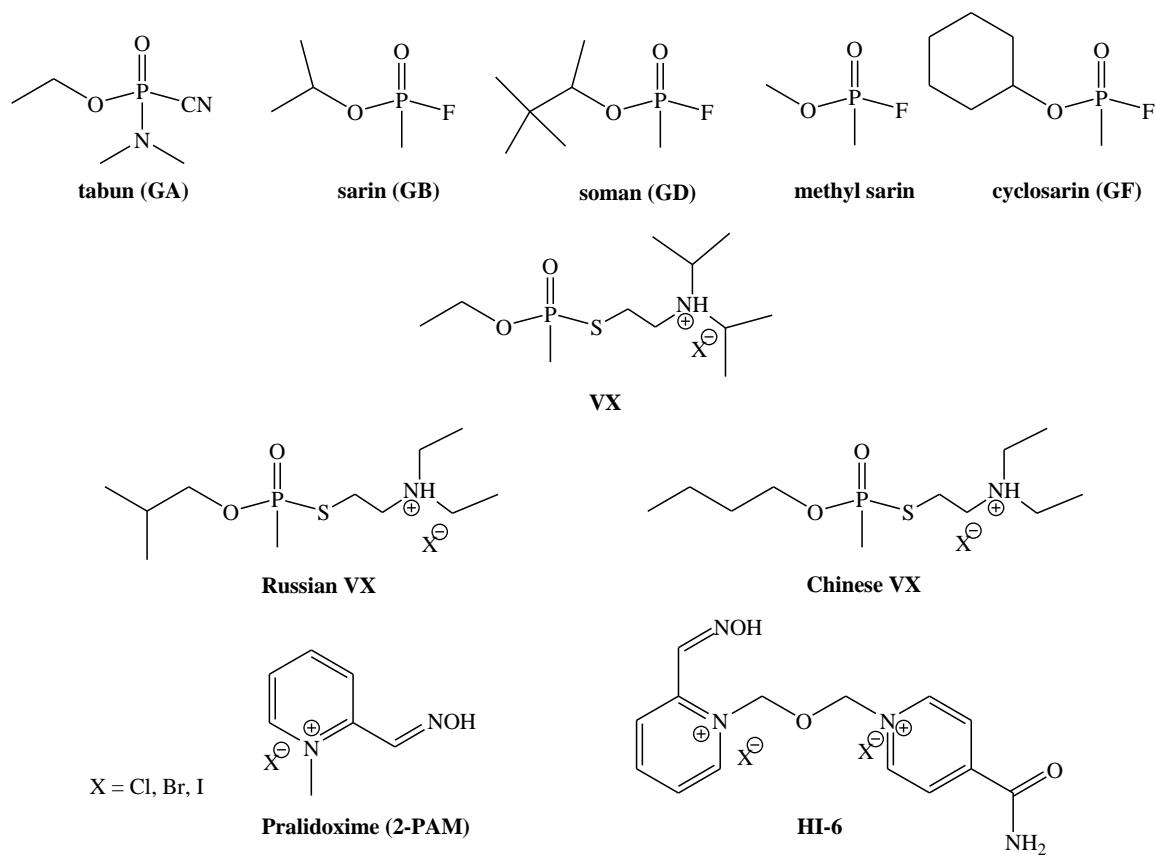


**Figure 1.9:** Chemical structures of well-known organophosphorus nerve agents and oxime antidotes

discovery in the 1940s (44, 45, 46). Greater interest in this area of AChE inhibition has centered on developing novel oximes, preventative measures, and OP detection technology. Despite such efforts, no known advancements have been reported to address the simultaneous “aging” process (41, 42). Aging of the phosphyl-AChE adduct occurs at different rates, depending on the structure of the OP. Powerful OP nerve agents sarin and soman (Fig. 1.9) have an aging half-life of 3 hours and 3 min, respectively (47, 48). It is abundantly clear that improvements regarding oxime efficacy fails to address the detrimental results of aging, especially with highly toxic OPs like sarin and soman.

#### Objectives of Study

The objectives of this study are to address several areas of interest regarding the inhibition and reactivation of recombinant human acetylcholinesterase (*hAChE*). This study will describe the synthesis of organophosphate inhibitor analogues and their kinetic evaluation for *hAChE* inhibition and aging. Further, we outline the development of an enzyme assay method for recovery of aged *hAChE* activity, which we have termed the “resurrection” assay, and kinetic evaluation of several classes of “resurrecting” compounds. Additionally, the inhibition kinetics profiles of pyridinium inhibitors ( $\beta$ -lactam & 6-fluoro-2-methoxy), ladderane, and paracyclophane inhibitors are described herein.

## CHAPTER 2: SYNTHESIS AND KINETIC EVALUATION OF ORGANOPHOSPHONATE INHIBITORS OF ACETYLCHOLINESTERASE

### Chemical Mechanism and Significance

Acetylcholinesterase (AChE) is a powerful enzyme in the serine hydrolase family that functions in mammalian central and peripheral nervous systems (*1*). Its primary function is the catalytic hydrolysis of the neurotransmitter acetylcholine (ACh), which produces an action potential across nerve-nerve and neuromuscular synapses. AChE's astounding ability to breakdown ACh ( $k_{\text{cat}} = 10^4 \text{ s}^{-1}$ ) works to efficiently regulate nerve impulse transmissions (*3, 23*). Since its discovery, AChE's structure, catalytic mechanism, inhibition, and non-cholinergic functions have been comprehensively investigated (*3, 6, 9, 20, 30*). Given the capacious amount of information regarding AChE's enzyme kinetic activity, one very significant area of research is its inhibition by chemical warfare agents (CWA).

CWAs have long been used in combat, dating back to 500 BC. Their use in modern warfare led to the discovery of a sinister class of nerve agents, organophosphorus (OP) agents (*49*). The OP nerve agent tabun (Fig 2.1) was originally discovered by German scientists during World War II, so all OPs of its structural type are termed German or G-type. During and post-World War II, OP advances continued with the development of more G-type OPs and venom-type OPs (i.e. VX) (*41*). Military stockpiles of OP nerve agents were eventually generated by several nations including the United States, reporting over 25,000 tons in military storage to date. Following the 1993 Chemical Weapons Convention, the destruction of OP stockpiles became an international



effort. With the recent war against domestic and international terrorists, greater attention to the regulation and urgent need to account for OP nerve agents has arisen. Iraqi attacks against Kurdish civilians, the Tokyo subway attacks, and the U.S. World Trade Center attack have made researching better prophylactic and therapeutic measures to OP exposure a high priority. Additionally, OP use as agricultural pesticides leading to over 200,000 fatalities world-wide adds to this need for better OP countermeasures (41).

As described in Chapter 1, the structural composition of OPs contributes greatly to their potent and lethal behavior. OP nerve agents exploit the AChE mechanism (Fig 2.2) of action by acting as “hemisubstrates”. Native substrate hydrolysis involves a two-stage acylation and deacylation process, where each stage involves the formation of a tetrahedral intermediate (50). Similar to the intrinsic mechanism for ACh hydrolysis, AChE’s active-site serine attacks the phosphorus center of OPs. Upon phosphorylation, a stabilized AChE-OP adduct that resembles the tetrahedral intermediate state experienced in the ACh hydrolysis mechanism forms (Fig. 2.3). Once covalently bound, the enzyme remains in the AChE-OP adduct state for hours or even days without undergoing hydrolysis to recover active enzyme. This has been attributed to the inability of water to effectively attack the phosphyl adduct in a similar fashion of the ACh hydrolysis mechanism.

X-ray crystal structure analysis of OP bound AChE sheds considerable light on the conformational shifts in the enzyme’s active site contributing to the enzyme’s inability to rapidly recover from OP exposure (50). The enzyme’s dependence on the base catalyzed hydrolysis involving the His and Glu residues of its catalytic site also leads to its incapacity once inhibited by an OP. Crystal structures of VX bound *TcAChE*

reveals that the phosphonyl adduct disrupts the hydrogen bonding network in the enzyme's catalytic gorge. This effectively mobilizes the active-site His residue such that nucleophilic attack by water is sterically unfavorable (9, 51). Recovery of an active-site conformation reminiscent of native AChE only occurs after reactivation with a nucleophile (i.e. oxime treatment) or dealkylation of the phosphonyl adduct (aging).

Reactivation of OP inhibited AChE occurs through either spontaneous nucleophilic attack by water or treatment with potent nucleophiles. In 1951, hydroxyl amine was discovered to counteract the effects of phosphylated AChE and reactivate enzymatic activity (52). Oxime use to regenerate OP inhibited AChE activity was first employed in treating Japanese soldiers in 1956, where the oxime 2-PAM was used (44, 53). The development of bispyridinium oximes (i.e. HI-6, Fig. 2.1) soon followed this therapeutic discovery. 2-PAM's ability to effectively alleviate the inhibitory action of OPs lies in its affinity for the AChE enzyme. Its quaternary pyridinium structure promotes binding at the AChE PAS, however, it acts only as a mild, reversible inhibitor of AChE ( $IC_{50} = \text{ca. } 100 \mu\text{M}$ ) (54). Current clinical administration of oxime therapy to nerve agent exposure is as a cocktail with the muscarinic antagonist atropine and anticonvulsant diazepam. Although the discovery of 2-PAM as an antidotal remedy for OP exposure was over a half a century ago, little advancements in clinical treatment has occurred (61).

Reactivation of OP inhibited AChE follows Scheme 2.1. When the effective oxime concentration is relatively large compared to the AChE-OP adduct concentration ( $[\text{Oxime}] \gg [\text{E-OP}]$ ), the rate of oxime induced reactivation is pseudo-first order and defined by Eq. 2.1. The reactivation rate is second-order ( $k_{r2}$ ) when the oxime

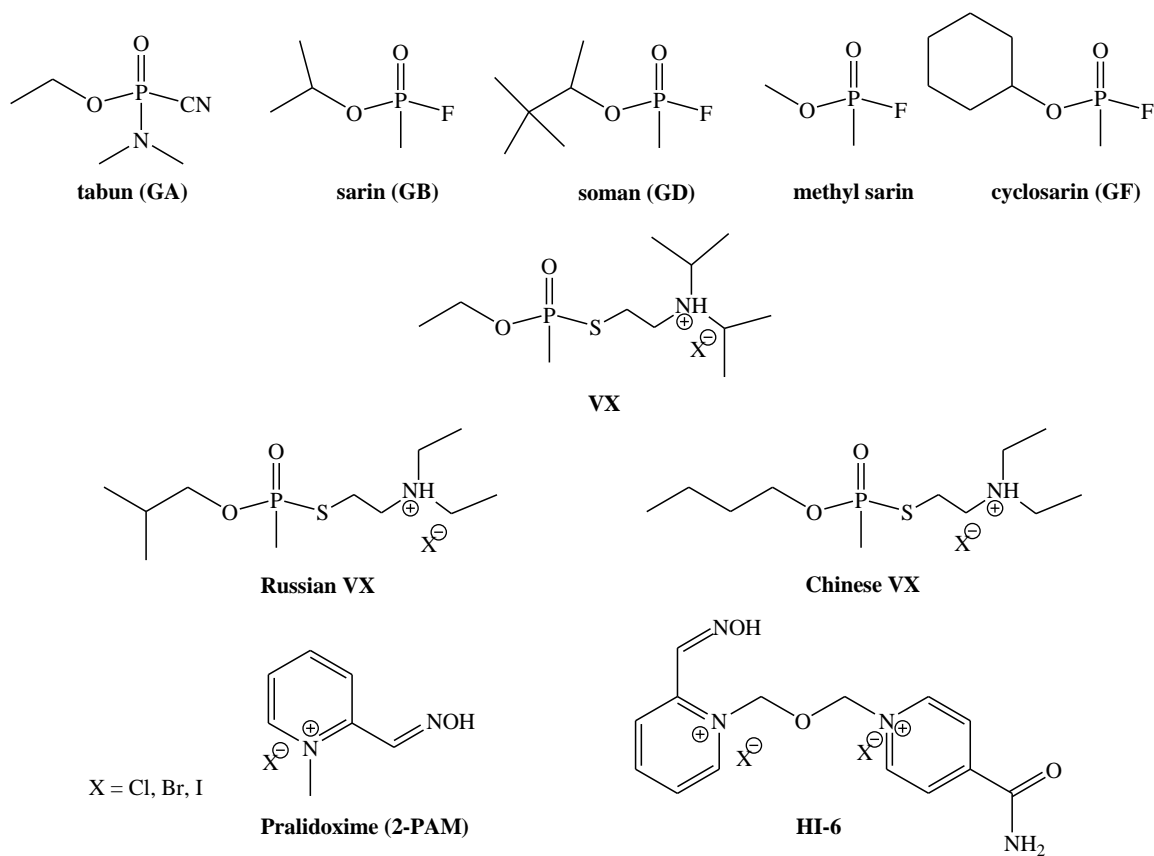


**Figure 2.1:** Chemical structures of well-known organophosphorus nerve agents and oxime antidotes

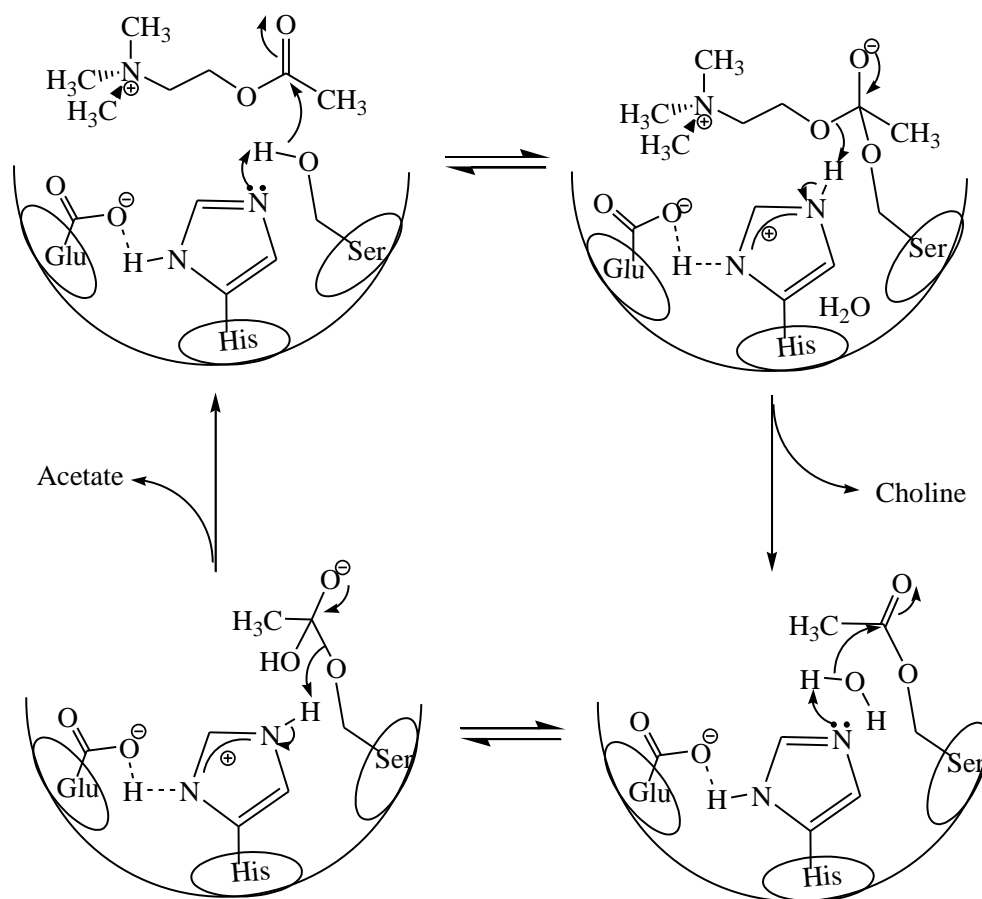


**Figure 2.2:** AChE catalytic mechanism of action.

**Source:** Delfino, R.T.; Ribeiro, T.S.; FigueroaVillar, J.D. *J. Braz. Chem. Soc.*, **2009**, 20, 407-429

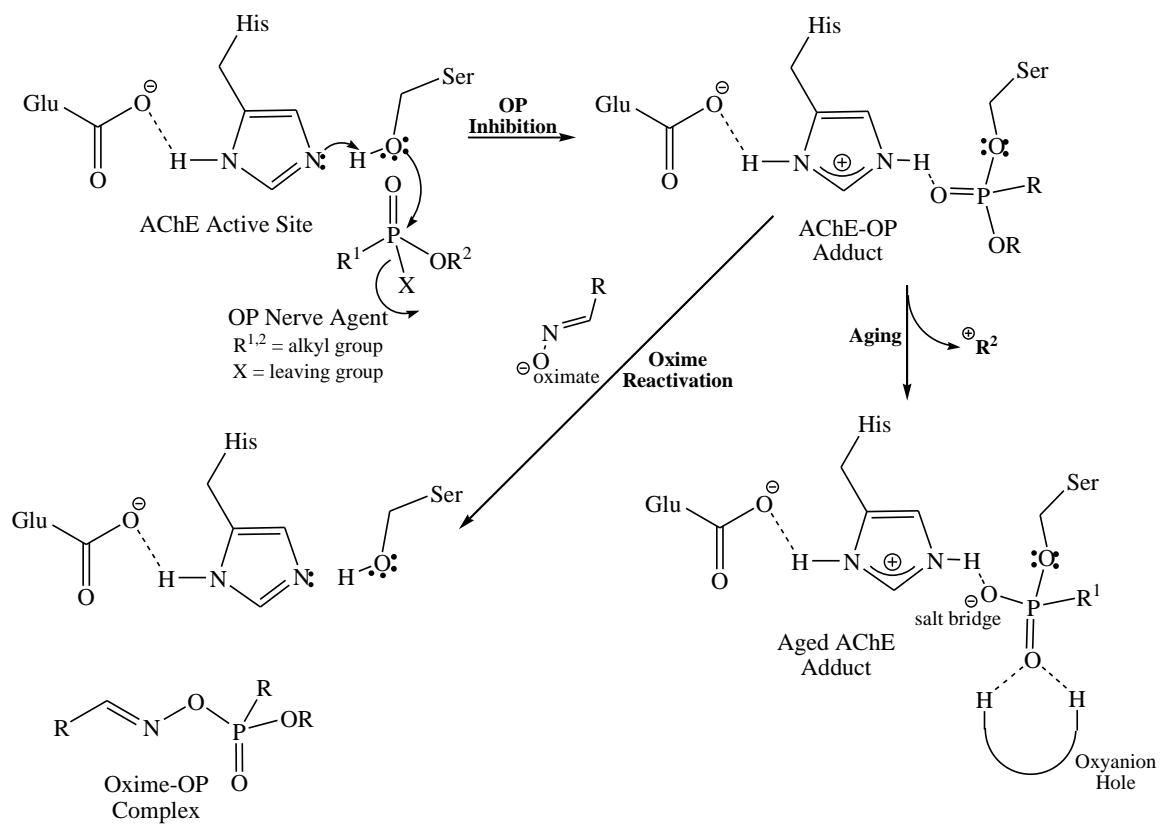
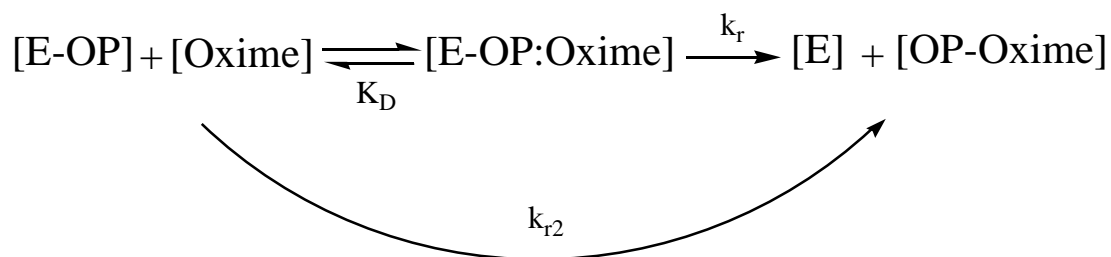


**Figure 2.3:** Mechanism of action for the inhibition, oxime reactivation, and aging of AChE by OP nerve agent

concentration is relatively small compared to  $K_D$ , the dissociation constant associated with oxime binding to the AChE-OP adduct (47). Eq. 2.2 defines the kinetic relationship for second-order reactivation of AChE-OP with oxime.



**Scheme 2.1:** Reaction scheme for oxime reactivation of OP inhibited AChE. [E-OP]  $\equiv$  AChE-OP adduct; [Oxime]  $\equiv$  oxime concentration (i.e. 2-PAM); [E-OP:Oxime]  $\equiv$  oxime bound AChE-OP Michaelis-like complex; [E]  $\equiv$  free AChE; [OP-Oxime]  $\equiv$  phosphylated oxime;  $K_D$   $\equiv$  dissociation constant for oxime bound AChE-OP complex;  $k_r$   $\equiv$  rate constant for phosphyl displacement;  $k_{r2}$   $\equiv$  second-order rate constant for phosphyl displacement

$$k_{obs} = \frac{k_r [Oxime]}{K_D + [Oxime]}$$

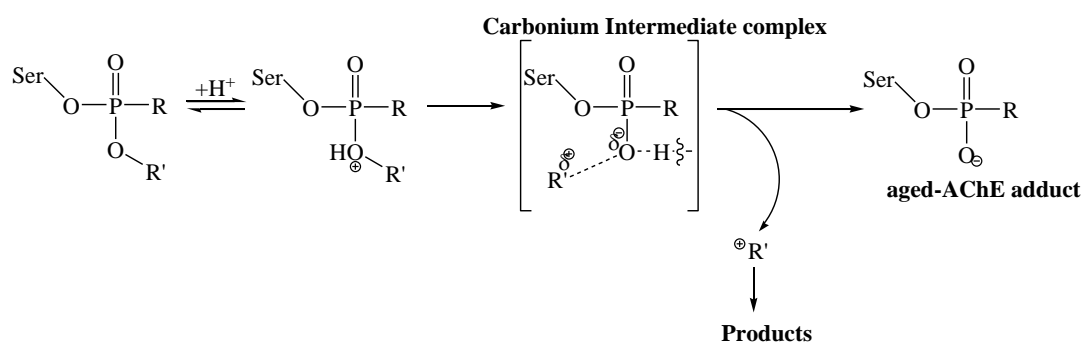
**Equation 2.1:** Rate equation for reactivation of AChE-OP adduct as a function of oxime concentration.

$$k_{obs} = \left(\frac{k_r}{K_D}\right) [Oxime]; k_{r2} = \frac{k_{obs}}{[Oxime]} = \frac{k_r}{K_D}$$

**Equation 2.2:** Second-order reactivation rate equation where  $k_{r2}$  is subsequently derived as the ratio of the first-order rate constant ( $k_r$ ) and the dissociation constant for the oxime bound AChE-OP adduct ( $K_D$ ).

As mentioned previously, the AChE active-site undergoes a conformational shift of the catalytic-triad's His residue (51). An alternative process to nucleophilic recovery of the AChE's active site conformation is the intramolecular dealkylation of the phosphyl

moiety, a process termed “aging”, which forms an enzyme-bound phosphyl oxyanion (41). A salt bridge between the phosphyl oxyanion and the protonated nitrogen of the active site histidine stabilizes the aged-AChE adduct in the enzyme’s catalytic gorge. Treatment with oxime nucleophiles fails to recover activity once the aged-AChE adduct forms. The exact mechanism of aging is still highly contested, however, it is conceded that residues in AChE’s binding pocket facilitates dealkylation of the phosphyl alkoxyl group. Prevailing views describe the aging as an acid/base “push-pull” mechanism that is dependent on a latent Glu residue in the enzymes catalytic site, a process that yields a carbonium intermediate apt to nucleophilic attack or elimination product formation (55, 56, 57). Alternatively, the opposing notion to the mechanism of aging is one that lessens the dependence of the latent Glu residue and supports a  $\pi$ - $\pi$ /cation- $\pi$  driven mechanism critically dependent on the Trp residue of the AChE anionic site and a Phe residue near the acyl binding pocket (58, 59, 60). Notwithstanding the driving force behind aging of the AChE-OP adduct, it can be agreed that the general dealkylation mechanism follows Scheme 2.2.



**Scheme 2.2:** Proposed mechanism of aging for AChE-OP adduct. R, R'  $\equiv$  alkyl substituents

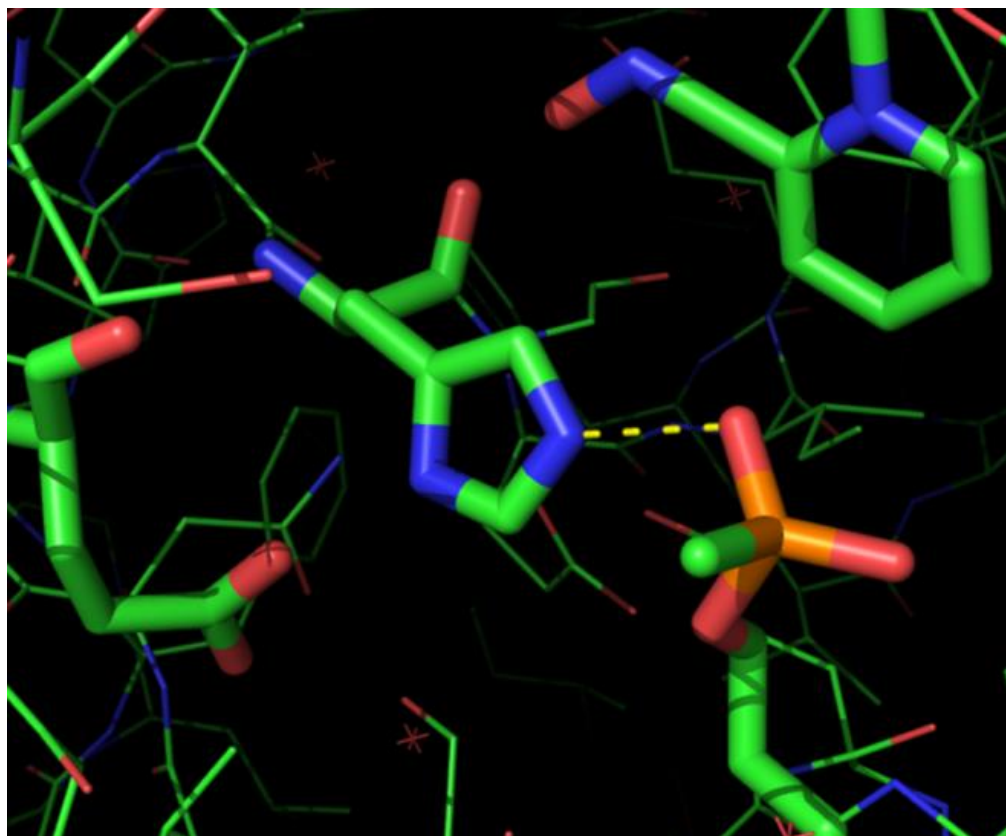


**Figure 2.4:** 3D crystal structure of aged-AChE adduct (*TcAChE*) with 2-PAM bound in the catalytic active site.

---

**Source:** Sanson, B.; Nachon, F.; Colletier, J.P.; Froment, M.T.; Toker, L.; Greenblatt, H.M.; Sussman, J.L.; Ashani, Y.; Masson, P.; Silman, I.; and Weik, M. *J. Med. Chem.*, **2009**, 52, 7593-7603; Image generated in PyMol



Further investigation of the crystal structure attributing to the aged-AChE adduct depicts 2-PAM in the enzyme active-site of soman inhibited and aged *TcAChE* (60). This view of the enzyme active site shows 2-PAM bound to Trp84 (86, *hAChE*) with its oximate oxygen oriented away from the phosphonyl center of the aged-AChE adduct (Fig. 2.4). Given what is known about the steric and electrostatic limitation involved in reactivation of an aged-AChE adduct, rates of aging for very potent OP inhibitors further complicate counteraction of nerve agent exposure. Potent OPs, sarin and soman (Fig. 2.5), have been reported to have aging half-lives of approximately 3 h and 3 min respectively (41, 61). There is a clear necessity to develop more efficient ways to combat OP poisoning.

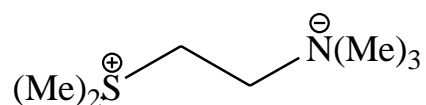
Aside from the known process of aging occurring when OP bound AChE is untreated, accumulation of ACh at neuromuscular and neuronal synapses also occurs. Once ACh accumulation occurs, saturation and subsequent overstimulation of nicotinic ACh receptors create a systematic shutdown of these receptors. Seizures, paralysis, and muscle fasciculation ensue due to this hyper-stimulation and can ultimately lead to death. Undoubtedly, with the current global terrorist threat and considerable pesticide use, advancements must be made to combat the rapid inhibition and aging process involved with OP poisoning. Synthesis and kinetic evaluation of non-volatile OP analogues of sarin and soman are addressed in this chapter. In Chapter 3, we will further evaluate attempts to recover enzymatic activity of aged-AChE in detail by novel alkylating agents for which we have termed “resurrection”.

There is a desperate need to reverse aging of OP inhibited AChE. Approaching this issue involves a multi-faceted exploratory and evaluation process. This multi-tiered

investigation involves developing compounds able to alkylate the phosphonyl oxyanion.

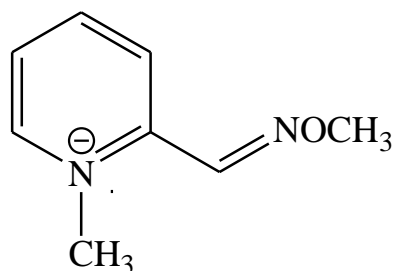
Initial conceptions for alkylating compounds fell under the following classes and structural themes that would potentially methylate the phosphonic oxyanion:

1. Hydrolysis product analogues (ACh/ATCh analogues):

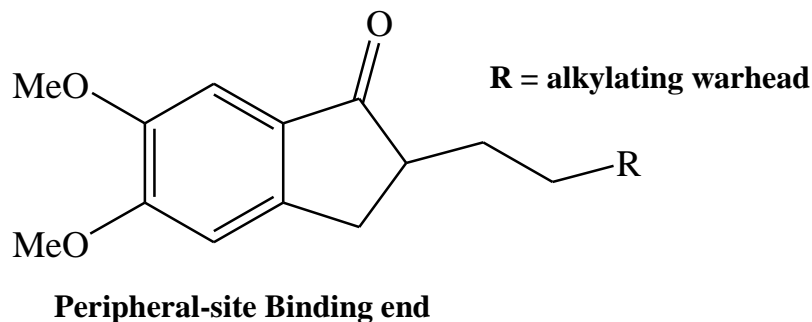


Thiocholine sulfonium analogue

2. Oxime analogues



3. Gorge-spanning (Dual-binding) analogues

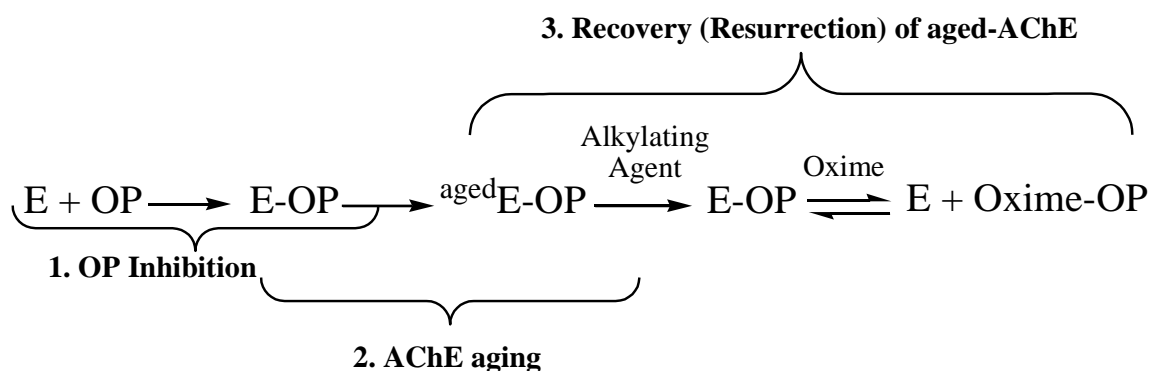


Chapter 3 will discuss the *in situ* methyl transfer evaluations (88) and kinetic evaluations of their affinity for the apo hAChE active-site.

The complementary portion of this study involves the development of an enzyme assay method that evaluates the ability of these agents to recover aged-AChE activity.

Design of this methodology, depicted in Scheme 2.3, is in three parts of the enzyme

evaluation process: OP inhibition of AChE, aging of AChE, and recovery of aged-AChE activity (termed resurrection). In this chapter, we address the first two steps of this kinetic evaluation process through the synthesis of OP analogues and their aging kinetic behavior. These OP nerve agent analogues are designed to have non-volatile fluorescent leaving groups.



**Scheme 2.3:** Stepwise approach to kinetically evaluate recovery of aged-AChE activity

### Objective of Study

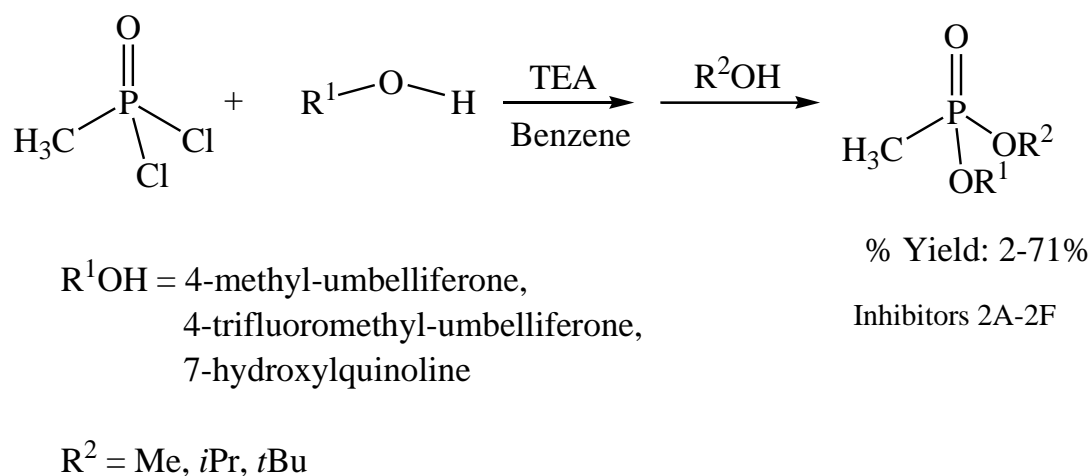
Synthesis of non-volatile organophosphonate analogues bearing fluorescence active leaving groups of sarin and soman is described herein. Evaluation of the inhibition kinetics and aging rates is also described for these OP analogues.

### Materials and Methods

Detailed materials and general methods are described in Appendix A and Appendix B.

#### *Synthesis of Non-volatile Sarin and Soman Analogues*

Sarin and soman analogues described in this work were prepared by a literature procedure (62). Figure 2.5 shows all OP analogues synthesized in this study. Detailed reaction conditions are described in Appendix A and outlined by the general reaction in Scheme 2.4:



**Scheme 2.4:** General reaction scheme for preparation of sarin and soman OP analogues

Installation of the  $\text{R}^1$  alkoxy moiety was carried out by base catalyzed nucleophilic substitution. Displacement of the chlorine of the dichloro methylphosphonic acid precursor is performed in this “one pot” synthesis by substitution with the desired alkyl alcohol (MeOH, *i*PrOH, or *t*BuOH). N-methylation of the product for  $\text{R}^1 = 7$ -hydroxyquinoline was carried out by Dr. Joseph J. Topczewski by dissolving **2E** in  $\text{CH}_2\text{Cl}_2$  and stoichiometric treatment with methyl trifluoromethylsulfonate (MeOTf) to

yield **2F**. Compound purity was determined by  $^1\text{H}$  NMR,  $^{13}\text{C}$  NMR,  $^{31}\text{P}$  NMR,  $^{19}\text{F}$  NMR, and HREIMS.

### *Enzyme Kinetic Analysis*

Phosphate buffer (PB) at 50 mM concentration was prepared in bulk at pH ranging from 7.2-7.3. The pH was determined by an ion selective pH electrode that was calibrated prior to each measurement. All stock solutions were prepared from solid material and stored in polypropylene containers at 4 °C as follows: 0.1% (w/v) BSA solution in PB, 45 mM ATCh in DD-H<sub>2</sub>O, 20 mM DTNB in PB, 3 mM 2-PAM in DD-H<sub>2</sub>O, and 1.4 nM hAChE in 0.1% (w/v) BSA solution. Working solutions were prepared using calibrated micropipettes and solvent matching the parent stock. To ensure sample integrity, all OP inhibitors (**2A-2F**) were prepared from solid and used immediately after preparation.

Assays were conducted on a Molecular Devices SpectraMaxM2 micro-plate reader and on polystyrene 96-well plates (Costar, round bottom). Activity of hAChE was measured spectrophotometrically at 412 nm and 27 °C following the Ellman assay method (26). Time point readings were obtained at the minimum possible interval over a 10 min duration. Incubation was performed in duplicate for each inhibitor concentration. Initial rates ( $v_i$ , mA/min) were calculated by least-squares analysis of the time courses at less than 10% turnover of the initial substrate concentration. Non-linear regression analysis was performed using SigmaPlot 12.0 to obtain kinetic inhibition parameters; data were corrected for background interference. From here on, the denotation for inhibitors **2A-2F** excludes kinetic data for **2E**.

First order kinetics were observed for the inhibition of hAChE with the

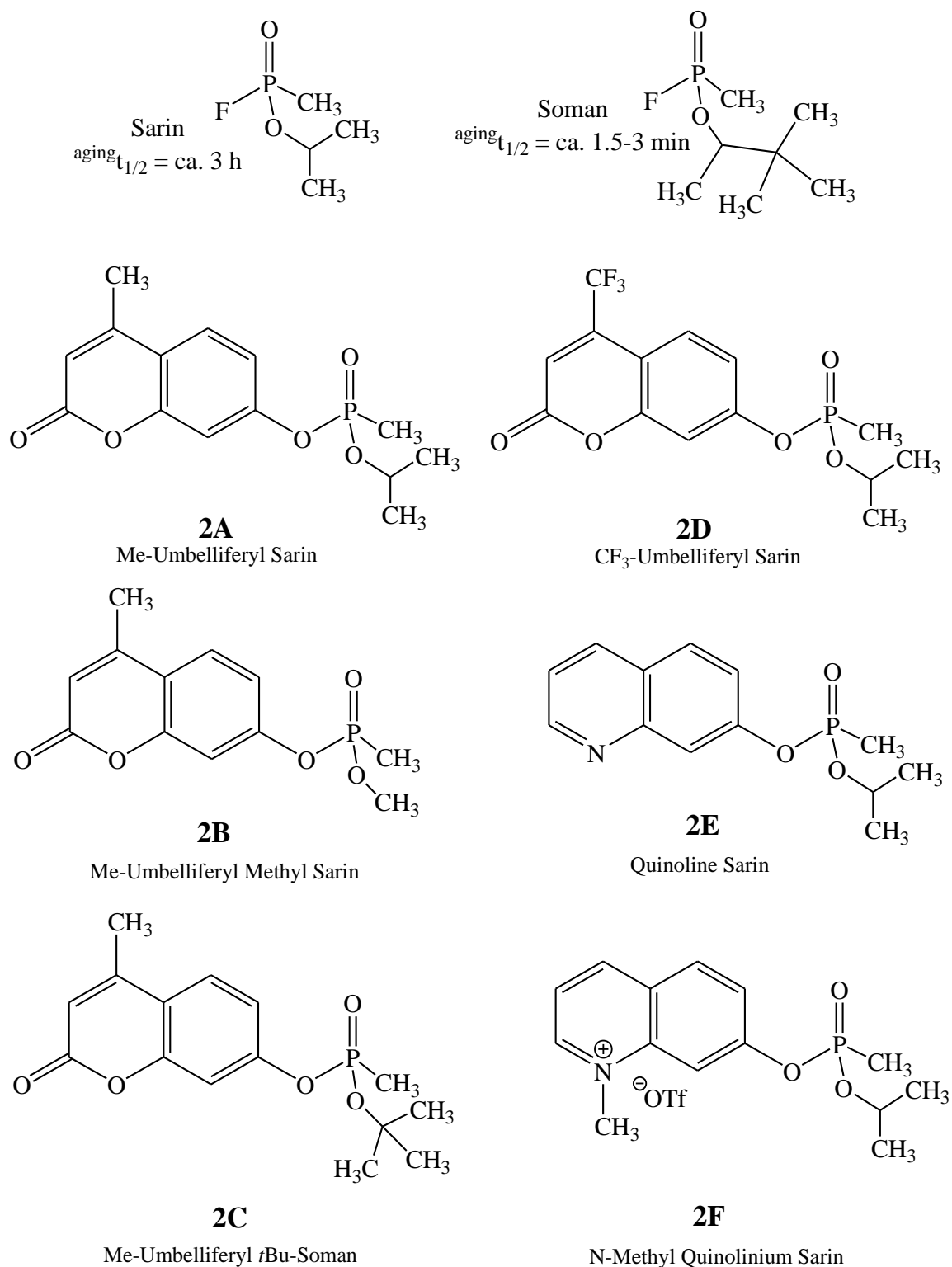


**Figure 2.5:** Chemical structures for OP inhibitors (Sarin and Soman) and OP analogues **2A-2F**. Though a single configuration about P is shown, all analogues and sarin are racemic mixtures and soman is a mixture of racemic diastereomers.

organophosphonates used in this study. The assay was conducted by the following method: Each well was loaded with buffer containing DTNB (270  $\mu$ L) and a solution of *hAChE* (10  $\mu$ L, 50 pM, in 0.1% BSA). To the experimental wells, organophosphonate was added (10  $\mu$ L, .03-3 mM in acetonitrile). To the control wells, acetonitrile was added (10  $\mu$ L). At the time points reported, ATCh (10  $\mu$ L, 4.5 mM, in water) was added to the well and *hAChE* activity was monitored at 412 nm to obtain initial rates ( $v_i$ , mA/min). The pseudo-first order rate constant ( $k_{obs}$ ) was obtained by finding the percent of control activity remaining at each time point as described by Eq. 2.3 and Eq. 2.4:

$$\%hAChE_{OP} = \frac{v_i hAChE_{OP}}{v_i hAChE_{control}} \times 100$$

**Equation 2.3:** Equation for the residual activity of OP inhibited *hAChE* ( $\%hAChE_{OP}$ ) which is defined by the ratio of the initial ATCh hydrolysis rate of OP inhibited *hAChE* ( $v_i hAChE_{OP}$ , mA/min) and uninhibited *hAChE* ( $v_i hAChE_{control}$ , mA/min)

$$\%hAChE \text{ Activity}_{recovered} = \%hAChE \text{ Activity}_{control} e^{-k_{obs}t}$$

**Equation 2.4:** Pseudo first-order rate equation for OP inhibition of *hAChE*;  $k_{obs} \equiv$  observed pseudo first-order rate constant;  $t \equiv$  time;  $\%hAChE \text{ Activity}_{recovered} \equiv$  recovered activity of OP inhibited *hAChE*;  $\%hAChE \text{ Activity}_{control} \equiv$  activity of the uninhibited *hAChE* enzyme

Following initial determinations for irreversible inhibition, inhibitors **2A**, **2C**, **2D**, and **2F** were evaluated for their inhibition rates in a continuous assay. Each well was prepared as follows: 265  $\mu$ L of 0.5 mM DTNB in 50 mM PB (pH 7.3), 10  $\mu$ L of inhibitors **2A**, **2C**, **2D**, or **2F** in acetonitrile (in well concentration range from 10 nM-10  $\mu$ M), 20  $\mu$ L of 4.5 mM ATCh (0.30 mM in well concentration), and 5  $\mu$ L of 0.5 nM *hAChE*. Control reaction time courses were performed with a blank injection of acetonitrile instead of inhibitor and remained linear throughout the duration of each assay. All assays were performed in triplicate following the Ellman method as described

in the general procedure. Time courses were followed for 3 hours and the pseudo-first order rate constants of inhibition,  $k_{obs}$  ( $\text{min}^{-1}$ ), were determined from fits to first-order exponential function, Eq. 2.5.

$$A = A_{\infty} + (A_0 - A_{\infty})e^{-k_{obs}t}$$

**Equation 2.5:** Equation for first-order rate constant determination; A (absorbance),  $A_0$  (initial absorbance value),  $A_{\infty}$  (absorbance at  $t_{\infty}$ ),  $k_{obs}$  (observed first-order rate constant,  $\text{s}^{-1}$ ),  $t$  (time, s)

Observed pseudo first-order rate constants ( $k_{obs}$ ) were plotted to Eq. 2.6 as a function of inhibitor concentration to obtain second-order, bimolecular rate constants ( $k_i/K_I$ ) where  $[\text{OP}] \ll K_I$ .

$$k_{obs} = \frac{k_i[\text{OP}]}{K_I + [\text{OP}]}; k_{obs} = \frac{k_i}{K_I}[\text{OP}] \text{ at } [\text{OP}] \ll K_I$$

**Equation 2.6:** Equation defining the observed pseudo first-order rate constant,  $k_{obs}$ ; where  $[\text{OP}] \equiv \text{OP}$  inhibitor concentration (**2A, 2C, 2D, and 2F**);  $k_i \equiv$  first-order inhibition rate constant;  $K_I \equiv$  inhibitor dissociation constant;

Inactivation was achieved by incubating 483  $\mu\text{L}$  of 4.8 nM *hAChE* in 0.1% (w/v) BSA buffer (50 mM PB, pH 7.3) with 17  $\mu\text{L}$  of inhibitor (**2A-2C**). Stock inhibitor solutions were prepared in acetonitrile and assayed at a final concentration of 10  $\mu\text{M}$ . Control enzyme was prepared in the absence of inhibitor by adding a blank of acetonitrile. After 30 minutes of incubation at 27  $^{\circ}\text{C}$ , excess inhibitor was separated from enzyme using a Sephadex G-50 Quick Spin Column (Roche). Prior to separation, the column was standardized with 0.1% (w/v) BSA in 50 mM PB (pH 7.3) and packed by centrifugation at 1100 x  $g$  for 4 minutes. The 500  $\mu\text{L}$  aliquot of inactivated *hAChE* was loaded to the packed Sephadex G-50 column bed and centrifuged at 600 x  $g$  for 6 minutes. Separated enzyme was collected and 15  $\mu\text{L}$  aliquots were assayed at various



time points following 30 minute incubation with 100  $\mu$ M 2-PAM at 27 °C. Ellman assay conditions as previously described were used to determine the percent of reactivated *hAChE* ( $\%hAChE_{OP}$  Reactivated) activity as defined by Eq. 2.7.  $\%hAChE_{OP}$  Reactivated is the ratio of the initial rates for OP inhibited *hAChE* ( $hAChE_{OP}$ ) and control *hAChE* ( $hAChE_{control}$ ) catalyzed hydrolysis of ATCh. The exponential rate constant of “aging” ( $k_a$ ) was calculated using non-linear regression analysis in SigmaPlot 12.0 through fit to Eq. 2.7.

$$\%hAChE_{OP} \text{ Reactivated} = \frac{v_i \text{ of } hAChE_{OP}}{v_i \text{ of } hAChE_{control}} \times 100$$

**Equation 2.7:** Equation for the residual activity of OP inhibited *hAChE* ( $\%hAChE_{OP}$  Reactivated) following treatment with 2-PAM which is defined by the ratio of the initial ATCh hydrolysis rate of OP inhibited *hAChE* ( $v_i hAChE_{OP}$ , mA/min) and uninhibited *hAChE* ( $v_i hAChE_{control}$ , mA/min)

The extent of aging ( $\%hAChE_{aged}$ ) is defined by Eq. 2.8:

$$\%hAChE_{aged} = 100 - \%hAChE_{OP} \text{ Reactivated}$$

**Equation 2.8:** Defines the amount of *hAChE* that has aged and is unrecovered by treatment with 2-PAM; where  $\%hAChE_{OP}$  Reactivated  $\equiv$  recovered enzyme activity after treatment with 2-PAM

Plots for  $k_a$  rate constants were fit to Eq. 2.9 (**2A** and **2B**) and Eq. 2.10 (**2C**):

$$\%hAChE_{OP} \text{ Reactivated} = \%hAChE \text{ Activity}_{control} e^{-k_a t}$$

**Equation 2.9:** Exponential decay of *hAChE* activity after treatment with 2-PAM as a function of time; where  $k_a \equiv$  the observed first-order rate constant for aging,  $\%hAChE \text{ Activity}_{control} \equiv$  activity of the uninhibited *hAChE* enzyme

$$\%hAChE_{OP} \text{ Reactivated} = \%hAChE_{control} - \frac{k_a \%hAChE_{control}}{k_a + k_s} (1 - e^{-(k_a + k_s)t})$$

**Equation 2.10:** Exponential decay of *hAChE* activity after treatment with 2-PAM as a function of time; where  $k_a$   $\equiv$  the observed first-order kinetic rate constant for aging;  $\%hAChE_{control}$   $\equiv$  control *hAChE* enzyme activity;  $k_s$   $\equiv$  first-order kinetic rate constant for the spontaneous reactivation of *hAChE*-OP adduct

### Results and Discussion

Five classes of organophosphonate sarin and soman analogues were synthesized following conditions described in Scheme 2.3 and in Appendix A. Inhibitors **2B**, **2C**, **2E**, and **2F** are all presented as novel OP inhibitors of *hAChE*, where inhibitor **2A** and **2D** were previously reported in literature (62). OPs **2A-2F** resemble the core structures of either sarin or soman. Inhibitors **2A**, **2D**, and **2F** possess the core structure of the OP sarin with the exception of the fluorine leaving group, which is replaced with a fluorescence active moiety (R = 4-methylumbelliferyl, 4-trifluoromethylumbelliferyl, or N-methylquinolinium). Their fluorescence activity profile is described in Appendix B. Synthesis of **2B**, the methyl sarin analogue, afforded a novel OP inhibitor resembling the core structure of sarin bearing methoxy and 4-methylumbelliferyl substituents to the phosphorous center. The final novel OP analogue synthesized was a *t*Bu soman analogue. Soman's core substituents are a pinacoloxo and fluorine, for which the final structure bears two stereogenic centers (phosphorous and C $\alpha$ -pinacolyl centers). In order to reduce the number diastereomers produced, *t*-butoxy and 4-methylumbelliferyl substituents were installed.

Evaluation of the irreversible kinetic behavior for OP inhibitors **2A-2D,2F** was conducted by discontinuous stop-time assay following the Ellman assay method (26). Figs. 2.6-2.10 represent plots of the pseudo first-order rate determinations for OP

inhibitors **2A-2D**, **2F**. Table 2.1 shows the bimolecular rate constants obtained for each inhibitor calculated from the ratio of the  $k_{\text{obs}}$  ( $\text{min}^{-1}$ ) and the inhibitor concentration ( $[\text{OP}]$ , M). Inhibitor **2F** showed the most potent inhibition generating an inhibition half-life ( $t_{1/2} = \frac{\ln 2}{k_{i,\text{obs}}}$ ) of approximately 10 min at 1 nM concentration. Inhibitors **2A-2D** generated  $t_{1/2}$  values between 6 min-16 min at 1  $\mu\text{M}$  (**2A**, **2B**, **2D**) and 10  $\mu\text{M}$  (**2C**). The increased potency observed in the inhibition of *hAChE* for **2F** is attributed to the quaternized quinolinium leaving group. Cationic substrates and inhibitors are drawn into the mouth of *AChE*'s catalytic gorge, a result of the enzyme's polar nature (7). Understanding this property of *AChE* provides a useful insight into the added potency of **2F**. Compounds with neutral umbelliferyl leaving group inhibitors were 3-4 orders of magnitude less potent than its N-methylquinolinium counterpart.

OP analogues **2A-2C** all bear a 4-methylumbelliferyl leaving group but differ in the alkoxy substituent ( $R = \text{Me}$ , *i*Pr, or *t*Bu). First-order rates for **2B**, the methyl sarin analogue, yielded an inhibition  $t_{1/2}$  of 6 mins where OP analogues **2A** and **2C** were 12 min and 16 min respectively. This difference in inhibition rate is attributed to the increased size of the alkoxy substituent, where the bulkier *t*Bu substituent inhibits an order of magnitude slower than **2A** or **2B**. To compare the rate constants of our sarin analogues (**2A**, **2D**, and **2F**), continuous assays were performed. Binding affinity due to the size of the phosphonyl alkoxy group is thought to be affected by steric interaction in the enzyme's acyl binding pocket (63). Fig. 2.11 is a representative plot of the continuous assay performed for inhibitors **2A**, **2D**, and **2F** each differing in the fluorescent active leaving group. Following Eq. 2.5,  $k_{\text{obs}}$  were obtained at various

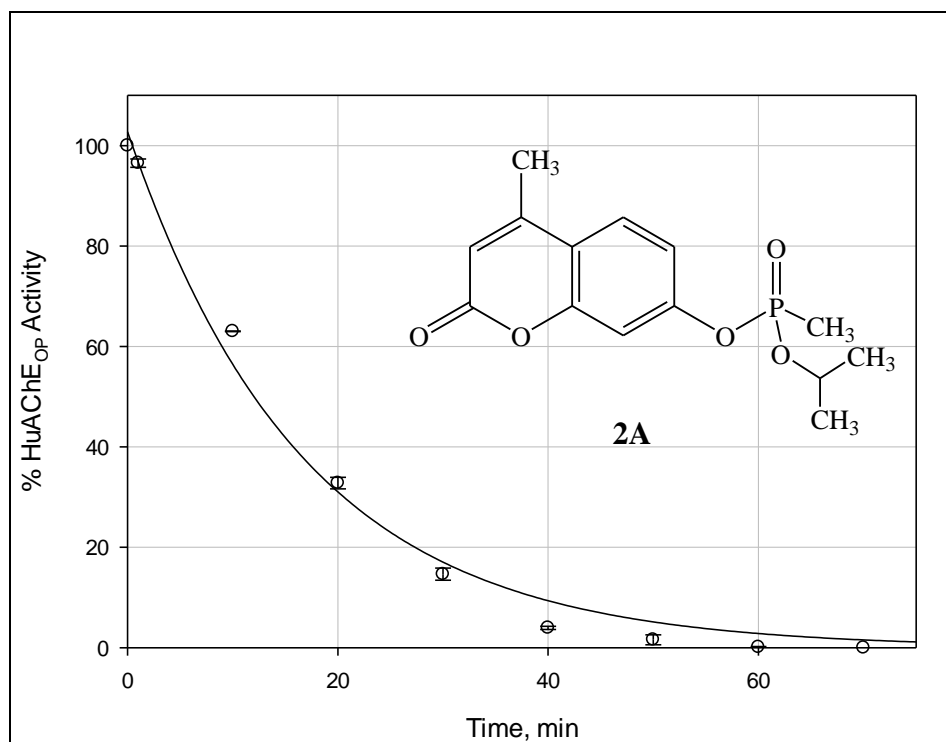


**Figure 2.6:** Stop-time assay plot for **2A** (1 μM) for pseudo first-order rate constant determination

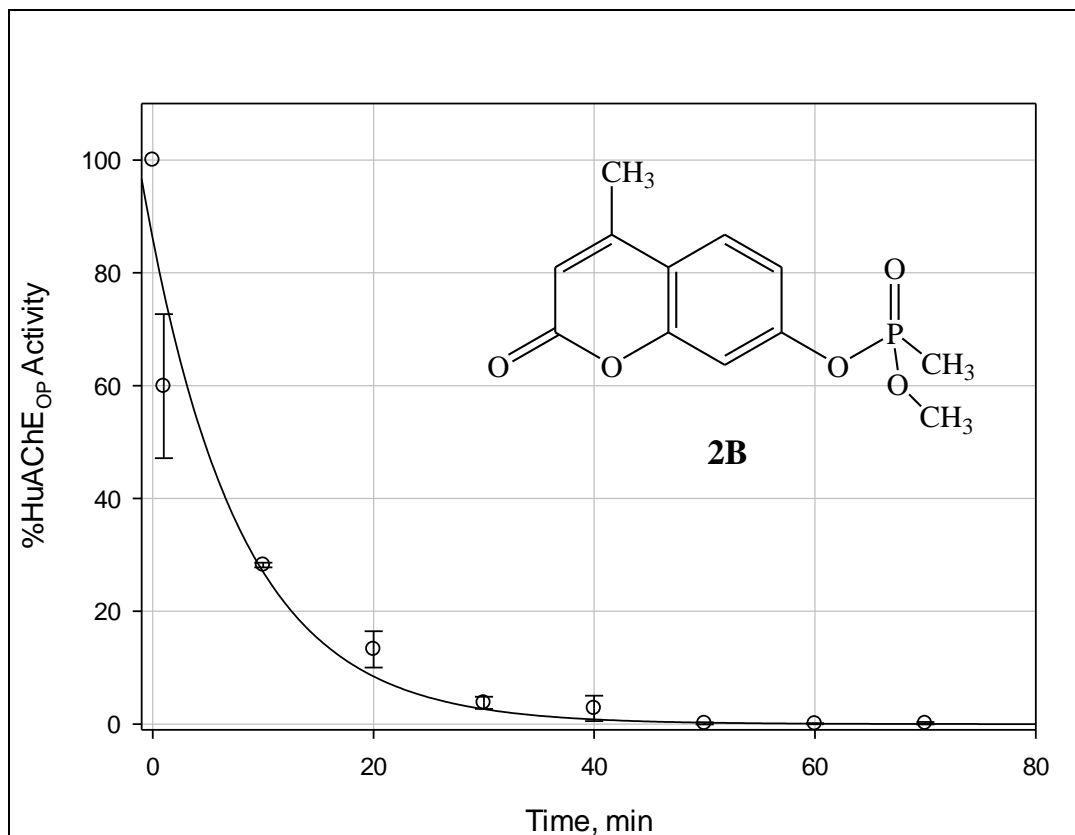


**Figure 2.7:** Stop-time assay plot for **2B** (1  $\mu\text{M}$ ) for pseudo first-order rate constant determination

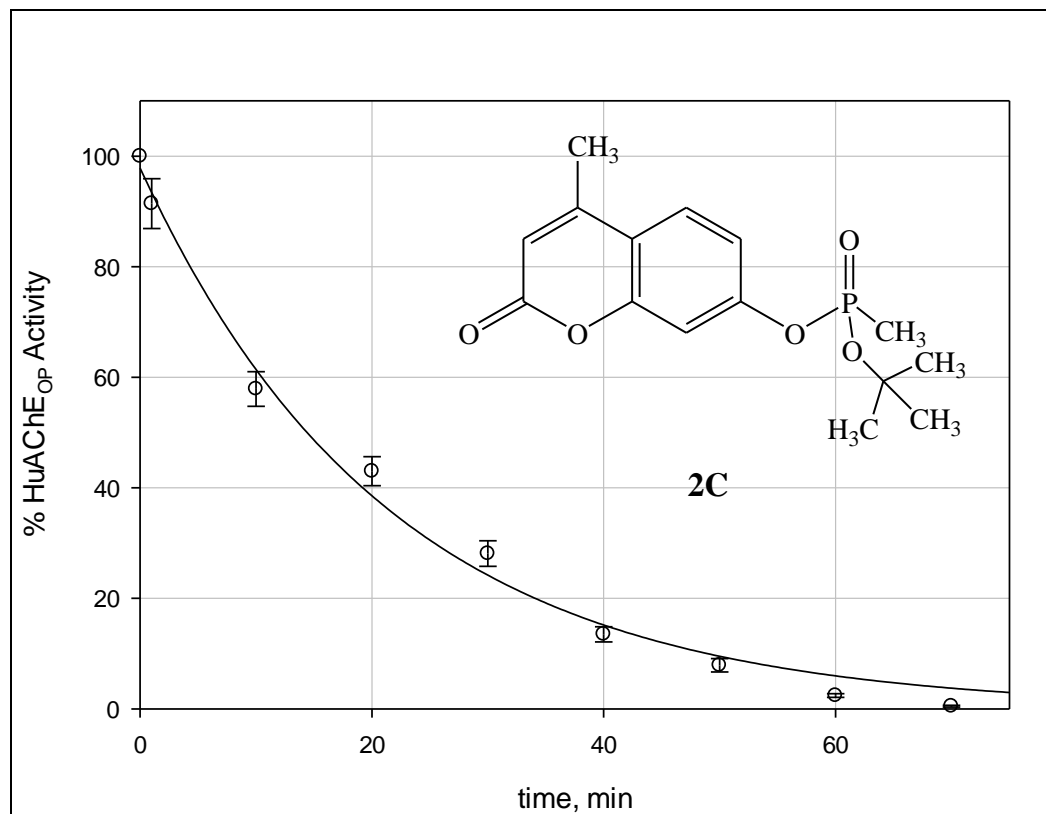


**Figure 2.8:** Stop-time assay plot for **2C** (10  $\mu\text{M}$ ) for pseudo first-order rate constant determination

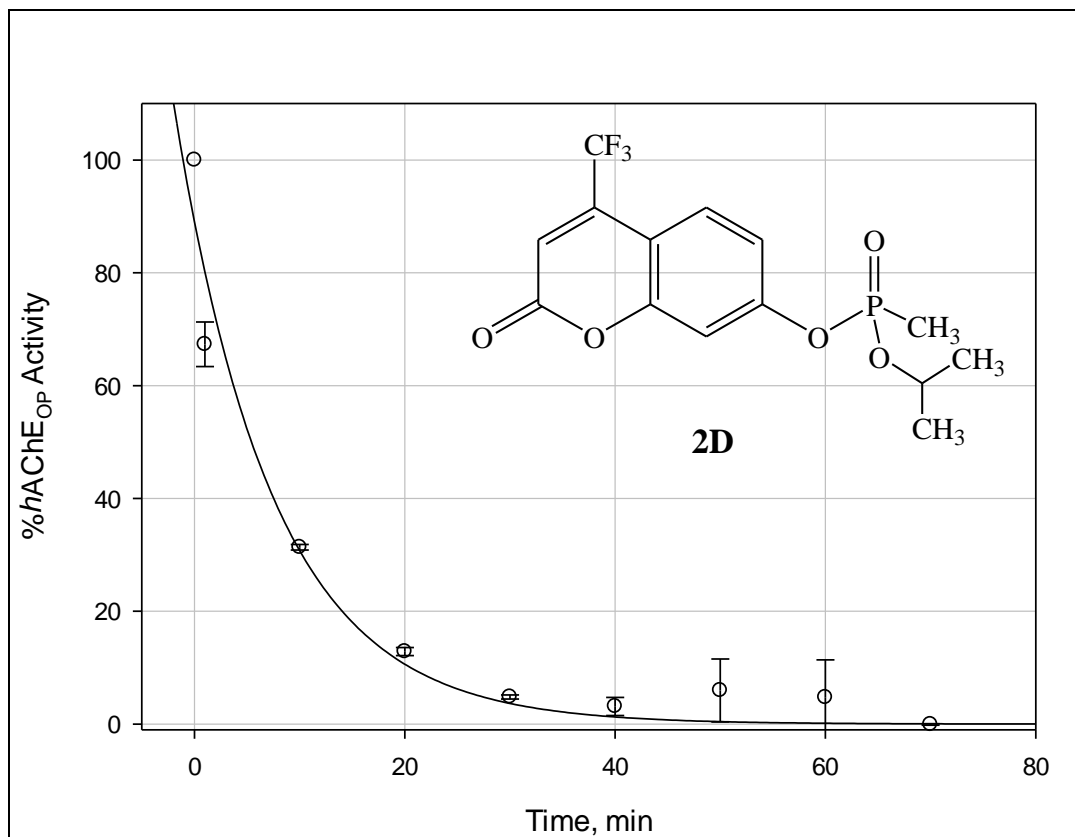


**Figure 2.9:** Stop-time assay plot for **2D** (1  $\mu\text{M}$ ) for pseudo first-order rate constant determination

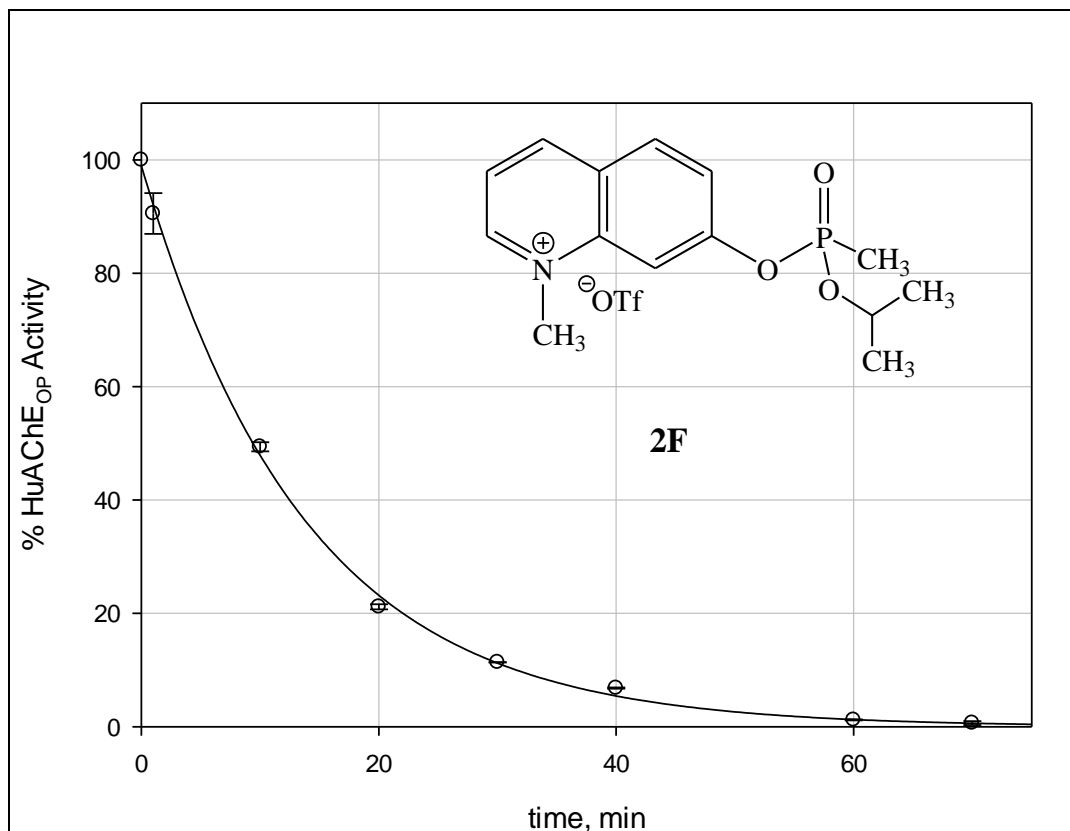


**Figure 2.10:** Stop-time assay plot for **2F** (10 nM) for pseudo first-order rate constant determination



**Table 2.1:** Bimolecular rate constants from the pseudo first-order rate constants ( $k_{\text{obs}}$ ) and the OP inhibitor (**2A-2F**) concentration, ( $k_{\text{obs}}/[\text{OP}]$ ,  $\text{M}^{-1} \text{min}^{-1}$ ) at 27 °C

<u>Inhibitor</u>	<u>[OP]</u>	<u><math>k_{\text{obs}}/[\text{OP}]</math> (<math>\text{M}^{-1} \text{min}^{-1}</math>)</u>
<b>2F</b>	10 nM	$7.3 (\pm 0.3) \times 10^6$
<b>2A</b>	1 $\mu\text{M}$	$5.7 (\pm 0.4) \times 10^4$
<b>2C</b>	10 $\mu\text{M}$	$4.7 (\pm 0.2) \times 10^3$
<b>2D</b>	1 $\mu\text{M}$	$8.4 (\pm 0.7) \times 10^4$
<b>2B</b>	1 $\mu\text{M}$	$1.2 (\pm 0.2) \times 10^5$

concentrations for inhibitors **2A** (1-10  $\mu\text{M}$ ), **2D** (1-10  $\mu\text{M}$ ), and **2F** (10-100 nM). Linear plots of the  $k_{\text{obs}}$ , described by Eq. 2.6 at  $[\text{OP}] \ll K_{\text{I}}$ , were fit as a function of inhibitor concentration (Fig. 2.12-2.14). Table 2.2 shows the resultant second-order bimolecular rate constants ( $k_{\text{i}}/K_{\text{I}}$ ,  $\text{M}^{-1} \text{min}^{-1}$ ) for *hAChE* inhibition showing slightly less potency overall for each inhibitor. Data from continuous assay analysis show that **2F** is more potent than its umbelliferyl OP analogue counterparts by 2 orders of magnitude.

Upon resolving the inhibition profile of inhibitors **2A-2D**, **2F**, inhibitor analogues bearing one of the fluorescent leaving groups were profiled for aging kinetics. Inhibitors **2A-2C**, bearing the 4-methylumbelliferyl fluorophore, were evaluated for their rates of aging. Upon inactivation of *hAChE* with inhibitors **2A-2C**, excess inhibitor was removed via separation on a Sephadex column and the resultant inactivated enzyme was assayed following 30 min incubation with 2-PAM. Fig. 2.15 shows a plot of the recovered OP inhibited *hAChE* activity following treatment with 2-PAM as a function of time. First-order rate constants for aging were determined, yielding stark differences in their half-lives for aging ( $^{\text{aging}}t_{1/2}$ , min). Observed rates of aging for our *hAChE*-OP adducts were inverse to the observed inhibition rates for OPs **2A-2C**. The bulkier *t*Bu-Soman analogue, **2C**, showed a faster rate of aging, an order of magnitude higher than our sarin analogue, **2A**. In the case of the methyl sarin analogue, **2B**, it showed a rate of aging two and three orders of magnitude slower than **2A** and **2C**, respectively. The half-life of aging for **2B** was calculated to be a little more than nine days. As will be described in Chapter 3, this is an important kinetic parameter to note in the development of novel alkylating agents for the *AChE* bound phosphonic oxyanion and subsequent assay procedure.

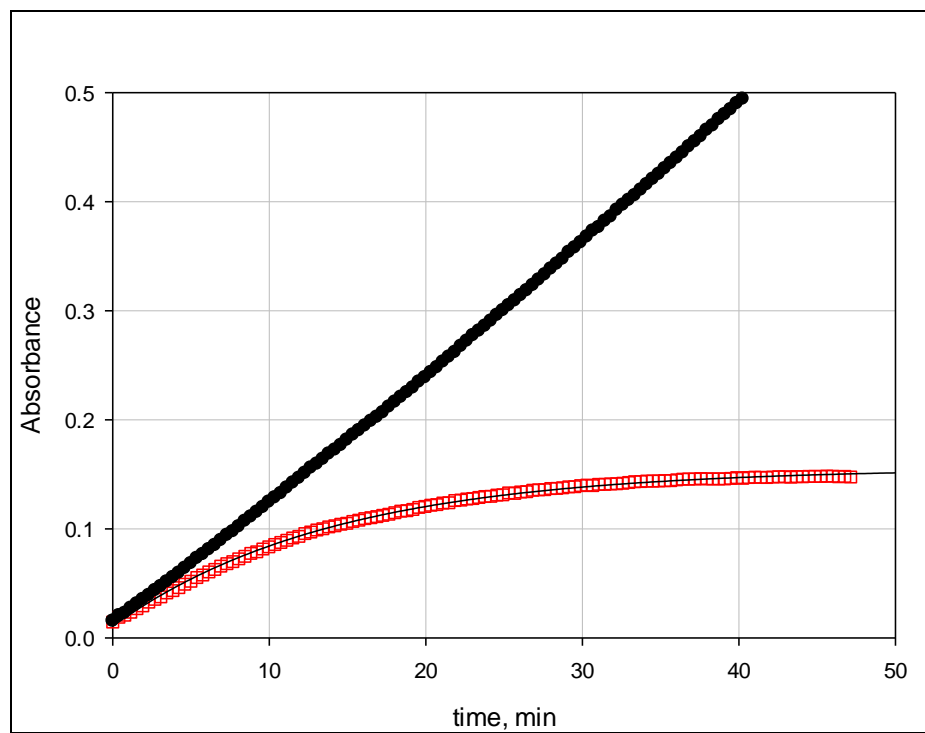


**Figure 2.11:** Full time course for sarin analogue inhibitor **2A** (2  $\mu\text{M}$ ) fit to Eq. 2.5 followed by Ellman method (26) ( $\lambda = 412 \text{ nm}$ )

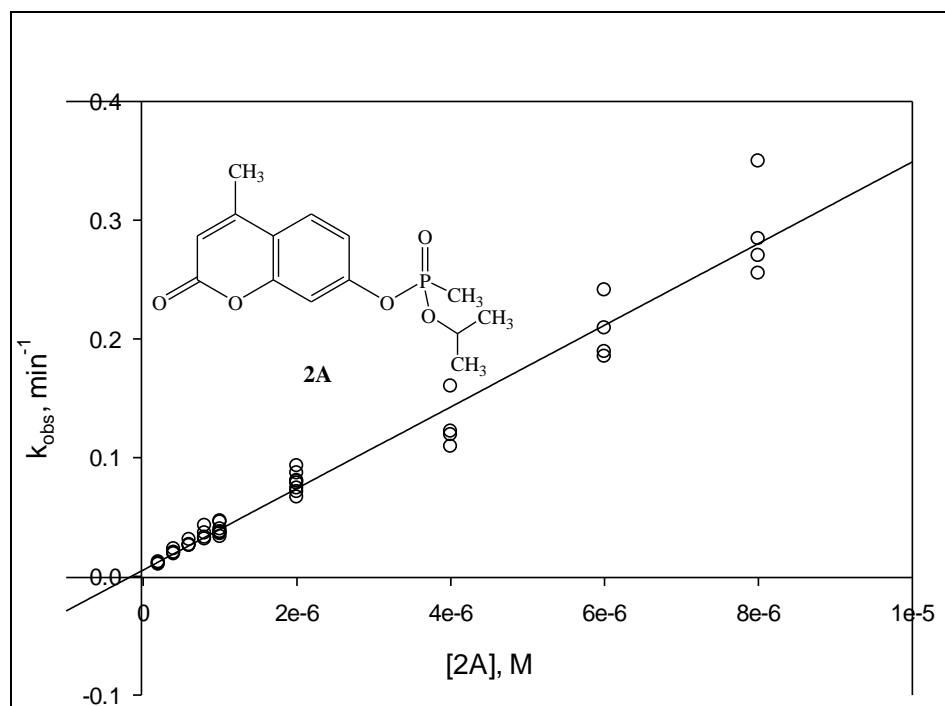


**Figure 2.12:** Second-order plot of  $k_{\text{obs}}$  ( $\text{min}^{-1}$ , pseudo-first order rate constant) as a function of inhibitor **2A** concentration (Eq. 2.6).

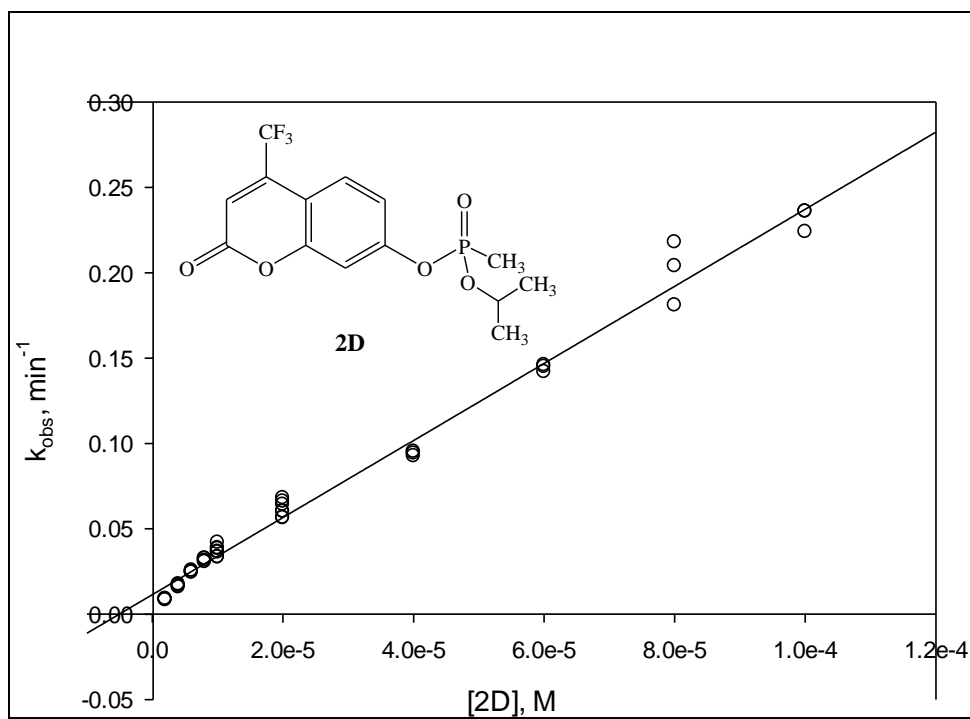


**Figure 2.13:** Second-order plot of  $k_{\text{obs}}$  ( $\text{min}^{-1}$ , pseudo-first order rate constant) as a function of inhibitor **2D** concentration (Eq. 2.6).

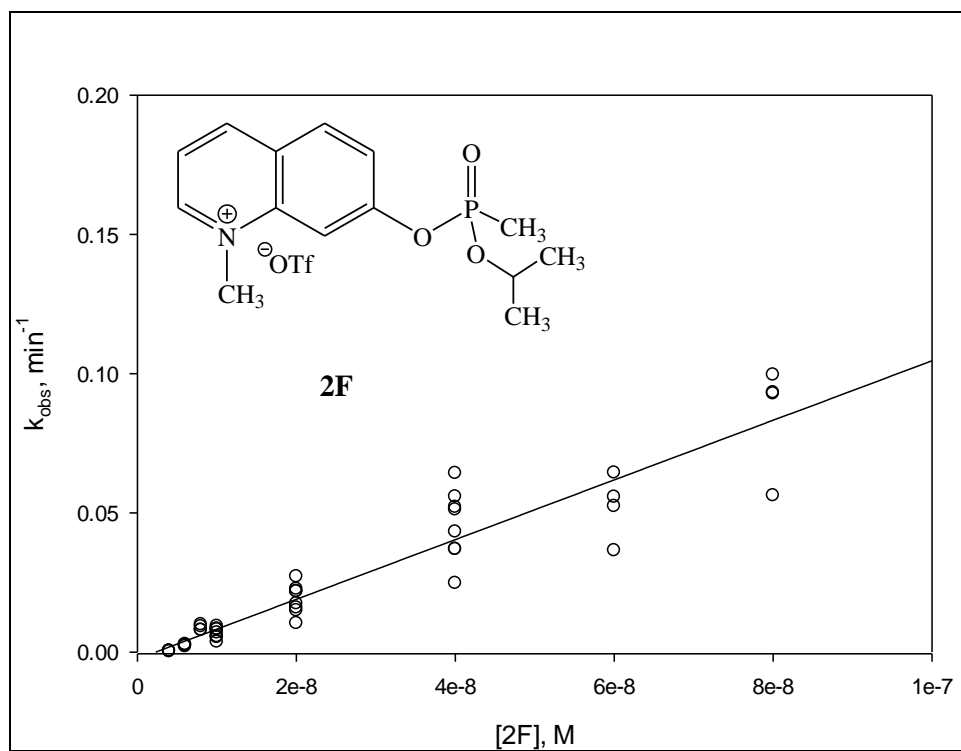


**Figure 2.14:** Second-order plot of  $k_{\text{obs}}$  ( $\text{min}^{-1}$ , pseudo-first order rate constat) as a function of inhibitor **2F** concentration (Eq. 2.6).

**Table 2.2:** Second-order bimolecular rate constants (defined by Eq. 2.6 where  $K_I \gg [I]$  such that  $k_{\text{obs}} = \frac{k_i}{K_I} [I]$ ) from continuous assays for Sarin analogue inhibitors **2A**, **2D**, and **2F** at 27°C

<b>Inhibitor</b>	<b><math>k_i/K_i(\text{M}^{-1}\text{min}^{-1})</math></b>
<i>2A</i>	$1.2 (\pm 0.1) \times 10^6$
<i>2D</i>	$3.4 (\pm 0.1) \times 10^4$
<i>2F</i>	$2.3 (\pm 0.1) \times 10^4$

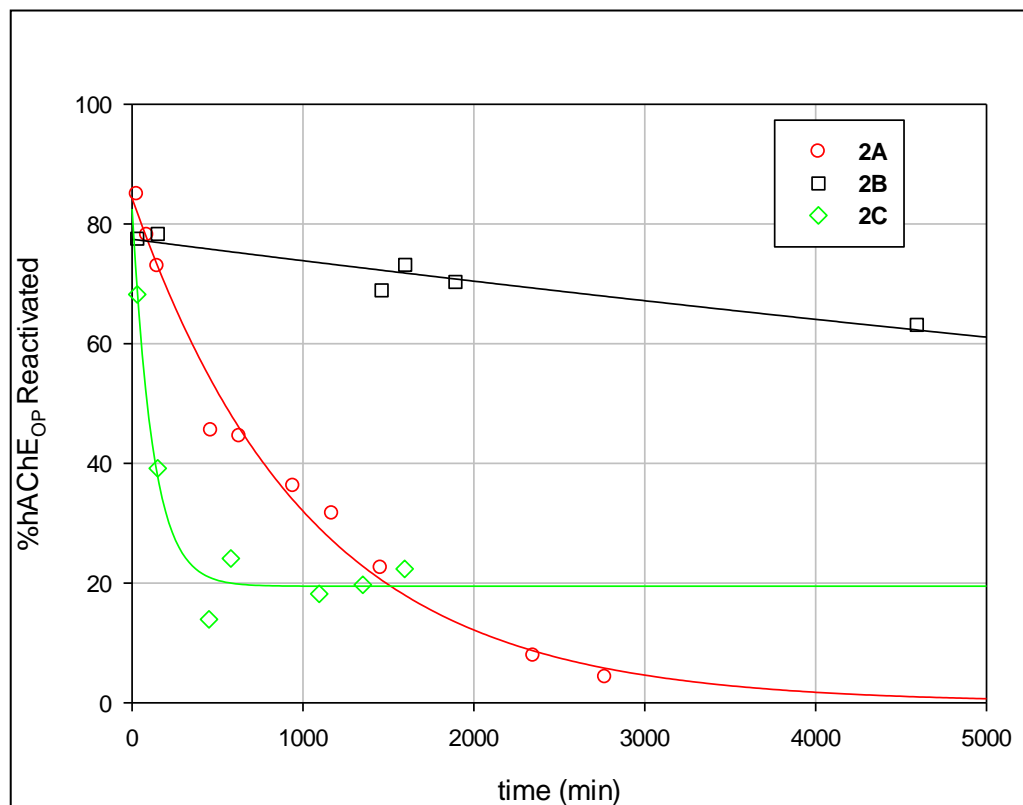
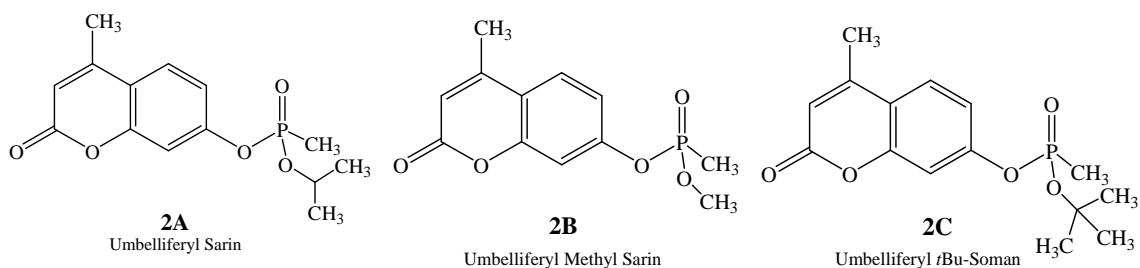


**Figure 2.15:** First-order plot of the recovered OP inhibited *h*AChE activity as a function of time to determine extent of aging for *h*AChE-OP adduct formed from inactivation by inhibitors **2A-2C**



**Table 2.3:** First-order rate constant for aging of *h*AChE-OP adduct formed from inhibition by inhibitors **2A-2C**.  $t_{1/2} \equiv$  half-life of aging

<b><u>Inhibitor</u></b>	<b><u><math>k_a(\text{min}^{-1})</math></u></b>	<b><u>aging<math>t_{1/2}(\text{min})</math></u></b>
R = Me	$4.7 (\pm 0.8) \times 10^{-5}$	>14000
R = <i>i</i> Pr	$1.1 (\pm 0.1) \times 10^{-3}$	630
R = <i>t</i> -Bu	$9.2 (\pm 0.8) \times 10^{-3}$	75

The difference in the rate of aging for inhibitors **2A-2C** is attributable to the aging mechanism outlined in Scheme 2.2. Formation of a carbonium ion intermediate that is stabilized by Glu, Phe, and His residues in the AChE catalytic gorge facilitates dealkylation of the phosphonyl AChE-OP adduct. This mechanism supports formation of  $S_N1$  and elimination products. Smaller alkyl chains, i.e. methyl, form energetically unfavorable carbocations resulting in a considerably slower aging process. Inhibition forms a phosphonyl adduct from OP **2B** in the *h*AChE active-site that ages considerably slow compared to the rate of nucleophilic reactivation by 2-PAM. On the contrary, OPs **2A** and **2B** age at a much faster rate because of their ability to form more stable carbonium intermediates, as its formation is a critical step in the aging mechanism.

### Conclusion

Novel sarin and soman analogues, **2A-2F** were prepared and shown to have irreversible and potent inhibitory activity for *h*AChE. Installation of three different fluorescence active leaving groups produced non-volatile inhibitors. Bimolecular inhibition rate constants were obtained by stop-time and continuous assay methods and show that the quarternized N-methylquinolinium sarin analogue, **2F**, has the most potent inhibitory behavior. Comparison of the inhibitory effects of alkoxy substituents for the 4-methylumbellifryl OP analogues, **2A-2C**, revealed rates were dependent on the size of the alkyl substituent, consistent with observations reported in literature (41, 42, 63). Also consistent with literature reports, rate of aging is dependent on the identity of the alkyl substituent, as evidenced with inhibitors **2A-2C** in which *t*Bu showed the highest rate of aging. Additionally, we have suggested that formation of the methoxy

methylphosphonyl-AChE adduct is a useful motif in developing alkylating agents that can work as reactivators of aged-AChE.

## CHAPTER 3: KINETIC EVALUATION FOR THE REACTIVATION OF AGED HUMAN ACETYLCHOLINESTERASE BY NOVEL ALKYLATING AGENTS

### Chemical Mechanism and Significance

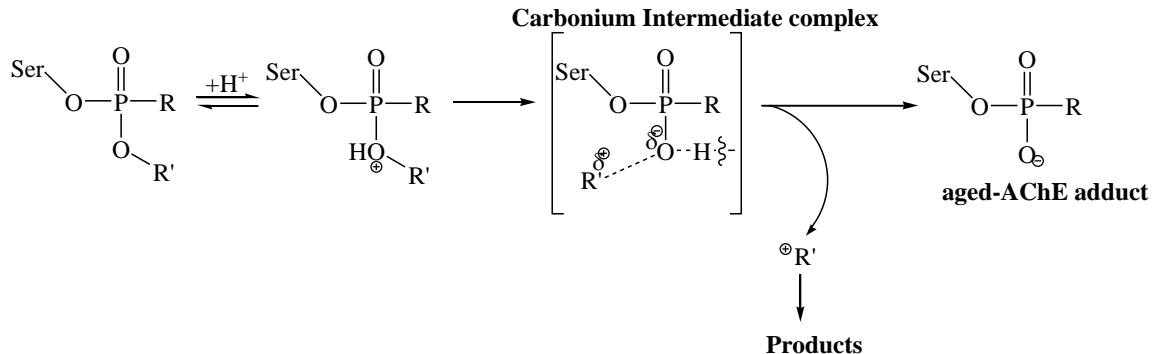
As outlined in Chapters 1 and 2, inhibition of AChE by organophosphorus (OP) nerve agents poses a significant global threat. Their use as chemical warfare agents (CWA) has been documented for centuries; however, the development of nefarious OP nerve agents during World War II and the Cold War amplified the threat in the post-modern warfare era (49). International and domestic terrorist events, including the U.S. World Trade Center attacks on September 11, 2001, resulted in a resurgent emphasis on regulating global stockpiles and production of OP nerve agents (49). Ease of synthesis of these highly treacherous nerve agents, such as sarin and soman, add to the tangible terrorist threat of current interest. It is plausible that access to and synthesis of OPs by rogue terrorist groups, as evidenced in the 1995 Tokyo subway attacks, is what makes this such an alarming threat (41, 42). Undoubtedly, aggressive countermeasures must be implemented for the safe destruction of OPs as well as antidotal response to OP poisoning (64).

Acute OP poisoning occurs when the AChE active-site serine attacks the phosphyl center of an OP nerve agent, as depicted in Fig. 3.1. Even at sub-lethal levels, this process happens rapidly and irreversibly as the phosphyl adduct forms in the AChE catalytic center (64). When left untreated, accumulation of ACh leads to saturation of nicotinic ACh receptors that initiate ion-channel opening across the neuromuscular endplate. Overstimulation of the neuromuscular receptors leads to a systematic shutdown

of neuronal receptors (42). Convulsions, seizures, muscle fasciculation, and eventual cessation of cardio-pulmonary function can make OP exposure fatal.

Reactivation with oxime nucleophiles, i.e. 2-PAM and HI-6, is the current antidotal treatment method for OP exposure (22, 44, 61). Advancements towards new and more effective oxime treatments to OP exposure are limited by their inability to reverse the effects of aging. As described in previous chapters, aging occurs when the phosphyl moiety of the AChE-OP adduct undergoes dealkylation of its alkoxy substituent. Even though the process of AChE-OP aging has been well documented since the 1950s (65, 66, 67), no therapeutic treatments have been introduced. What specifically causes the inability for oxime reactivation of the aged-AChE adduct is a current research target. What is known is that the AChE active-site experiences a conformational change attributable to a mobile His residue after OP inhibition (51). The AChE active-site conformation is restored following the aging process. This is because the catalytic site His residue forms a tight salt bridge network with the phosphonic oxyanion and stabilizes the aged-AChE adduct in the enzyme's catalytic gorge (Fig. 3.1).

A mechanism for aging is shown in Scheme 3.1, and is characterized by the formation of a carbonium ion intermediate leading to  $S_N1$  or elimination products. The driving force behind the spontaneous phenomena of aging is debatable (55, 56, 57, 58, 59, 60). But what can be ascertained is the aging process is facilitated by residues lining the catalytic active-site gorge, making reactivation challenging. Crystal structure elucidation of 2-PAM bound to the aged-AChE adduct (Fig. 3.2) provides important insight into limitations for reactivation (51). In Chapter 2, the synthesis of novel OP inhibitors was reported along with their inhibition and aging kinetics (Fig. 3.3). The type



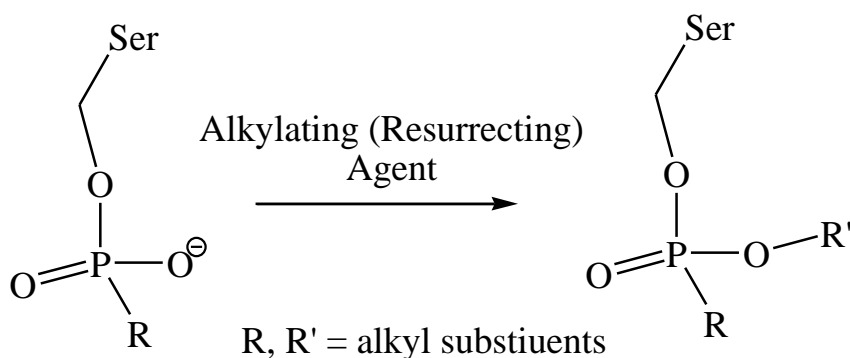
**Scheme 3.1:** General mechanism of aging for AChE-OP adduct. R, R'  $\equiv$  alkyl substituent

of substituent bound to the phosphorous center was shown to have a significant effect on both inhibition and aging rates, also reported in literature (47). As supported by the general mechanism in Scheme 3.1, aging rates for inhibitor **2B** were two orders of magnitude slower than its 4-methylumbelliferyl sarin analogue (**2A**). This is attributed to the fact that the methoxy methyl group will not form  $S_N1$  or elimination products, thus giving a considerably slower rate of aging ( $^{aging}t_{1/2} = 9$  days) that must proceed via an  $S_N2$  mechanism.

It has been well reported that oxime antidotal treatments to OP nerve agent poisoning are ineffective in recovering activity of the aged-AChE adduct (41, 50). For powerful OP nerve agents like sarin and soman, this process occurs 3h and 3 min after initial exposure, respectively (47). Undeniably, any advancement in oxime therapeutic measures will have little or no effect in recovering aged enzyme. Because the process of aging renders an AChE enzyme fully inactive and unrecoverable, the enzyme is essentially dead. In this chapter, I will describe the assay development and general

concept for recovering an aged-AChE adduct utilizing known methods for following AChE enzyme activity. The aged-AChE adduct is for all purposes a dead, or completely inactive species. We have termed the recovery of activity for an aged-AChE adduct “resurrection”, and from here on out assay methods and compounds associated with this line of research will be described by the same lexicon.

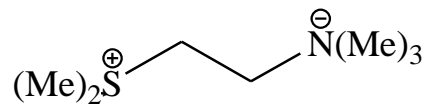
It is proposed that resurrection of an aged-AChE adduct is possible with treatment of an alkylating agent for the phosphonic oxyanion adduct (Scheme 3.2).



**Scheme 3.2:** Concept for resurrection of an aged-AChE adduct

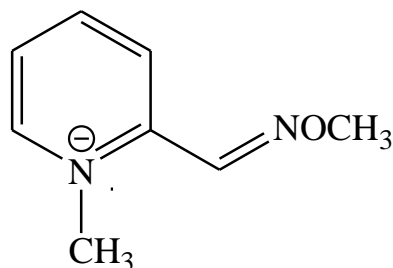
Resurrection of the aged-AChE adduct would essentially shift the progression of the aging process one step backwards, affording recovery of enzyme activity post oxime treatment. Fig. 3.4 summarizes this concept. The idea of recovering activity of an aged-AChE adduct is one of paramount necessity to counter aging of OP inhibited AChE. Concepts for novel “resurrecting” agents were approached in the following general categories:

1. Hydrolysis product analogues (ACh/ATCh analogues):

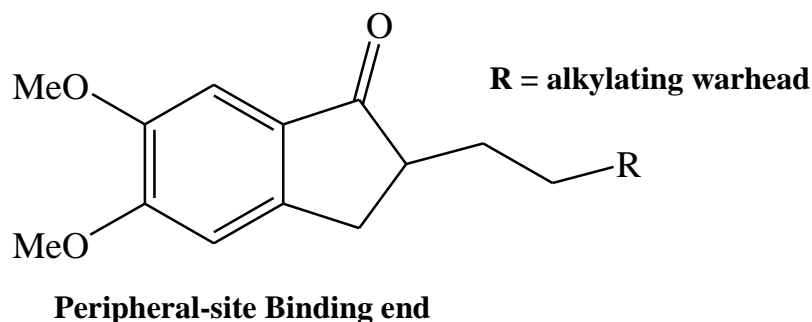


Thiocholine sulfonium analogue

## 2. Oxime analogues



## 3. Gorge-spanning (Dual-binding) analogues



Dr. Joseph J. Topczewski, a post-doctoral associate in the Quinn research lab, synthesized and evaluated a class of 2-methoxypyridinium compounds for their rate of methyl transfer to a methylphosphonic oxyanion *in situ* (88). Rates of methyl transfer and hydrolytic stability were followed by  $^1\text{H}$  and  $^{31}\text{P}$  NMR. It was determined that the installation and position of electron-withdrawing or electron-donating groups on the pyridine ring significantly lessen or enhance methyl transfer rate. Methyl transfer of these simple pyridinium compounds yielded dimethyl methylphosphonate and N-methyl pyridone products (Fig 3.5). These studies revealed a highly tunable structural core that



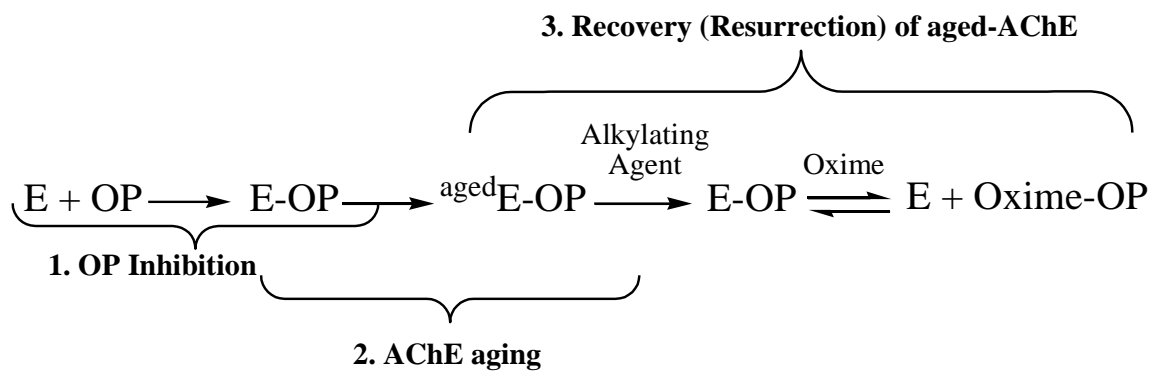
can be utilized in developing resurrecting agents to fit into one of the general conceptual approaches.

Comprehensive development of an enzyme assay methodology that can effectively follow the recovery of enzyme activity is paramount. Chapter 2 also describes the inhibition and aging kinetics for novel OPs, so in this chapter we will describe methodology for resurrecting the aged-AChE adduct. Several classes of novel resurrecting agents, derived from the general structural concepts and simple pyridiniums, were synthesized by various members of the Quinn research group. As noted earlier, the complementary portion of this study involves the development of an enzyme assay method that evaluates the resurrection of aged-AChE activity. Design of this methodology, depicted in Scheme 3.3, is in three steps: OP inhibition of AChE, aging of AChE, and resurrection of aged-AChE activity. In this chapter, we address the third step of this kinetic evaluation process, profiling the aged enzyme resurrection. The nerve agent analogue **2A** was selected as the OP inhibitor to precede the resurrection step of the assay procedure.

Several families of compounds were assayed as potential resurrecting agents for aged-AChE. These families fall under two general motifs: simple pyridinium resurrecting agents (**R1-R32**) and gorge-spanning resurrecting agents (**R33-R77**) (Fig. 3.6). Each family of compounds is depicted in detail in Appendix B.

#### Objective of Study

The aim of this work is development of an enzyme assay method to evaluate the recovery, termed resurrection, of fully aged-*h*AChE. A large class of novel alkylating or acylating (resurrecting) agents for the phosphonic oxyanion *h*AChE adduct is assayed



**Scheme 3.3:** Stepwise approach to kinetically evaluate recovery of aged-AChE activity. E  $\equiv$  free enzyme; OP  $\equiv$  organophosphonate inhibitor; E-OP  $\equiv$  OP bound enzyme adduct;  $\text{aged E-OP}$   $\equiv$  aged enzyme adduct; Oxime-OP  $\equiv$  phosphorylated oxime product

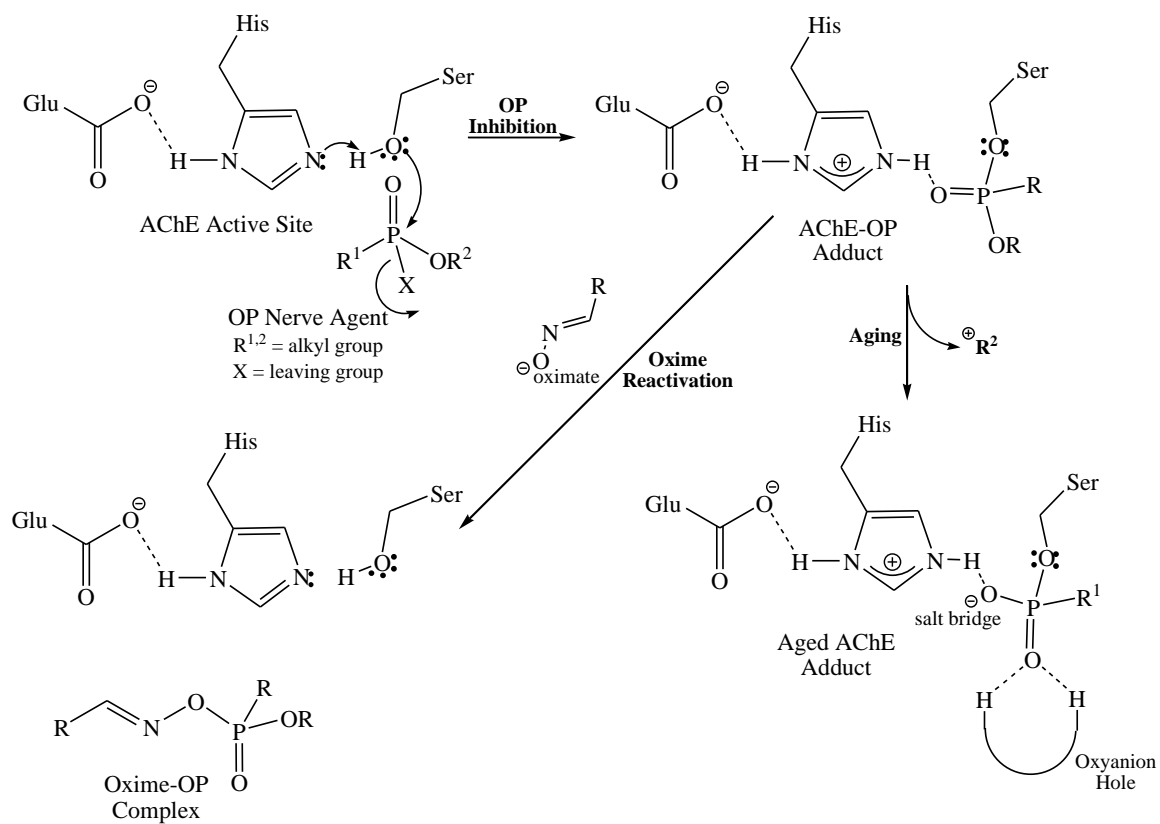


**Figure 3.1:** Mechanism of action for the inhibition, oxime reactivation, and aging of AChE by OP nerve agent

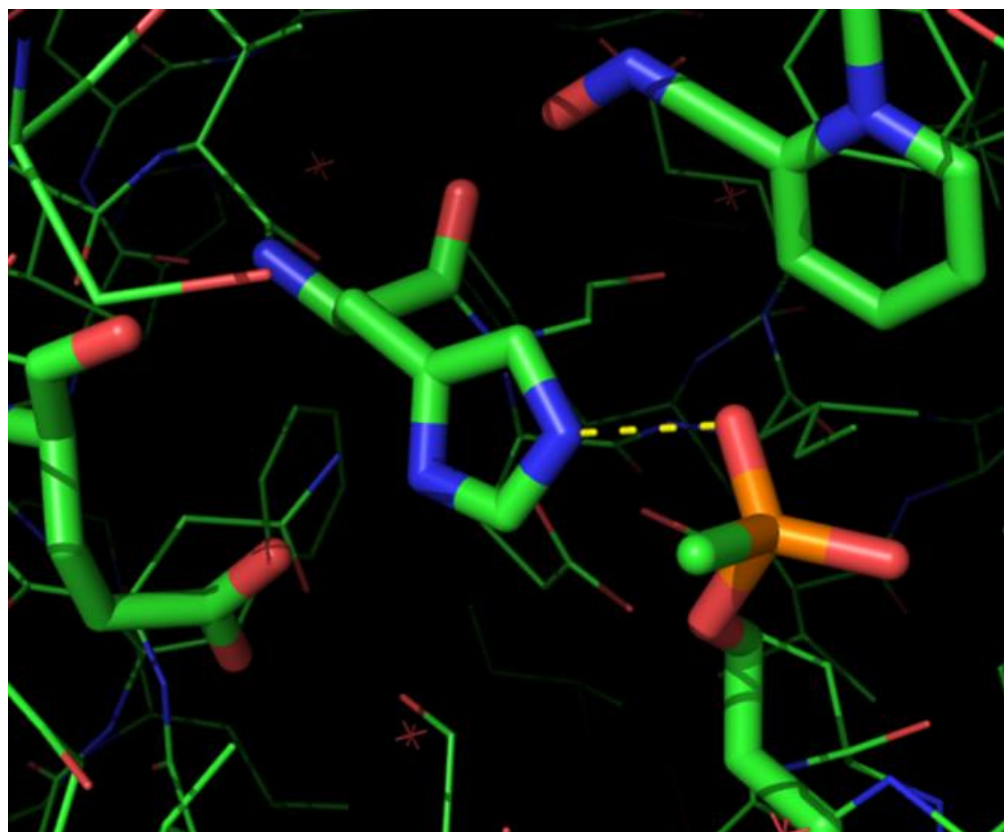


**Figure 3.2:** 3D crystal structure of aged-AChE adduct (*TcAChE*) with 2-PAM bound in the catalytic active site.

---

**Source:** Sanson, B.; Nachon, F.; Colletier, J.P.; Froment, M.T.; Toker, L.; Greenblatt, H.M.; Sussman, J.L.; Ashani, Y.; Masson, P.; Silman, I.; and Weik, M. *J. Med. Chem.*, **2009**, 52, 7593-7603; Image generated in PyMol

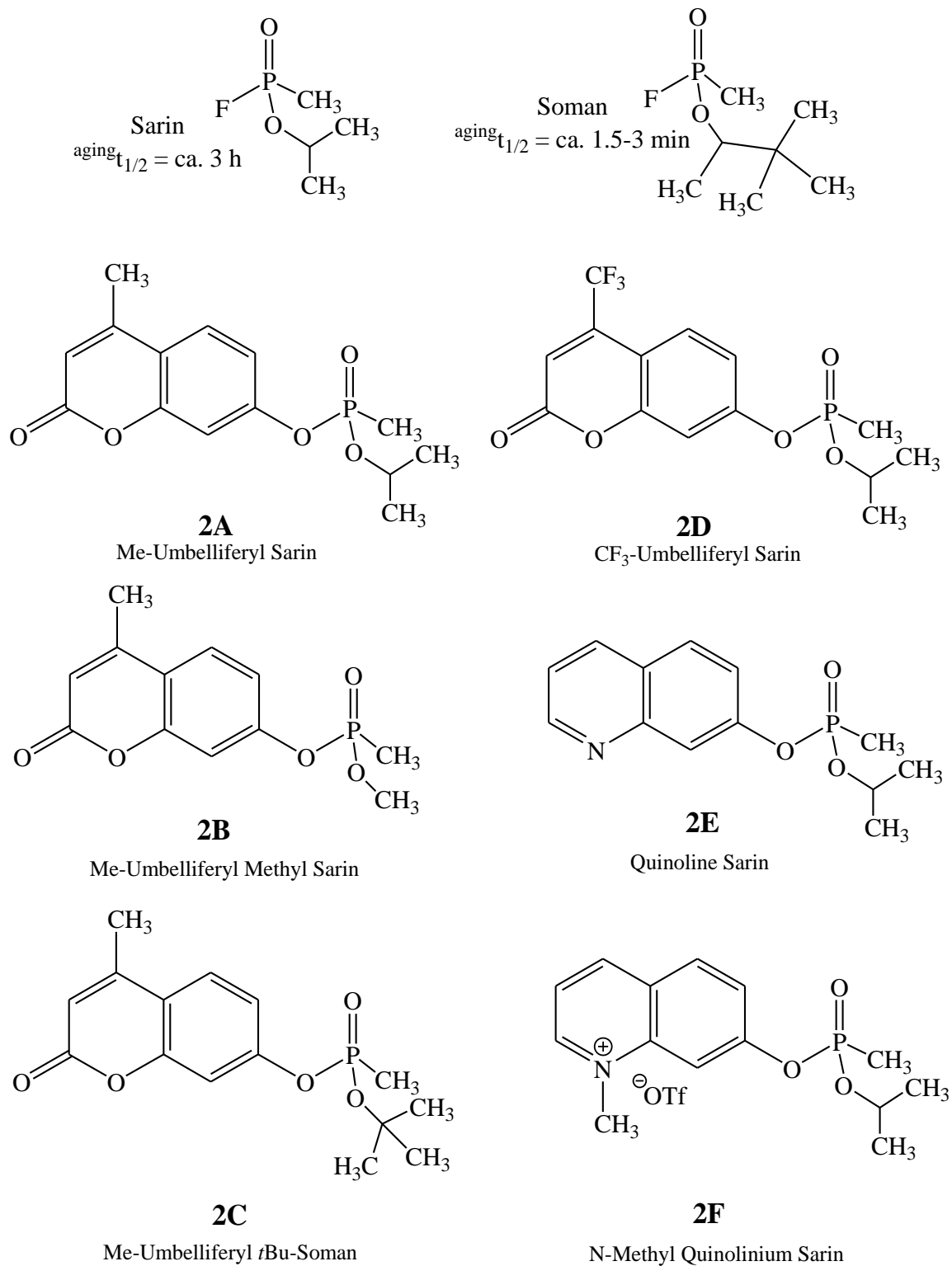


**Figure 3.3:** Chemical structures for OP inhibitors (sarin and soman) and OP analogues **2A-2F**

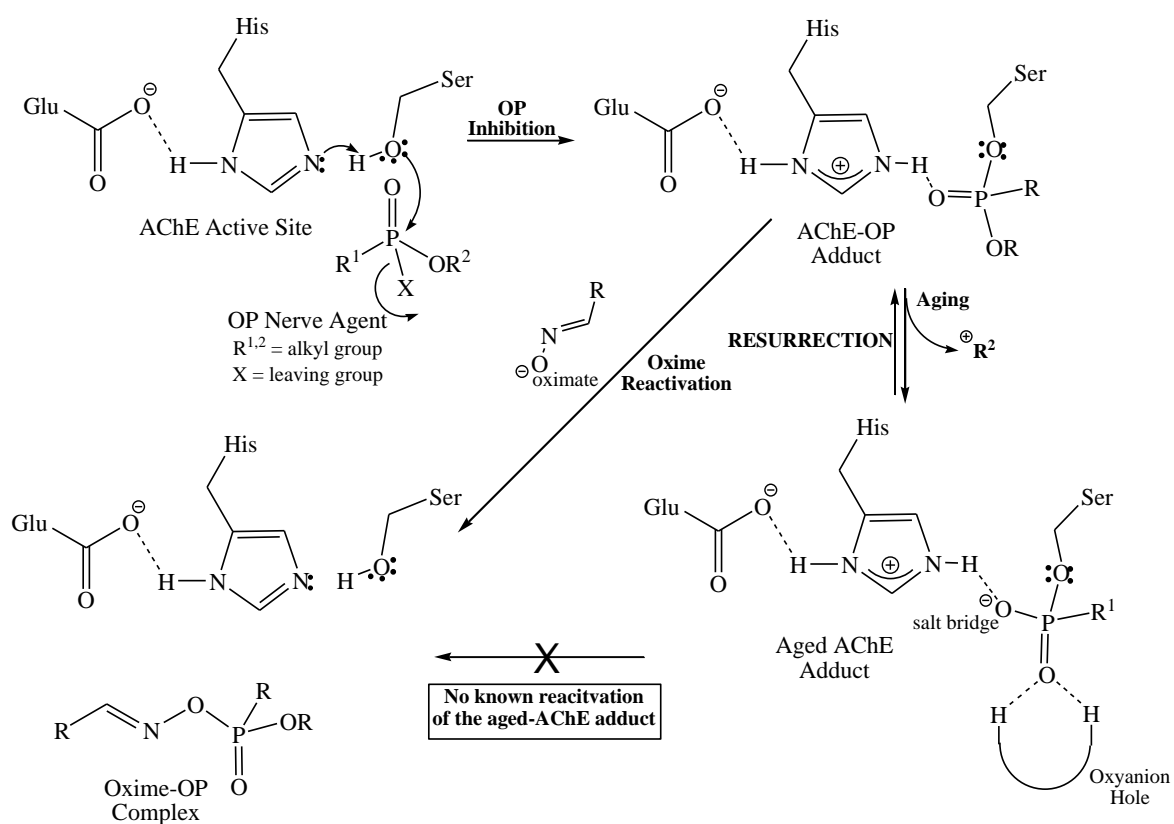
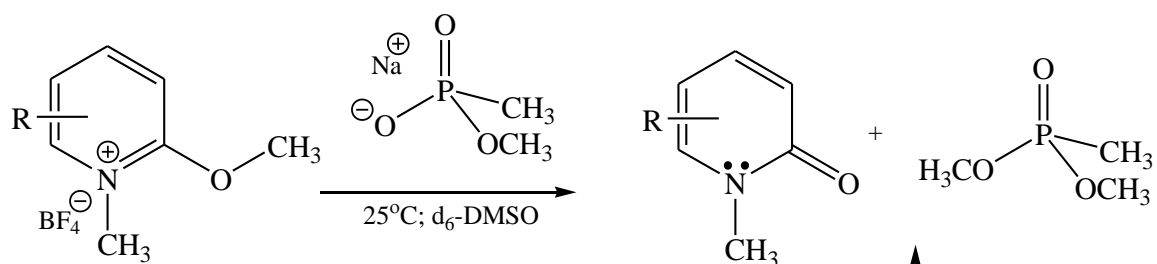
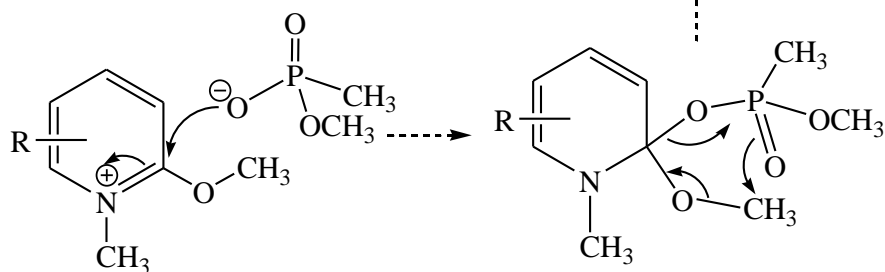


**Figure 3.4:** Mechanism of action for OP inhibition, reactivation, aging, and proposed resurrection of AChE

### General Methyl-transfer Scheme



### Mechanism for methyl-transfer



### Scheme for Resurrection of aged-AChE adduct

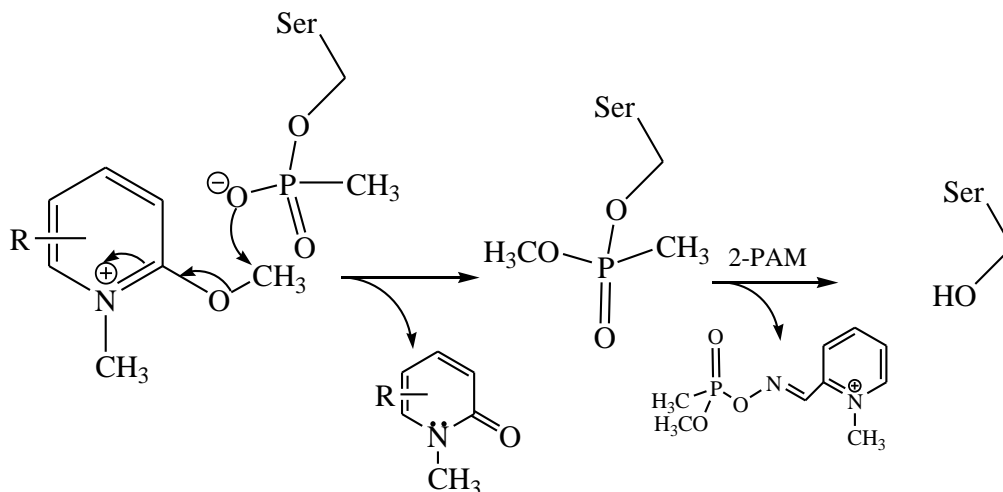
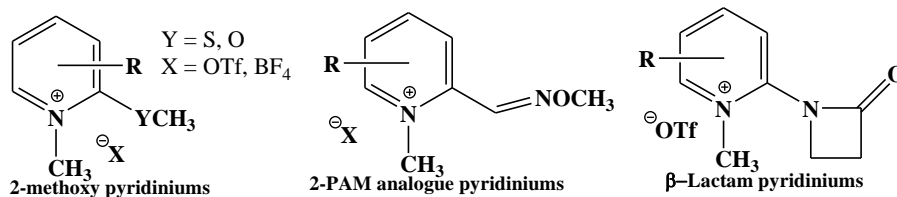


**Figure 3.5:** Reaction scheme and mechanism for model methyl transfer reaction and scheme for aged-AChE resurrection

### Simple Pyridinium Compounds (R1-R32)



### Gorge Spanning Compounds (R33-R77)

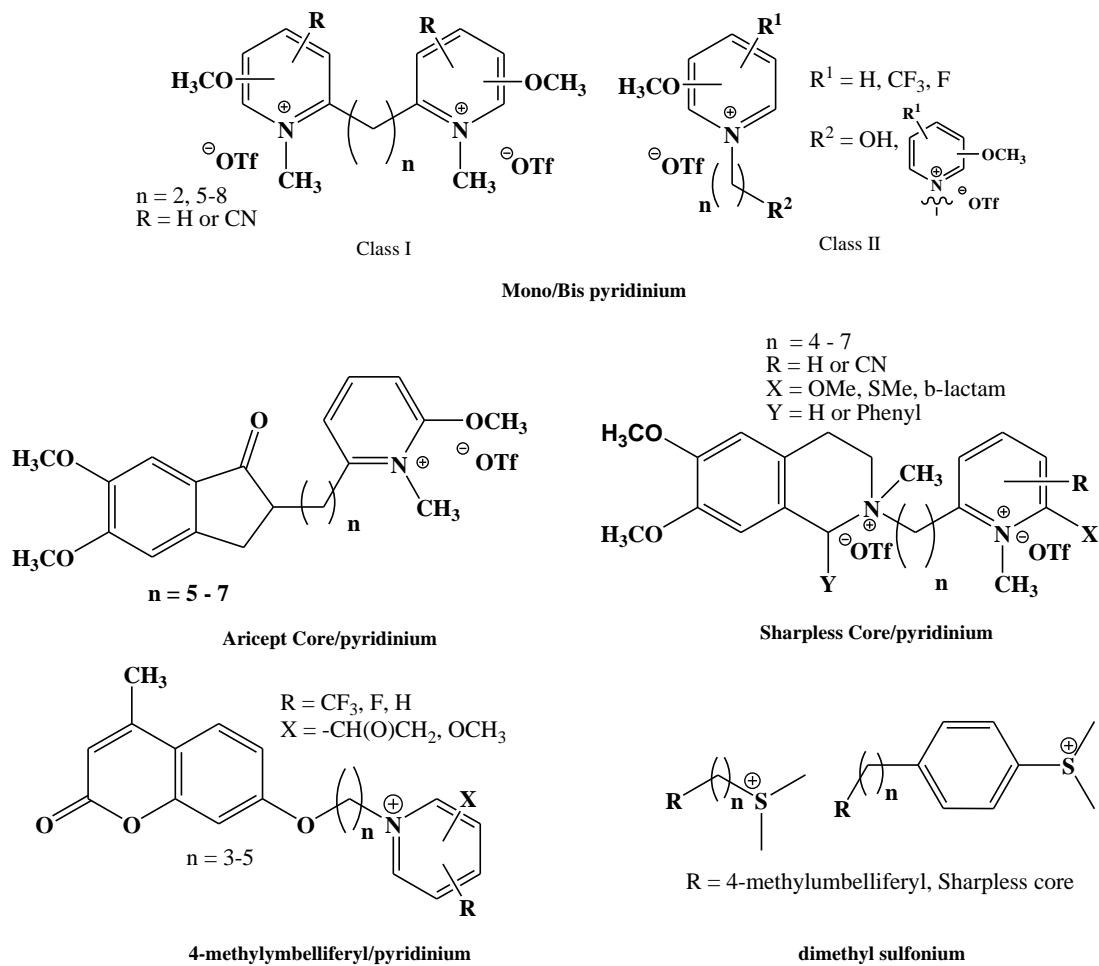


**Figure 3.6:** Structure of resurrecting compounds (88, 89, 90)



using the *hAChE* enzyme. Given the wide breadth of compound structures that can be derived from this library of potential aged-AChE active-site ligands, a consistent and reliable bioassay method was developed that accomplishes the following:

1. Synthesis of non-volatile OP inhibitor analogues of sarin and soman (Chapter 2)
2. Comprehensive kinetic evaluation of inhibition and aging rates for OP analogues (Chapter 2)
3. Assay procedure to test novel resurrecting agents ability to recover aged-AChE activity

### Materials and Methods

Detailed materials and general methods are outlined in Appendix B.

#### *IC<sub>50</sub> Determination of Resurrecting agents (R1-R77)*

All alkyl or acyltransfer compounds assayed were synthesized by Joseph J. Topczewski, S. Nilanthi Yasapala, Pedrom M. Keshavarzi, or Jacob Freuh in the Quinn research group of the University of Iowa Department of Chemistry. Compounds with limited water solubility were prepared in acetonitrile. 50 mM phosphate buffer (PB) was prepared in bulk at pH ranging from 7.3-7.5 as measured via an ion selective pH electrode which was calibrated prior to each measurement. All stock solutions were prepared from solid material and stored in polypropylene containers at 4 °C or -4 °C as follows: 0.1% (w/v) BSA solution in PB, 45 mM ATCh in DD-H<sub>2</sub>O, 20 mM DTNB in PB, and 1.4 nM *hAChE* in 0.1% BSA solution. Working solutions were prepared for use in biological assay in which all solutions were prepared using calibrated micropipettes in identical solvents as parent stock.

Assays were conducted on a Molecular Devices SpectraMaxM2 micro-plate reader and on polystyrene 96-well plates (Costar, round bottom). Activity of hAChE was measured spectrophotometrically at 412 nm and 27 °C following the Ellman assay method (24). Time dependent inhibition was measured at the minimum possible interval over 10 min durations at each incubation time point and performed in duplicate. Initial rates ( $v_i$ , mA/min) were calculated by least-squares analysis of the time courses at less than 10% turnover of the initial substrate concentration. Non-linear regression analysis was performed using SigmaPlot 12.0 to obtain inhibition kinetic parameters.  $K_i^{app}$  values were calculated by plotting  $v_i$  as a function of inhibitor concentration by fitting to Eq. 3.1:

$$v_i = \frac{v_o}{1 + \frac{10^{\log[I]}}{K_i^{app}}}$$

**Equation 3.1:** Initial rate equation for inhibited AChE hydrolysis of ATCh.  $v_i$   $\equiv$  initial rate (mA/min);  $v_o$   $\equiv$  rate of uninhibited reaction (mA/min);  $[I]$   $\equiv$  inhibitor concentration;  $K_i^{app}$   $\equiv$  apparent inhibitor dissociation constant (M)

From the  $K_i^{app}$ ,  $IC_{50}$  values were calculated using equation 3.2:

$$IC_{50} = \frac{K_i^{app}}{1 + \frac{[A]}{K_m}}$$

**Equation 3.2:** Equation describing the half maximal inhibitor concentration ( $IC_{50}$ , M).  $K_i^{app}$   $\equiv$  apparent inhibitor dissociation constant (M);  $K_m$   $\equiv$  Michaelis constant (M);  $[A]$   $\equiv$  substrate concentration (M).

### *Resurrection Assay Procedure*

Inactivation was achieved by incubating 483  $\mu\text{L}$  of 57 nM *hAChE* in 0.1% (w/v) BSA buffer (50 mM PB, pH 7.3) with 17  $\mu\text{L}$  of sarin analogue **2A**. Stock **2A** solutions were prepared in acetonitrile and assayed at a final concentration of 10  $\mu\text{M}$ . Control enzyme was prepared in the absence of inhibitor by adding a blank of acetonitrile. After 30 minutes of incubation at 27°C, excess inhibitor was separated from enzyme using a Sephadex G-50 Quick Spin Column (Roche). Prior to separation, the column was standardized with 0.1% (w/v) BSA in 50 mM PB (pH 7.3) and packed by centrifugation at 1100 x *g* for 4 minutes. The 500  $\mu\text{L}$  aliquot of inactivated *hAChE* was loaded to the packed Sephadex G-50 column bed and centrifuged at 600 x *g* for 6 minutes. Separated enzyme was collected and assayed immediately after inhibition and after 48 hours following 30 minute incubation with 100  $\mu\text{M}$  2-PAM at 27 °C. Ellman assay conditions as described in Appendix B were used to determine the percent of reactivated *hAChE* ( $\%hAChE_{OP}$  Residual) activity as defined by Eq. 3.3.  $\%hAChE_{OP}$  Residual is the ratio of the initial rates for OP inhibited *hAChE* ( $hAChE_{OP}$ ) and control *hAChE* ( $hAChE_{control}$ ) catalyzed hydrolysis of ATCh.

$$\%hAChE_{OP} \text{ Residual} = \frac{v_i \text{ of } hAChE_{OP}}{v_i \text{ of } hAChE_{control}} \times 100$$

**Equation 3.3:** Equation for the residual activity of OP inhibited *hAChE* ( $\%hAChE_{OP}$  Reactivated) following treatment with 2-PAM which is defined by the ratio of the initial ATCh hydrolysis rate of OP inhibited *hAChE* ( $v_i hAChE_{OP}$ , mA/min) and uninhibited *hAChE* ( $v_i hAChE_{control}$ , mA/min)

The extent of aging ( $\%hAChE_{aged}$ ) is defined by Eq. 3.4:

$$\%hAChE_{aged} = 100 - \%hAChE_{OP} \text{ Residual}$$

**Equation 3.4:** Defines the amount of *hAChE* that has aged and is unrecovered by treatment with 2-PAM; where  $\%hAChE_{OP}$  Residual  $\equiv$  recovered enzyme activity after treatment with 2-PAM

Resurrection assays were performed by preparing a 100  $\mu\text{L}$  incubation solution of 0.024  $\mu\text{g}$  of aged-*hAChE* in 0.1% (w/v) BSA, 50 mM phosphate buffer (pH 7.3), and 5 x  $K_i^{\text{app}}$  concentration of resurrecting agents (**R1-R77**). Aged-*hAChE* was incubated for 1 hour, 4 hour, and 24 hour periods at 27  $^{\circ}\text{C}$  in solution with a resurrecting agent (**R1-R77**). Following each incubation period, a 10  $\mu\text{L}$  aliquot of the aged-*hAChE* incubation solution was assayed in 50 mM phosphate buffer (pH 7.3), 0.3 mM ATCh and 0.45 mM DTNB following a 30 minute incubation with 100  $\mu\text{M}$  2-PAM and a total volume of 300  $\mu\text{L}$ . The percent of aged-*hAChE* reactivated ( $h\text{AChE}_{\text{react}}$ ) by 2-PAM was calculated using Eq. 3.5, which contains the ratio of the initial rates of aged-*hAChE* ( $h\text{AChE}_{\text{aged}}$ ) and  $h\text{AChE}_{\text{free}}$  catalyzed hydrolysis of ATCh assayed following each incubation with a resurrecting agent. From Eq. 3.6, we determine the percent of resurrected *hAChE*.

$$\%h\text{AChE}_{\text{react}} \text{ activity} = (v_i h\text{AChE}_{\text{aged}} / v_i h\text{AChE}_{\text{free}}) \times 100$$

**Equation 3.5:** Determination of the recovered activity of aged-*hAChE* following incubation with resurrecting agent

$$\%h\text{AChE}_{\text{Res.}} \text{ activity} = \%h\text{AChE}_{\text{React.}} \text{ activity} - \%h\text{AChE}_{\text{OP}} \text{ Residual}$$

**Equation 3.6:** Determination of the recovered activity of aged-*hAChE* following incubation with resurrecting agent.  $\%h\text{AChE}_{\text{Res.}} \text{ activity} \equiv$  percent of aged-*hAChE* recovered after treatment with resurrecting agent,  $\%h\text{AChE}_{\text{React.}} \text{ activity} \equiv$  percent of aged-*hAChE* reactivated by 2-PAM after treatment with resurrecting agent,  $\%h\text{AChE}_{\text{OP}} \text{ Residual} \equiv$  percent activity of untreated aged-*hAChE*

Figure 3.7 shows the detailed “roadmap” for the resurrection assay procedure. In this roadmap, steps involved in inhibiting, aging, and assaying the ability of novel resurrecting agents to recover *hAChE* activity are outlined in detail.

### Results and Discussion

Novel resurrecting agents (**R1-R77**) were successfully assayed for their affinity

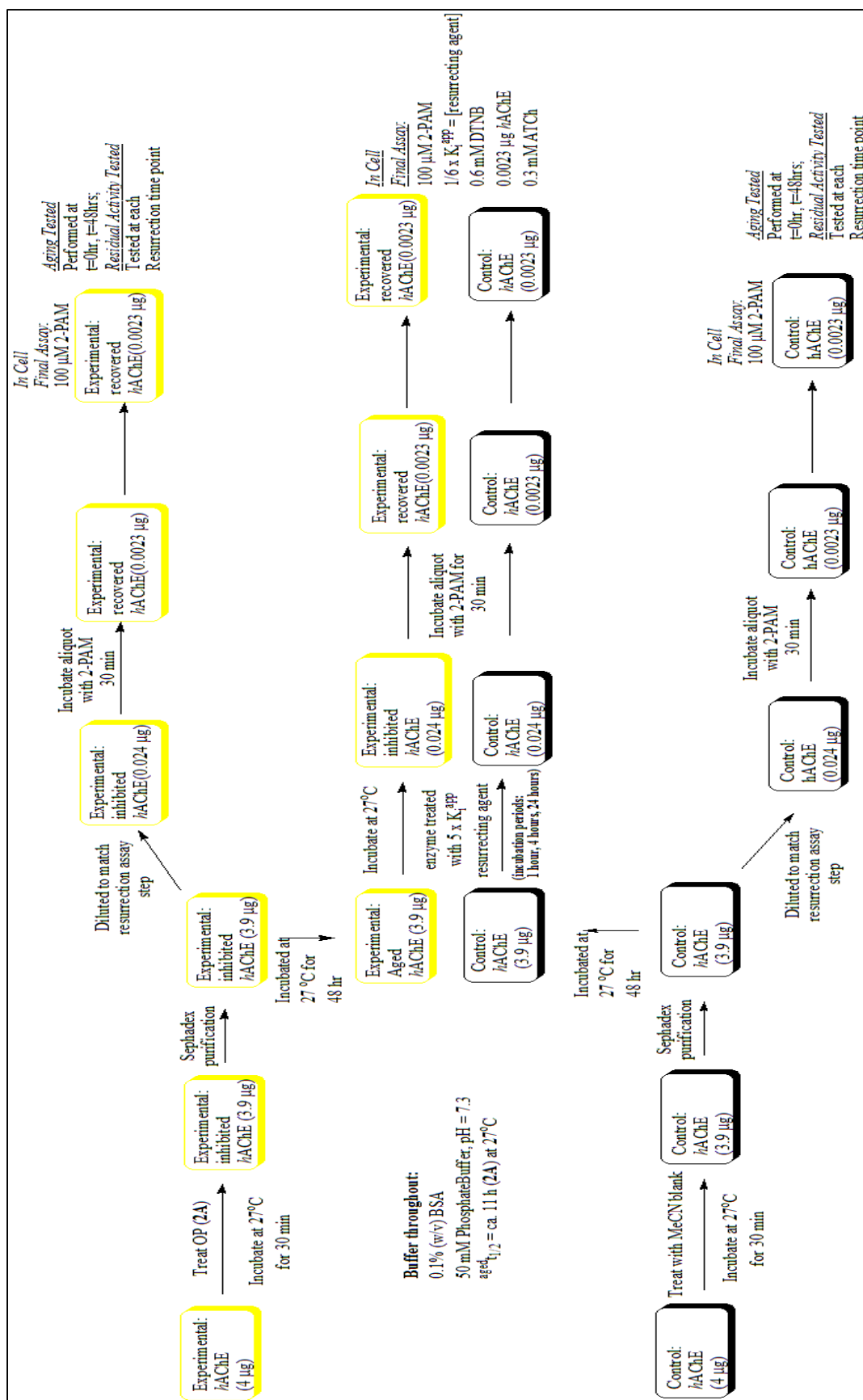
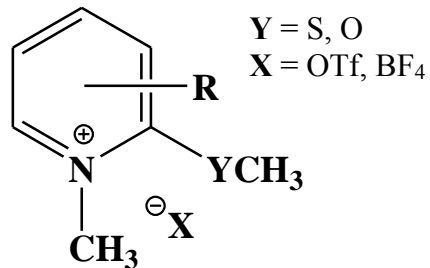


Figure 3.7: Roadmap for “resurrection” assay procedure

(IC<sub>50</sub>) for the apo *hAChE* enzyme (see Appendix B). The first of the two major classes of resurrecting agents were the simple pyridinium species. Overall assays of these compounds yielded IC<sub>50</sub> values between 7-500 μM (see Appendix B). From this family of compounds, two classes of time-dependent inhibitors were observed. These are the pyridinium β-lactams (**R24-R28**) and a 6-fluor-2-methoxy N-methyl pyridinium compound (**R10**), for which their inhibitions are profiled in Chapters 4 and 5. IC<sub>50</sub> determination of the gorge-spanning resurrecting agents (**R33-R77**) showed a higher potency to that of the simple pyridinium family of compounds. These values were as high as three orders of magnitude more potent, yielding IC<sub>50</sub> values between 50 nM and 150 μM.

Each inhibitor was independently evaluated in the resurrection assay model (Fig. 3.7) and compared at concentrations five times their K<sub>I</sub><sup>app</sup> values (10 x IC<sub>50</sub>). Once placed into the resurrection assay, each inhibitor was screened at three incubation time points (t = 1 h, 4 h, and 24h). Statistical analysis was performed for each value including appropriate propagation of values. As depicted in Fig. 3.7, the aged-*hAChE* and its complementary control were assayed absent of resurrecting agent for extent of aging (%*hAChE*<sub>OP</sub> Residual) and used in Eq. 3.6. Table 3.1 shows the results for resurrecting agents **R1-R18**, simple pyridiniums. These compounds were reported by Topczewski et al. to methylate methoxymethylphosphonic oxyanion in DMSO (88). None of the resurrecting compounds in this class showed significant recovery of enzyme activity, including the 3-F substituted compound (**R6**) that showed the highest rate of methyl transfer in the DMSO model system.

One well investigated observation was an apparent recovery of enzyme activity

**Table 3.1:** Resurrection assay data for **R1-R18** (methoxy N-methyl pyridiniums)

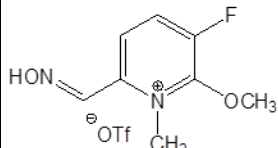
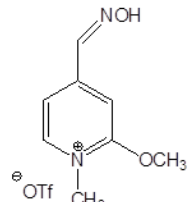
<u>Resurrecting Agent</u>	<u>Chemical Structure</u>	<u>K<sub>i</sub><sup>app</sup></u>	<u>%Resurrection:</u>		
			<u>t=1hr</u>	<u>t=4hr</u>	<u>t=24hr</u>
R1		73 (± 8) μM	0.2 (± 0.3)	0.9 (± 1.7)	-0.2 (± 0.4)
R2		28(± 2) μM	0.1 (± 0.5)	-0.3 (± 1.0)	-0.3 (± 0.5)
R3		90 (± 10) μM	1.5 (± 0.6)	0.4 (± 0.9)	-0.5 (± 1.2)
R4		103 (± 15) μM	0.9 (± 0.4)	0.4 (± 0.9)	-0.8 (± 1.0)
R5		33 (± 3) μM	0.04 (± 1.03)	0.3 (± 1.0)	1.2 (± 1.5)
R6		136(± 20) μM	0.02 (± 1.02)	0.02 (± 1.03)	-0.6 (± 1.1)
R7		46 (± 2) μM	-0.05 (± 0.32)	0.5 (± 1.1)	-0.4 (± 0.3)

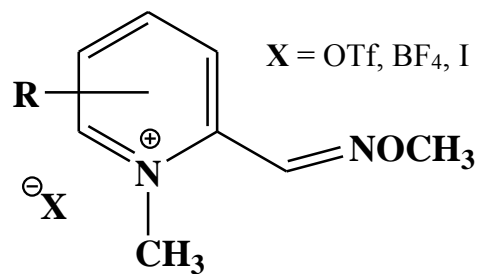
Table 3.1: continued

R8		72 ( $\pm$ 4) $\mu$ M	0.0.6 ( $\pm$ 1.1)	-0.2 ( $\pm$ 1.4)	0.9 ( $\pm$ 1.7)
R9		15 ( $\pm$ 1) $\mu$ M	0.5 ( $\pm$ 1.1)	0.3 ( $\pm$ 0.9)	-0.6 ( $\pm$ 1.0)
R10		27 ( $\pm$ 2) $\mu$ M	3 ( $\pm$ 1)	<i>nd</i>	<i>nd</i>
R11		41 ( $\pm$ 4) $\mu$ M	-1.4 ( $\pm$ 0.8)	-1.6 ( $\pm$ 0.8)	1.4 ( $\pm$ 0.8)
R12		170 ( $\pm$ 20) $\mu$ M	-0.2 ( $\pm$ 0.4)	0.8 ( $\pm$ 0.8)	1.2 ( $\pm$ 0.7)
R13		180 ( $\pm$ 10) $\mu$ M	0.4 ( $\pm$ 1.0)	6.0 ( $\pm$ 0.9)	13 ( $\pm$ 1)
R14		200 ( $\pm$ 10) $\mu$ M	-0.3 ( $\pm$ 0.9)	-0.4 ( $\pm$ 0.9)	-0.2 ( $\pm$ 1.0)
R15		110 ( $\pm$ 15) $\mu$ M	1.0 ( $\pm$ 0.8)	4.6 ( $\pm$ 1.0)	12.0 ( $\pm$ 0.9)
R16		230 ( $\pm$ 20) $\mu$ M	-0.2 ( $\pm$ 0.8)	-0.6 ( $\pm$ 0.8)	-0.5 ( $\pm$ 0.8)

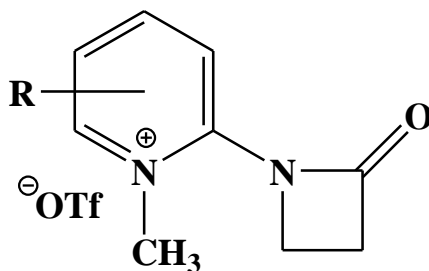


**Table 3.1:** continued

R17		1.2 ( $\pm 0.1$ ) mM	-0.1 ( $\pm 0.9$ )	0.7 ( $\pm 1.0$ )	4.7 ( $\pm 0.9$ )
R18		170 ( $\pm 10$ ) $\mu$ M	-1.6 ( $\pm 1.4$ )	-0.5 ( $\pm 1.4$ )	3.0 ( $\pm 1.4$ )

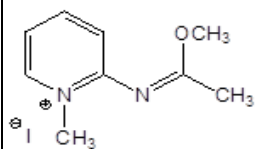
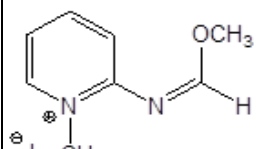
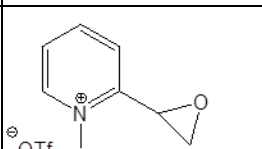
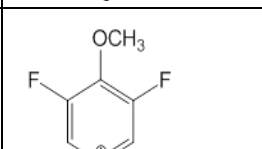
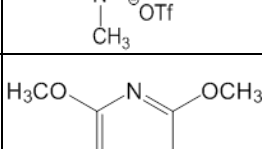
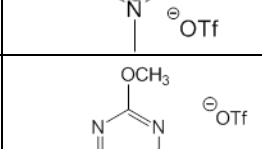
**Table 3.2:** Resurrection assay data for **R19-R23** (2-PAM analogues)

<u>Resurrecting Agent</u>	<u>Chemical Structure</u>	<u><math>K_i^{\text{app}}</math></u>	<u>%Resurrection:</u>		
			<u>t=1hr</u>	<u>t=4hr</u>	<u>t=24hr</u>
R19		140 ( $\pm$ 40) $\mu\text{M}$	0.3 ( $\pm$ 0.4)	0.2 ( $\pm$ 0.4)	-0.3 ( $\pm$ 0.5)
R20		66 ( $\pm$ 14) $\mu\text{M}$	0.5 ( $\pm$ 0.4)	0.7 ( $\pm$ 0.4)	-0.2 ( $\pm$ 1.1)
R21		220 ( $\pm$ 40) $\mu\text{M}$	<i>nd</i>	<i>nd</i>	<i>nd</i>
R22		680 ( $\pm$ 80) $\mu\text{M}$	-2.2 ( $\pm$ 1.4)	-1.3 ( $\pm$ 1.4)	-1.2 ( $\pm$ 1.8)
R23		180 ( $\pm$ 4) $\mu\text{M}$	0.2 ( $\pm$ 0.3)	-0.2 ( $\pm$ 0.4)	-0.1( $\pm$ 0.3)

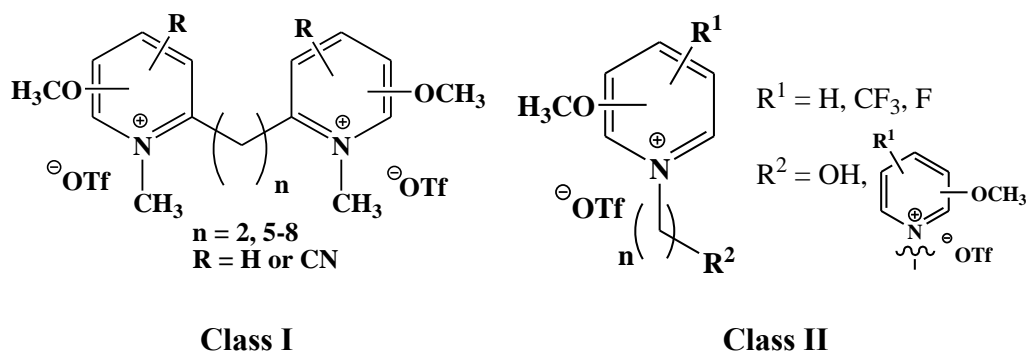
**Table 3.3:** Resurrection assay data for **R24-R29** (pyridinium  $\beta$ -lactams)

<u>Resurrecting Agent</u>	<u>Chemical Structure</u>	<u><math>K_i^{app}</math></u>	<u>%Resurrection:</u>		
			<u>t=1hr</u>	<u>t=4hr</u>	<u>t=24hr</u>
R24		56 ( $\pm$ 3) $\mu$ M	2.5 ( $\pm$ 0.7)	3.7 ( $\pm$ 2.8)	0.6 ( $\pm$ 2.0)
R25		160 ( $\pm$ 30) $\mu$ M	<i>nd</i>	0.8 ( $\pm$ 0.8)	0.7 ( $\pm$ 0.7)
R26		270 ( $\pm$ 40) $\mu$ M	-0.01 ( $\pm$ 0.30)	-0.05 ( $\pm$ 0.30)	-3.3 ( $\pm$ 0.8)
R27		110 ( $\pm$ 10) $\mu$ M	-0.3 ( $\pm$ 0.3)	0.5 ( $\pm$ 0.8)	-11 ( $\pm$ 11)
R28		28 ( $\pm$ 2) $\mu$ M	-0.5 ( $\pm$ 0.3)	-0.07 ( $\pm$ 0.4)	-1.2 ( $\pm$ 0.3)
R29		200 ( $\pm$ 20) $\mu$ M	-0.1 ( $\pm$ 0.2)	0.07 ( $\pm$ 0.20)	-0.4 ( $\pm$ 0.4)

**Table 3.4:** Resurrection assay data for **R30-R35** (other aromatic alkylating compounds)

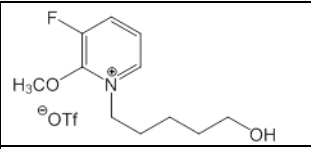
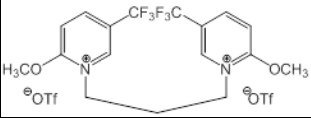
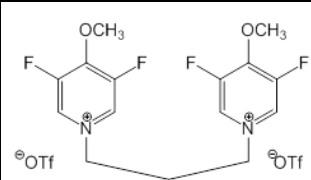
<u>Resurrecting Agent</u>	<u>Chemical Structure</u>	<u>K<sub>i</sub><sup>app</sup></u>	<u>%Resurrection:</u>		
			<u>t=1hr</u>	<u>t=4hr</u>	<u>t=24hr</u>
R30		81 (±9) μM	0.04 (± 0.30)	0.1 (± 0.5)	-0.4 (± 0.5)
R31		260 (±30) μM	-1.2 (± 1.4)	-1.5 (± 0.8)	-0.1 (± 0.4)
R32		400 (± 60) μM	-0.40 (± 0.4)	0.3 (± 0.3)	-0.4 (± 0.3)
R33		160 (± 6) μM	0.3 (± 0.3)	-0.1 (± 0.3)	0.1(± 0.3)
R34		99 μM ± 5 μM	0.6 (± 0.3)	0.04 (± 0.30)	0.2(± 0.3)
R35		1.1 (± 0.9) mM	1.0 (± 0.8)	-1.1 (± 1.4)	0.7 (± 0.4)

**Table 3.5:** Resurrection assay data for **R36-R46** (gorge-spanning methoxyN-methyl pyridiniums)

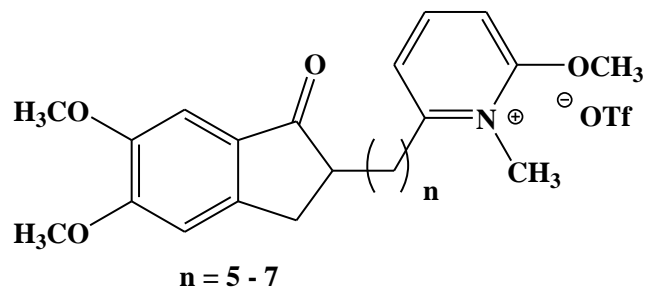


Resurrecting Agent	Chemical Structure	$K_i^{ADP}$	%Resurrection:		
			t=1hr	t=4hr	t=24hr
R36		140(±30) nM	0.9 (± 0.4)	-1.1 (± 2.6)	-0.8 (± 0.3)
R37		350 (±100) nM	0.1 (± 0.9)	0.2 (± 0.9)	0.02 (± 1.00)
R38		200 (± 40) nM	0.2 (± 0.9)	0.4 (± 0.9)	-0.2 (± 0.9)
R39		240 (± 40) nM	1.3 (± 1.1)	1.3 (± 1.4)	-0.2 (± 1.2)
R40		1.6 (±0.1) μM	0.5 (± 0.4)	0.8 (± 0.4)	-0.2 (± 0.4)
R41		600 (± 160) nM	-0.2 (± 0.3)	0.1 (± 0.2)	-0.7 (± 0.2)
R42		45 (± 2) μM	0.6 (± 0.6)	0.6 (± 0.6)	0.4 (± 0.7)
R43		195 (± 7) μM	0.4 (± 0.6)	0.5 (± 0.6)	0.6 (±0.6)

Table 3.5: continued

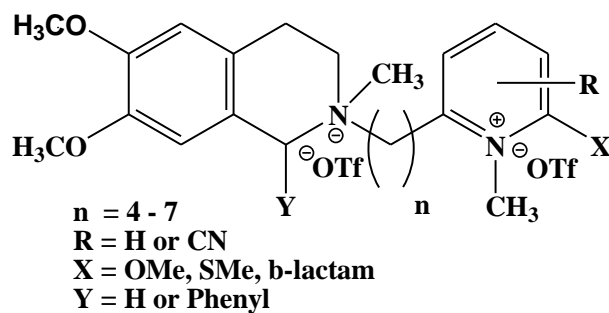
R44		$32 (\pm 1) \mu\text{M}$	$0.5 (\pm 0.6)$	$0.5 (\pm 0.8)$	$2.1 (\pm 2.6)$
R45		$22 (\pm 1) \mu\text{M}$	$0.8 (\pm 0.7)$	$-0.04 (\pm 0.60)$	$0.4 (\pm 0.6)$
R46		$43 (\pm 2) \mu\text{M}$	$0.6 (\pm 0.3)$	$-0.3 (\pm 0.5)$	$-0.2 (\pm 0.5)$

**Table 3.6:** Resurrection assay data for **R47-R50** (Aricept core/pyridinium gorge-spanners)



<u>Resurrecting Agent</u>	<u>Chemical Structure</u>	<u><math>K_i^{app}</math></u>	<u>%Resurrection:</u>		
			<u>t=1hr</u>	<u>t=4hr</u>	<u>t=24hr</u>
R47		240 ( $\pm$ 30) nM	0.6 ( $\pm$ 1.0)	0.2 ( $\pm$ 0.9)	-0.5 ( $\pm$ 0.9)
R48		590 ( $\pm$ 60) nM	-0.04 ( $\pm$ 0.90)	0.1 ( $\pm$ 1.0)	-0.4 ( $\pm$ 1.0)
R49		150 ( $\pm$ 20) nM	0.5 ( $\pm$ 0.9)	0.1 ( $\pm$ 0.9)	-0.7 ( $\pm$ 0.9)
R50		380 ( $\pm$ 40) nM	0.3 ( $\pm$ 0.9)	0.1 ( $\pm$ 0.9)	-1.1 ( $\pm$ 1.0)

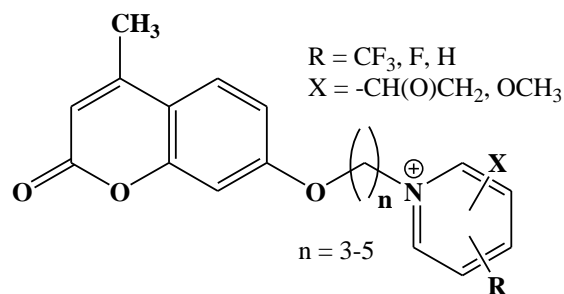
**Table 3.7:** Resurrection assay data for **R51-R59** (Sharpless core/pyridinium gorge-spanners)



Resurrecting Agent	Chemical Structure	$K_i^{app}$	%Resurrection:		
			t=1hr	t=4hr	t=24hr
R51		4.3 ( $\pm$ 0.2) $\mu$ M	-2.0 ( $\pm$ 1.4)	-0.9 ( $\pm$ 0.7)	0.4 ( $\pm$ 0.4)
R52		10 ( $\pm$ 2) $\mu$ M	0.7 ( $\pm$ 1.0)	0.2 ( $\pm$ 1.0)	-0.2 ( $\pm$ 1.0)
R53		1.5 ( $\pm$ 0.4) $\mu$ M	-0.3 ( $\pm$ 0.8)	0.2 ( $\pm$ 0.5)	-1.0 ( $\pm$ 0.3)
R54		4 ( $\pm$ 2) $\mu$ M	0.3 ( $\pm$ 0.4)	0.5 ( $\pm$ 0.4)	0.2 ( $\pm$ 0.4)
R55		24 ( $\pm$ 5) $\mu$ M	0.4 ( $\pm$ 0.4)	0.9 ( $\pm$ 0.4)	0.2 ( $\pm$ 0.5)
R56		270 ( $\pm$ 50) $\mu$ M	0.3 ( $\pm$ 0.9)	-0.1 ( $\pm$ 0.5)	0.3 ( $\pm$ 0.6)
R57		1.0 ( $\pm$ 0.1) $\mu$ M	0.6 ( $\pm$ 0.4)	0.5 ( $\pm$ 0.4)	-0.3 ( $\pm$ 0.4)
R58		300 ( $\pm$ 50) nM	0.5 ( $\pm$ 0.4)	0.04 ( $\pm$ 0.40)	-0.3 ( $\pm$ 0.40)
R59		100 ( $\pm$ 10) nM	0.02 ( $\pm$ 0.50)	-0.01 ( $\pm$ 0.40)	-0.3 ( $\pm$ 0.4)



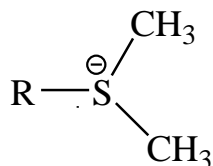
**Table 3.8:** Resurrection assay data for **R60-R70** (umbelliferyl pyridiniums gorge-spanners)



<u>Resurrecting Agent</u>	<u>Chemical Structure</u>	<u><math>K_i^{\text{app}}</math></u>	<u>%Resurrection:</u>		
			<u>t=1hr</u>	<u>t=4hr</u>	<u>t=24hr</u>
R60		930 ( $\pm$ 130) nM	0.3 ( $\pm$ 0.3)	0.6 ( $\pm$ 0.3)	-0.1( $\pm$ 1.8)
R61		970 ( $\pm$ 40) nM	0.4 ( $\pm$ 0.3)	1.0 ( $\pm$ 0.3)	-0.1( $\pm$ 0.6)
R62		2.0 ( $\pm$ 0.1) $\mu$ M	-0.4 ( $\pm$ 0.5)	0.8 ( $\pm$ 0.4)	-0.1( $\pm$ 0.3)
R63		2.0 ( $\pm$ 0.1) $\mu$ M	-0.4 ( $\pm$ 0.3)	1.1 ( $\pm$ 1.3)	-0.5( $\pm$ 0.2)
R64		10 ( $\pm$ 1) $\mu$ M	-1.5 ( $\pm$ 2.0)	1.1 ( $\pm$ 0.5)	0.6( $\pm$ 2.9)
R65		930 ( $\pm$ 40)nM	-0.04 ( $\pm$ 0.40)	1.5 ( $\pm$ 0.3)	-1.4( $\pm$ 2.5)
R66		7 ( $\pm$ 1) $\mu$ M	-0.01 ( $\pm$ 0.90)	0.4 ( $\pm$ 0.6)	1.6( $\pm$ 1.5)

Table 3.8: continued

R67		56 ( $\pm$ 6) $\mu$ M	0.3 ( $\pm$ 0.5)	0.7 ( $\pm$ 0.4)	0.02( $\pm$ 0.60)
R68		1.4 ( $\pm$ 0.1) $\mu$ M	-1 ( $\pm$ 1)	0.9 ( $\pm$ 0.3)	0.2 ( $\pm$ 1.1)
R69		1.5 ( $\pm$ 0.2) $\mu$ M	-0.4 ( $\pm$ 0.9)	0.6 ( $\pm$ 1.0)	-0.1( $\pm$ 0.2)
R70		3.4 ( $\pm$ 0.2) $\mu$ M	-1.0 ( $\pm$ 0.5)	0.9 ( $\pm$ 0.3)	-0.6 ( $\pm$ 1.3)

**Table 3.9:** Resurrection assay data for **R71-R77** (dimethylsulfonium compounds)

<u>Resurrecting Agent</u>	<u>Chemical Structure</u>	<u>K<sub>1/2</sub><sup>app</sup></u>	<u>%Resurrection:</u>		
			<u>t=1hr</u>	<u>t=4hr</u>	<u>t=24hr</u>
R71		490 (± 30) μM	0.6 (± 0.6)	0.6 (± 0.6)	1.8(± 0.6)
R72		15 (± 1) μM	1.0 (± 0.5)	3.4 (± 0.7)	3.0(±1.9)
R73		9 (± 1) μM	-0.3 (± 1.2)	1.7 (± 0.8)	2.0 (± 2.8)
R74		13 (± 1) μM	0.3 (± 1.5)	1 (± 2)	nd
R75		11 (± 2) μM	0.6 (± 1.6)	-0.8 (± 1.3)	nd
R76		35 (± 2) μM	1.8 (± 1.6)	nd	nd
R77		12 (± 1) μM	2.2 (± 1.8)	0.4 (± 1.6)	-4.1 (± 5.2)

with the oxime substituted simple pyridinium resurrecting agents, **R13** and **R15**.

Placement in the resurrection assay showed an apparent recovery of aged-*hAChE* activity between 8-10% (Fig. 3.8 and Appendix B). Further investigation into the apparent recovered activity entailed assaying at multiple points to resolve the rate of resurrection and added dosing after 24 hours. In both cases, recovered aged enzyme activity was observed. Because of the presence of an oxime substituent, 2-PAM was tested as a control parallel to these resurrecting agents. 2-PAM also showed an apparent recovery between 8-10% of enzyme activity when treated as a resurrecting agent (Fig. 3.8).

This observed recovery was attributed to having a mixture of OP analogue (**2A**) enantiomers. Previous studies have shown a significant effect between  $S_P$  and  $R_P$  OP enantiomers on their inhibition and aging rates (63, 91, 92). Two important notes about chirality effects on OP inhibition and aging rates should be made. The first is that  $R_P$  chiral OPs' inhibition and oxime reactivation rates are slower than  $S_P$  chiral OPs. In terms of the observed recovery of aged-*hAChE* activity, it is most likely attributed to slow oxime reactivation of un-aged  $R_P$  chiral OP. Subsequent testing for recovery of aged enzyme activity in the resurrection absent of a resurrecting agent, following the resurrection assay roadmap in Fig. 3.7, showed no observed recovery of aged-*hAChE* activity (Fig. 3.8). This suggests that 30 min exposure with 100  $\mu$ M 2-PAM, as part of the resurrection assay procedure, does not recover the un-aged  $R_P$  chiral OP-AChE adduct. Use of 2-PAM can in turn be used as a positive control for the resurrection assay method.

Table 3.1, 3.2, and 3.3 show the resurrection assay results for the  $\beta$ -lactam family, 6-fluoro-2-methoxy N-methyl pyridinium, and other aromatic resurrecting agents, all of which showed no apparent recovery of aged-*hAChE* activity. As mentioned previously, compounds **R24-28** and **R10** showed time-dependent inhibition of apo *hAChE* and their

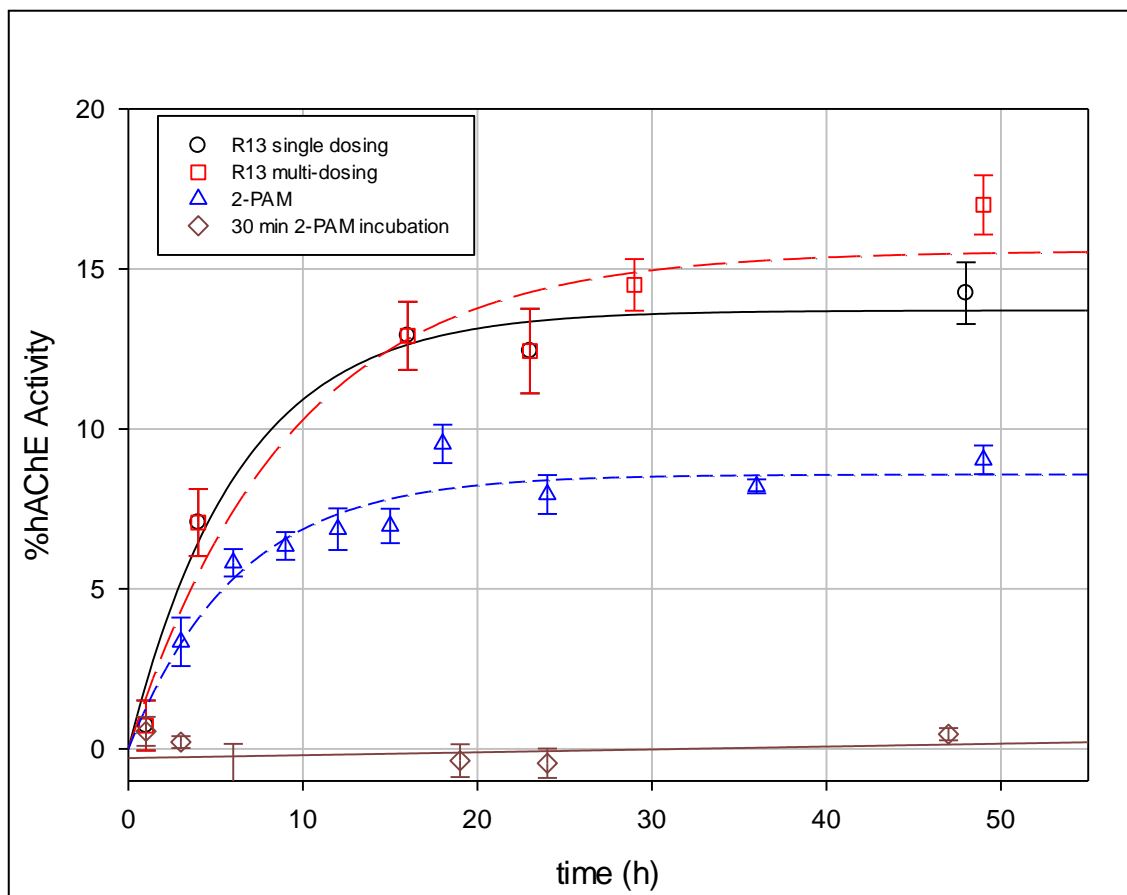


**Figure 3.8:** Plot of recovered aged-*hAChE* activity by treatment with oximes 2-PAM and **R13** at  $5 \times K_I^{\text{app}}$  concentrations.

inhibitory behavior is detailed in Chapters 4 and 5. Tables 3.4-3.9 show the resurrection assay data for the gorge-spanning resurrecting agents. These classes of compounds are designed to be multifunctional bearing a peripheral site binder (Aricept core, Sharpless core, pyridinium moiety) tethered to a phosphonic oxyanion alkylating or acylating “warhead” (89, 90). Inhibitors **R33-R77**, showed no apparent recovery of aged-*hAChE* activity in the resurrection assay.

### Conclusion

OP nerve agents remain a significant global threat and there is still an unmet need for efficacious antidotes, especially for soman. This chapter describes compounds capable of resurrecting activity from an aged-AChE adduct, which would form from sarin or soman exposure. However, a comprehensive, reproducible, and reliable assay model that assesses the ability of novel resurrecting agents’ ability to recover aged-*hAChE* adduct activity was successfully developed. Of the more than 70 compounds placed in the resurrection assay, none showed an appreciable recovery of aged-*hAChE* activity. Of the compounds that showed any extent of recovered aged-*hAChE*, there was a significant loss in activity of the control *apo hAChE* experiment. Additionally, 2-PAM and novel oxime moieties were proven to work as useful positive controls in assaying potential resurrecting agents by this methodology.

## CHAPTER 4: KINETIC EVALUATION OF N-METHYL PYRIDINIUM $\beta$ -LACTAM INHIBITORS OF HUMAN ACETYLCHOLINESTERASE

### Chemical Mechanism and Significance

Acetylcholinesterase (acetylcholine acetylhydrolase, EC 3.1.1.7; abbreviated herein AChE) is a powerful serine hydrolase that functions in both the central and peripheral nervous systems to terminate impulse transmission of the neurotransmitter ACh (1,5). Release of ACh across cholinergic synapses triggers an action potential for a voluminous number of cognitive and motor sensory activities. AChE is best characterized by its astounding catalytic efficiency for ACh turnover,  $k_{\text{cat}}/K_m = 10^8 \text{ M}^{-1} \text{ s}^{-1}$  (3), and catalyzes the hydrolysis of a broad range of substrates. Its promiscuous catalytic nature makes AChE susceptible to inhibition at the Ser residue of its catalytic triad (3). Inhibitors of AChE are of interest in the treatment of various neurological disorders including glaucoma, myasthenia gravis, and most notably Alzheimer's Disease (30, 31, 32, 33, 34). Organophosphate (OP) nerve agents, such as sarin and soman, can cause large scale inactivation of AChE from which exposure can be fatal (41, 42). Undoubtedly, there is significant utility in evaluating the kinetic behavior of AChE including drug design, therapeutic measures for OP exposure, and mechanistic appraisal of AChE's high catalytic efficiency.

$\beta$ -lactams are widely used as antibacterial agents targeting the active site serine of surface enzymes essential to the production of bacterial cell walls (68, 69, 70). Evolutionary resistance or allergies to antibiotics, such as penicillin and amoxicillin, pose a challenge to develop and evaluate new classes of  $\beta$ -lactams that have potential

medicinal use. The core four-membered ring system of  $\beta$ -lactams is highly reactive and susceptible to nucleophilic attack, making them candidates for hydrolysis by the active site serinyl hydroxyl group (71). Bacterial serine proteases, i.e. transpeptidases and elastases, are irreversibly inhibited by  $\beta$ -lactams leading to cell death (72).  $\beta$ -lactamases serve to turn over  $\beta$ -lactams, giving rise to antibiotic resistance. To combat this evolutionary response, several families of  $\beta$ -lactams have been developed that are either slowly hydrolyzed by  $\beta$ -lactamases or irreversibly inhibit them (73). Hydrolytic stability poses an additional challenge to the development of potential  $\beta$ -lactam inhibitors, which hydrolyze significantly faster than larger lactam ring systems (74).

Despite the vast extent of information known about  $\beta$ -lactam inhibition of serine proteases, AChE is seldom used to profile this well-known class of inhibitors (75). Due to AChE's established mechanism of action (3, 9, 10), it serves as an ideal probe for the inhibitory efficacy of potential  $\beta$ -lactam inhibitors. Additionally, AChE's active site, peripheral binding site, and allosteric binding loci provide a provocative system to compare with serine proteases that act by an acylation mechanism of action. The present study describes the synthesis of a class of *N*-methyl pyridinium  $\beta$ -lactams, evaluation of their inhibitory action for human acetylcholinesterase (hAChE), docking calculations, and reaction modeling.

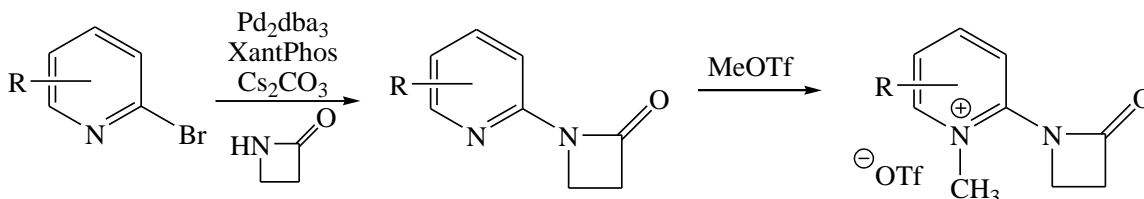
### Materials and Methods

Additional materials and general methods are described in Appendix C.

#### *Synthesis of $\beta$ -Lactam Inhibitors*



$\beta$ -Lactam inhibitors **R24-R28** were synthesized by Dr. Joseph T. Topczewski, post-doctoral fellow in the Quinn research group, using the following reaction method (Scheme 4.1).



**Scheme 4.1:** Synthesis of Inhibitors **R24-R28**, R = H, 5-F, 3-F, 5-CF<sub>3</sub>, or 4-N(Me)<sub>2</sub>.

Scheme 4.1 describes the synthesis of a class of *N*-methylpyridinium  $\beta$ -lactam inhibitors **R24-R28**. A series of bromopyridines (R = H, 5-F, 3-F, 5-CF<sub>3</sub>, or 4-N(Me)<sub>2</sub>) were coupled to azetidin-2-one via Buchwald-Hartwig conditions to yield *N*-pyridinyl  $\beta$ -lactams. Treatment with methyl trifluoromethylsulfonate (MeOTf) afforded the desired quaternized pyridinium  $\beta$ -lactam inhibitors. Compound purity was characterized via <sup>1</sup>H NMR, <sup>13</sup>C NMR, <sup>19</sup>F NMR, HREIMS, and elemental analysis.

#### *Hydrolytic Stability of Inhibitors in Phosphate Buffer*

The rate of hydrolysis for the inhibitors was determined in 50 mM phosphate buffer by UV analysis. Absorbance maxima for the  $\beta$ -lactam inhibitors **R24-R28** were obtained at a concentration of 100  $\mu$ M in DD-H<sub>2</sub>O. Inhibitors **R24-R28** were allowed to incubate at 27 °C for 30 min in 1 mM NaOH to produce their respective hydrolysis products. Each inhibitor solution was prepared fresh from solid prior to use. Absorbance

data were obtained in a black walled, 1 mL, 10 mm quartz cuvette using a Molecular Devices SpectraMaxM2 micro-plate reader's single cuvette cell. Data were collected from 250 nm to 750 nm at 1 nm increments. The UV spectra of hydrolyzed inhibitor products were obtained from solutions of inhibitors **R24-R28** in 1 mM NaOH 27 °C. Absorbance spectra for **R24-R28** can be found in Appendix C.

Because the  $\Delta\lambda_{\max}$  values were small, absolute maximum  $\Delta A$  values were calculated between the two absorbance curves. The corresponding wavelength for the absolute maximum  $\Delta A$  ( $\lambda_{\Delta A}$ ) values was used to monitor reactant depletion and/or product formation. The change in molar absorptivity ( $\Delta\varepsilon$ ) was calculated from Eq. 4.1 for each inhibitor. Rate constants of hydrolysis ( $k_{\text{hyd}}$ ,  $\text{s}^{-1}$ ) were estimated at 50  $\mu\text{M}$  in 50 mM phosphate buffer at pH 7.3 following Eq. 4.2 for inhibitors **R24**, **R26** and **R27**, or by fitting data to equation Eq 4.3 for inhibitor **R25** ( $\text{R}=5\text{-CF}_3$ ). Data were collected over a 4 hour period and measured at the minimum allowable interval. Hydrolysis was monitored via UV at 4 wavelengths (297 nm, 302 nm, 322 nm and 335 nm) in polystyrene 96 well-plate. The wavelength 297 nm corresponds to inhibitors **R24** and **R25**, where the wavelength 302 nm corresponds to **R26** and **R27**. Wavelengths for monitoring the hydrolysis product formations for **R24** and **R27** were 322 nm and 335 nm respectively. Wavelengths correspond to the  $\lambda_{\Delta A}$  favoring either  $\beta$ -lactam reactants or products. A  $k_{\text{hyd}}$  for inhibitor **R28** was not determined because no reactant depletion or product formation was observed via UV analysis.

$$\Delta\varepsilon = \frac{\Delta A}{[I]}$$

**Equation 4.1:** Equation defining change in molar absorptivity ( $\Delta\varepsilon$ , Abs/M), calculated from  $\Delta A$  (absorbance), and  $[I]$  (inhibitor concentration, M)

$$k_{hyd} = \frac{v_i/\Delta\varepsilon}{[I]}$$

**Equation 4.2:** Equation for determining the rate constant of hydrolysis ( $k_{hyd}$ ,  $s^{-1}$ ) from the initial rate  $v_i$  (A/s)

$$A = A_{\infty} + (A_o - A_{\infty})e^{-k_{hyd}t}$$

**Equation 4.3:** Equation for the first-order hydrolytic degradation of inhibitors **R24-28**; A (absorbance),  $A_{\infty}$  (absorbance at  $t_{\infty}$ ),  $A_o$  (initial absorbance), t (time, s),  $k_{hyd}$  (rate constant,  $s^{-1}$ ).

#### *Enzyme Assay Procedures and Kinetic Analysis*

Phosphate buffer (PB) at 50 mM concentration was prepared in bulk at pH ranging from 7.2-7.3. The pH was determined by an ion selective pH electrode that was calibrated prior to each measurement. All stock solutions were prepared from solid material and stored in polypropylene containers at 4 °C as follows: 0.1% (w/v) BSA solution in PB, 45 mM ATCh in DD-H<sub>2</sub>O, 20 mM DTNB in PB, 14 nM hAChE in 0.1% (w/v) BSA solution, and 1.4 nM hAChE in 0.1% (w/v) BSA solution. Working solutions were prepared using calibrated micropipettes and solvents matching the parent stock. To ensure sample integrity, all  $\beta$ -lactam inhibitors (**R24-R28**) were prepared from solid and used immediately after preparation.

Assays were conducted on a Molecular Devices SpectraMaxM2 micro-plate reader and on polystyrene 96-well plates (Costar, round bottom). Activity of hAChE was measured spectrophotometrically at 412 nm and 27 °C following the Ellman assay method (26). Time point readings were obtained at the minimum possible interval over a

10 min duration. Incubation was performed in duplicate for each inhibitor concentration. Initial rates ( $v_i$ , mA/min) were calculated by least-squares analysis of the time courses at less than 10% turnover of the initial substrate concentration. Non-linear regression analysis was performed using SigmaPlot 12.0 to obtain inhibition parameters. Initial rates were corrected for background (nonenzymic) hydrolysis..

#### *IC<sub>50</sub> Determination*

Each assay was performed under the following conditions: 270  $\mu$ L of 0.5 mM DTNB in 50 mM PB (pH 7.3), 10  $\mu$ L of inhibitors **R24-R28** in DD-H<sub>2</sub>O, 10  $\mu$ L of 4.5 mM ATCh, and 10  $\mu$ L of 1.4 nM hAChE prepared in 0.1% (w/v) BSA. Time dependent inhibition was measured following conditions described in the general methods section of Appendix C. IC<sub>50</sub> plots for inhibitors **R24-R28** can be found in Appendix C.

$K_i^{\text{app}}$  values were calculated by plotting  $v_i$  as a function of inhibitor concentration by fitting to equation Eq. 4.4:

$$v_i = \frac{v_o}{1 + \frac{10^{\log[I]}}{K_i^{\text{app}}}}$$

**Equation 4.4:** Equation for initial rates ( $v_i$ ) as a function of  $K_i^{\text{app}}$  (apparent inhibitor dissociation constant, M) and inhibitor concentration ( $[I]$ , M)

From the  $K_i^{\text{app}}$ , IC<sub>50</sub> values were calculated using equation Eq. 4.5:

$$IC_{50} = \frac{K_i^{\text{app}}}{1 + \frac{[A]}{K_m}}$$

**Equation 4.5:** Equation for IC<sub>50</sub> (maximal inhibitory concentration, M) as a function of  $K_i^{\text{app}}$  (M),  $[A]$  substrate concentration, and Michaelis constant for AChE hydrolysis of ATCh ( $K_m$ , M)

#### *Continuous Assay (Inhibition Rate Constant)*

Following initial determinations of time dependent inhibition, inhibitors **R24-R28** were evaluated for their inhibition rates in a continuous assay. Each well was prepared as follows: 255  $\mu\text{L}$  of 0.5 mM DTNB in 50 mM PB (pH 7.3), 10  $\mu\text{L}$  of inhibitors **R24-R28** in DD-H<sub>2</sub>O (in well concentration ranged from 40  $\mu\text{M}$ -1 mM), 35  $\mu\text{L}$  of 4.5 mM ATCh (0.53 mM in well concentration), and 5  $\mu\text{L}$  of 0.5 nM hAChE. Control reaction time courses were performed with a blank injection of DD-H<sub>2</sub>O instead of inhibitor and remained linear throughout the duration of each assay. All assays were performed in duplicate following the Ellman method as described in the general procedure. Time courses were followed for 3 hours and the observed pseudo-first order rate constants of inhibition,  $k_{\text{obs}}$  ( $\text{min}^{-1}$ ), were calculated by fitting data to a biphasic function, Eq.4.6.

$$A = A_o + \frac{v_o - v_{ss}}{k_{obs}} (1 - e^{-k_{obs}t}) + v_{ss}t$$

**Equation 4.6:** Equation for steady-state kinetic rate determination; A (absorbance),  $A_o$  (initial absorbance value),  $v_o$  (initial rate, A/s),  $v_{ss}$  (steady state rate, A/s),  $k_{\text{obs}}$  (observed first-order rate constant,  $\text{s}^{-1}$ ), t (time, s)

For inhibitor **R25** (5-CF<sub>3</sub>), pseudo first-order inhibition rate constants were also obtained by truncating the data and fitting to a first order kinetic Eq. 4.7.

$$A = A_{\infty} + (A_o - A_{\infty})e^{-k_{obs}t}$$

**Equation 4.7:** Equation for first-order rate constant determination; A (absorbance),  $A_o$  (initial absorbance value),  $A_{\infty}$  (absorbance at  $t_{\infty}$ ),  $k_{\text{obs}}$  (observed first-order rate constant,  $\text{s}^{-1}$ ), t (time, s)

For Inhibitor **R28**, data were fit to a linear function (Eq. 4.8).

$$A = vt + A_o$$

**Equation 4.8:** Linear time course plot for inhibited AChE reaction rate ( $v$ , A/s); t (time, s), and  $A_o$  (initial absorbance)

Figures 4.2 and 4.3 are representative plots of continuous assay data fits to equations 4.7 and 4.8.

Utilizing the steady state rate ( $v_{ss}$ , mA/min) values from biphasic kinetic functions for inhibitors **R24**, **R26**, and **R27** and the linear slope ( $v$ , Abs/min) from Eq. 4.8 for inhibitor **R28**, the resultant rate values for each inhibitor were fit to a Dixon plot (Eq. 4.9):

$$v = \frac{v_o}{1 + \frac{[I]^n}{K_i^n}}$$

**Equation 4.9:** Equation for Dixon plots of reaction rate ( $v$ , **R28**) and steady state rate ( $v_{ss}$ , **R24**, **R26**, **R27**) where  $v_o \equiv$  enzymatic reaction rate in the absence of inhibitor,  $[I] \equiv$  inhibitor concentration,  $K_i \equiv$  inhibitor dissociation constant, and  $n \equiv$  fixed exponent ( $n > 1$ ).

In the case of inhibitor **R28**, rate values obtained from Eq. 4.8 were fit initially to a floating exponent which was determined to be  $n = 1.14$ . A fixed exponent of  $n = 1.14$  was then utilized to determine  $K_i$ .

#### *Determination of Inhibition Mode*

The Michaelis-Menten Eq. 4.10 was used to fit the inhibitory profile of inhibitor **R24** (R=H):

$$v_i = \frac{V_{max}^{app} [A]}{[A] + K_m^{app}}$$

**Equation 4.10:** Michaelis-Menten equation for the inhibited *hAChE* catalyzed hydrolysis of ATCh where  $K_m^{app}$  is the observed Michaelis constant and  $V_{max}^{app}$  is the observed maximum reaction velocity.

Values for the maximum velocity ( $V_{max}$ ) and Michaelis constant ( $K_m$ ) were used to calculate the slopes for the double reciprocal plot, Eq. 4.11:

$$\frac{1}{v_i} = \frac{V_{max}^{app}}{K_m^{app}} \frac{1}{[A]} + \frac{1}{V_{max}^{app}}$$

**Equation 4.11:** Double-reciprocal Lineweaver-Burk equation

Lineweaver-Burk plots and three dimensional fits (Eq. 4.12) indicate competitive mode of inhibition for inhibitor **R24**.

In order to better assess the type of inhibition for inhibitor **R24**, the initial rates versus [S] and [I] were fit by non-linear regression analysis to Eq. 4.12 for competitive inhibition:

$$v_i = \frac{V_{max}[A]}{[A] + K_m \left(1 + \frac{[I]}{K_I}\right)}$$

**Equation 4.12:** Equation defining competitive inhibition where  $K_I$  is the inhibitor dissociation equilibrium constant

Computational modeling and docking data were provided by of Dr. Jason A. Morrill of William Jewell College-Department of Chemistry. Corresponding methods and supporting information are detailed in Appendix C.

### Results and Discussion

Evaluation of hydrolytic stability in phosphate buffer (50 mM, pH 7.3) for inhibitors **R24-28** was conducted to determine spontaneous hydrolysis rates and how it contributes to their inhibition kinetics profiles. UV absorbance spectra for inhibitors **R24-28** and their hydrolysis products were obtained and the difference in molar absorptivity ( $\Delta\epsilon$ ) was calculated. Table 4.1 lists the absorbance maxima for both reactants and hydrolysis products for each inhibitor. From the spectra,  $\Delta\epsilon$  values at optimal wavelengths were selected for monitoring the hydrolytic degradation of

inhibitors **R24-28** by UV spectroscopy. Hydrolysis rate constants ( $k_{\text{hyd}}$ ) were calculated from plots of the observed hydrolytic degradation for each  $\beta$ -lactam. Inhibitors **R24**, **R26** and **R27** were relatively hydrolytically stable, with spontaneous hydrolysis half-lives ranging from 8 h to 22 h. Plots for inhibitor **R25**'s hydrolytic degradation yielded a  $k_{\text{hyd}}$  value of  $5.41 \pm 0.02 \times 10^{-4} \text{ s}^{-1}$ , corresponding to a half-life of 21 min. No hydrolytic degradation was observed for inhibitor **R28**. This evaluation provides insight into the observed *hAChE* inhibition behavior.

The half maximal inhibitory concentration ( $\text{IC}_{50}$ ) for inhibitors **R24-28** was determined initially and after 2 h incubation to yield values 25 to 141  $\mu\text{M}$  (Table 4.2). Slight decrease in the  $\text{IC}_{50}$  values over 2 h incubation prompted further evaluation for time-dependent inhibition. Time-dependent inhibition was measured over 24 h where each inhibitor, except **R28**, showed time-dependence with an observed reduction in apparent  $\text{IC}_{50}$  of up to an order of magnitude (see Table 4.2 and Appendix C for details). Regioisomers **R26** and **R27** show a 3-fold difference in observed initial  $\text{IC}_{50}$  value. This difference in activity is paralleled with the observed  $k_{\text{hyd}}$  values for **R26** and **R27**. With inhibitor **R28**, we observe more potent inhibition upon initial exposure to *hAChE* ( $\text{IC}_{50} = 25 \pm 2 \mu\text{M}$  at 0 h incubation) but no time dependent inhibitory activity ( $\text{IC}_{50} = 20 \pm 6 \mu\text{M}$  after 24 h incubation). This is the only inhibitor where no time dependence is observed, for which presence of an electron donating group or sterics may attribute to this inhibitory behavior.

Rate constants for irreversible inhibition were determined by continuous assay for each inhibitor. Fig. 4.1 is a representative plot for continuous assay rate determination conducted for inhibitors **R24**, **R26-R27**. Observed pseudo-first order rate constants ( $k_{\text{obs}}$ )

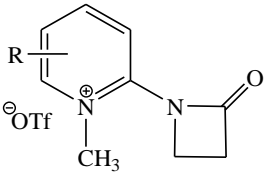


were calculated by non-linear fit of time courses for *hAChE* activity at varied concentrations of **R24-28**. Time courses for inhibitors **R24**, **R26** and **R27** showed an apparent fit to biphasic inhibition kinetics, and bimolecular rate constants ( $k_i/K_i$ ) were calculated from linear plots of  $k_{obs}$  as a function of inhibitor concentration (Table 4.3; see Figs. C13-C16 in Appendix C). Inhibitors **R25** and **R28** did not fit biphasic inhibition (see Figs. C11 and C12) and data was fit to equations 4.7 and 4.8.

First-order non-linear fits were performed on truncated time courses (see Fig. C11 for representative plot) for inhibitor **R25**, where a  $k_i/K_i$  of  $1.2 (\pm 0.1) \times 10^3 \text{ M}^{-1} \text{ min}^{-1}$  was obtained. Inhibitor **R28** time courses were fit linearly to give reaction rates ( $v$ , A/min) which were fit to Dixon plots yielding an inhibitor dissociation constant ( $K_i$ ) of  $2.3 (\pm 0.5) \times 10^{-5} \text{ M}$  (see Appendix C for corresponding plots). Fitting the steady state reaction rates ( $v_{ss}$ , A/min) obtained from biphasic fits of time courses for **R24**, **R26** and **R27** gave  $K_i$  values of  $1.3 (\pm 0.3) \times 10^{-4} \text{ M}$ ,  $1.7 (\pm 0.1) \times 10^{-4} \text{ M}$ , and  $2.1 (\pm 0.3) \times 10^{-4} \text{ M}$  respectively. Complete inhibition of *hAChE* was not observed, even at relatively high concentrations of **R24-28**. Fits to biphasic inhibition kinetics suggest that inhibition of *hAChE* by  $\beta$ -lactams **R24-28** is gradually reversed due to catalytic turnover.

Inhibitor **R24** was evaluated to determine the mode of reversible *hAChE* inhibition. Michaelis-Menten kinetic parameters were obtained at varied substrate (acetylthiocholine, ATCh) and inhibitor concentrations. Values for  $V_{max}$  and  $K_m$  were generated from non-linear plots and the values were used to generate Lineweaver-Burk plots, which support a competitive inhibition model (see Figs. 4.2 & 4.3). However, at higher concentrations of inhibitor (170-341  $\mu\text{M}$ ) there is a shift from competitive inhibition. This may be attributed to either binding of the inhibitor to both *hAChE*'s PAS

**Table 4.1:** Absorbance maxima for inhibitors **R24-R28**, corresponding hydrolysis products for each inhibitor,  $\Delta A$  values, and  $\lambda_{\Delta\epsilon}$  values favoring reactants.

						
entry	R =	$\lambda_{\text{max}}(\text{nm})$	$\lambda_{\text{max}}(\text{nm})$	$\Delta\epsilon (\Delta A/M \times 10^3)$	$k_{\text{hyd}} (\text{s}^{-1})$	Assay $\lambda$ (nm)
<b>R24</b>	H	296	311	5.8	$1.5 \times 10^{-5}$	297
<b>R26</b>	5-F	306	325	6.1	$2.0 \times 10^{-5}$	302
<b>R27</b>	3-F	298	294	4.0	$1.5 \times 10^{-5}$	302
<b>R25</b>	5-CF <sub>3</sub>	301	303	6.4	$5.4 \times 10^{-4}$	297
<b>R28</b>	4-N(Me) <sub>2</sub>	290	287	1.7	ND	297

**Table 4.2:** IC<sub>50</sub> values for inhibitors **R24-28** over 24 hour incubation period.

Inhibitors <b>R24-28</b>		IC <sub>50</sub> (μM)					
entry	R =	0hr	2hr	4hr	6hr	10hr	24hr
R24	H	43 ± 3	31 ± 6	15 ± 5	8 ± 3	-	-
R26	5-F	47 ± 8	30 ± 2	30 ± 9	16 ± 4	13 ± 6	-
R27	3-F	140 ± 30	50 ± 10	40 ± 10	50 ± 10	40 ± 11	24 ± 6
R25	5-CF <sub>3</sub>	33 ± 6	6 ± 2	7 ± 3	13 ± 4	15 ± 5	14 ± 4
R28	4-N(Me) <sub>2</sub>	25 ± 2	34 ± 3	30 ± 3	34 ± 3	21 ± 4	20 ± 6

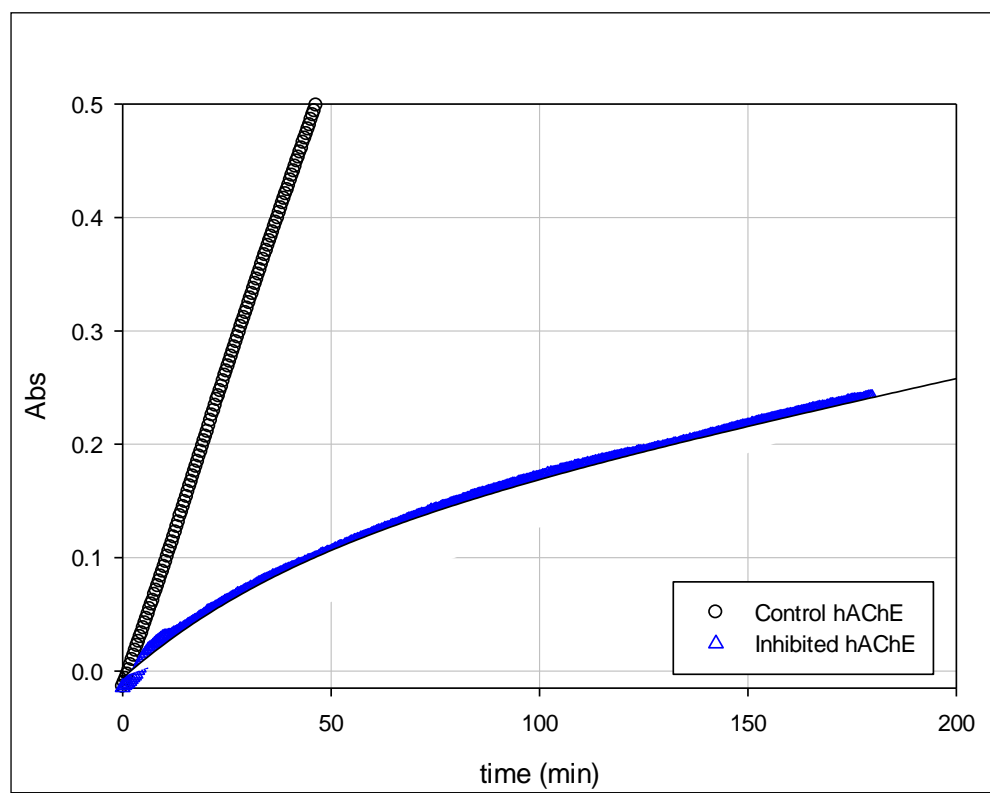


**Figure 4.1:** Full time course for  $\beta$ -lactam inhibitor **R24** (R=H, 400  $\mu$ M) fit to Eq. 4.6.

**Table 4.3.** Summary of Kinetic Data for  $\beta$ -lactam inhibitors **R24-28**

	<sup>a</sup> $\Delta\epsilon$ ( $\Delta A/M \times 10^3$ )	<sup>b</sup> $k_{\text{hyd}}$	<sup>c</sup> $t_{1/2}^{\text{hyd}}$	<sup>d</sup> $IC_{50}$	<sup>e</sup> $k_i/K_i$	<sup>f</sup> $K_i$
<b>R24</b>	5.8	$1.5 \times 10^{-5}$	13	$43 \pm 3$	$7 (\pm 1) \times 10^1$	$1.3 (\pm 0.3) \times 10^{-4}$
<b>R26</b>	6.1	$2.0 \times 10^{-5}$	9	$47 \pm 8$	$2.9(\pm 0.3) \times 10^1$	$1.7 (\pm 0.1) \times 10^{-4}$
<b>R27</b>	4.0	$1.5 \times 10^{-5}$	13	$140 \pm 30$	$2.9(\pm 0.2) \times 10^1$	$2.1 (\pm 0.3) \times 10^{-4}$
<b>R25</b>	6.4	$5.4 \times 10^{-4}$	0.4	$33 \pm 6$	$1.2 (\pm 0.1) \times 10^3$	ND
<b>R28</b>	1.7	ND	ND	$25 \pm 2$	ND	$2.3 (\pm 0.5) \times 10^{-5}$

<sup>a</sup>Molar absorptivity constant ( $\Delta\epsilon$ ,  $\Delta A/M$ ), <sup>b</sup>hydrolysis rate constant ( $k_{\text{hyd}}$ ,  $s^{-1}$ ), <sup>c</sup>half-life for spontaneous hydrolysis ( $t_{1/2}^{\text{hyd}}$ , h), <sup>d</sup> $IC_{50}$  ( $\mu M$ ) from dose-response assay, <sup>e</sup>bimolecular rate constant ( $k_i/K_i$ ,  $M^{-1} \text{min}^{-1}$ ), and <sup>f</sup>inhibitor dissociation constant ( $K_i$ , M)

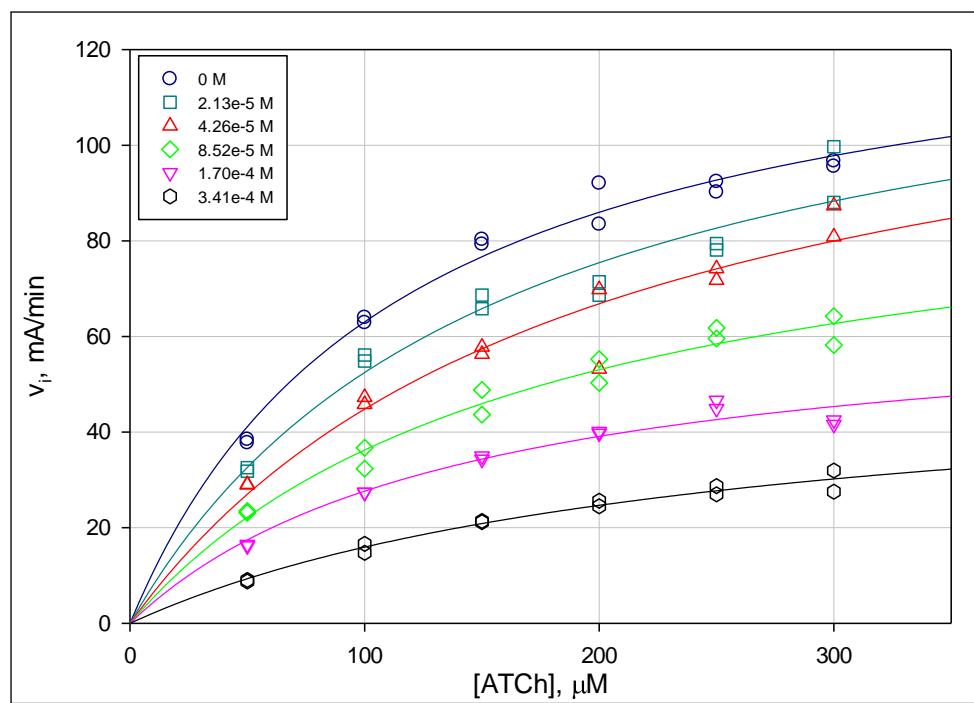


**Figure 4.2:** Michaelis-Menten Plot for inhibitor **R24** (0-341  $\mu M$ ) fit to Eq. 4.10

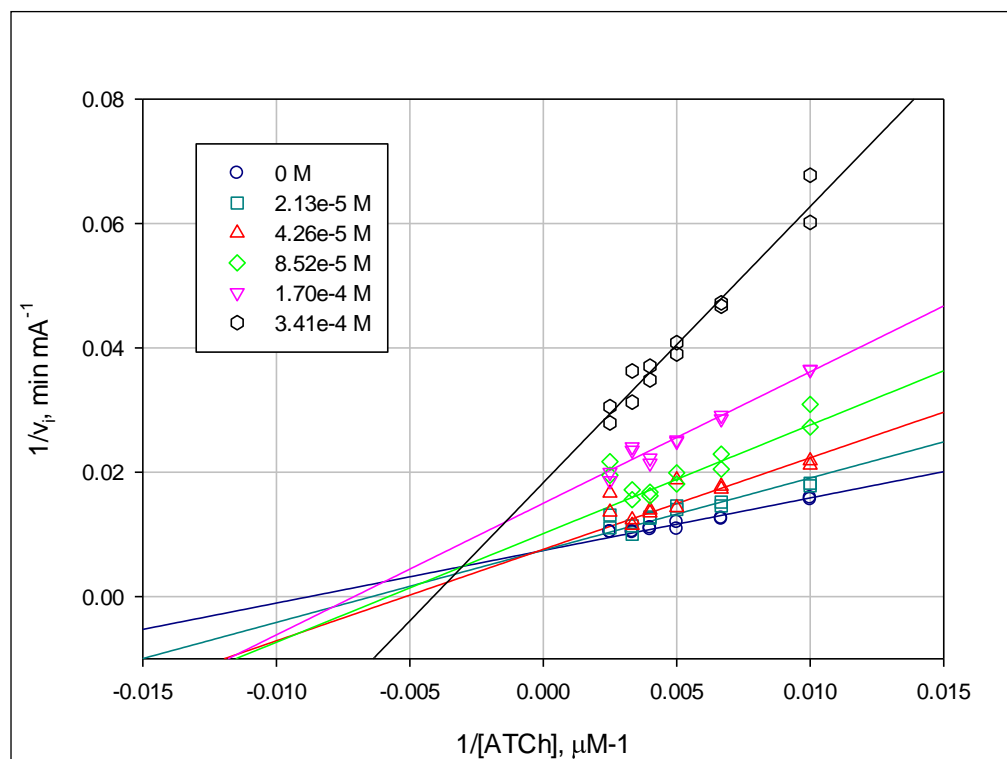


**Figure 4.3:** Double reciprocal plot of the inverse initial rate ( $v_i^{-1}$ ,  $\text{min mA}^{-1}$ ) versus the inverse ATCh concentration ( $\mu\text{M}^{-1}$ ). Slopes were calculated from  $V_{\text{max}}$  and  $K_m$  values generated from data fit to equation 4.10.

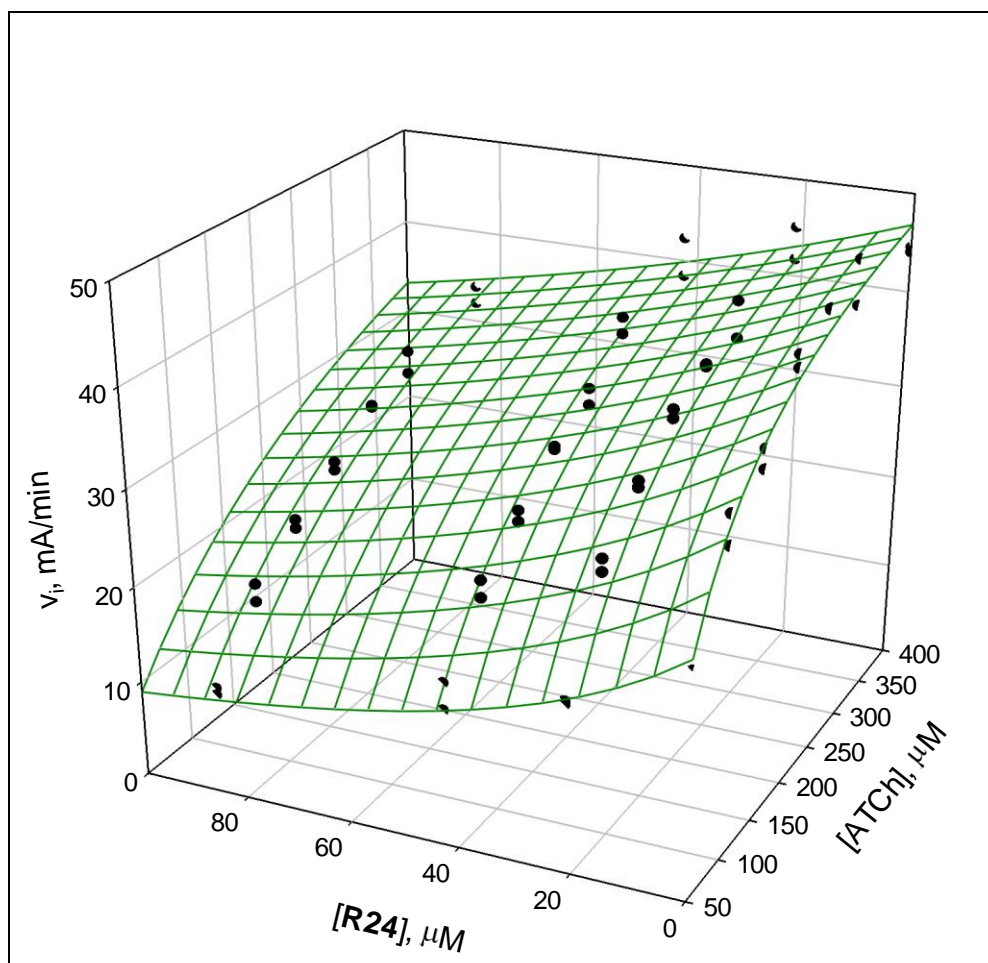


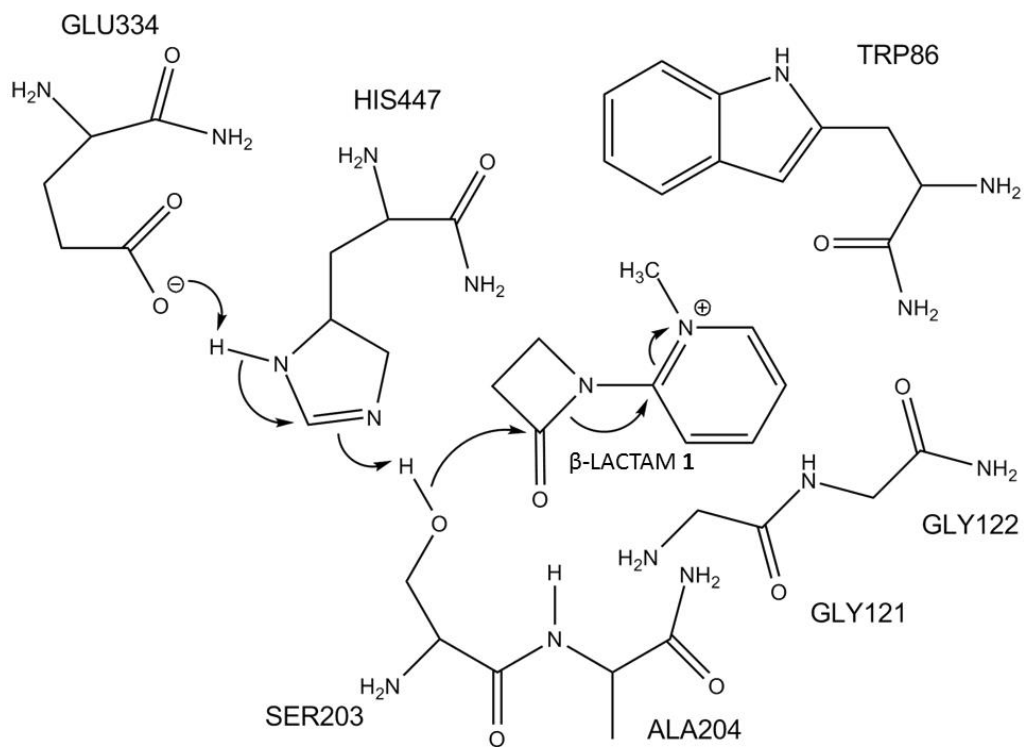
**Figure 4.4:** Three-dimensional plot of initial rate ( $v_i$ , mA/min), versus ATCh concentration (50-300  $\mu M$ ), and inhibitor **R24** concentration (0-85  $\mu M$ ) fit to Eq. 4.12



**Table 4.4:** Computed Enthalpies (kcal/mol) of Formation, Activation, and Reaction for Modeled Acylation Reactions (Calculated by Dr. Jason A. Morrill, William Jewell College-Department of Chemistry)

Entry	Reactant Complex ( $H_f$ )	TS ( $H_f$ )	Product Complex ( $H_f$ )	$H_{act}$	$H_{rxn}$
<b>R24</b>	-310.26	-302.76	-353.55	7.5	-43.29
<b>R26</b>	-352.16	-339.62	-394.89	12.54	-42.73
<b>R27</b>	-355.71	-329.04	-399.93	26.67	-44.22
<b>R25</b>	-463.89	-450.29	-510.15	13.6	-46.26
<b>R28</b>	-335.41	-298.39	-351.48	37.02	-16.07

*$H_f$  ≡ enthalpy of formation; TS ≡ transition state;  $H_{act}$  ≡ enthalpy of activation ;  $H_{rxn}$  ≡ enthalpy of reaction*



**Scheme 4.2:** Mechanism corresponding to the reactions that were modeled computationally ( $\beta$ -Lactam 1  $\equiv$  **R24**)

and active site such that mixed inhibition prevails, or inhibition occurs immediately upon mixing such that there is a significant effect on the measured initial rate values. If the latter is true, this is a limitation in the experimental procedure. Data was subsequently fit to a competitive inhibition equation at concentrations (0-85  $\mu\text{M}$  **R24**) and gave a  $K_i$  of  $32 \pm 2 \mu\text{M}$ . Inhibitor **R24** was further evaluated to understand the extent of observed recovery of inhibited *hAChE* activity. Fit to biphasic kinetics implies that the  $\beta$ -lactam inhibitor is catalyzed to its hydrolysis product and released from the *hAChE* active site. A slight recovery of inhibited *hAChE* activity was observed after 17 h incubation following initial exposure to inhibitor **R24** (See Fig. C17 in Appendix C). This supports biphasic kinetics observed in the data plots for the continuous assay of inhibitor **R24**.

The following computer modeling experiments were conducted in the laboratory of Dr. Jason Morrill of William Jewell College. To further investigate the likely mode of binding for  $\beta$ -lactams **R24-28** in the active site of *hAChE* (PDB code: 4EY4) (76), docking simulations were carried out using Autodock Vina (77). The lowest energy binding mode for nearly all ligands is aligned with the carbonyl group of the lactam in close proximity of the  $\gamma$ -oxygen of Ser203 (see Table C3). For  $\beta$ -lactam inhibitor **R25**, the lowest energy binding mode has the carbonyl of the  $\beta$ -lactam moiety aligned away from the  $\gamma$ -oxygen of Ser203, while the  $\text{CF}_3$  group is positioned in close proximity to Ser203. To investigate the extent to which *hAChE* inhibition is a function of the intrinsic reactivity of the ligands we also modeled their acylation of Ser203 using the SAM1 semiempirical quantum mechanical method as implemented in the program, AMPAC. All critical points along the modeled reaction pathways were characterized by means of normal mode analysis. The reactions were modeled beginning with the lowest energy

binding mode geometry and correspond to simultaneous nucleophilic acyl substitution of Ser203 at the lactam carbonyl group, with double proton transfer from Ser203 to His447 and from His447 to Glu334 (see Table 4.4, and Scheme 4.2). All modeled reactions included ring-opening of the  $\beta$ -lactam ring, as well.

### Conclusion

We have described the inhibitory activity of *N*-methylpyridinium  $\beta$ -lactam inhibitors **R24-28** for *hAChE* along with their hydrolytic stability, computational docking, and reaction modeling. All inhibitors showed  $\mu\text{M}$  range affinity for *hAChE* inhibition and **R24** gave evidence for a competitive mode of inhibition. Functionalization of the pyridine ring proved to have a contribution to both inhibitor potency and spontaneous hydrolysis rate, with the strong electron withdrawing  $\text{CF}_3$  group showing the highest reactivity. Continuous assays of inhibitors **R24-R27** showed biphasic (**R24, R26-27**) or triphasic (**R25**) inhibitory behavior. This suggested the  $\beta$ -lactam pyridiniums behave as suicide inhibitors in which *hAChE* activity is only partially recovered. Computational docking studies strongly favored this correlation and reaction modeling further supports acylation of *hAChE*'s Ser203 as the likely inhibitory mechanism.

CHAPTER 5: KINETIC EVALUATION OF 6-FLUORO-2-METHOXY N-METHYL  
PYRIDINIUM INHIBITOR OF HUMAN ACETYLCHOLINESTERASE

Chemical Mechanism and Significance

Acetylcholinesterase (acetylcholine acetylhydrolase, EC 3.1.1.7; abbreviated herein AChE) functions to terminate impulse transmission of the neurotransmitter ACh efficiently via a two-step catalytic mechanism, Fig. 5.1 (1). Release of ACh across cholinergic synapses triggers an action potential for a voluminous number of cognitive and motor sensory activities. AChE is highly susceptible to inhibition at the Ser residue of its catalytic triad (3). Inhibitors of AChE are of interest in the treatment of various neurological disorders including Alzheimer's Disease (34). Organophosphate (OP) nerve agents, described in detail in Chapters 1-3, can cause large scale shutdown of AChE activity with acute exposure (41, 42).

The catalytic triad for AChE lies at the bottom of a 20 Å deep gorge and is comprised of glutamate, histidine, and serine residues that induce general acid/base catalyzed hydrolysis of ACh (Fig. 5.1). Acylation of the active-site serine residue completes the first mechanistic step, generating an acylenzyme, which is then hydrolyzed by a conserved water molecule leading to substrate turnover and deacylation to restore the enzyme to its unbound state (4, 8). A peripheral anionic site (PAS) lying 14 Å from the enzyme's active-site acts as an allosteric regulator to ACh hydrolysis. The PAS is comprised of two tyrosines, a tryptophan, and aspartate residues, and interacts with the quaternary ammonium moiety of ACh (11). Additionally, the PAS is a primary binding site for non-competitive AChE inhibitors (12).

In Chapter 3 and Appendix B, we introduce several time-dependent inhibitors of *hAChE*, from our class of novel resurrecting agents. This included the  $\beta$ -lactam family of inhibitors (**R24-R28**), which showed competitive inhibitory activity towards *hAChE*. An additional time-dependent inhibitor was profiled from the 2-methoxypyridinium family of resurrecting agents, 6-fluoro-2-methoxy N-methylpyridinium (**R10**). Inhibitor **R10** (Fig. 5.2), is unique in that we are proposing it inhibits the enzyme by nucleophilic aromatic substitution ( $S_NAr$ ).

Observations from initial dose response data (Appendix B, Figure B10) showed the  $IC_{50}$  increased in potency by an order of magnitude after a two hour incubation period. Placement in the “resurrection” assay, described in Chapter 3, revealed significant reduction of *hAChE* activity after 24 hour incubation in the control enzyme system. Nucleophilic aromatic substitution ( $S_NAr$ ) presents itself as a plausible means to inhibit the AChE enzyme. The F substituent provides a favorable leaving group for such a reaction mechanism to occur. However, an in-depth look into the inhibition kinetics is necessary to resolve questions regarding this proposed inhibitory profile.

#### Objective of Study

Profile the kinetic inhibitory behavior for 6-fluoro-2-methoxy N-methyl pyridinium’s inhibition of human acetylcholinesterase as an irreversible, time-dependent inhibitor.

#### Materials and Methods

##### *Synthesis of R10*

Inhibitor **R10** was synthesized by Dr. Joseph J. Topczewski, post-doctoral fellow in the Quinn research group, as depicted in the following reaction scheme (Scheme 5.1).

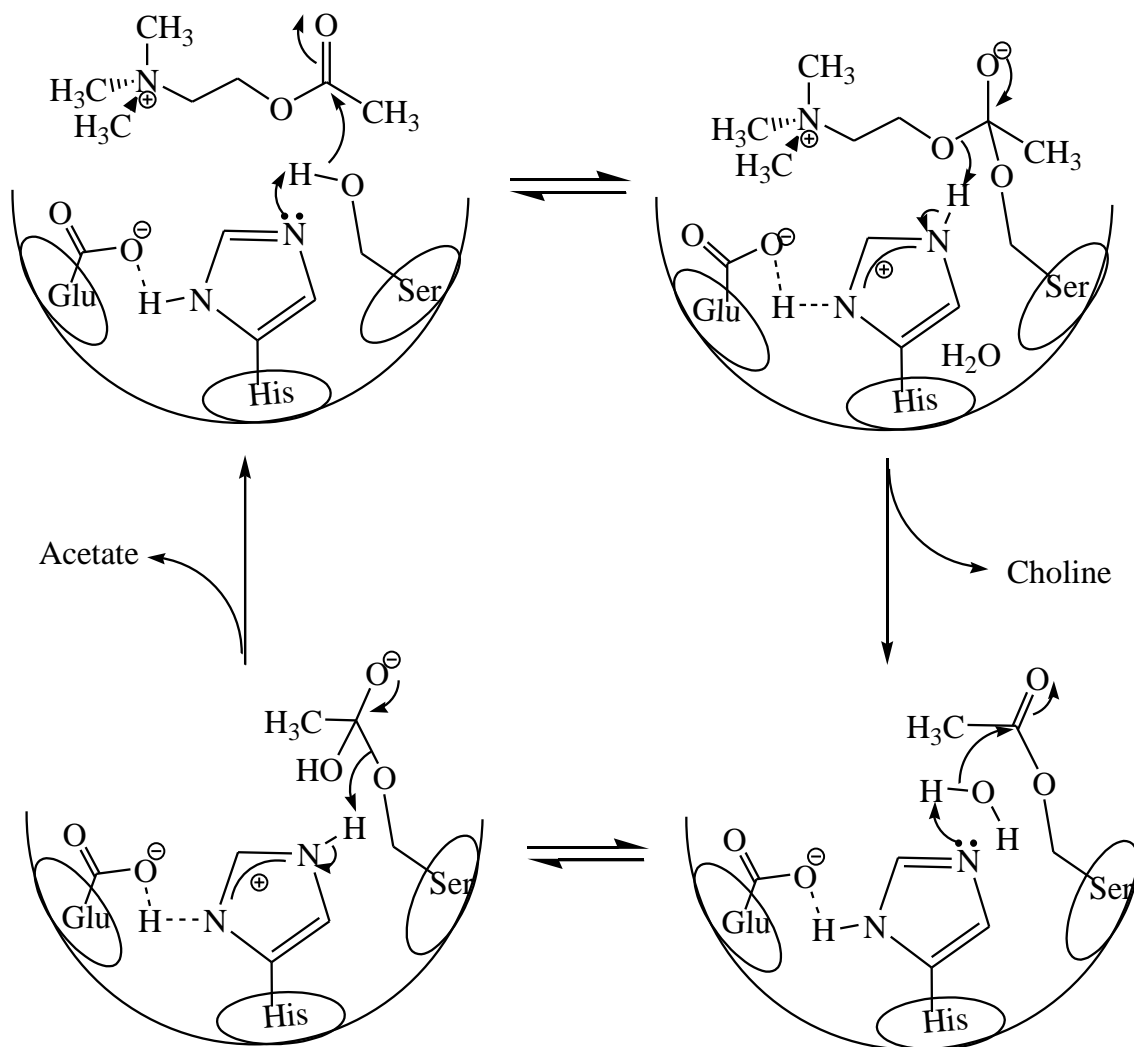
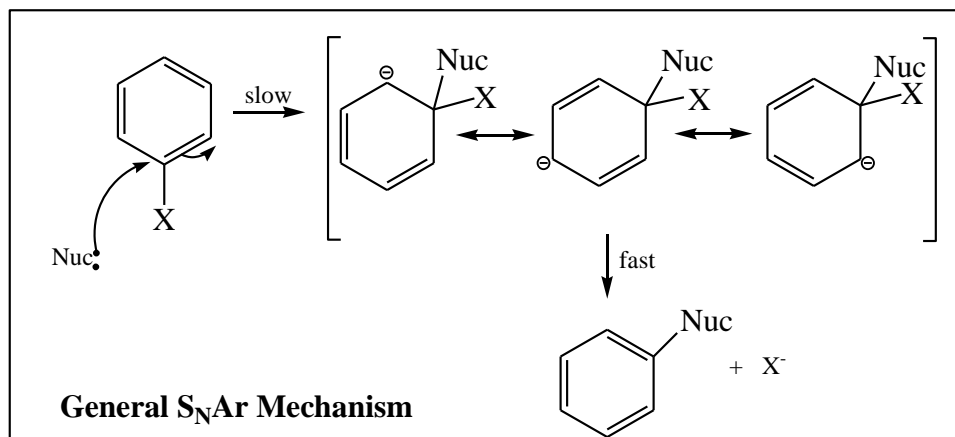


**Figure 5.1:** AChE catalytic mechanism of action.

**Source:** Delfino, R.T.; Ribeiro, T.S.; Figueroa-Villar, J.D. *J. Braz. Chem. Soc.*, **2009**, 20, 407-429



**Proposed S<sub>N</sub>Ar Inhibition Mechanism(R10)**

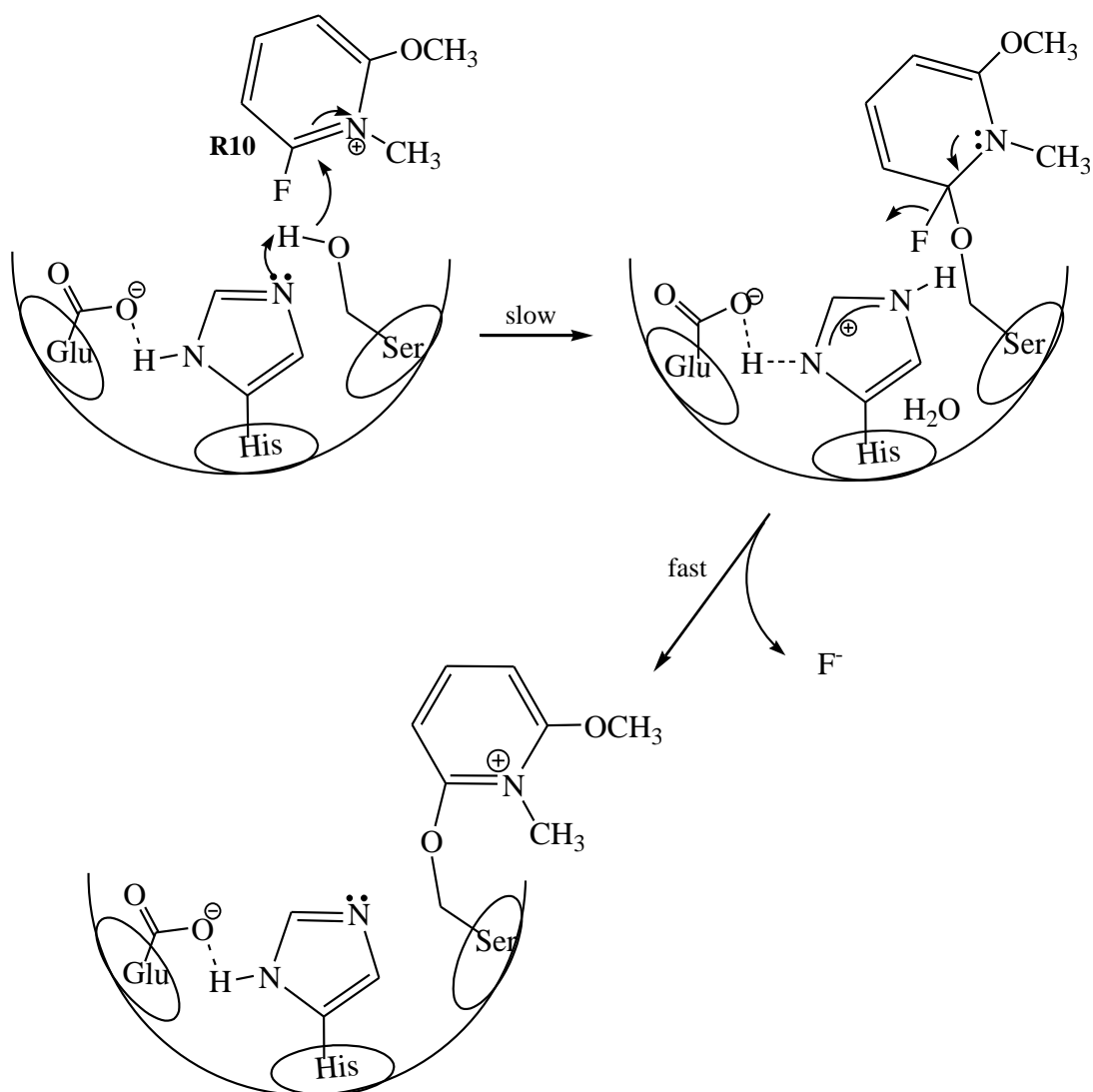
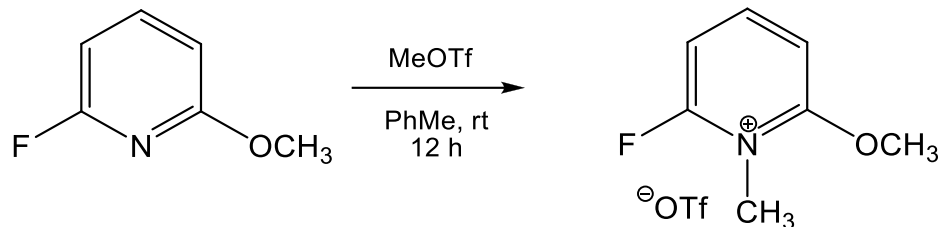


**Figure 5.2:** General mechanism for S<sub>N</sub>Ar and proposed AChE inhibition mechanism by S<sub>N</sub>Ar





**Scheme 5.1:** Synthesis of Inhibitors **R10**

Scheme 5.1 describes the synthesis of **R10**, 6-fluoro-2-methoxy-N-methylpyridinium triflate. The synthetic preparation by Dr. Topczewski is described as follows: A 3 mL glass vial was equipped with a rubber septum and magnetic stir bar. The vial was brought into a glove box and charged with methyl trifluoromethylsulfonate (MeOTf, 98  $\mu$ L, 0.89 mmol) by micropipette with polypropylene tip. The vial was sealed and removed from the glove box. A separate 3 mL vial was charged with substrate (113 mg, 0.89 mmol) and was dissolved in PhMe (0.3 mL). The solution of pyridine was added via syringe into the sealed vial of MeOTf at rt. The vial which contained the pyridine was rinsed with PhMe (0.1 mL) and the rinse solution was injected into the reaction vial. The reaction vial was kept at room temperature and stirring was maintained at ca. 400-600 rpm. Over 18 h, a precipitate gradually formed. At the end of the reaction, PhMe (2 mL) was added after which stirring was stopped. Any solid or oil was allowed to settle and the solvent was removed by glass pipette. The solid was rinsed with several portions of hexanes, again removing the solvent by pipette. Residual solvent was then removed *in vacuo* to provide the title compound (249 mg, 96%).  **$^1\text{H NMR}$  (acetone- $d_6$ , 500 MHz):**  $\delta$  = 8.68 (dd,  $J$  = 8.6 Hz, 1H), 7.70 (d,  $J$  = 9.0 Hz, 1H), 7.53 (dd,  $J$  = 8.5, 4.3

Hz, 1H), 4.45 (s, 3H), 4.08 (s, 3H). **<sup>19</sup>F NMR (acetone-d<sub>6</sub>, 470 MHz):**  $\delta$  = -78.9 (3F), -83.7 (1F). **<sup>13</sup>C NMR (acetone-d<sub>6</sub>, 125 MHz):**  $\delta$  = 161.2 (d,  $J_{C-F}$  = 3.5 Hz), 158.2 (d,  $J_{C-F}$  = 274 Hz), 151.4 (d,  $J_{C-F}$  = 12.4 Hz), 121.4 (q,  $J_{C-F}$  = 322 Hz), 107.7 (d,  $J_{C-F}$  = 3.9 Hz), 104.3 (d,  $J_{C-F}$  = 21.2 Hz), 61.0, 33.7 (d,  $J_{C-F}$  = 7.9 Hz). **IR (film, cm<sup>-1</sup>):**  $\nu$  = 1691, 1657, 1586, 1518, 1281, 1031. **HRMS (TOF ES+):** calc. for C<sub>7</sub>H<sub>9</sub>ONF (M-OTf)<sup>+</sup>: 142.0668; found: 142.0659. **Anal. Calcd.** for C<sub>8</sub>H<sub>9</sub>F<sub>4</sub>NO<sub>4</sub>S: C, 32.99; H, 3.11 Found: C, 32.94; H, 3.03 Found: C, 32.88; H, 3.12.

### *Enzyme Assay Procedures and Kinetic Analysis*

Phosphate buffer (PB) at 50 mM concentration was prepared in bulk at pH ranging from 7.2-7.3. The pH was determined by an ion selective pH electrode that was calibrated prior to each measurement. All stock solutions were prepared from solid material and stored in polypropylene containers at 4 °C as follows: 0.1% (w/v) BSA solution in PB, 45 mM ATCh in DD-H<sub>2</sub>O, 20 mM DTNB in PB, 14 nM hAChE in 0.1% (w/v) BSA solution, and 1.4 nM hAChE in 0.1% (w/v) BSA solution. Working solutions were prepared using calibrated micropipettes and solvents matching the parent stock. To ensure sample integrity, inhibitor solutions for **R10** were prepared from solid and used immediately after preparation.

Assays were conducted on a Molecular Devices SpectraMaxM2 micro-plate reader and on polystyrene 96-well plates (Costar, round bottom). Activity of hAChE was measured spectrophotometrically at 412 nm and 27 °C following the Ellman assay method (26). Time point readings were obtained at the minimum possible interval over a 10 min duration. Incubation was performed in duplicate for each inhibitor concentration. Initial rates ( $v_i$ , mA/min) were calculated by least-squares analysis of the time courses at

less than 10% turnover of the initial substrate concentration. Non-linear regression analysis was performed using SigmaPlot 12.0 to obtain kinetic inhibition parameters. Initial rates were corrected for background (nonenzymic) hydrolysis of ATCh.

Each assay was performed under the following conditions: 270  $\mu\text{L}$  of 0.5 mM DTNB in 50 mM PB (pH 7.3), 10  $\mu\text{L}$  of inhibitor **R10** in DD- $\text{H}_2\text{O}$ , 10  $\mu\text{L}$  of 4.5 mM ATCh, and 10  $\mu\text{L}$  of 1.4 nM *hAChE* prepared in 0.1% (w/v) BSA.

$\text{IC}_{50}$  plots for inhibitors **R10**.

$K_i^{\text{app}}$  values were calculated by plotting  $v_i$  as a function of inhibitor concentration by fitting to equation Eq. 5.1:

$$v_i = \frac{v_o}{1 + \frac{10^{\log[I]}}{K_i^{\text{app}}}}$$

**Equation 5.1:** Equation for initial rates ( $v_i$ ) as a function of  $K_i^{\text{app}}$  (apparent inhibitor dissociation constant, M) and inhibitor concentration ( $[I]$ , M)

From the  $K_i^{\text{app}}$ ,  $\text{IC}_{50}$  values were calculated using equation Eq. 5.2:

$$\text{IC}_{50} = \frac{K_i^{\text{app}}}{1 + \frac{[A]}{K_m}}$$

**Equation 5.2:** Equation for  $\text{IC}_{50}$  (50% inhibitory concentration, M) as a function of  $K_i^{\text{app}}$  (M),  $[A]$  substrate concentration, and Michaelis constant for AChE hydrolysis of ATCh ( $K_m$ , M)

First order rates for the inhibition of *hAChE* with the inhibitor **R10** were evaluated under the following conditions: Each well was loaded with 270  $\mu\text{L}$  of 50 mM PB containing 0.5 mM DTNB and 10  $\mu\text{L}$  1.4 nM *hAChE*. To the experimental wells, 10  $\mu\text{L}$  of inhibitor **R10** in DD- $\text{H}_2\text{O}$  was added (in well conc. 30-600  $\mu\text{M}$ ). To the control

wells, 10  $\mu\text{L}$  of DD- $\text{H}_2\text{O}$  was added. At the time points reported, 10  $\mu\text{L}$  of 4.5 mM ATCh was added to each well and *hAChE* activity was monitored at 412 nm to obtain initial rates ( $v_i$ , mA/min). The pseudo-first order rate constant ( $k_{\text{obs}}$ ) was obtained by finding the percent control activity at each time point as described by Eq. 5.3-5.5:

$$\%hAChE_{\text{activity}} = \frac{v_i hAChE_{\text{inhibited}}}{v_i hAChE_{\text{control}}} \times 100$$

**Equation 5.3:** Equation for the activity of **R10** inhibited *hAChE* ( $\%hAChE_{\text{inhibited}}$ ) which is defined by the ratio of the initial ATCh hydrolysis rate of **R10** inhibited *hAChE* ( $v_i hAChE_{\text{inhibited}}$ , mA/min) and uninhibited *hAChE* ( $v_i hAChE_{\text{control}}$ , mA/min)

$$\%hAChE_{\text{activity}} = \%hAChE_{\text{activity}}^0 e^{-k_{\text{obs}}t}$$

**Equation 5.4:** Pseudo first-order kinetic rate equation for OP inhibition of *hAChE*;  $k_{\text{obs}} \equiv$  observed pseudo first-order rate constant;  $t \equiv$  time;  $\%hAChE_{\text{activity}} \equiv$  observed activity for inhibited *hAChE*;  $\%hAChE_{\text{activity}}^0 \equiv hAChE$  activity at  $t = 0$

$$\%hAChE_{\text{activity}} = \%hAChE_{\text{activity}}^{\infty} + (\%hAChE_{\text{activity}}^0 - \%hAChE_{\text{activity}}^{\infty})e^{-k_{\text{obs}}t}$$

**Equation 5.5:** Pseudo first-order kinetic rate equation for OP inhibition of *hAChE*;  $k_{\text{obs}} \equiv$  observed pseudo first-order rate constant;  $t \equiv$  time;  $\%hAChE_{\text{activity}} \equiv$  observed activity for inhibited *hAChE*;  $\%hAChE_{\text{activity}}^0 \equiv hAChE$  activity at  $t = 0$ ; and  $\%hAChE_{\text{activity}}^{\infty} \equiv hAChE$  activity at  $t = \infty$

Inhibition studies were performed and Lineweaver-Burk plots generated in order to determine the mode of *hAChE* inhibition. Each assay was conducted at a fixed concentration of *hAChE* (48 pM in assay concentration) and at varied concentrations of both substrates (ATCh: 50-400  $\mu\text{M}$ ) and inhibitor **R10** (0-108  $\mu\text{M}$ ). Analysis was performed in duplicate following the Ellman method as described in the general procedure. Michaelis-Menten plots were generated and fit via non-linear regression analysis from  $v_i$  using Eq. 5.6.

$$v_i = \frac{V_{max}^{app} [A]}{[A] + K_m^{app}}$$

**Equation 5.6:** Michaelis-Menten equation for the inhibited *hAChE* catalyzed hydrolysis of ATCh where  $K_m^{app}$  is the observed Michaelis constant and  $V_{max}^{app}$  is the observed maximum reaction velocity.

Values for the maximum velocity ( $V_{max}$ ) and Michaelis constant ( $K_m$ ) were used to calculate the slopes for the double reciprocal plot, Eq. 5.7:

$$\frac{1}{v_i} = \frac{V_{max}^{app}}{K_m^{app}} \frac{1}{[A]} + \frac{1}{V_{max}^{app}}$$

**Equation 5.7:** Double-reciprocal Lineweaver-Burk equation

In order to better assess the type of inhibition for inhibitor **R10**, initial rates were fit by three dimensional non-linear regression analysis to Eq. 5.8 for non-competitive inhibition:

$$v_i = \frac{V_{max}[A]}{([A] + K_m) \times (1 + \frac{[I]}{K_I})}$$

**Equation 5.8:** Equation defining noncompetitive inhibition where  $K_I$  is the inhibitor dissociation equilibrium constant

Inhibitor **R10** was assayed to determine the extent of inhibited *hAChE* activity that is recovered spontaneously. This experiment was conducted by preparing a solution containing 167  $\mu$ L of 14 nM *hAChE* in 0.1% BSA buffer with 7  $\mu$ L of 35 mM inhibitor **R10** and 326  $\mu$ L of 0.1% (w/v) BSA buffer. A control solution was prepared with a 7  $\mu$ L blank of DD-H<sub>2</sub>O. After 2 h of incubation at 27 °C, excess inhibitor was separated from enzyme using a Sephadex G-50 Quick Spin Column (Roche). Prior to separation, the

column was standardized with 0.1% (w/v) BSA in 50 mM PB (pH 7.3) and packed by centrifugation at 1100 x *g* for 4 minutes. The 500  $\mu$ L aliquot of inactivated *hAChE* was loaded on the packed Sephadex G-50 column bed and centrifuged at 600 x *g* for 6 minutes. Separated enzyme was collected and 3  $\mu$ L aliquots were assayed at various time points. A parallel assay was performed in which the aliquots were assayed following 30 minute incubation with 100  $\mu$ M 2-PAM at 27 °C. Assay wells were prepared as follows: 10  $\mu$ L of inhibited /control 1.4 nM *hAChE*, 10  $\mu$ L of 20 mM DTNB, 10  $\mu$ L of 4.5 mM ATCh, and 270  $\mu$ L of 50 mM PB (pH 7.3). Initial rates ( $v_i$ , mA/min) were calculated by least-squares analysis of the time courses at less than 10% turnover of the initial substrate concentration. Initial rates were corrected for background (nonenzymic) hydrolysis of ATCh and performed in duplicate. The overall percent activity was determined by equation 5.9:

$$\%hAChE \text{ Activity} = \left( \frac{v_{i,inhibited}}{v_{i,control}} \right) \times 100$$

**Equation 5.9:** Ratio of the initial rates ( $v_i$ , mA/min) for the inhibited and control *hAChE* reactions with inhibitor **R10**

### Results and Discussion

The half maximal inhibitory concentration ( $IC_{50}$ ) for inhibitor **R10** was evaluated over a 7.5 h time period to determine time dependent inhibition (Table 5.1). Time-dependent inhibition was observed with a reduction in apparent  $IC_{50}$  value that increases its potency 2-fold with an initial  $IC_{50}$  of 63  $\mu$ M and an  $IC_{50}$  of 28  $\mu$ M after 7.5 h (Table 5.1, Fig. 5.3). Following this initial profile of the inhibitory activity of **R10**, stop-time assays were performed in order to gauge whether irreversible inhibition takes place. Inhibitor **R10** was assayed at 4 different concentrations (30-250  $\mu$ M), for which

**Table 5.1:** IC<sub>50</sub> values for inhibitors **R10** over 7.5 hour incubation period.

	<b>IC<sub>50</sub> (μM)</b>									
<b>time</b>	<b>0 h</b>	<b>0.5 h</b>	<b>1 h</b>	<b>1.5 h</b>	<b>2 h</b>	<b>2.5 h</b>	<b>4.5 h</b>	<b>5.5 h</b>	<b>6.5 h</b>	<b>7.5 h</b>
<b>R10</b>	63 ± 5	36 ± 3	31 ± 3	32 ± 5	26 ± 3	24 ± 3	28 ± 3	24 ± 3	28 ± 4	27 ± 4

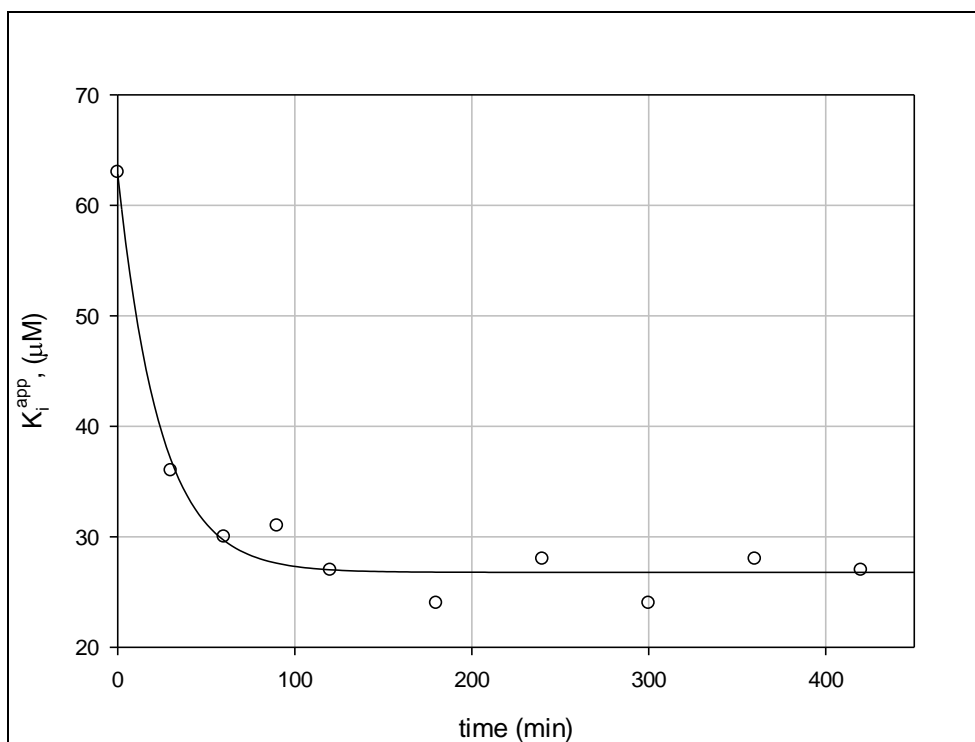


**Figure 5.3:** Plot of  $K_i^{\text{app}}$  ( $\mu\text{M}$ ) as a function of time (min) fit to  $K_i^{\text{app}} = K_{i,\infty}^{\text{app}} + (K_{i,0}^{\text{app}} - K_{i,\infty}^{\text{app}})e^{-kt}$  where  $K_{i,0}^{\text{app}} \equiv$  the observed inhibitor dissociation constant at  $t = 0$ ,  $K_{i,\infty}^{\text{app}} \equiv$  the observed inhibitor dissociation constant at  $t = \infty$ ,  $k \equiv$  the inhibition rate constant, and  $t \equiv$  time (min)



inhibited. This is attributed to the observed spontaneous hydrolysis of **R10** in 50 mM phosphate buffer ( $k_{\text{hyd}}^{\text{aPP}} = 2.51 (\pm 0.04) \times 10^{-4} \text{ min}^{-1}$ ;  $t_{1/2} = 46 \text{ min}$ ). A  $k_{\text{obs}}$  rate constant was obtained at each concentration and plotted as a function of **R10** concentration from which a bimolecular rate constant,  $k_i/K_I$ , of  $1.5 (\pm 0.1) \times 10^2 \text{ M}^{-1} \text{ min}^{-1}$  for inhibition of *hAChE* was determined (Fig. 5.5). This suggests that the irreversible inhibition behavior observed for **R10** is concentration dependent and can be defined by Eq. 5.10.

$$k_{\text{obs}} = \frac{k_i[\text{I}]}{K_I + [\text{I}]}; k_{\text{obs}} = \frac{k_i}{K_I} [\text{I}] \text{ at } [\text{I}] \ll K_I$$

**Equation 5.10:** Equation defining the observed pseudo first-order rate constant,  $k_{\text{obs}}$ ; where  $[\text{I}] \equiv$  inhibitor concentration (**R10**);  $k_i \equiv$  first-order inhibition rate constant;  $K_I \equiv$  inhibitor dissociation constant;

Stop-time assays support the notion that **R10** inhibition of *hAChE* is irreversible.

In order to resolve whether **R10** may inhibit by  $S_NAr$ , the first step in the mechanistic process should be slow and rate-limiting. To do this inhibitor **R10** was evaluated to determine its general mode of *hAChE* inhibition. Michaelis-Menten kinetic parameters were obtained at varied substrate (acetylthiocholine, ATCh) and inhibitor concentrations. Values for  $V_{\text{max}}$  and  $K_m$  were generated from non-linear plots to Eq. 5.6 and the values were used to generate Lineweaver-Burk plots (Eq. 5.7), which suggested initial inhibition character is a non-competitive (see Figs. 5.6 & 5.7). At the highest concentration of inhibitor **R10**, there is an observed deviation from non-competitive inhibition behavior. This behavior may be attributed to mixed inhibition at the 108  $\mu\text{M}$  concentration of **R10**, where inhibitor binds at both the *hAChE* PAS and active site. However, the observed deviation in inhibitory behavior is most likely attributed to limitations in measuring initial rate. This limitation arises because inhibition occurs

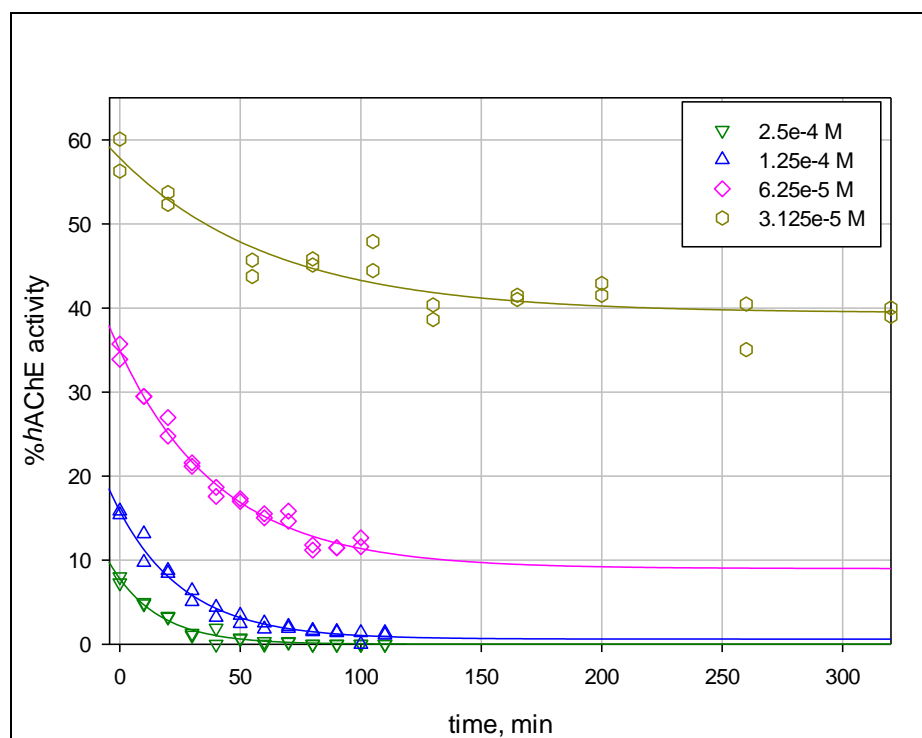


**Figure 5.4:** Plot of pseudo first-order rate of inhibition for **R10** (30-600  $\mu\text{M}$ ) as defined by equations 5.4 ( $[\text{I}] = 1.25\text{e-}4 \text{ M}$  to  $2.5\text{e-}4 \text{ M}$ ) and 5.5 ( $[\text{I}] = 3.125\text{e-}5 \text{ M}$  to  $6.25\text{e-}5 \text{ M}$ ) respectively

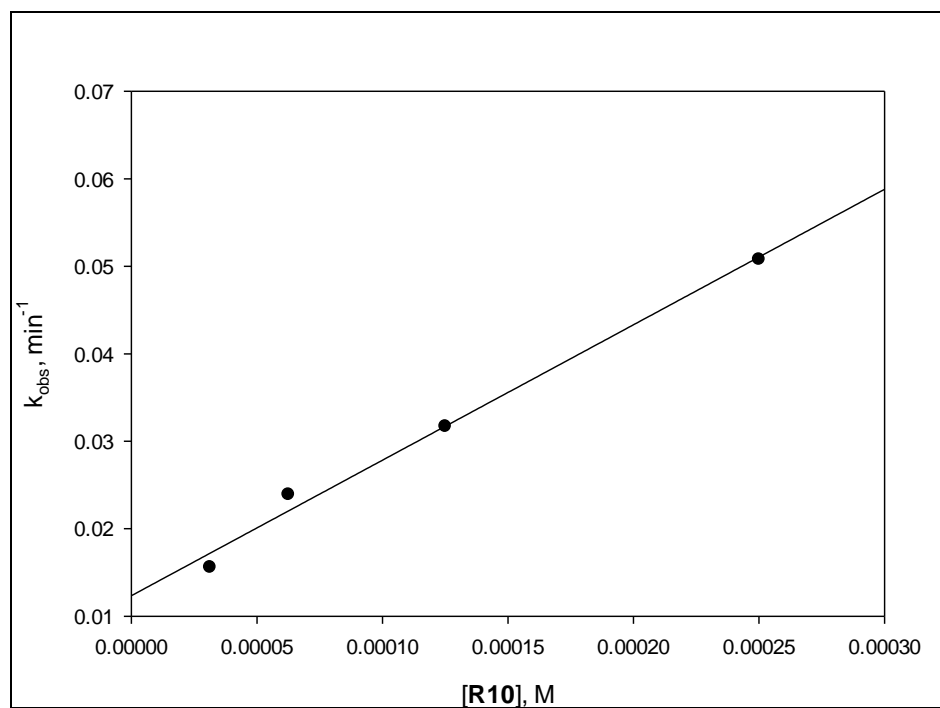


**Figure 5.5:** Second-order plot of  $k_{\text{obs}}$  as a function of **R10** concentration from stop-time assays (Eq. 5.10)

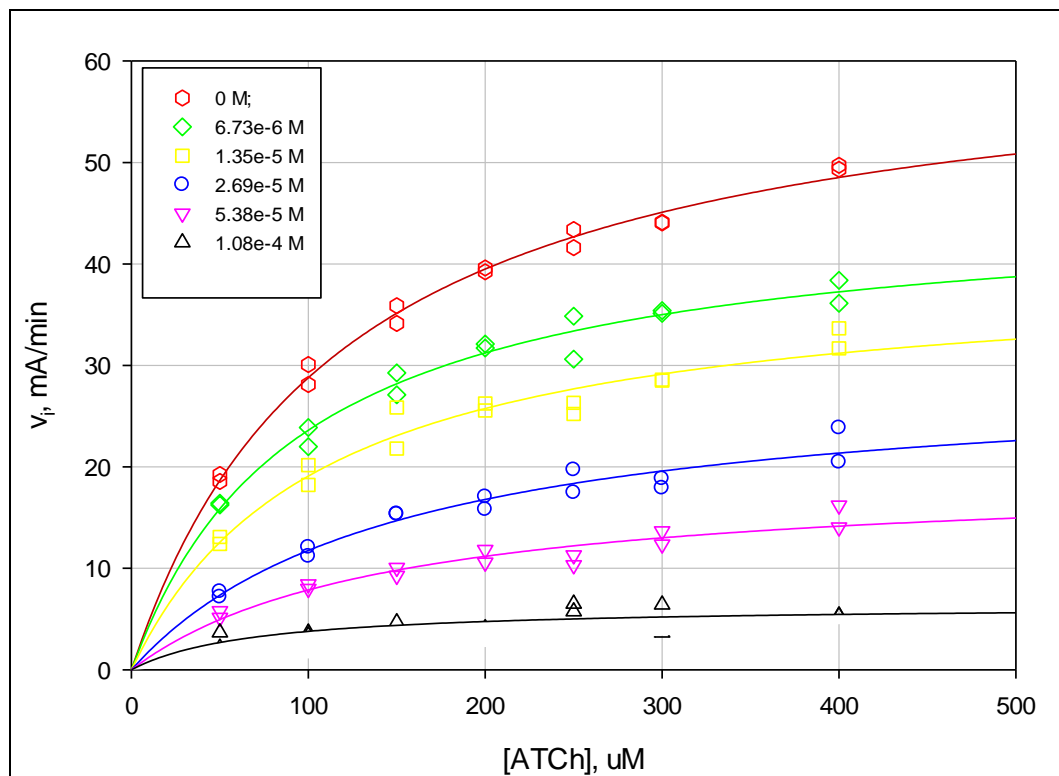


**Figure 5.6:** Michaelis-Menten plots of  $v_i$  (mA/min) versus ATCh concentration ( $\mu\text{M}$ ) for various concentrations of inhibitor **R10**, Eq. 5.6

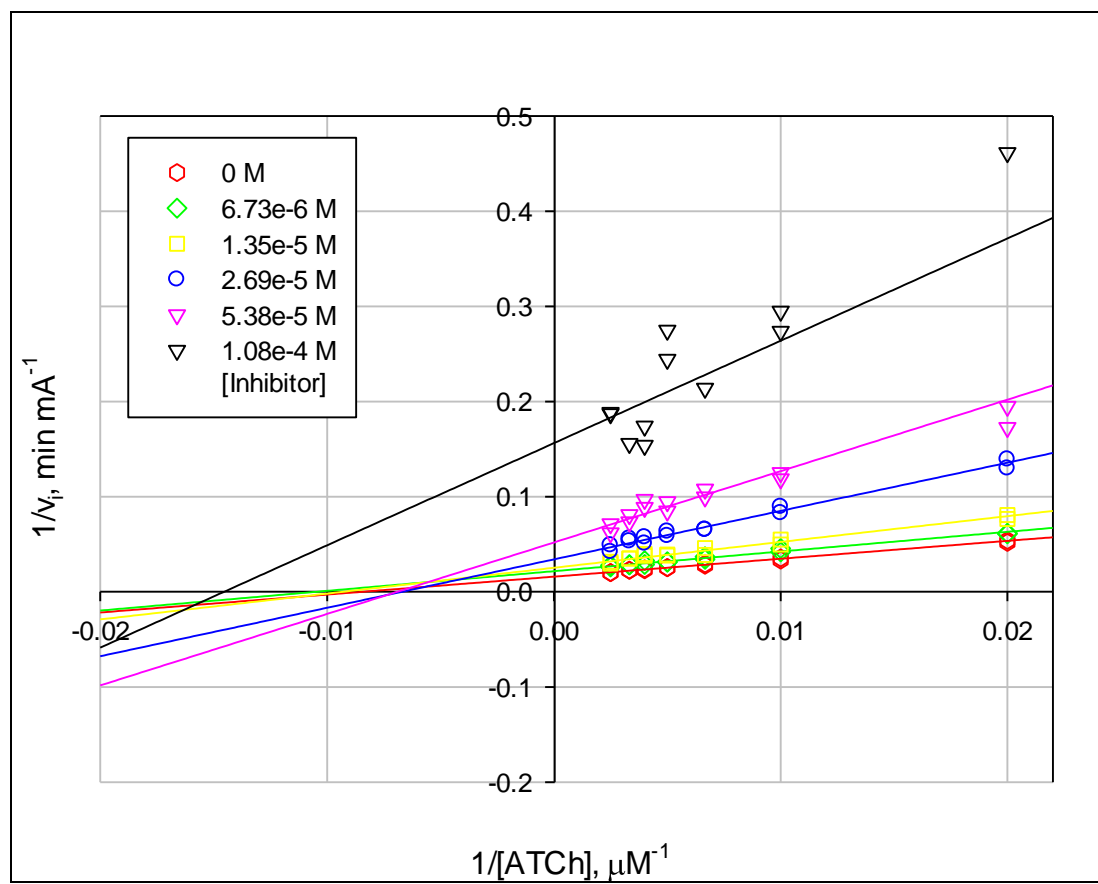


**Figure 5.7:** Double-reciprocal plot of the inverse initial rate ( $v_i^{-1}$ ,  $\text{min mA}^{-1}$ ) versus the inverse of ATCh concentration ( $\mu\text{M}^{-1}$ ) for various concentrations of inhibitor **R10**, Eq. 5.7

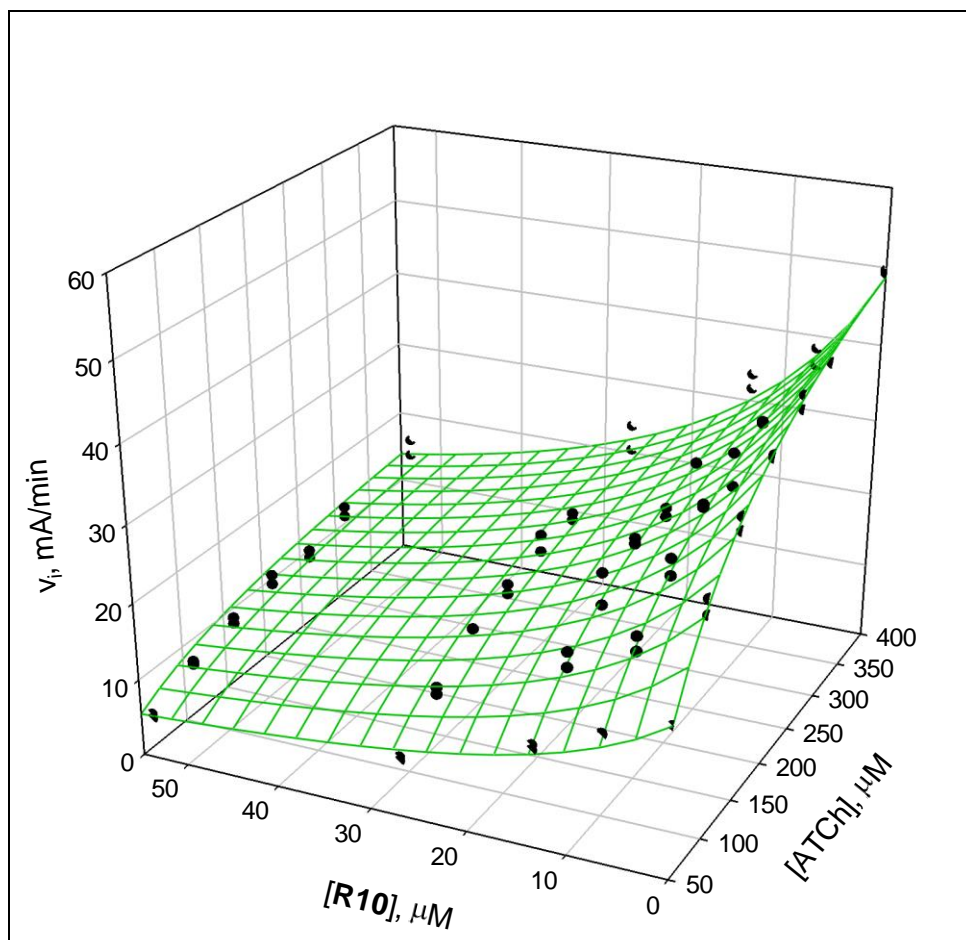


**Figure 5.8:** Three-dimensional plot of initial rate ( $v_i$ , mA/min) versus the substrate concentration (ATCh, 0-400  $\mu M$ ) and inhibitor **R10** concentration, Eq. 5.8

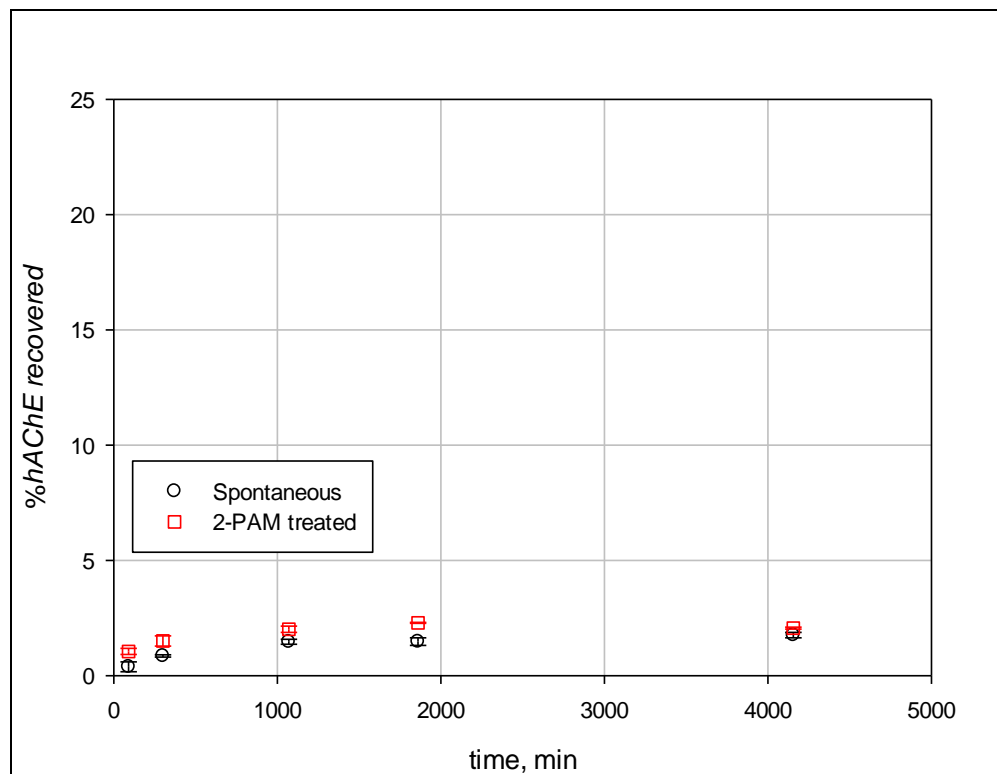


**Figure 5.9:** Recovered *hAChE* activity for inhibition by **R10** following separation of excess inhibitor, Eq. 5.9

rapidly upon mixing such that the enzyme is inhibited considerably before an initial rate measurement is taken. Data fit to non-competitive inhibition equation gave a  $K_i$  of  $22.9 \pm 0.7 \mu\text{M}$  (Fig. 5.8) at **R10** concentrations 0-50  $\mu\text{M}$ .

Both stop-time and initial rate Michaelis-Menten assays suggest two different modes of inhibition. This can be assessed in terms of the  $S_NAr$  mechanistic steps, in that initial inhibition (initial rate fits to Michaelis-Menten kinetics) would be non-competitive. Nucleophilic attack on the fluorine substituted carbon ortho to the quarternized nitrogen is rate-limiting, therefore, competitive inhibition would not be observed in initial rate evaluations. However, once the initial  $S_NAr$  mechanistic step occurs, **R10** would be covalently bound to the *hAChE* active-site serine. The observed time-dependent inhibition,  $IC_{50}$  and stop-time assays, support this idea.

To further support that **R10** inhibition is irreversible, assays to determine whether the inactivated *hAChE*'s activity is recovered either spontaneously or by treatment with a nucleophile (2-PAM) were performed. *hAChE* was inhibited with **R10**, purified to remove excess inhibitor, and assayed for recovered ability to hydrolyze ATCh. Fig. 5.9 illustrates the results of this assessment for which no apparent *hAChE* activity was recovered following inhibition with **R10**. This provided further evidence that **R10** could render the enzyme completely inactive by irreversibly binding to the catalytic-site serine (Fig 5.2).

### Conclusion

The inhibitor **R10** was evaluated as an irreversible inhibitor of human acetylcholinesterase. Kinetic evaluation of the fluorinated pyridinium inhibitor showed time-dependent inhibition, however, complete inactivation of the enzyme was not



observed after initial  $IC_{50}$  determinations. Further analysis by stop-time assay supports **R10** acts as an irreversible inhibitor of AChE. Initial rate assays to determine mode of inhibition for **R10** showed that the inhibitor, when evaluated at only its initial binding with *h*AChE, fit a non-competitive inhibitory mode. These results support the proposed mechanism of inhibition by  $S_NAr$  for which the first step, nucleophilic attack, is rate-limiting. Evaluation at longer incubation times, stop-time assay and washout assay, show that irreversible, competitive inhibition of *h*AChE by  $S_NAr$  is plausible and we are not simply observing inhibition by binding to the AChE allosteric site.

## CHAPTER 6: KINETIC EVALUATION OF PARACYCLOPHANE INHIBITORS OF HUMAN ACETYLCHOLINESTERASE

### Chemical Mechanism and Significance

The acetylcholinesterase (AChE) enzyme is the target for 4 of 5 of the current FDA-approved Alzheimer's Disease (AD) drug treatments (78). AD is said to affect fifty percent of individuals age 85 and older. Sufferers experience a progressive loss of neuronal cells and cognition caused by the presence of  $\beta$ -amyloid plaques, tau fibrils, and reduced levels of the neurotransmitter acetylcholine (ACh) (34). Inhibitors of AChE can compete with substrates at the enzyme's catalytic active site (A-site) which lies at the bottom of a narrow gorge, 20Å from the enzyme's surface (3). Inhibition also occurs at AChE's allosteric site, known as the peripheral anionic site (PAS), which lies near the mouth of the catalytic gorge (79, 11). AChE's PAS has also been found to promote the formation of  $\beta$ -amyloid plaques(36). Inhibitors that have the ability to bind to both the A-site and PAS of AChE provide dual benefits for AD treatment. This gorge spanning motif has been effective in the development of anticholinergic drugs, notably the discovery of the AChE inhibitor donepezil (Aricept<sup>®</sup>) which was an offshoot of a series of benzylpiperazine inhibitors showing modest AChE inhibitory activity (micromolar IC<sub>50</sub> range) (39).

[2.2] Paracyclophanes (pCp) are a class of uniquely structured hydrocarbons that provide an aromatic scaffold in which its two benzene rings are geometrically positioned face-to-face and covalently linked via ethano bridges (80). Research interest for pCps focus on its utility in synthetic efforts and most recently its optoelectronic properties (81).

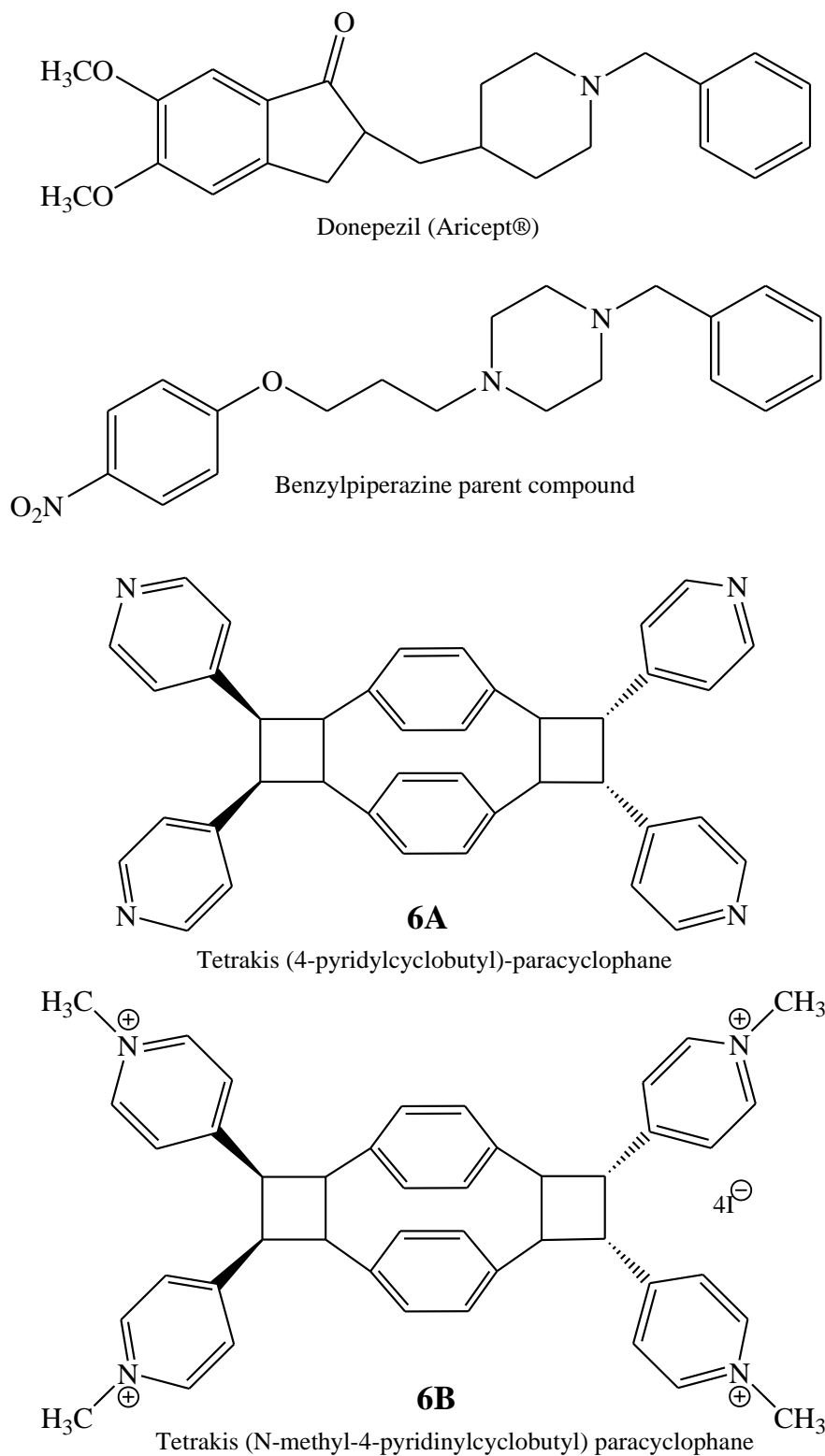


**Figure 6.1:** Chemical structures of donepezil, donepezil's parent compound, and novel paracyclophane AChE inhibitors **6A** and **6B**

Selective functionalization of the core pCp structure afford it use in a variety of applications, however, installation of substituents to the saturated bridges also give rise to changes in its photophysical properties (82). MacGillivray et al. have synthesized tetrakis(4-pyridylcyclobutyl)-pCps via [2+2] photoreaction in the solid state (80, 81, 82, 83, 84). This class of pCps has also shown distinct shifts in its excitation and emissions spectra by alkylating the pyridyl nitrogen. The rigid structure of pCps may provide a structural motif for the development of novel AChE inhibitors as well as biological probes for various applications. The present study evaluates tetrakis(4-pyridylcyclobutyl)-pCps for inhibitory activity in human AChE (hAChE) and further evaluation as a PAS-binding inhibitor.

#### Objective of Study

Study the inhibition kinetics of [2.2] paracyclophanes for human acetylcholinesterase and resolve its mode of inhibition.

#### Materials and General Method

Lyophilized human recombinant acetylcholinesterase (hAChE), acetylthiocholine iodide (ATCh), 5,5'-dithiobis(2-nitrobenzoic acid) (DTNB), bovine serum albumin (BSA), and p-nitrophenyl acetate (pNPA) were obtained from Sigma Aldrich. All solvents were obtained from commercial vendors at the highest purity available. Tetrakis(4-pyridylcyclobutyl) paracyclophane (**6A**) and tetrakis(4-(tetra-N-methylpyridinium)cyclobutyl) paracyclophane iodide (**6B**) inhibitors were synthesized by Elizabeth Elacqua of the Leonard R. MacGillivray research group at the University of Iowa Department of Chemistry (81).

Deionized distilled water (DD-H<sub>2</sub>O), which was used to prepare all assay solutions, was filtered through a Barnstead International hose nipple organic removal ion exchange cartridge. Inhibitors with limited water solubility were prepared in methanol. 100 mM phosphate buffer (PB) was prepared in bulk at pH ranging from 7.3-7.5 as measured via an ion selective pH electrode and calibrated prior to each measurement. All stock solutions were prepared from solid material and stored in polypropylene containers at 4 °C or -4 °C as follows: 0.1% (w/v) BSA solution in PB, 45 mM ATCh in DD-H<sub>2</sub>O, 20 mM DTNB in PB, 14 nM hAChE in BSA solution, and 1.4 nM hAChE in BSA solution. Working solutions were prepared for use in biological assays using calibrated micropipettes in solvents from parent stocks.

Assays were conducted on a Molecular Devices SpectraMaxPlus384 micro-plate reader and on polystyrene 96-well plates (Costar, round bottom). Activity of hAChE was measured spectrophotometrically at 412 nm and 27 °C following the Ellman assay method (26). Time dependent inhibition was measured at the minimum possible interval over 10 min durations at each incubation time point and performed in duplicate. Initial rates ( $v_i$ , mA/min) were calculated by least-squares analysis of the time courses at less than 10% turnover of the initial substrate concentration. Non-linear regression analysis was performed using SigmaPlot 12.0 to obtain inhibition parameters.

Each inhibitor was evaluated for inhibitory activity of free hAChE. The assay was performed under the following conditions: each assay well was loaded with DTNB (270  $\mu$ L, 0.5 mM, in PB), hAChE (10  $\mu$ L, 1.4 nM, in 0.1% BSA), inhibitors **6A** or **6B** (10  $\mu$ L, 0.1 nM-10  $\mu$ M, in DD-H<sub>2</sub>O or methanol), and ATCh (10  $\mu$ L, 4.5 mM, in DD-H<sub>2</sub>O). Initial rates ( $v_i$ , mA/min) of hAChE activity were obtained as described in the general

procedure.  $K_i^{app}$  values were calculated by plotting  $v_i$  as a function of inhibitor concentration and by fitting to Eq. 6.1:

$$v_i = \frac{v_o}{1 + \frac{10^{\log[I]}}{K_i^{app}}}$$

**Equation 6.1:** Equation for initial rates ( $v_i$ ) as a function of  $K_i^{app}$  (apparent inhibitor dissociation constant, M) and inhibitor concentration ( $[I]$ , M)

From the  $K_i^{app}$ ,  $IC_{50}$  values were calculated using Eq. 6.2:

$$IC_{50} = \frac{K_i^{app}}{1 + \frac{[A]}{K_m}}$$

**Equation 6.2:** Equation for  $IC_{50}$  (50% inhibitory concentration, M) as a function of  $K_i^{app}$  (M),  $[A]$  substrate concentration, and Michaelis constant for AChE hydrolysis of ATCh ( $K_m$ , M)

Inhibition studies were performed and Lineweaver-Burk plots generated in order to determine the mode of hAChE inhibition. Each assay was conducted at a fixed concentration of hAChE (48 pM) and at varied concentrations of both substrates (ATCh: 50-400  $\mu$ M; p-NPA: 0.025-3.2 mM) and inhibitor **6B** (0-8  $\mu$ M). p-NPA was used as a slow hydrolyzing substrate with a  $k_{cat}/K_m$  three orders of magnitude slower than ATCh by AChE (3). Experiments using p-NPA were conducted to confirm inhibitor **6B** inhibits hAChE at its peripheral active site. Analysis was performed in duplicate following the Ellman method as described in the general procedure. Michaelis-Menten plots were generated and fit via non-linear regression analysis from  $v_i$  using Eq. 6.3.

$$v_i = \frac{V_{max}^{app} [A]}{[A] + K_m^{app}}$$

**Equation 6.3:** Michaelis-Menten equation for the inhibited hAChE catalyzed hydrolysis of ATCh where  $K_m^{app}$  is the observed Michaelis constant and  $V_{max}^{app}$  is the observed maximum reaction velocity.

Values for the maximum velocity ( $V_{max}$ ) and Michaelis constant ( $K_m$ ) were used to calculate the slopes and intercepts for the double reciprocal plot, Eq. 6.4:

$$\frac{1}{v_i} = \frac{V_{max}}{K_m} \frac{1}{[A]} + \frac{1}{V_{max}}$$

**Equation 6.4:** Double-reciprocal Lineweaver-Burk equation

In order to better assess the type of inhibition for inhibitor **6B**, the resultant Michaelis-Menten values were fit by three dimensional regression analyses to Eq. 6.5 for nonlinear noncompetitive inhibition.

$$v_i = \frac{V_{max}[A](1 + \frac{\beta[I]}{\alpha K_I})}{K_m x (1 + \frac{[I]}{K_I})}$$

**Equation 6.5:** Equation defining nonlinear non-competitive inhibition where  $K_I$  is the inhibitor dissociation equilibrium constant

Rosenberry et al. (85) reported that inhibition of hAChE at its peripheral site can be confirmed through utilizing slow hydrolyzing substrates. This study utilizes p-NPA, which has a  $k_{cat}/K_m$  that is three orders of magnitude slower than ATCh by hAChE. A range of p-NPA concentrations was assayed in duplicate to determine the Michaelis-Menten constants  $K_m$  and  $V_{max}$  under the following conditions: each assay well was loaded with 0.1 M phosphate buffer (250  $\mu$ L, pH 7.3), hAChE (40  $\mu$ L, 14 nM, in 0.1% BSA), and p-NPA (10  $\mu$ L, 0.75-40 mM in acetonitrile). The catalytic turnover of p-NPA

to p-nitrophenol was followed spectrophotometrically at 400 nm for 20 minutes using the minimum interval possible. Initial rates ( $v_i$ , mA/min) of hAChE activity were obtained as described in the general procedure to obtain a  $K_m$  of  $1.4 \pm 0.2$  mM and  $V_{max}$  of 200 mA/min from non-linear regression plot of  $v_i$  versus p-NPA concentration.

Pseudo-first order rate constants ( $k_i$ ,  $s^{-1}$ ) for inhibition of hAChE by inhibitor **6B** were assayed following conditions similar to those described above. Each assay was conducted at fixed concentrations of hAChE (2 nM) and p-NPA (0.15 mM). Concentrations of inhibitor **6B** were varied (0-16  $\mu$ M) and the production of p-nitrophenol was followed at 400 nm for 90 min. The resultant absorbance values were fit to Eq. 6.6 by non-linear regression analysis.

$$A = A_{\infty} + (A_o - A_{\infty})e^{-k_{obs}t}$$

**Equation 6.6:** Equation for first-order rate determination, A (absorbance),  $A_o$  (initial absorbance value),  $A_{\infty}$  (absorbance at  $t_{\infty}$ ),  $k_{obs}$  (observed first-order rate,  $s^{-1}$ ), t (time, s)

Values for  $k_i$  were fit to Eq. 6.7

$$k_i = \frac{k_o(1+c\frac{[I]}{K_i})}{(1+\frac{[I]}{K_i})}; c = \frac{\beta}{\alpha}$$

**Equation 6.7:** Equation defining  $k_i$  for non-linear non-competitive inhibition

### Results and Discussion

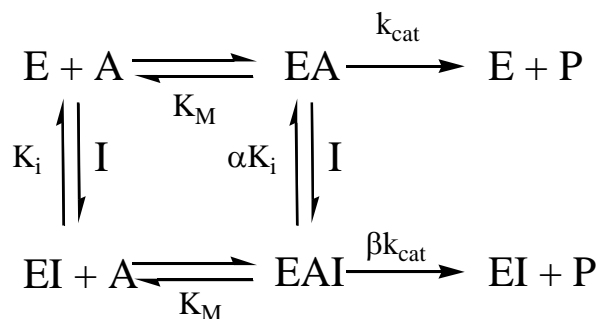
Neutral and N-methylated pCps, **6A** and **6B**, were synthesized by and obtained from Elizabeth Elacqua of the Department of Chemistry at the University of Iowa. Inhibitory activity of hAChE's hydrolysis of acetylthiocholine (ATCh) was assayed following methodology reported by Ellman et al.(26). Time-dependent dose response



assays were performed at concentrations between 100  $\mu\text{M}$  – 0.1 nM of **6A** and **6B**.

Kinetic evaluations of pCps **6A** and **6B** gave  $\text{IC}_{50}$  values of  $32 \pm 5 \mu\text{M}$  and  $1.0 \pm 0.2 \mu\text{M}$ , respectively, and showed reversible inhibition (Table 6.1).

N-methylated pCp (**6B**) showed the stronger inhibitory activity for *hAChE*. The mode of inhibition was assayed at varied concentrations of inhibitor **6B** (0 to 8  $\mu\text{M}$ ) and ATCh (0 to 500  $\mu\text{M}$ ). Resultant data were subjected to non-linear fit to the Michaelis-Menten equation, Eq. 6.3, and Lineweaver-Burk (86) analysis (Fig. 6.2 and 6.3). Plots generated from Lineweaver-Burk analyses and subsequent slope replot (Fig. 6.4) suggested that the mode of inhibition of *hAChE* by **6B** is non-competitive (Scheme 6.1). Given the suggested mode of inhibition, the assay data were plotted three dimensionally to equation 6.5 (Fig. 6.5). An inhibitor dissociation constant,  $K_i$ , of  $2.6 \pm 0.7 \mu\text{M}$  was calculated for *hAChE* inhibition by **6B**. Scheme 6.1 suggests that **6B** binds to AChE's PAS, which has been reported to provide an allosteric contribution to AChE's catalytic efficiency (21). Further investigation into whether inhibition is a result of interaction by **6B** with AChE's PAS was subsequently conducted.



**Scheme 6.1:** Reaction scheme for non-linear, non-competitive inhibition of *hAChE*

**Table 6.1:** IC<sub>50</sub> values for inhibitors **6A** and **6B**

<b>Inhibitor</b>		<b>IC<sub>50</sub> (μM)</b>					
	Time (h)	0	1	2	3	4	5
<b>6A</b>		32 ± 5	14 ± 2	11 ± 2	12 ± 1	13 ± 3	11 ± 2
<b>6B</b>		1.0 ± 0.2	1.2 ± 0.2	1.2 ± 0.2	1.2 ± 0.2	1.3 ± 0.2	1.1 ± 0.2

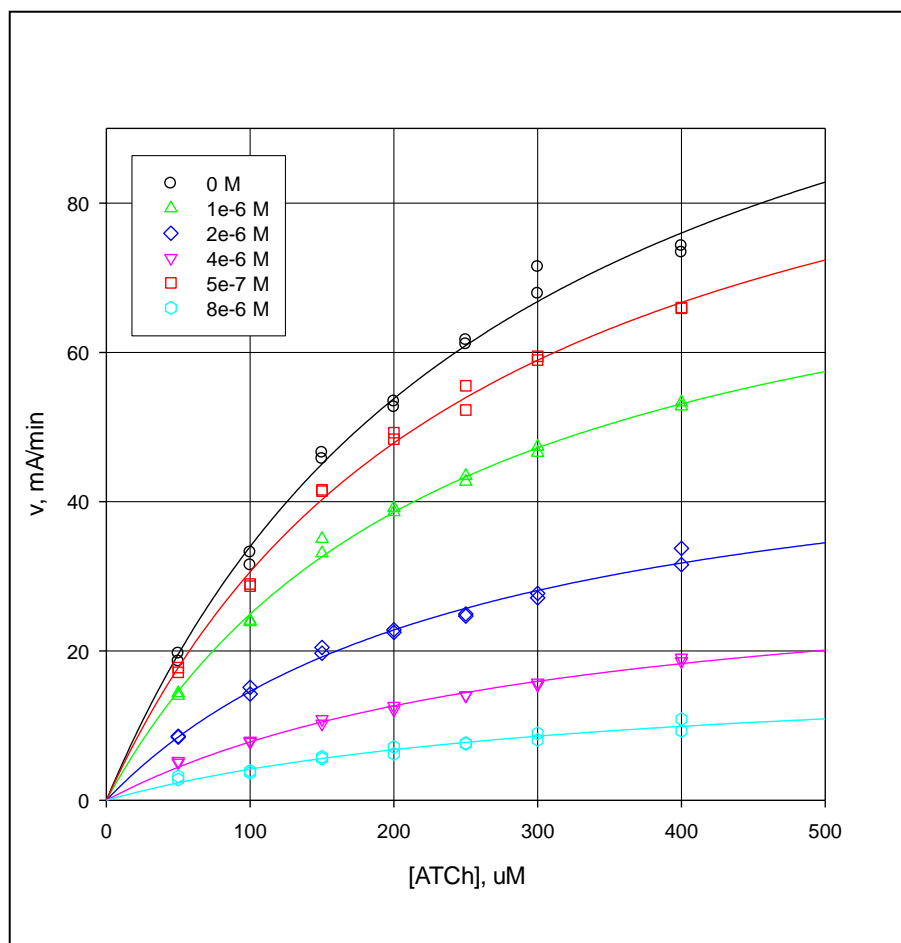


**Figure 6.2:** Michaelis-Menten plot of  $v_i$  (mA/min) versus ATCh concentration ( $\mu M$ ) for various concentrations of inhibitor **6B** (0-8  $\mu M$ )

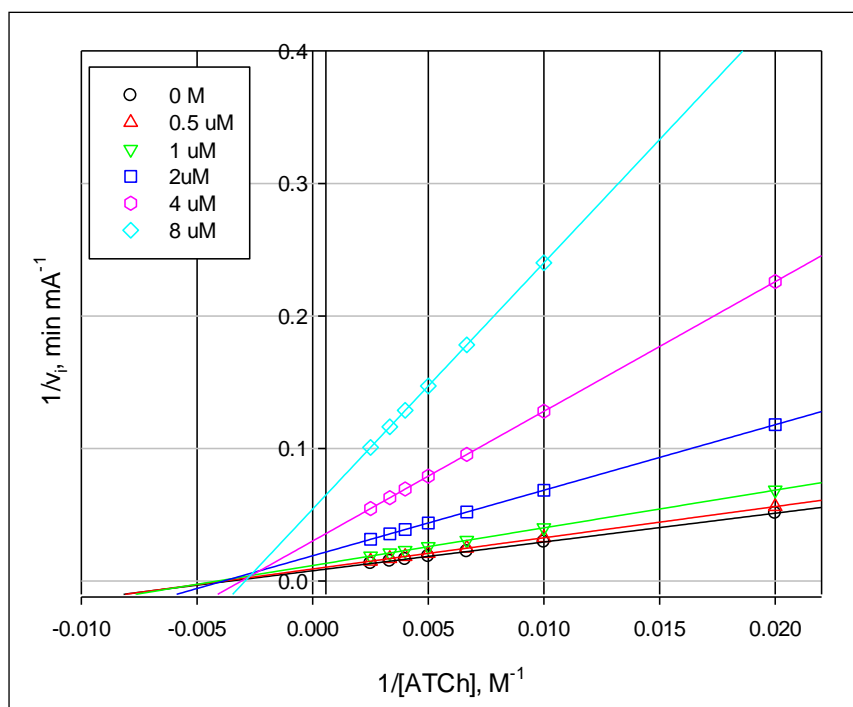


**Figure 6.3:** Double-reciprocal plot of the inverse initial rate ( $v_i^{-1}$ ,  $\text{min mA}^{-1}$ ) versus the inverse of ATCh concentration ( $\mu\text{M}^{-1}$ ) for various concentrations of inhibitor **6B** (0-8  $\mu\text{M}$ ).

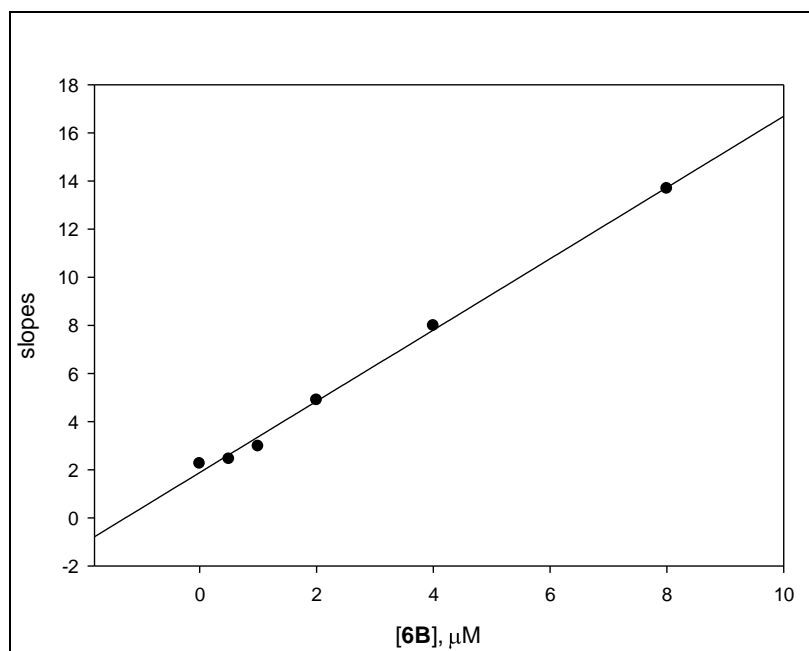


**Figure 6.4:** Slope replot from Lineweaver-Burk analysis of the slopes versus inhibitor **6B** concentration (0-8 μM) and described as the

$$\text{slope } (m) = \frac{K_m}{V_{max}} + \frac{K_m}{V_{max}K_I} [I]$$

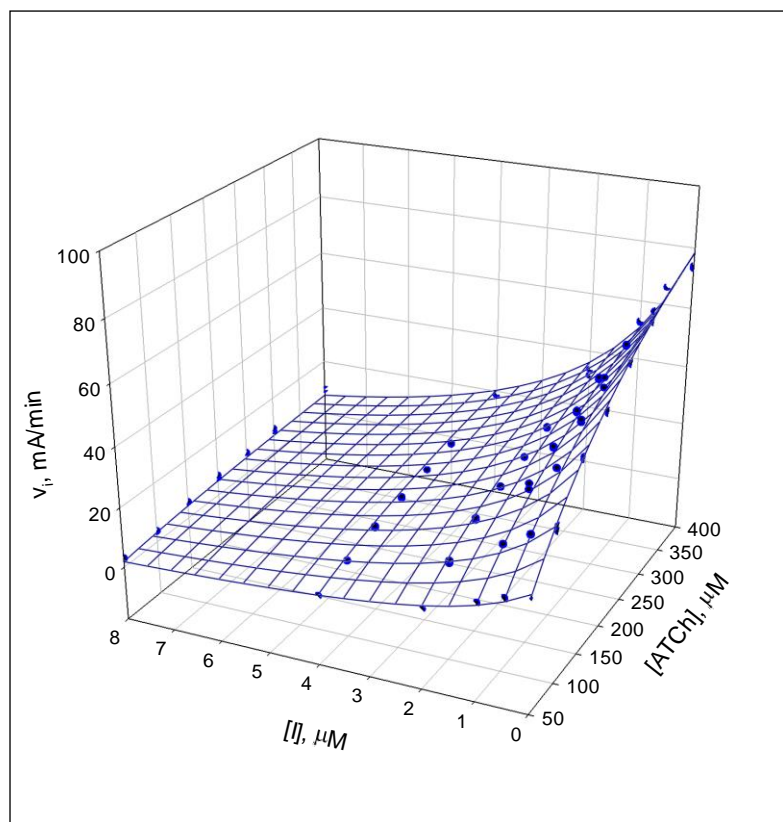


**Figure 6.5:** Three-dimensional plot of initial rate ( $v_i$ , mA/min) versus the substrate concentration (ATCh, 0-400  $\mu M$ ) and inhibitor **6B** concentration (0-8  $\mu M$ ).

Rosenberry et al. reported the use of slow hydrolyzing substrates to delineate between inhibition at either the A-site or PAS of AChE (85). We utilize this concept in determining the inhibition character of **6B** with the slow hydrolyzing substrate p-nitrophenylacetate (p-NPA), which is hydrolyzed by *hAChE* three orders of magnitude slower than ATCh (28). To initially evaluate this concept for inhibitor **6B**, *hAChE* hydrolysis of p-NPA to produce p-nitrophenol was monitored spectrophotometrically at 400 nm following similar conditions for the Ellman assay method.

Michaelis-Menten kinetic values were determined for p-NPA hydrolysis to p-nitrophenol yielding a  $K_M$  of 1.44 mM. Concentrations of **6B** (0 to 6.4  $\mu\text{M}$ ) and p-NPA (94 to 6000  $\mu\text{M}$ ) were assayed in the presence of *hAChE* and plotted to Eq. 6.3 to generate  $K_M$  and  $V_{\max}$  values (Fig. 6.6). Resultant data were subjected to Lineweaver-Burk analysis to determine the mode of inhibition which did not support a non-competitive mode of inhibition (Fig. 6.7). However, three-dimensional fit to Eq. 6.5 for non-linear, non-competitive inhibition gave the best fit by non-linear regression analysis ( $R^2 = 0.96$ ) and a  $K_i = 1.8 \pm 0.9 \mu\text{M}$  (Fig. 6.8). This initial evaluation of the inhibitory activity for **6B** prompted need for further analysis of the inhibitory mode.

As reported by Rosenberry et al., if **6B** inhibits *hAChE* non-competitively through binding to *hAChE*'s PAS, a significant reduction in *hAChE* activity should not be observed and rate constants for p-NPA hydrolysis should be relatively unaffected with increase in concentration of **6B**. Determination of first order rate constants ( $k_i, \text{s}^{-1}$ ) for *hAChE* inhibition was performed at varied concentrations of **6B** (0 to 16  $\mu\text{M}$ ) at a  $[A]_0$  concentration of 150  $\mu\text{M}$  for p-NPA. As shown in Fig. 6.9, inhibition of *hAChE* by inhibitor **6B** was observed for the slow-hydrolyzing substrate p-NPA. This brings to

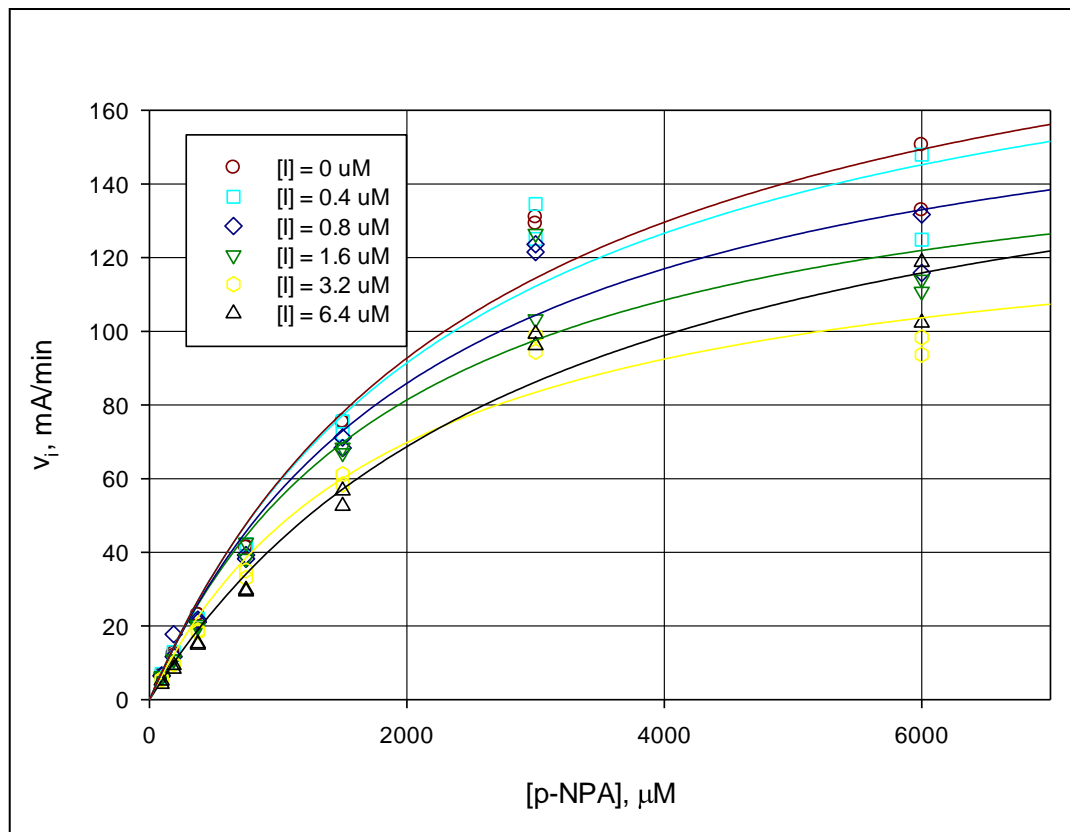


**Figure 6.6:** Michaelis-Menten Plot of  $v_i$  (mA/min) versus p-NPA concentration ( $\mu\text{M}$ ) for various concentrations of inhibitor **6B** (0-6.4  $\mu\text{M}$ )



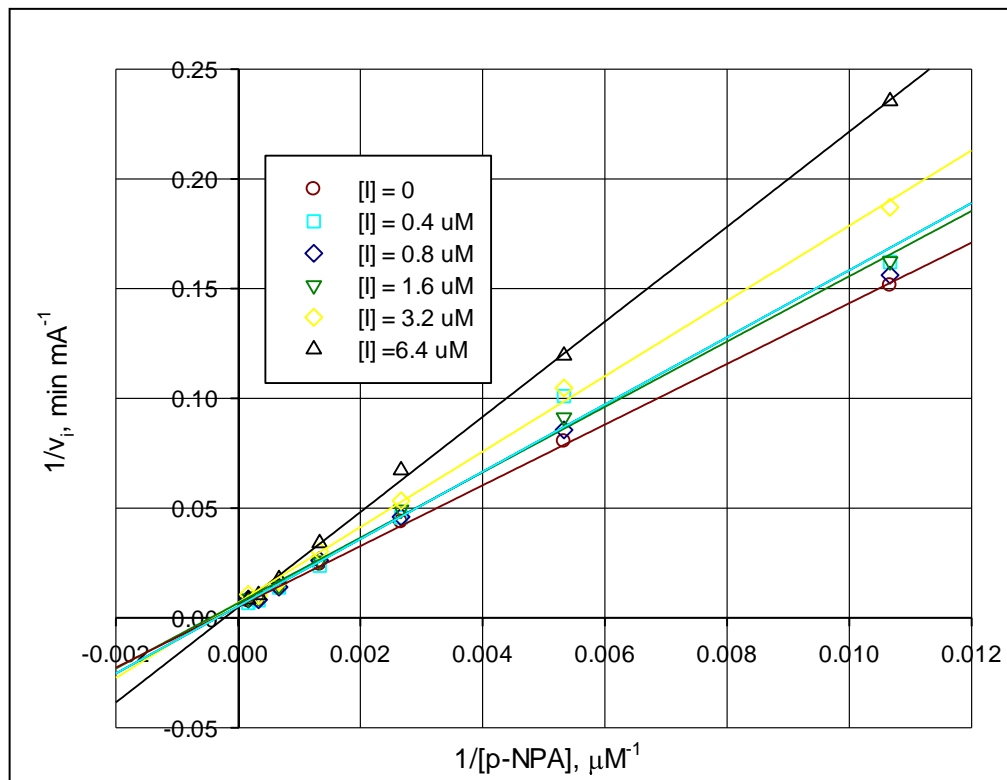


**Figure 6.7:** Double-reciprocal plot of the inverse initial rate ( $v_i^{-1}$  ( $\text{min}\cdot\text{mA}^{-1}$ ) versus the inverse of p-NPA concentration ( $\mu\text{M}^{-1}$ ) for various concentrations of inhibitor **6B** (0-6.4 $\mu\text{M}$ ).

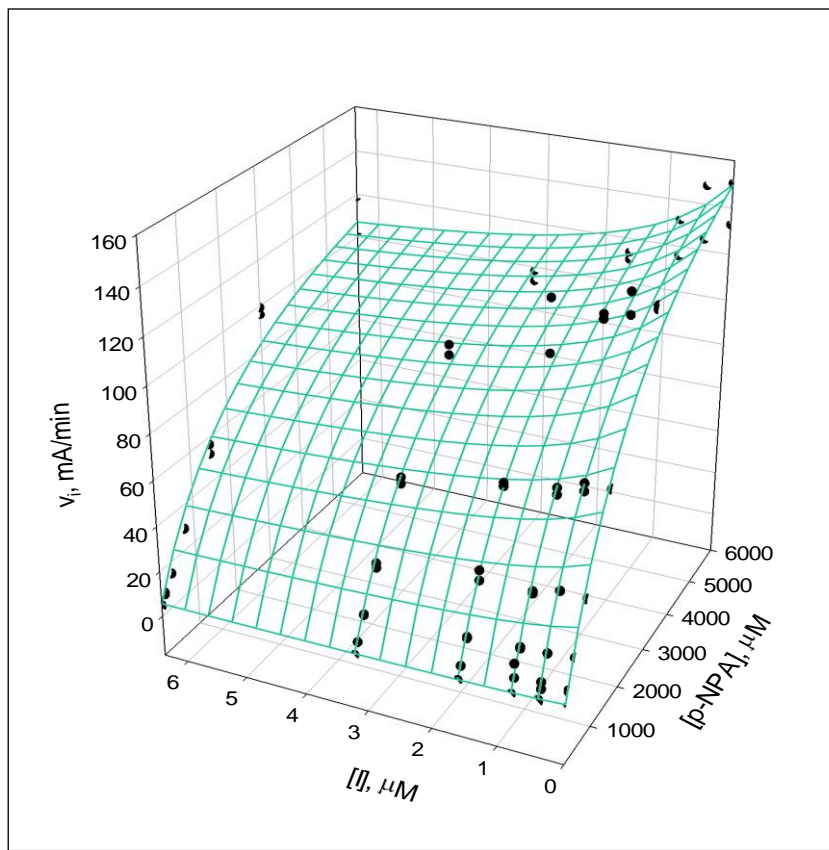


**Figure 6.8:** Three-dimensional plot of initial rate ( $v_i$ , mA/min) versus the substrate concentration (p-NPA, 0-6000  $\mu\text{M}$ ) and inhibitor **6B** concentration (0-6  $\mu\text{M}$ ).

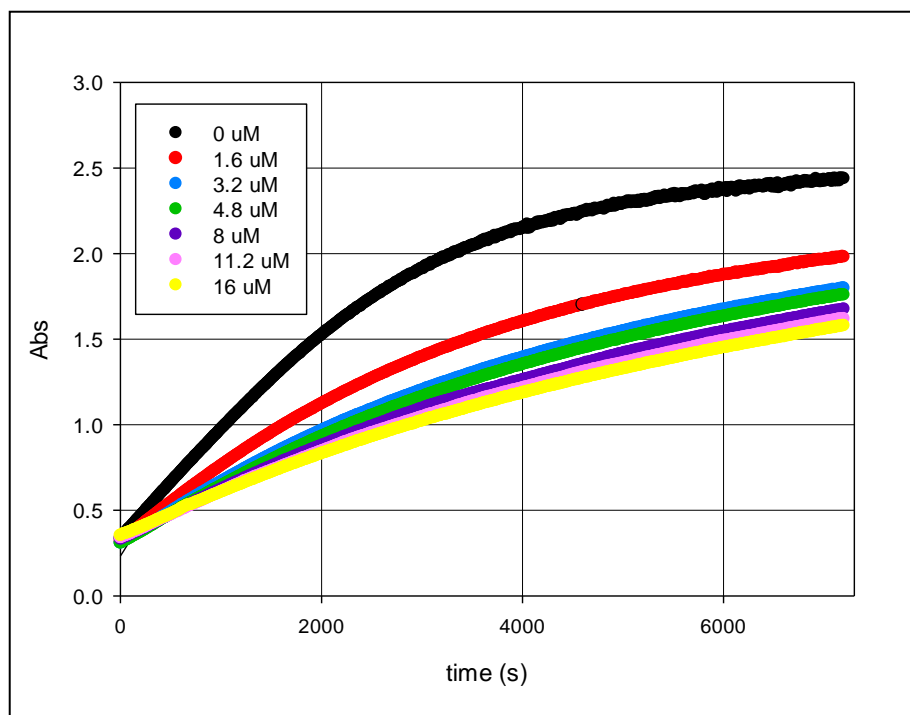


**Figure 6.9:** Time course plots of absorbance versus time (s) for various concentrations of inhibitor **6B** (0-16  $\mu\text{M}$ ).

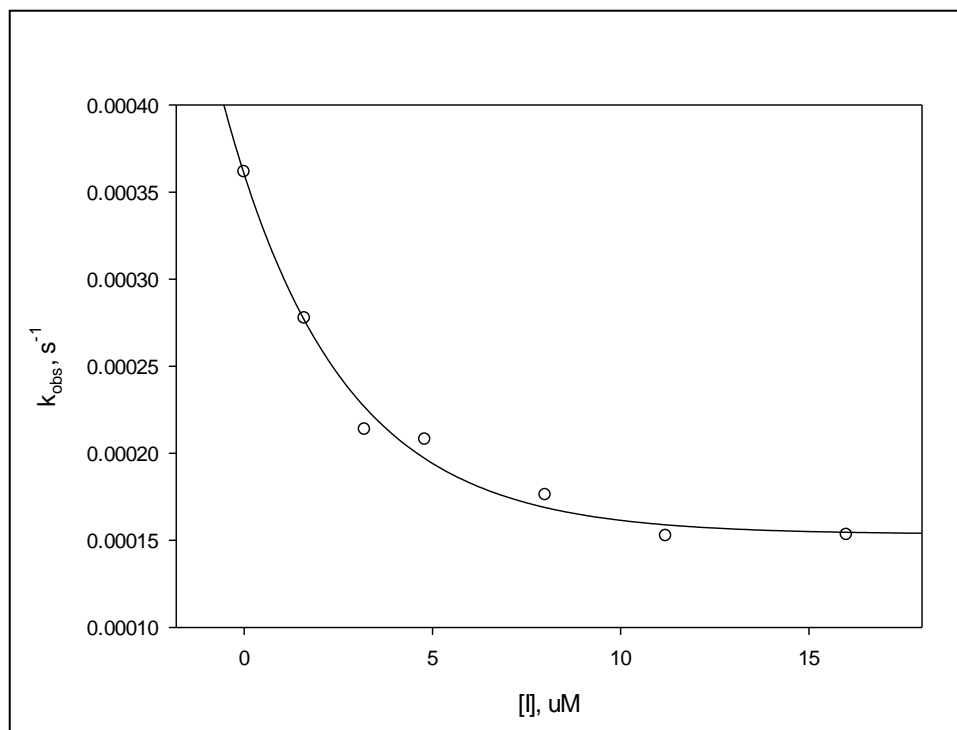


**Figure 6.10:** Non-linear plot for noncompetitive inhibition of first-order kinetic rate ( $k_i, \text{s}^{-1}$ ) versus concentration of inhibitor **6B** (0-16  $\mu\text{M}$ ).

question whether the observed non-competitive inhibition of *hAChE* hydrolysis of ATCh is due to binding of **6B** to the PAS. Further analyses was performed by fitting the  $k_i$  values obtained to Eq. 6.7, which was derived from Scheme 1 for non-linear, non-competitive inhibition (Fig. 6.10). This yielded a  $K_i$  of  $2.7 \pm 0.5 \mu\text{M}$ , which is in agreement with values obtained for *hAChE* inhibition by **6B** for ATCh hydrolysis. We also obtain a value of  $0.31 \pm 0.04$  for  $c$ , which is defined by the ratio  $\beta/\alpha$  where  $\alpha$  is the relative inhibitor binding affinity to the EA complex versus the free enzyme, and  $\beta$  is the relative acylation rate constant.

### Conclusion

Compounds **6A** and **6B** provide an interesting class of structurally rigid inhibitors of *hAChE*. Evaluation of **6B** as a PAS inhibitor poses the question of what interactions promote AChE inhibition by these compounds. In Rosenberry's study of PAS inhibitors thioflavin T and propidium, inhibition of  $V_{\max}/K_m$  was seen in ATCh hydrolysis but not for the slow hydrolyzing substrate ATMA (85). Inhibition of AChE was observed for p-NPA hydrolysis in the presence of **6B**. Kinetic evidence does not support a competitive mode of inhibition for **6B**, however, inhibition of  $V_{\max}/K_m$  *hAChE* catalyzed hydrolysis of p-NPA would suggest that competition for the enzyme's active site is occurring. Alternatively, inhibition experienced during p-NPA hydrolysis may be attributed to the phenomena known as steric blockade. Rapid reversible binding of the inhibitor at AChE's PAS, near the entrance to *hAChE*'s catalytic gorge, effectively blocks substrate access to the A-site. Due to the well-organized aromatic framework and bulky structure of both **6A** and **6B**, it is plausible that weak  $\pi$ - $\pi$  and  $\pi$ -cation interactions may promote binding to *hAChE*'s PAS. If steric blockade is occurring, migration of substrate from the

PAS to the A-site may be rate-limiting. This is supported by the value obtained for  $\beta$  in Eq. 6.5, which indicates that  $\beta$  is significantly smaller than 1 ( $\beta = 0.17 \pm 0.05$ ).

APPENDIX A:  
SUPPORTING INFORMATION  
ORGANOPHOSPHONATE INHIBITORS

Synthetic Procedure

*Materials and General Methods*

All reagents were purchased from a commercial vendor in the highest purity available and were used without further purification unless otherwise stated. Solvents were either used as received or dried over molecular sieves where noted.

Chemical syntheses were conducted in oven dried glassware under a positive pressure of argon with magnetic stirring. All reagents were transferred using standard dry techniques. Organic solutions were concentrated by rotary evaporation at or below 50 °C at 25 torr. Flash chromatography was performed on a Teledyne ISCO CombiFlash Rf system utilizing normal phase pre-column cartridges and gold high performance columns eluting with a gradient of ethyl acetate and hexanes or isopropyl alcohol and hexanes (Fischer Scientific) unless noted otherwise. Visualization was conducted with the instrument's internal UV detector using 215 nm, 258 nm, 280 nm wavelengths.

All proton ( $^1\text{H}$ ) nuclear magnetic resonance spectra were recorded on either a 400 MHz (Avance III) or 500 MHz (Avance) Bruker spectrometers. All carbon ( $^{13}\text{C}$ ) nuclear magnetic resonance spectra were recorded on a 100 MHz or 125 MHz NMR spectrometer. All fluorine ( $^{19}\text{F}$ ) nuclear magnetic resonance spectra were recorded on a 376 MHz or 470 MHz NMR spectrometer with proton decoupling. All phosphorous ( $^{31}\text{P}$ ) nuclear magnetic resonance spectra were recorded on an 80 MHz or 100 MHz NMR

spectrometer with proton decoupling. Chemical shifts are expressed in parts per million (scale) and are referenced to residual  $^1\text{H}$  in the NMR solvent ( $\text{CDCl}_3$ : 7.26 ppm, acetone- $\text{d}_6$ : 2.05 ppm,  $\text{DMSO-d}_6$ : 2.50 ppm), to the central carbon in the NMR solvent ( $\text{CDCl}_3$ : 77.0 ppm, acetone- $\text{d}_6$ : 30.0 ppm,  $\text{DMSO-d}_6$ : 39.5 ppm). Data are presented as follows: chemical shift, multiplicity (s = singlet, d = doublet, t = triplet, q = quartet, m = multiplet, or bs = broad singlet), integrated intensity, and coupling constant in Hertz (Hz). Infrared (IR) spectral data were collected on a JASCO FT/IR 4100 instrument and are reported in  $\text{cm}^{-1}$ . High resolution mass spectrometry utilizing electrospray ionization or electron impact ionization in positive mode was performed to confirm the identity of the compounds (UIowa HRMS facility). Elemental analyses were conducted by Atlantic Microlabs.

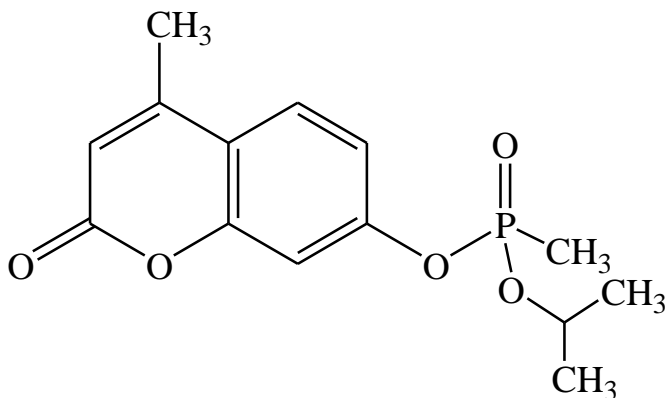
#### *Organophosphonate Inhibitors*

A literature procedure was modified for the preparation of sarin analogues; an example procedure is given for **2A62**): A round bottom flask was charged with solid 7-hydroxy-4-methylumbelliferone (167 mg, 0.97 mmol) and methylphosphonic dichloride (157 mg, 1.18 mmol) and these solids were dissolved in dry benzene (dried over molecular sieves, 5 mL). The flask was cooled to 0 °C and triethylamine (0.34 mL, 2.4 mmol) was added dropwise to the reaction mixture over 5 min. The mixture was allowed to warm gradually to room temperature over 2 h. After this time, dry isopropanol (dried over molecular sieves, 92  $\mu\text{L}$ , 1.2 mmol) was added to the reaction. After an additional 18 h, the reaction was diluted with ethyl acetate, gravity filtered, and concentrated *in vacuo*. The residue was purified by column chromatography (gradient 0%-100%

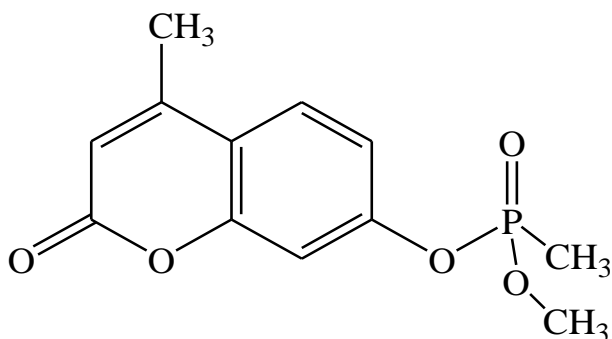


isopropanol in hexanes) to give the sarin analogue as a clear oil (135.5 mg, 44% yield).

All OP products were racemic mixtures.

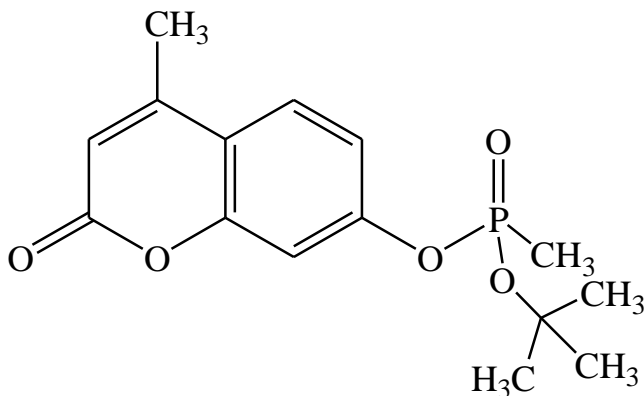


44% yield.  $^1\text{H NMR}$  (500 MHz, Chloroform-d):  $\delta = 1.32$  (dd, 6H), 1.59 (d,  $J = 17.6$  Hz, 3H),  $\delta = 2.42$  (s, 3H), 4.82 (m, 1H), 6.21 (s, 1H), 7.17 (m, 2H), 7.50 (d,  $J = 8.6$  Hz, 1H).  $^{13}\text{C NMR}$  (125 MHz, Chloroform-d):  $\delta = 12.21$  (d,  $J = 145.4$  Hz),  $\delta = 12.79$  (s), 18.65, 23.82 (d,  $J = 4.3$  Hz), 23.94 (d,  $J = 4.7$  Hz), 71.94 (d,  $J = 6.8$  Hz), 108.86 (d,  $J = 5.0$  Hz), 113.92, 116.90, 116.96 (d,  $J = 4.3$  Hz), 125.82, 152.01, 153.10 (d,  $J = 7.8$  Hz), 154.33, 160.42.  $^{31}\text{P NMR}$  (100 MHz, Chloroform-d):  $\delta = 26.93$

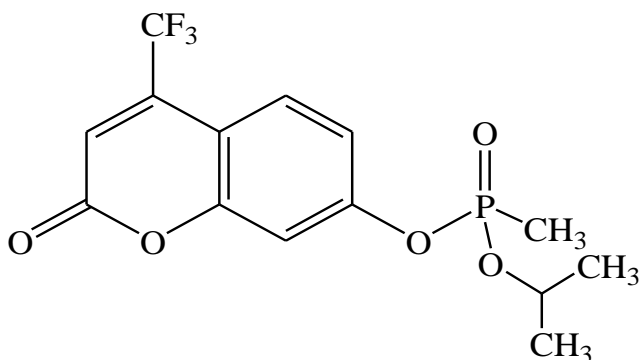


71% yield.  $^1\text{H NMR}$  ( $\text{CDCl}_3$ , 500 MHz):  $\delta = 7.50$  (d,  $J = 8.6$  Hz, 1H), 7.12 (ddd,  $J = 8.6$ , 2.4, 1.1 Hz, 1H), 7.08 (dd,  $J = 2.4$ , 1.1 Hz, 1H), 6.14 (q,  $J = 1.3$  Hz, 1H), 3.75 (d,  $J = 11.5$  Hz, 3H), 2.33 (d,  $J = 1.2$  Hz, 3H), 1.60 (d,  $J = 17.7$  Hz, 3H).  $^{13}\text{C NMR}$  ( $\text{CDCl}_3$ , 100 MHz):  $\delta = 160.2$ , 154.1, 152.7 (d,  $J_{\text{C-P}} = 8.1$  Hz), 151.8, 125.7, 116.9, 116.6 (d,  $J_{\text{C-P}} =$

4.4 Hz), 113.8, 108.6 (d,  $J_{C-P} = 4.4$  Hz), 52.8 (d,  $J_{C-P} = 6.7$  Hz), 18.4, 10.6 (d,  $J_{C-P} = 145$  Hz).  $^{31}\text{P}$  NMR ( $\text{CDCl}_3$ , 80 MHz):  $\delta = 29.4$ . HRMS (TOF EI+): calc. for  $\text{C}_{12}\text{H}_{14}\text{O}_5\text{P}$  ( $\text{M}^+$ ): 269.0579; found: 269.0579.

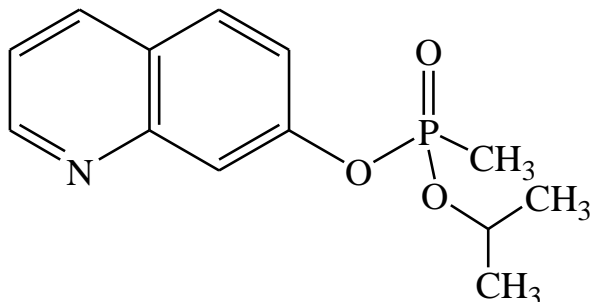


2.3% yield.  $^1\text{H}$  NMR (500 MHz, Chloroform-*d*):  $\delta = 1.56$  (s, 9H), 1.65 (d,  $J = 17.6$  Hz, 3H), 2.44 (d,  $J = 1.3$  Hz, 3H), 6.25 (d,  $J = 1.5$  Hz, 1H), 7.73 (m, 2H), 7.58 (d,  $J = 8.7$  Hz, 1H).  $^{13}\text{C}$  NMR (125 MHz, Chloroform-*d*):  $\delta = 13.69$  (d,  $J = 147.5$  Hz), 18.71, 30.37 (d,  $J = 4.1$  Hz), 84.66 (d,  $J = 8.7$  Hz), 108.97 (d,  $J = 5.1$  Hz), 113.9, 116.8, 117.09 (d,  $J = 4.4$  Hz), 125.68, 151.97, 153.48 (d,  $J = 7.4$  Hz), 154.44, 160.63.  $^{31}\text{P}$  NMR (100 MHz, Chloroform-*d*):  $\delta = 23.55$ . HRMS (TOF ES+): calc. for  $\text{C}_{15}\text{H}_{20}\text{O}_5\text{P}$  ( $\text{M}^+$ ): 311.1048; found: 311.1058.



8.6% yield.  $^1\text{H}$  NMR (500 MHz, Chloroform-*d*):  $\delta = 1.36$  (dd,  $J = 35.8, 6.2$  Hz, 6H), 1.36 (dd,  $J = 35.8, 6.2$  Hz, 6H), 4.81 (m, 1H), 6.75 (s, 1H), 7.31 (m, 2H), 7.73 (d, 1H).

**<sup>13</sup>C NMR (125 MHz, Chloroform-*d*):**  $\delta = 12.38$  (d,  $J = 145.6$  Hz), 23.92 (dd,  $J = 14.3$ , 4.5 Hz), 72.26 (d,  $J = 6.7$  Hz),  $\delta = 109.54$  (d,  $J = 5.1$  Hz), 110.4, 114.77 (q,  $J = 5.8$  Hz), 117.93 (d,  $J = 4.7$  Hz), 121.38 (q,  $J = 275.5$  Hz), 126.6, 141.13 (q,  $J = 33.0$  Hz), 154.22 (d,  $J = 7.8$  Hz), 155.35, 158.56. **<sup>31</sup>P NMR (100 MHz, Chloroform-*d*):**  $\delta = 27.2$ . **<sup>19</sup>F NMR (470 MHz, Chloroform-*d*)**  $\delta = 64.82$ .



7-hydroxyquinoline (145 mg, 0.92 mmol) and methylphosphonic dichloride (175 mg, 1.32 mmol) were dissolved into 5 mL of dry benzene at 0 °C (ice bath) in a septum sealed round bottom flask. Triethyl amine (0.37 mL, 2.6 mmol) was added drop wise to the reaction mixture and the mixture was allowed to warm gradually to room temperature for 2 hours. Dry isopropanol (100  $\mu$ L, 1.3 mmol) was added drop wise to the reaction and allowed to stir overnight. The reaction was diluted with ethyl acetate, gravity filtered, and concentrated in vacuo. The residue was purified by column chromatography (0%-100% isopropanol in ethyl acetate) to give phosphonylated 4-methylumbelliferone as a yellow oil (134.5 mg, 55%). **<sup>1</sup>H NMR (400 MHz, Chloroform-*d*)**  $\delta = 1.35$  (dd,  $J = 27.1$ , 6.0 Hz, 6H), 1.69 (d,  $J = 17.6$  Hz, 3H), 4.89 (dq,  $J = 13.0$ , 6.4 Hz, 1H), 7.41 (m, 1H), 7.54 (d,  $J = 8.9$  Hz, 1H), 7.90 (s, 1H), 7.83 (d,  $J = 8.8$  Hz, 1H), 8.18 (d,  $J = 8.2$  Hz, 1H), 8.94 (s, 1H). **<sup>13</sup>C NMR (100 MHz, Chloroform-*d*)**  $\delta = 12.17$  (d,  $J = 145.3$  Hz), 23.92 (dd,  $J = 15.4$ , 4.4 Hz), 71.76 (d,  $J = 6.7$  Hz), 118.14, 121.91 (d,  $J = 4.1$  Hz), 29.40,

136.32, 148.25, 151.34, 152.53.  $^{31}\text{P}$  NMR (162 MHz,  $\text{CDCl}_3$ )  $\delta$  26.84.  $\text{C}_{13}\text{H}_{17}\text{O}_3\text{NP}$

(M) $^+$ : 266.0927; found: 266.0946

Inhibitor **2F** was synthesized by Dr. Joseph J. Topczewski, post-doctoral associate in the Quinn group.

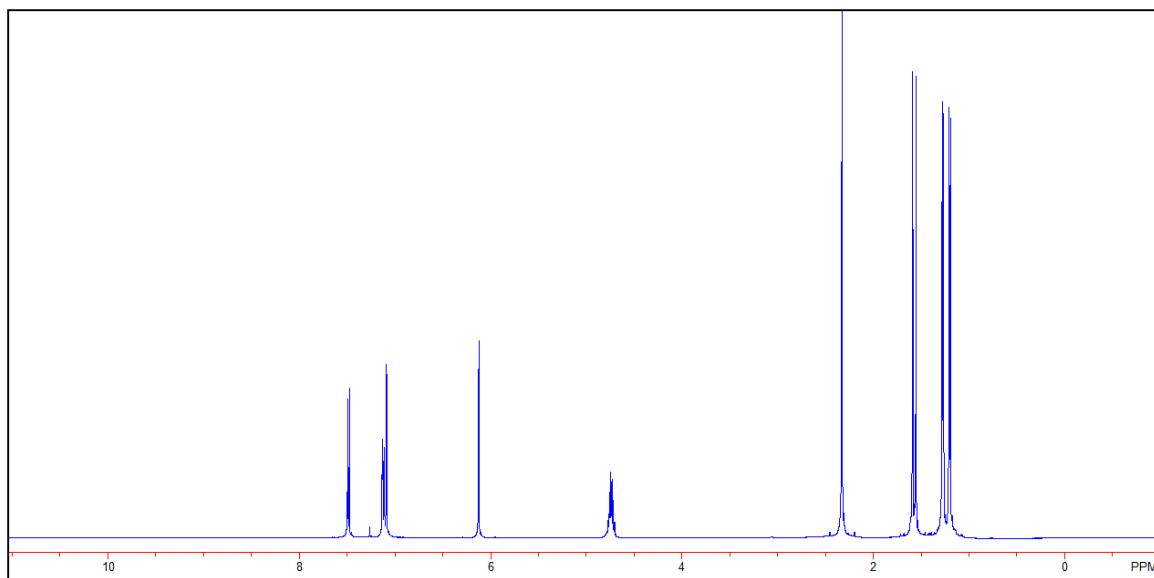


**Figure A1:** 500 MHz  $^1\text{H}$  NMR Spectrum in  $\text{CDCl}_3$  of **2A**

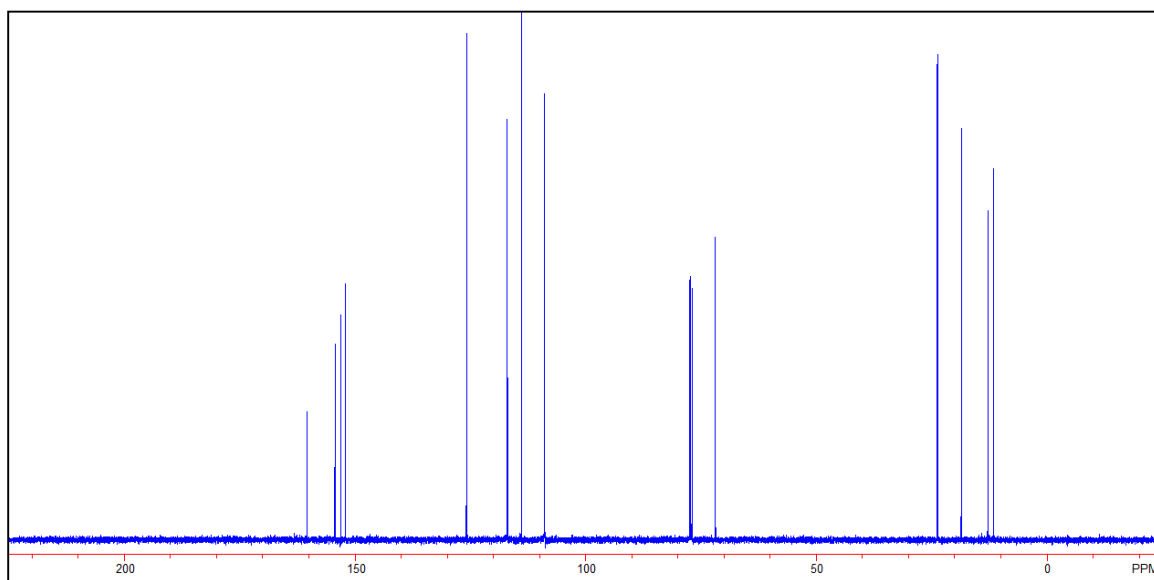


**Figure A2:** 125 MHz  $^{13}\text{C}$  NMR Spectrum in  $\text{CDCl}_3$  of **2A**

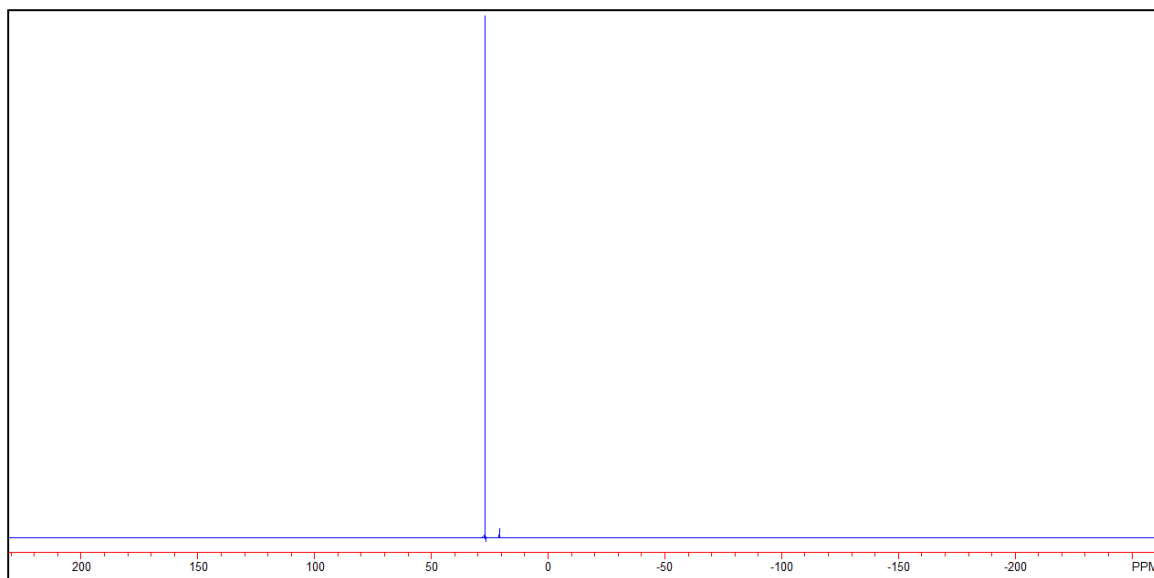


**Figure A3:** 100 MHz  $^{31}\text{P}$  NMR Spectrum in  $\text{CDCl}_3$  of **2A**

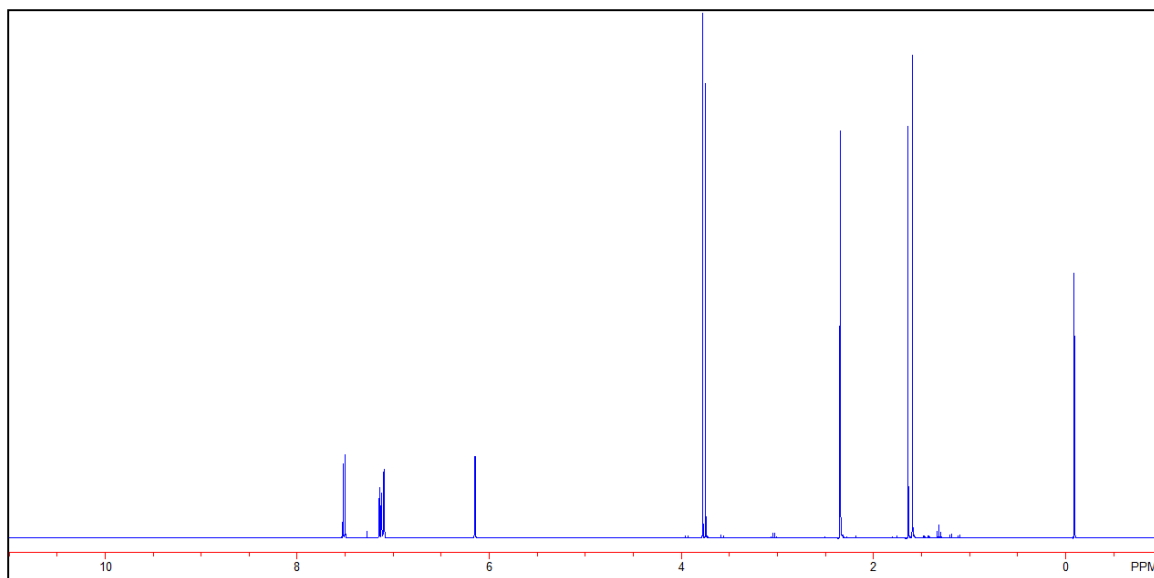


**Figure A4:** 400 MHz  $^1\text{H}$  NMR Spectrum in  $\text{CDCl}_3$  of **2B**

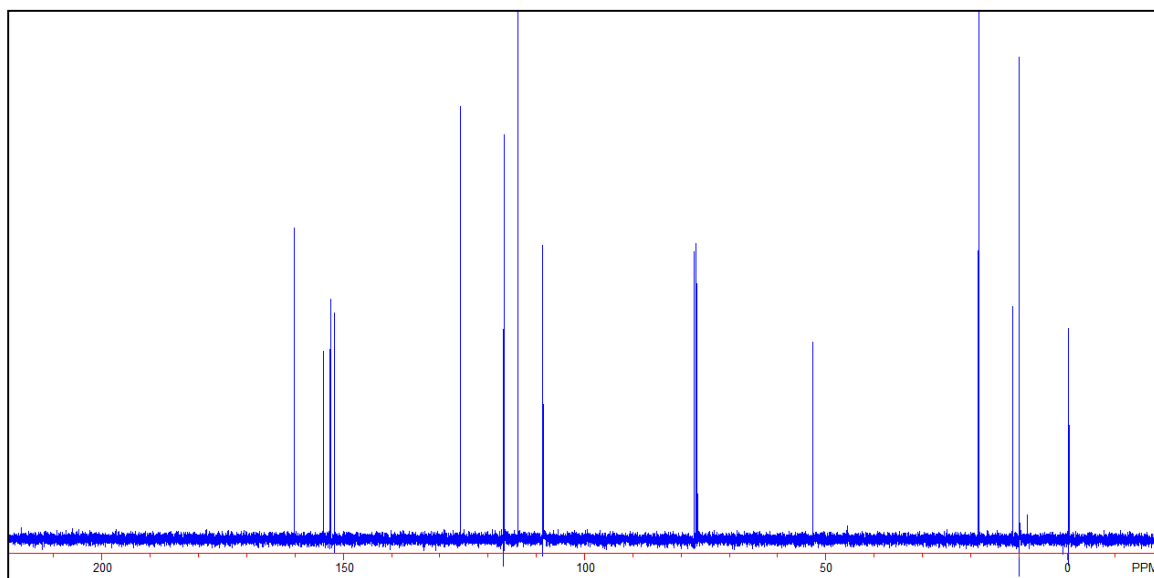


**Figure A5:** 100 MHz  $^{13}\text{C}$  NMR Spectrum in  $\text{CDCl}_3$  of **2B**

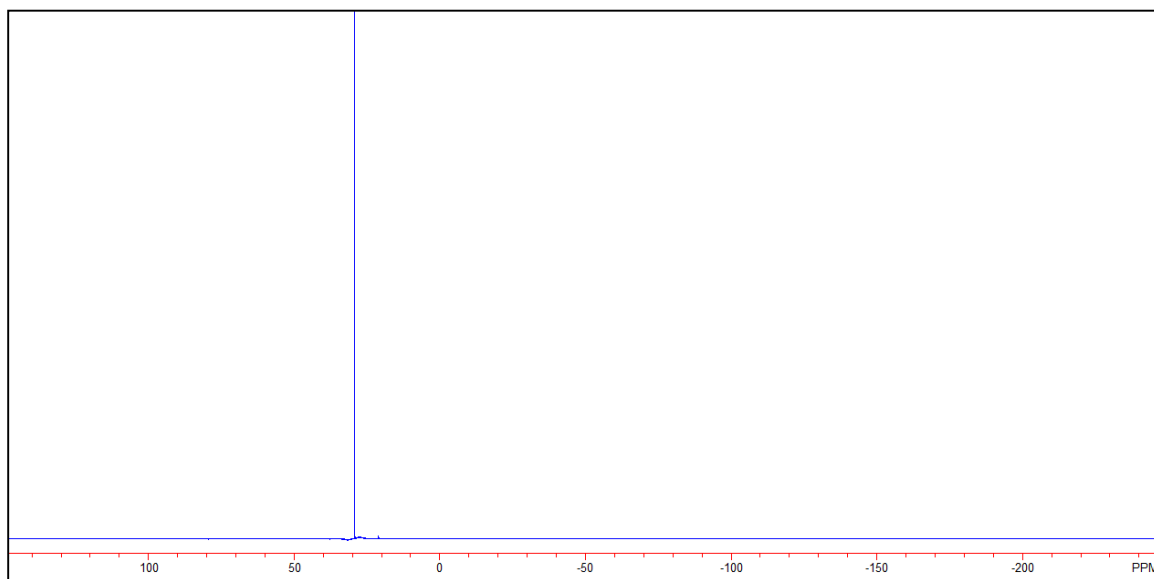


**Figure A6:** 80 MHz  $^{31}\text{P}$  NMR Spectrum in  $\text{CDCl}_3$  of **2B**



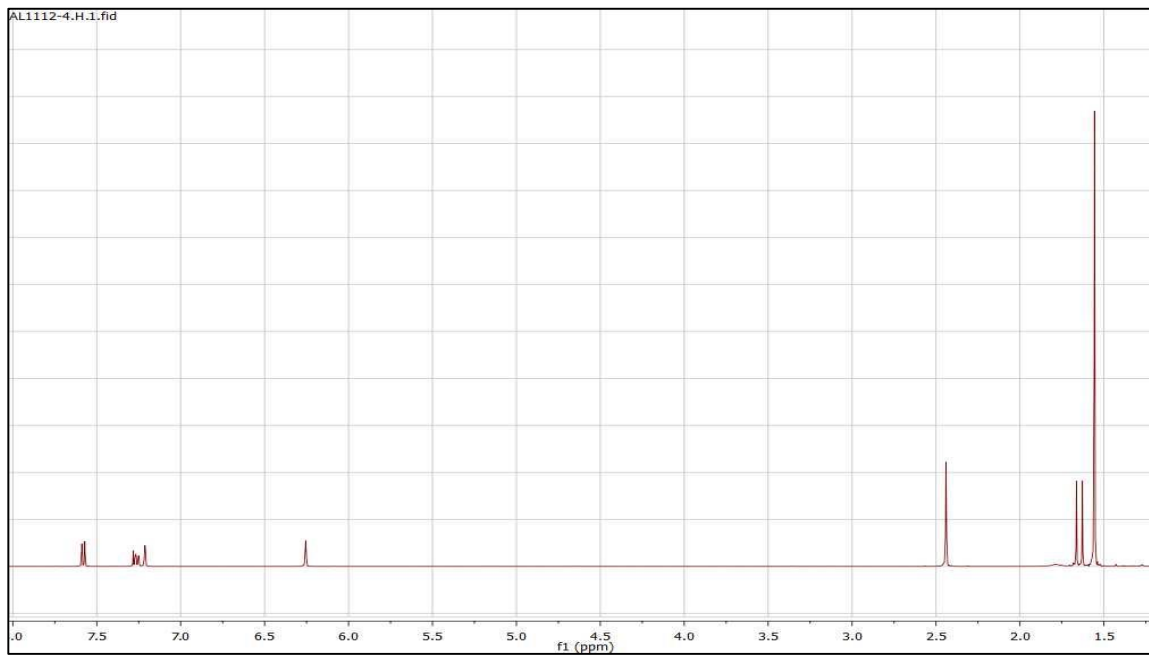


**Figure A7:** 500 MHz <sup>1</sup>H NMR Spectrum in CDCl<sub>3</sub> of **2C**

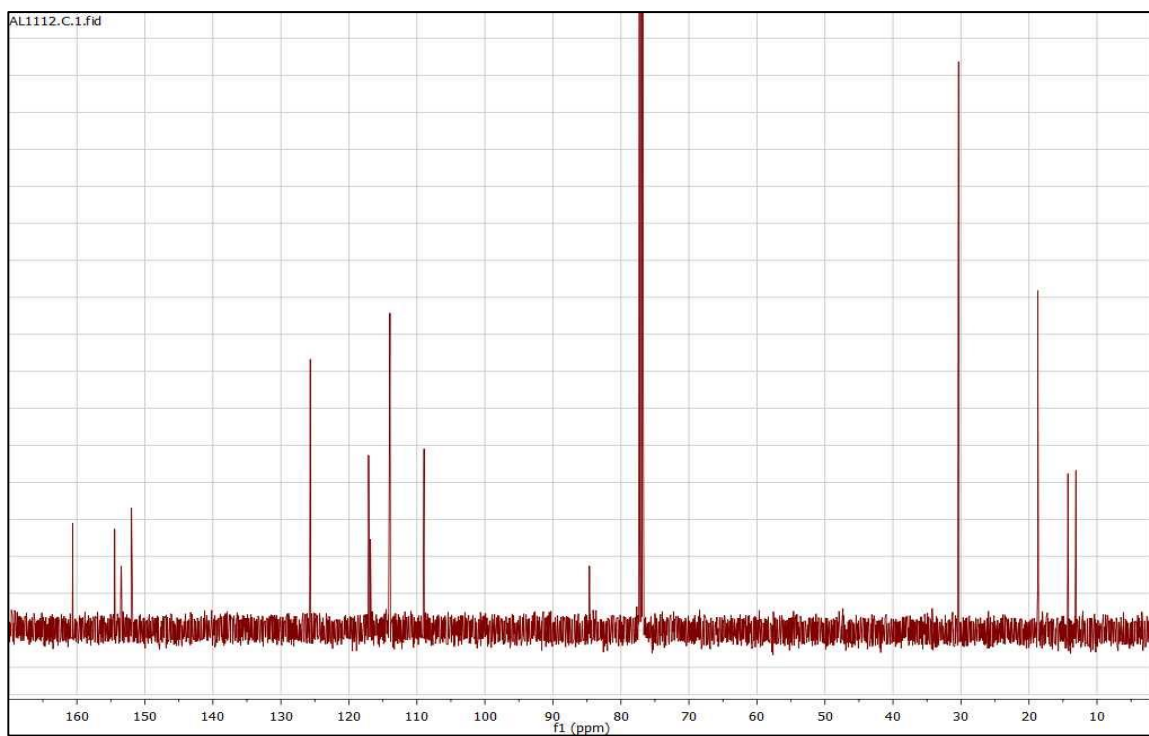


**Figure A8:** 125 MHz <sup>13</sup>C NMR Spectrum in CDCl<sub>3</sub> of **2C**

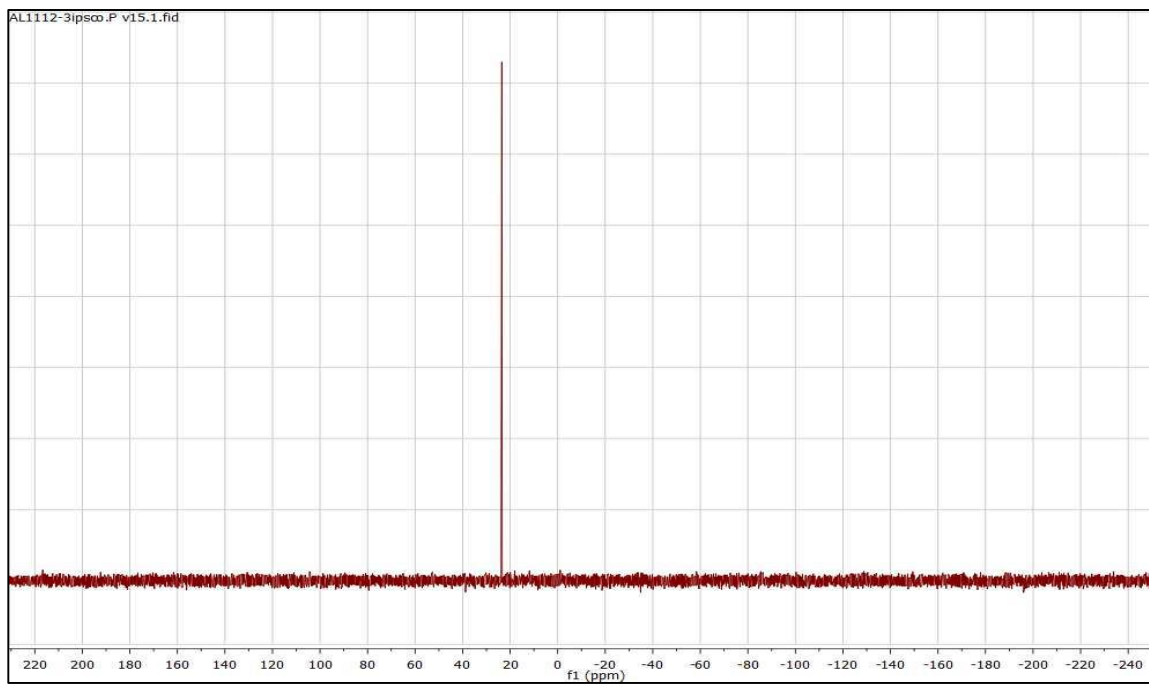


**Figure A9:** 100 MHz  $^{31}\text{P}$  NMR Spectrum in  $\text{CDCl}_3$  of **2C**

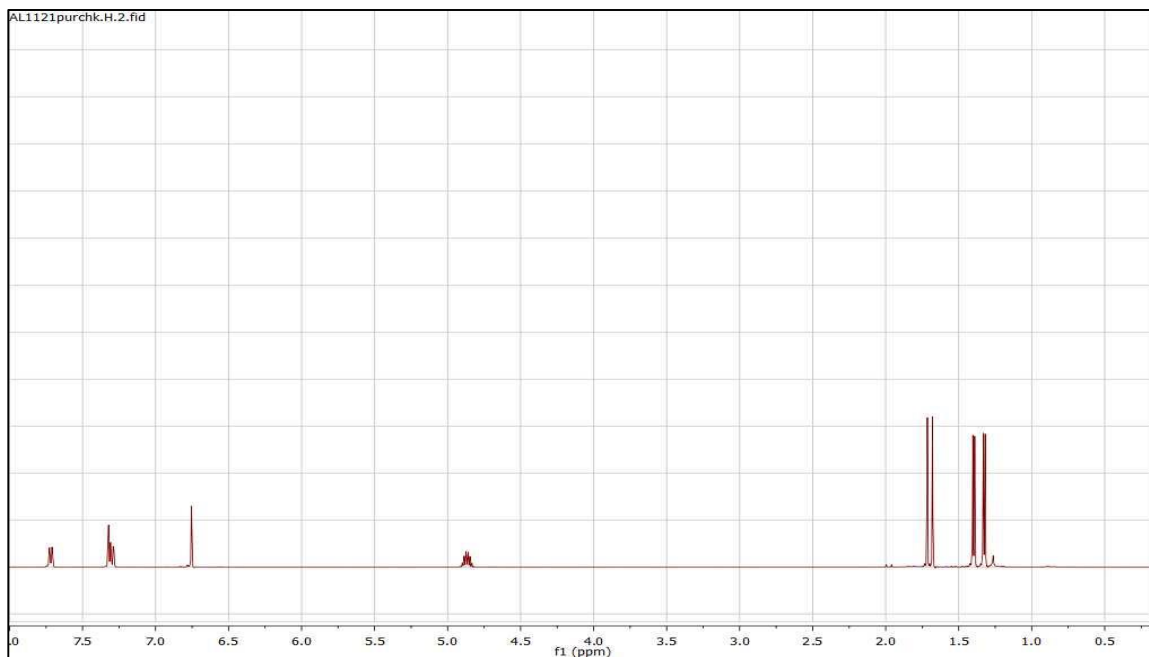


**Figure A10:** 500 MHz <sup>1</sup>H NMR Spectrum in CDCl<sub>3</sub> of **2D**

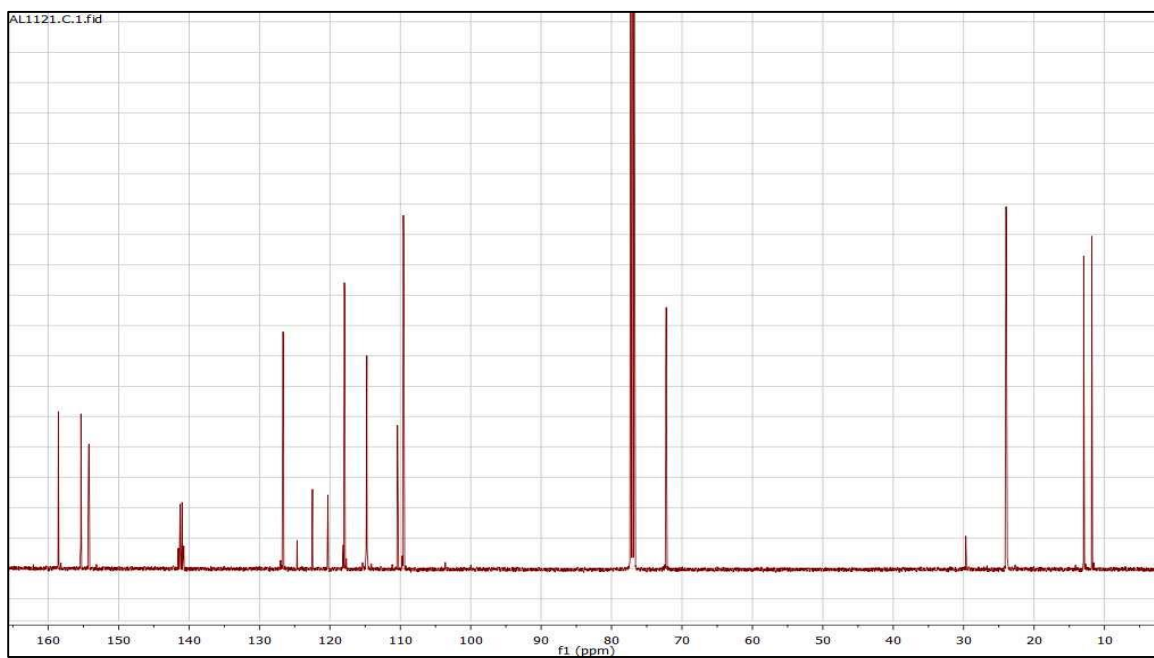


**Figure A11:** 125 MHz <sup>13</sup>C NMR Spectrum in CDCl<sub>3</sub> of **2D**

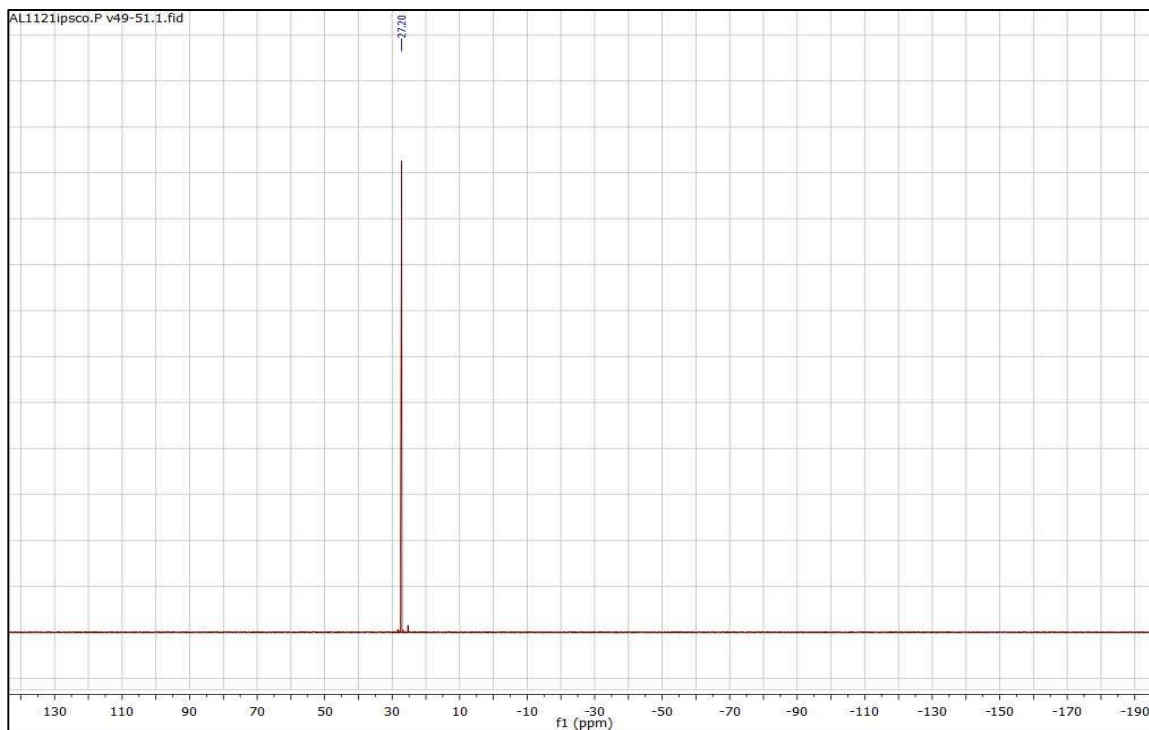


**Figure A12:** 100 MHz  $^{31}\text{P}$  NMR Spectrum in  $\text{CDCl}_3$  of **2D**

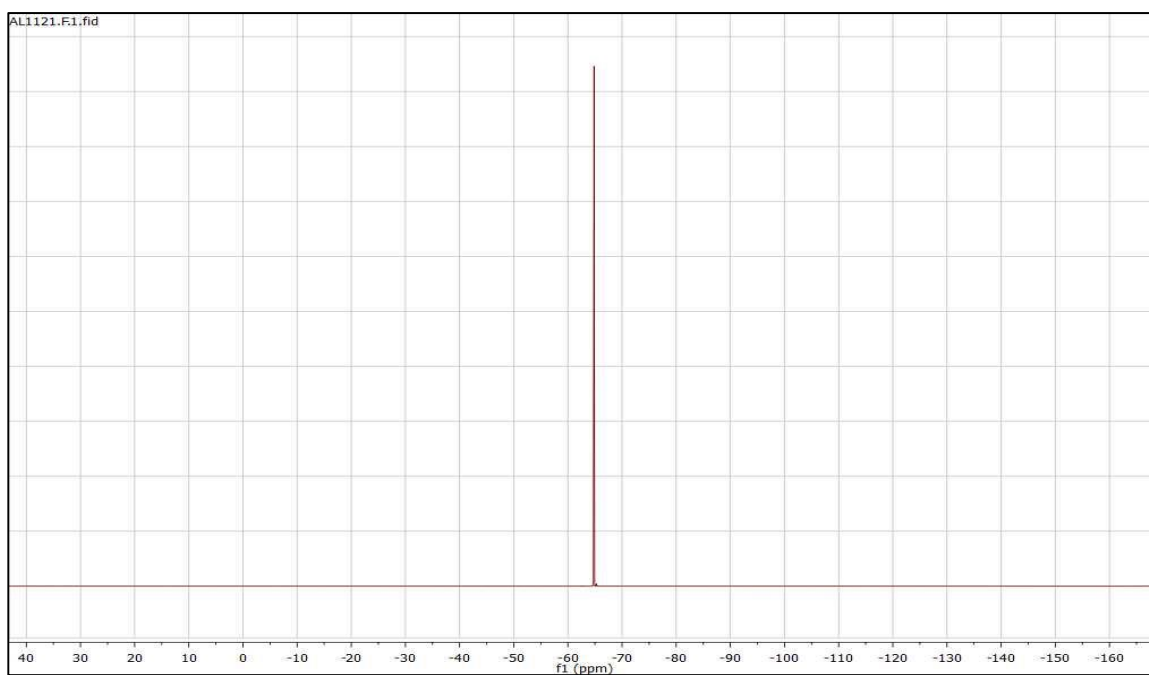


**Figure A13:** 470 MHz  $^{19}\text{F}$  NMR Spectrum in  $\text{CDCl}_3$  of **2D**

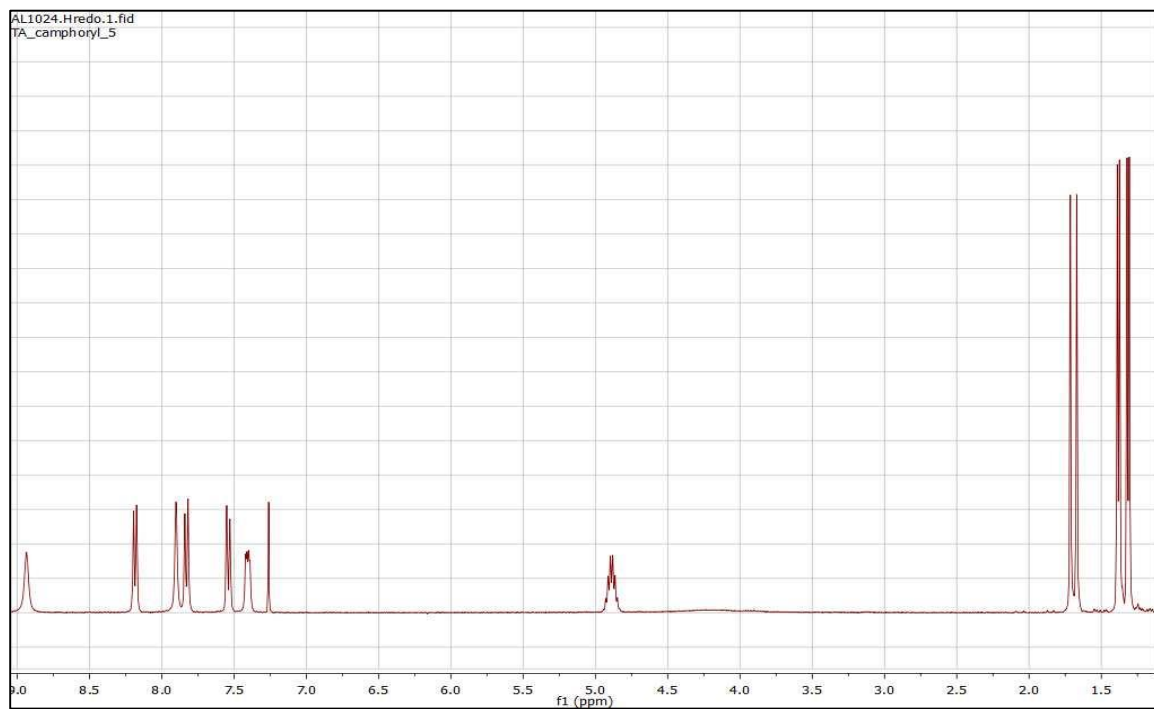


**Figure A14:** 400 MHz  $^1\text{H}$  NMR Spectrum in  $\text{CDCl}_3$  of **2E**

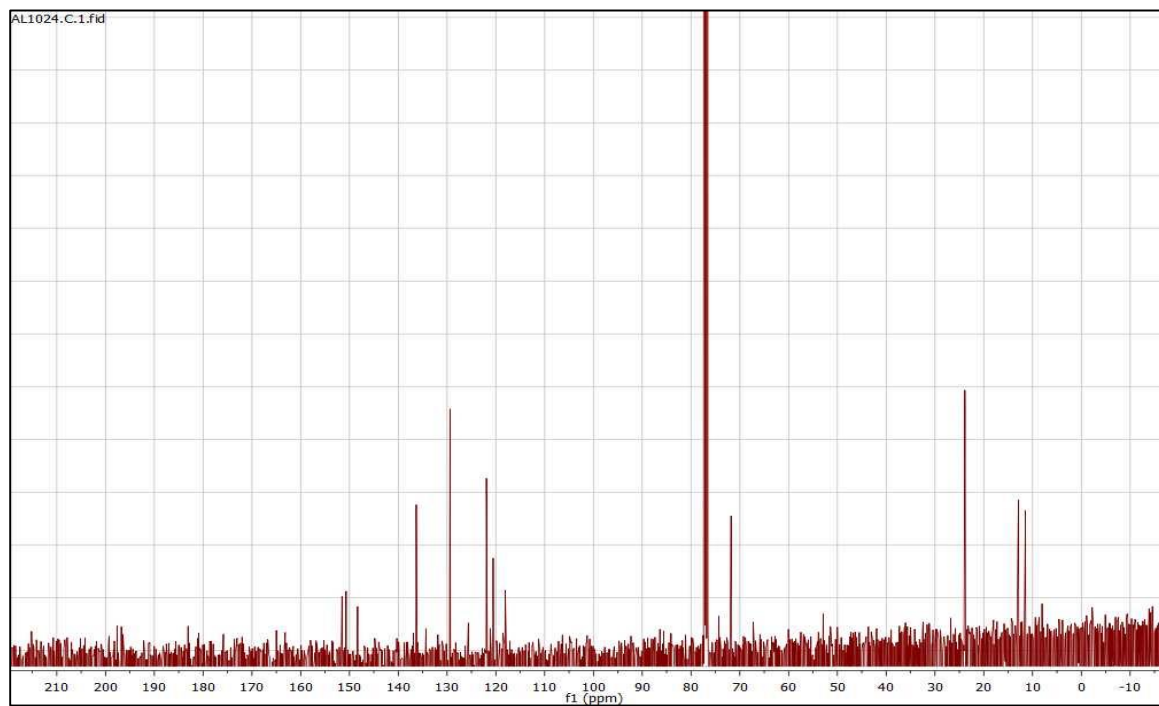


**Figure A15:** 100 MHz  $^{13}\text{C}$  NMR Spectrum in  $\text{CDCl}_3$  of **2E**

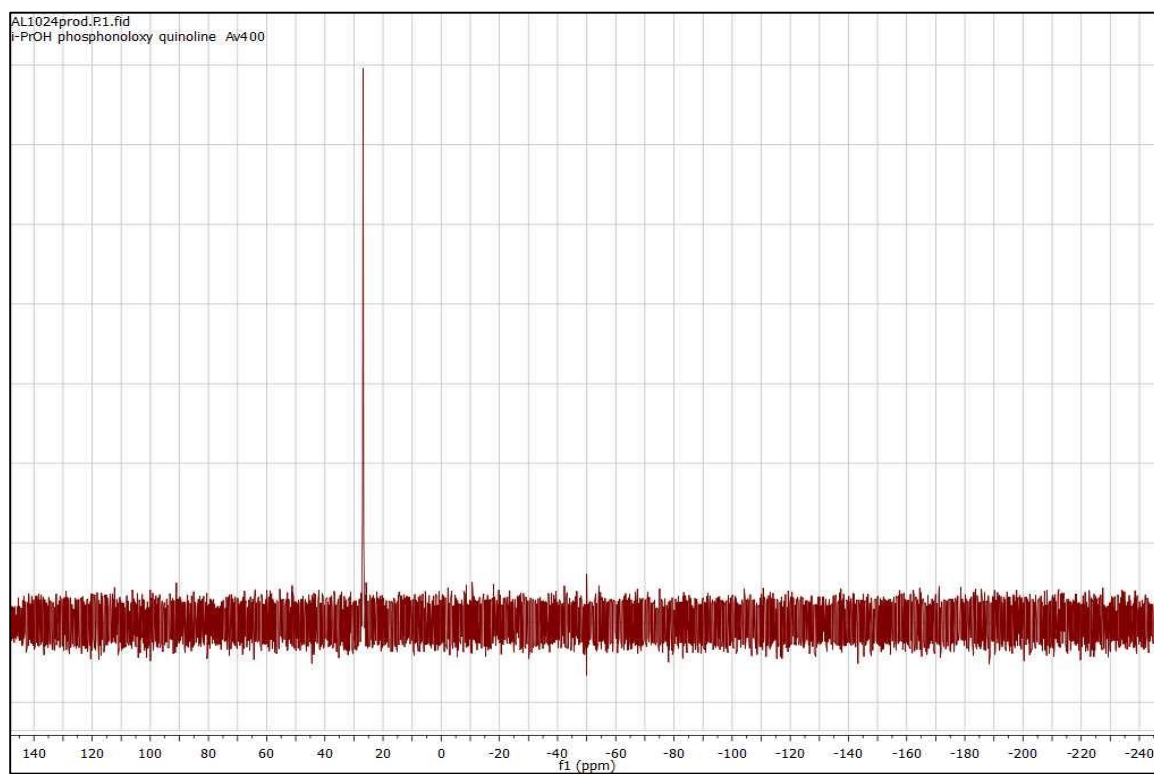


**Figure A16:** 80 MHz  $^{31}\text{P}$  NMR Spectrum in  $\text{CDCl}_3$  of **2E**

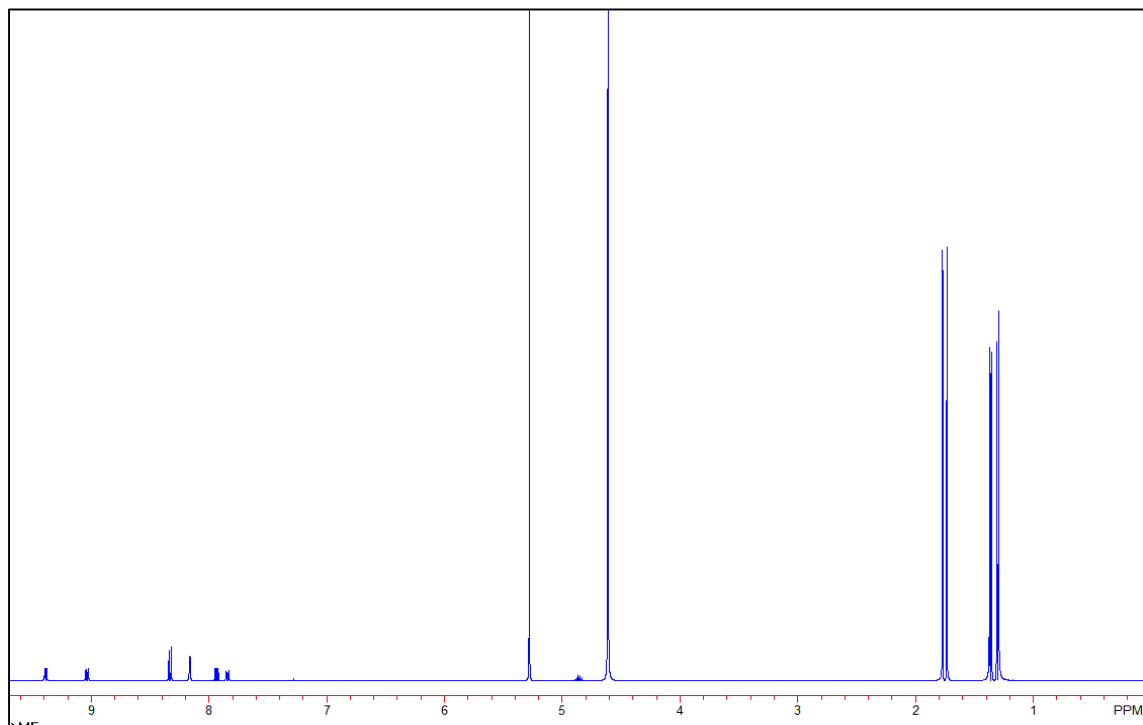


**Figure A17:** 500 MHz  $^1\text{H}$  NMR Spectrum in  $\text{CDCl}_3$  of **2F**

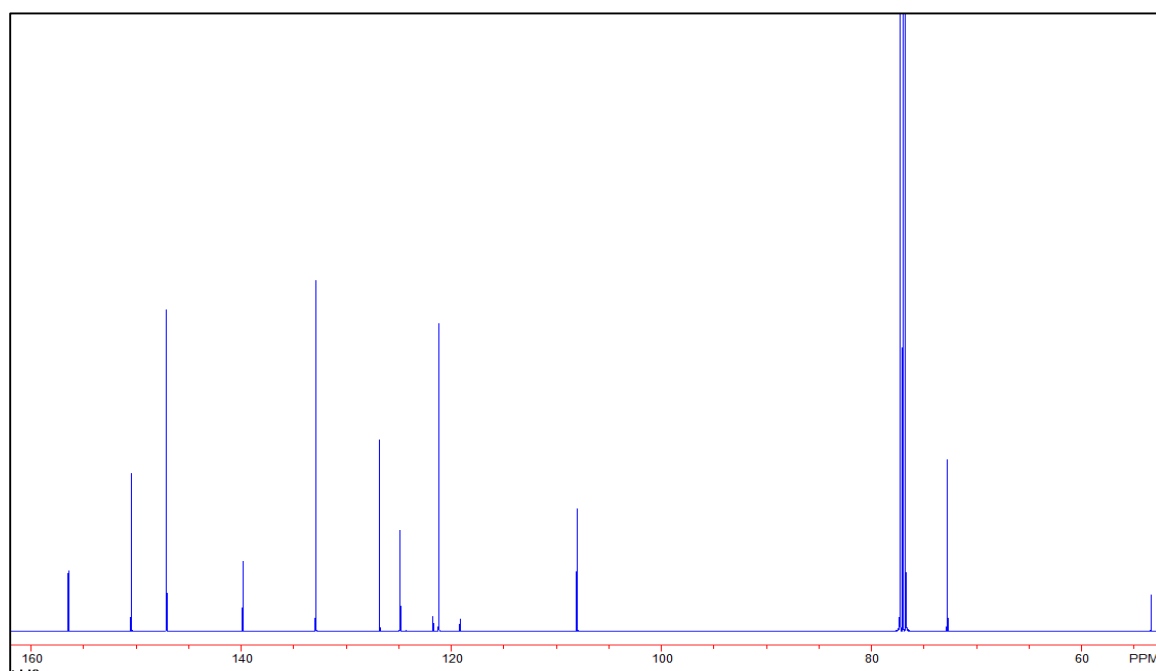


**Figure A18:** 125 MHz  $^{13}\text{C}$  NMR Spectrum in  $\text{CDCl}_3$  of **2F**

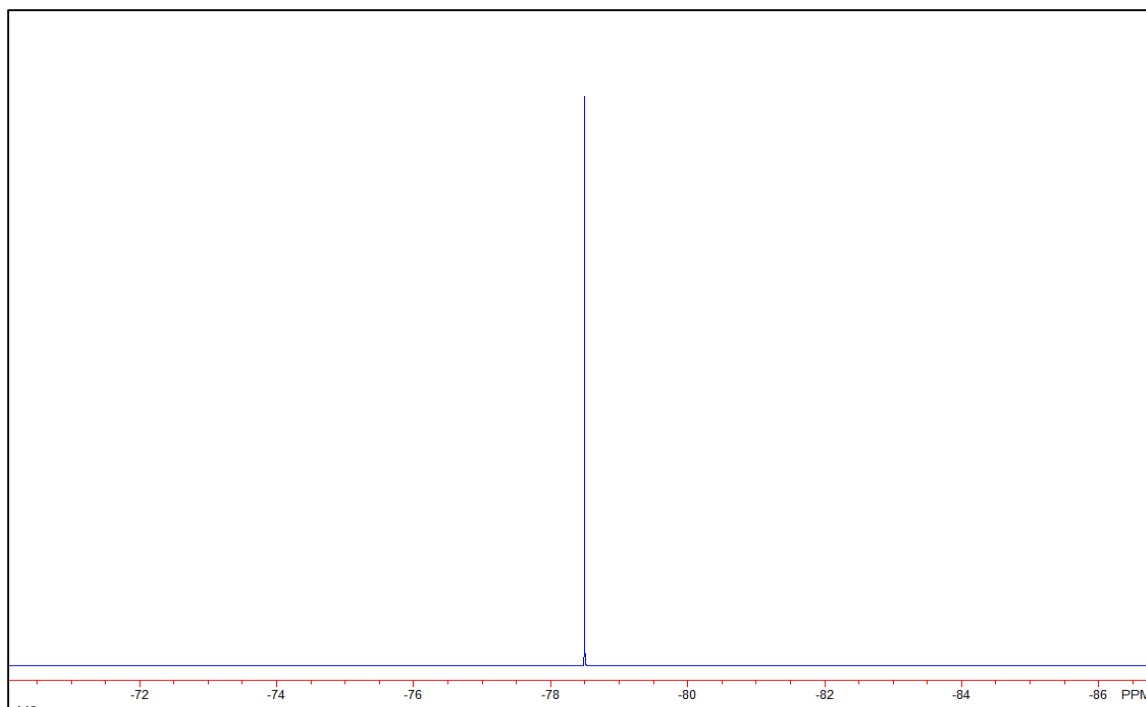


**Figure A19:** 470 MHz  $^{19}\text{F}$  NMR Spectrum in  $\text{CDCl}_3$  of **2F**



APPENDIX B  
DETAILED ENZYME ASSAY PROCEDURE AND SUPPORTING INFORMATION  
FOR RESURRECTION ASSAY

Materials and General Methods

All reagents were purchased from a commercial vendor in the highest purity available and were used without further purification unless otherwise stated.

Recombinant human acetylcholinesterase (*hAChE*), acetylthiocholine iodide (ATCh), 5,5'-dithiobis(2-nitro benzoic acid) (DTNB), and 2-PAM were obtained from Sigma-Aldrich. All solvents were either used as received or dried over molecular sieves where noted.

Assay solutions were prepared using distilled deionized water (DD-H<sub>2</sub>O) filtered through a Barnstead International hose nipple organic removal ion exchange cartridge. Alternatively, solutions were prepared in acetonitrile for inhibitors with limited water solubility. Phosphate buffer solutions were prepared in bulk and had a pH ranging from 7.28 – 7.32 as measured by an ion selective pH electrode, which was calibrated prior to every use. Unless otherwise stated, 50 mM phosphate buffer was used throughout this study. Stock solutions were prepared from solid material and stored in polypropylene containers at -4 °C as follows: 0.1% w/v bovine serum albumin (BSA) prepared in 50 mM phosphate buffer, 0.1 mg/1 mL *hAChE* in 0.1% BSA solution, 45 mM ATCh in DD-H<sub>2</sub>O, 20 mM DTNB in phosphate buffer, and 3 mM 2-PAM in DD-H<sub>2</sub>O. Inhibitor solutions were prepared in methanol, acetonitrile, or DD-H<sub>2</sub>O, or as otherwise specified. Dilutions were made by micropipette and all solutions were diluted with the same

solvents as their parent stock. To reduce the number of pipette manipulations, stock DTNB was diluted into 50 mM phosphate buffer to prepare 0.5 mM DTNB solutions, which were used for IC<sub>50</sub> determination assays.

Assays were performed on Molecular Devices SpectraMax M2 or SpectraMax384Plus micro-plate readers on polystyrene 96-well plates (Costar, round bottom). Centrifugation was conducted on a Beckman Coulter Allgera X-30 centrifuge. Measurements of *hAChE* activity were conducted spectrophotometrically at 412 nm following the assay method of Ellmann et al. (24). The activity of *hAChE* was assayed at 27 °C and was measured at the minimum time intervals allowed by the instrument for 10 min. All assays were conducted in duplicate or triplicate. Initial rates ( $v_i$ , mA/min) were calculated by least-squares analysis of the time courses at less than 10% turnover of the initial substrate concentration. Non-linear regression analyses were conducted in SigmaPlot 12.0. Enzyme separations were conducted on Sephadex G-50 Quick Spin Columns (Roche) which were pre-equilibrated with buffer (0.1% BSA, 50 mM phosphate) and packed by centrifugation at 1100 x *g* for 4 min prior to use.

#### IC<sub>50</sub> Determination for Alkyl-transfer (Resurrection Assay) Compounds

All alkyl-transfer compounds assayed were synthesized by Joseph J. Topczewski, S. Nilanthi Yasapla, Pedrom M. Keshavarzi, or Jacob Freuh in the Quinn research group of the University of Iowa-Department of Chemistry. Compounds with limited water solubility were dissolved in acetonitrile. Working solutions were prepared for use in biological assay using calibrated micropipettes in identical solvent as parent stock.

Time dependent inhibition was measured at the minimum possible interval over 10 min durations at each incubation time point and performed in duplicate.  $K_i^{app}$  values were calculated by fitting  $v_i$  as a function of inhibitor concentration to equation B1:

$$v_i = \frac{v_o}{1 + \frac{10^{\log[I]}}{K_i^{app}}}$$

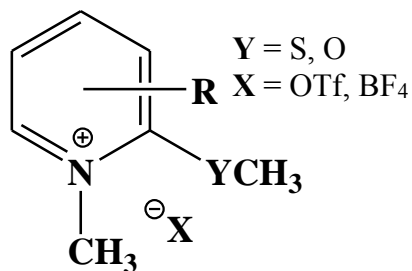
**Equation B1:** Initial rate equation for inhibited AChE hydrolysis of ATCh.  $v_i$   $\equiv$  initial rate (mA/min);  $v_o$   $\equiv$  rate of uninhibited reaction (mA/min);  $[I]$   $\equiv$  inhibitor concentration;  $K_i^{app}$   $\equiv$  apparent inhibitor dissociation constant (M)

From the  $K_i^{app}$ ,  $IC_{50}$  values were calculated using equation B2:

$$IC_{50} = \frac{K_i^{app}}{1 + \frac{[A]}{K_m}}$$

**Equation B2:** Equation describing the half maximal inhibitor concentration ( $IC_{50}$ , M).  $K_i^{app}$   $\equiv$  apparent inhibitor dissociation constant (M);  $K_m$   $\equiv$  Michaelis constant (M);  $[S]$   $\equiv$  substrate concentration (M).

### *Methoxy Methyl Pyridiniums*



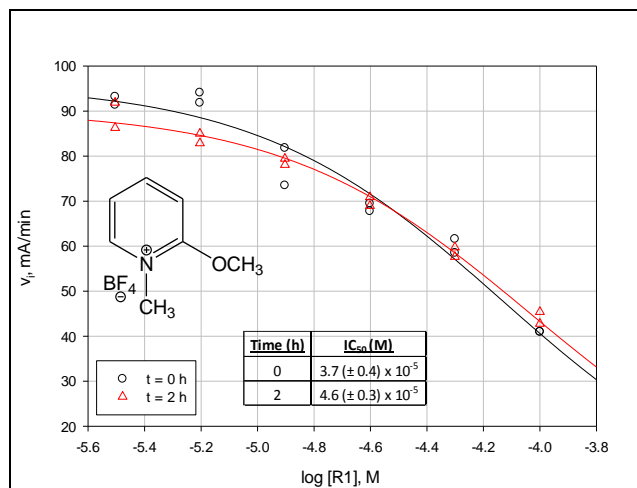


**Figure B1:** Dose Response plot for R1 (3-100  $\mu\text{M}$ )

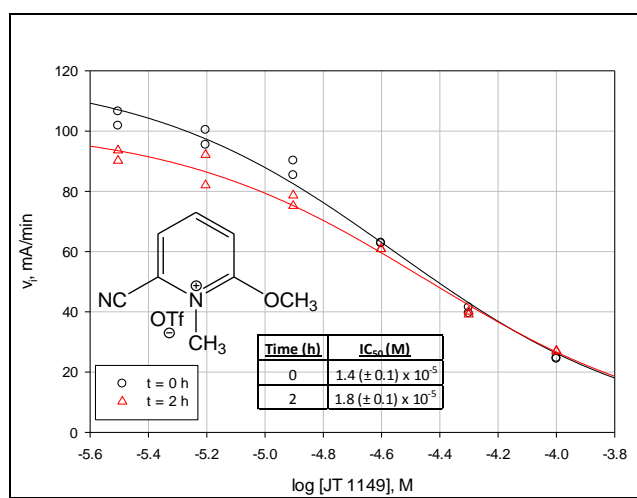


**Figure B2:** Dose Response Plot for R2 (3-100  $\mu\text{M}$ )

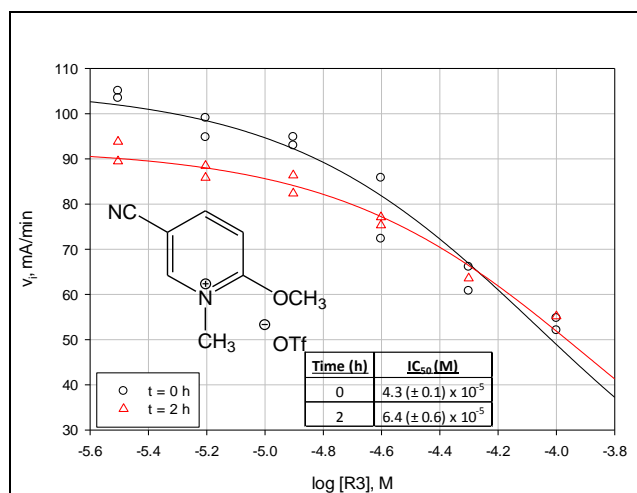


**Figure B3:** Dose Response plot for **R3** (3-100  $\mu$ M)

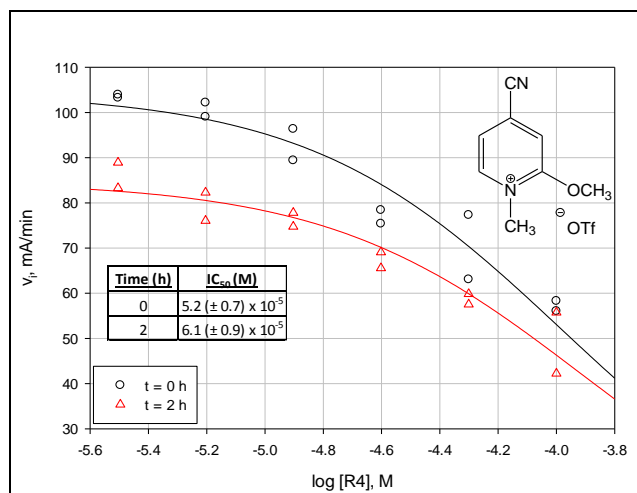


**Figure B4:** Dose Response plot for **R4** (3-100  $\mu$ M)

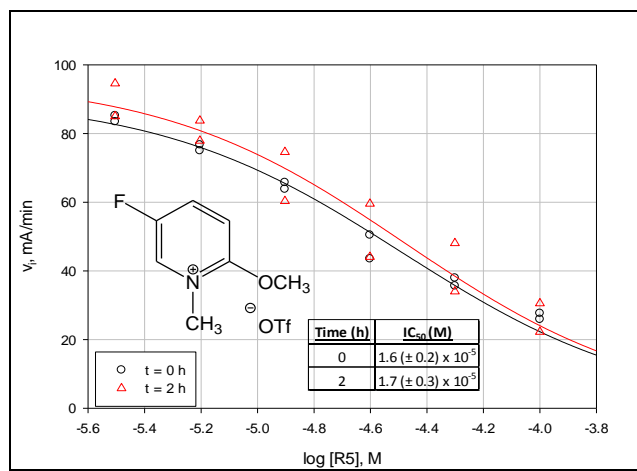


**Figure B5:** Dose Response plot for **R5** (3-100  $\mu\text{M}$ )

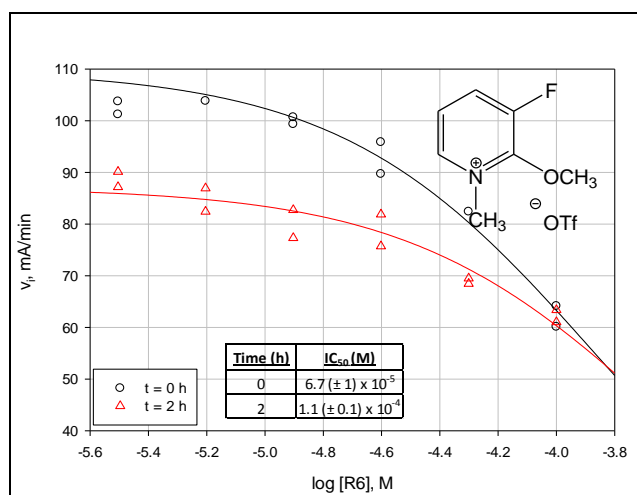


**Figure B6:** Dose Response plot for **R6** (3-100  $\mu\text{M}$ )

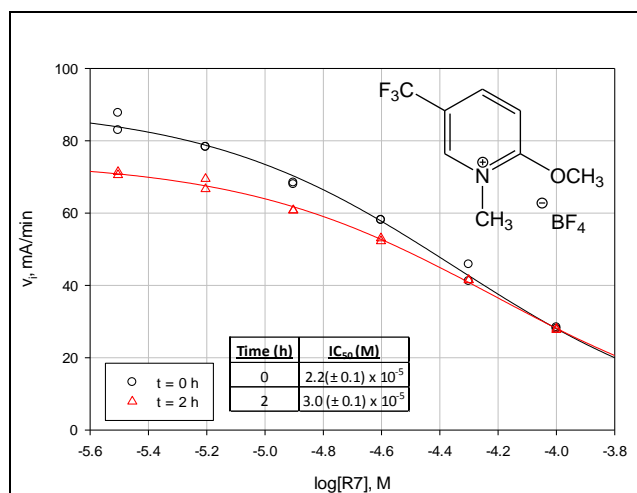


Figure B7: Dose Response plot for R7 (3-100  $\mu\text{M}$ )

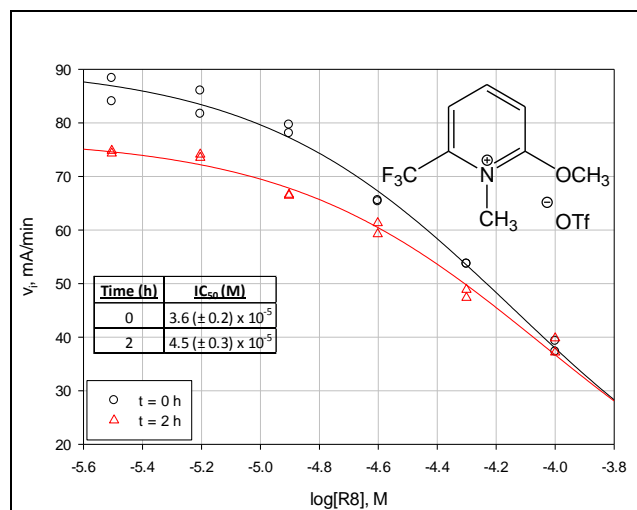
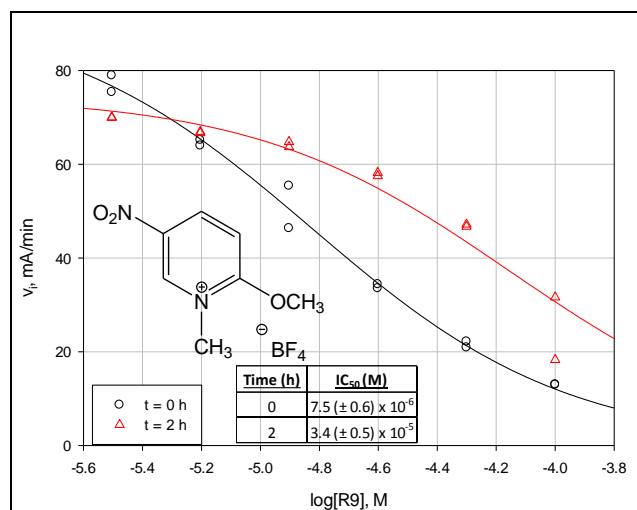
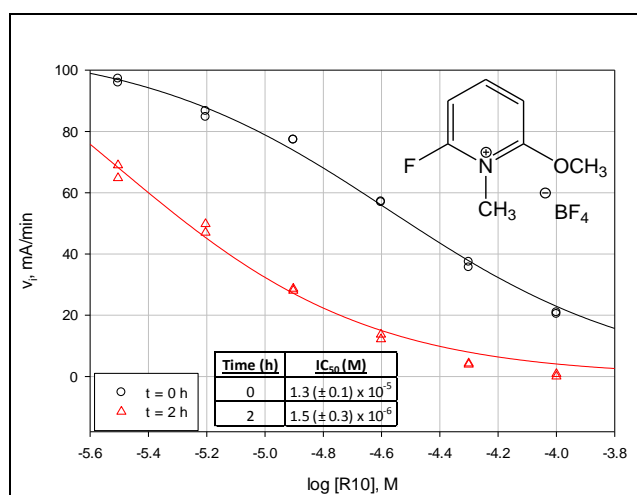


Figure B8: Dose Response plot for R8 (3-100  $\mu\text{M}$ )



**Figure B9:** Dose Response plot for R9 (3-100  $\mu\text{M}$ )



**Figure B10:** Dose Response plot for R10 (3-100  $\mu\text{M}$ )



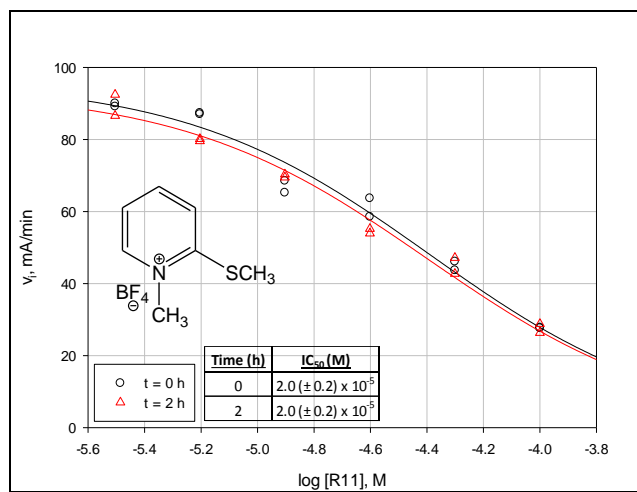


Figure B11: Dose Response plot for R11 (3-100  $\mu\text{M}$ )

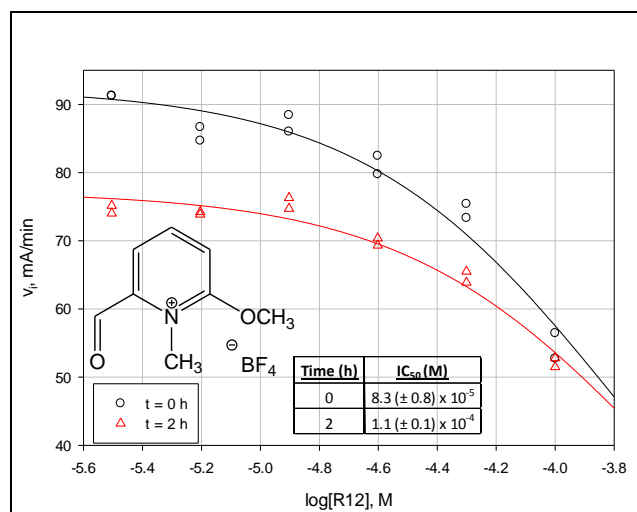
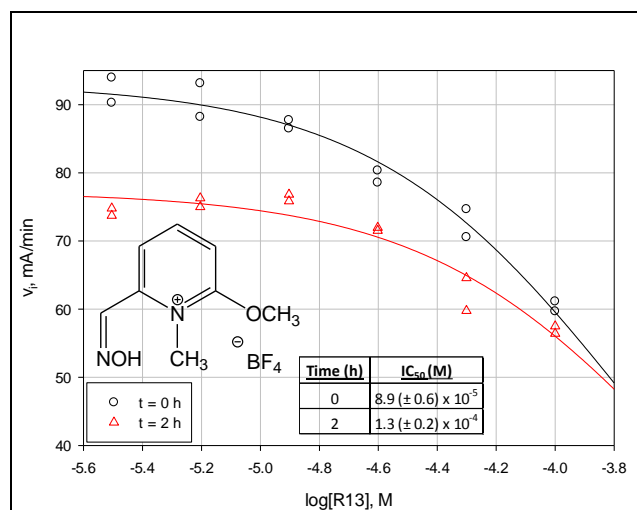
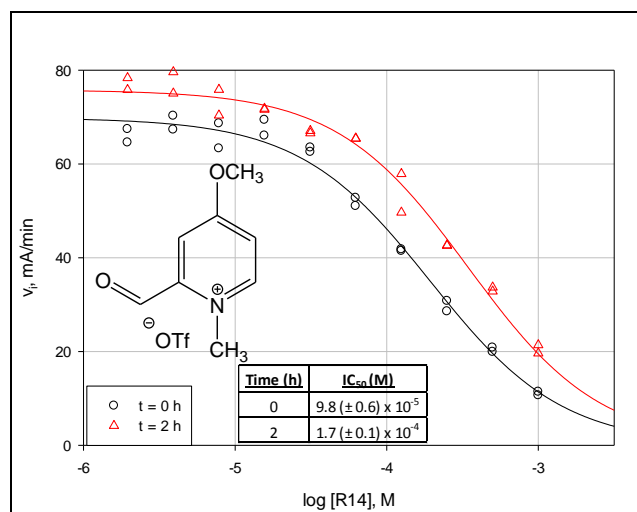


Figure B12: Dose Response plot for R12 (3-100  $\mu\text{M}$ )



**Figure B13:** Dose Response plot for **R13** (3-100  $\mu\text{M}$ )



**Figure B14:** Dose Response plot for **R14** (2  $\mu\text{M}$ -1 mM)

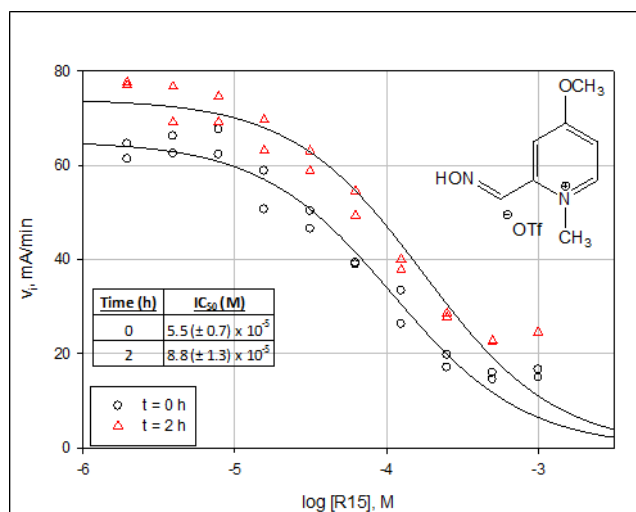


**Figure B15:** Dose Response plot for **R15** (2  $\mu$ M-1 mM)

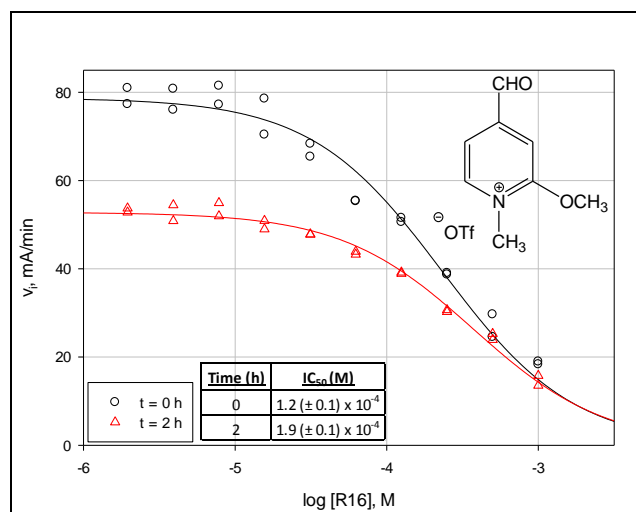


**Figure B16:** Dose Response plot for **R16** (2  $\mu$ M-1 mM)

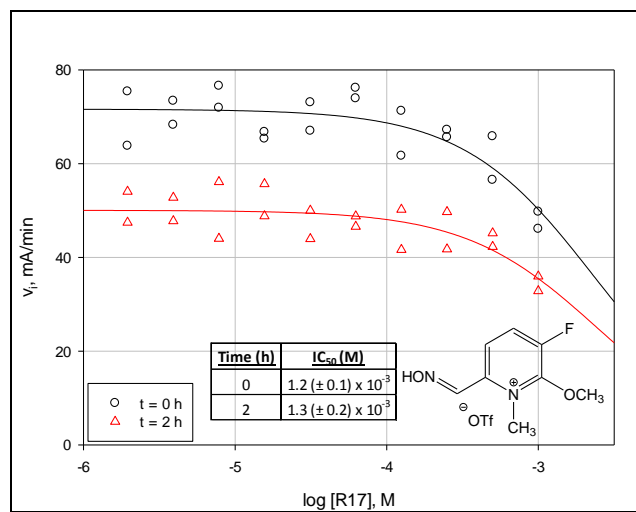


Figure B17: Dose Response plot for R17 (2  $\mu$ M-1 mM)

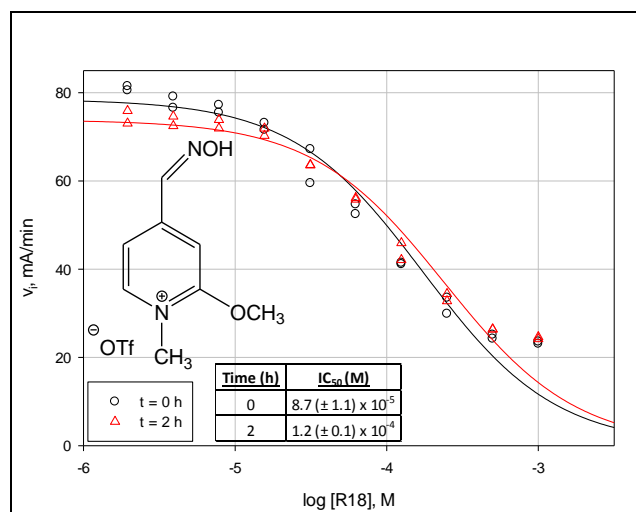
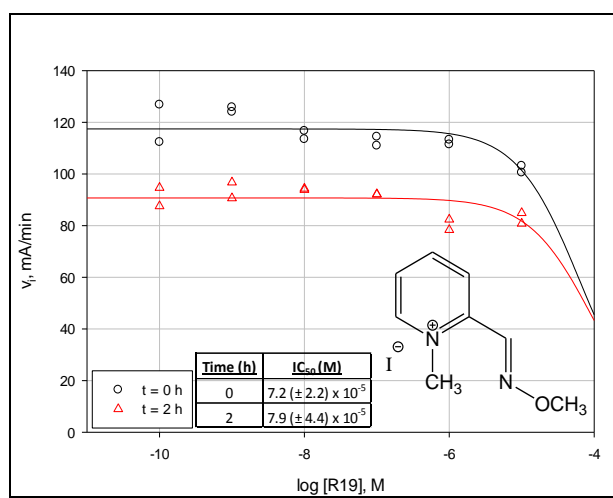
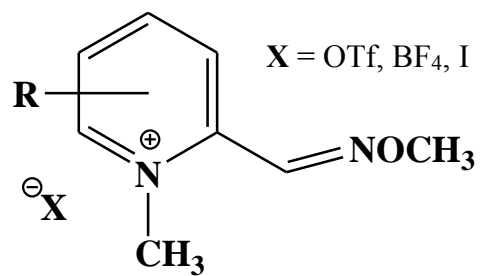
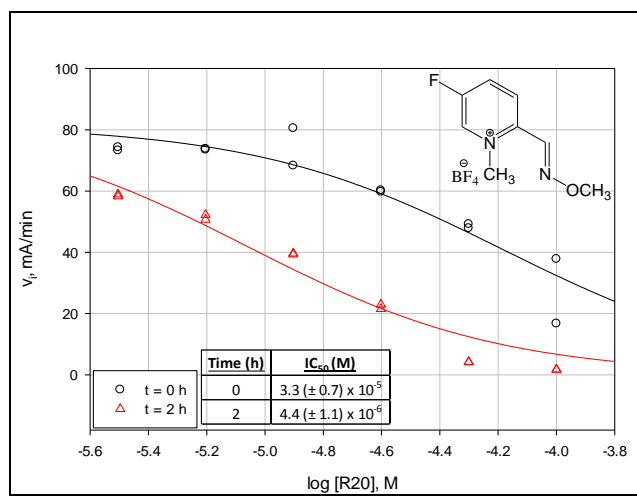


Figure B18: Dose Response plot for R18 (2  $\mu$ M- 1 mM)

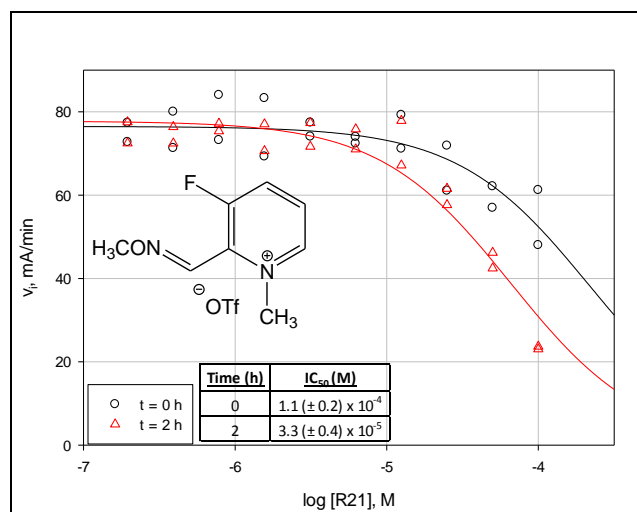
## 2-PAM Analogues



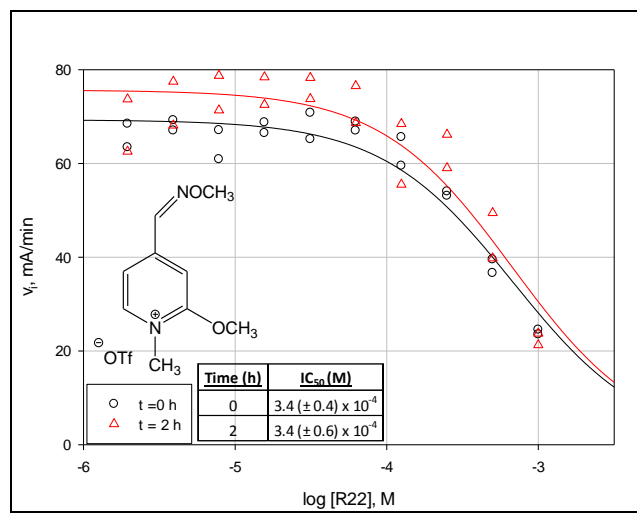
**Figure B19:** Dose Response plot for **R19** (3-100  $\mu\text{M}$ )



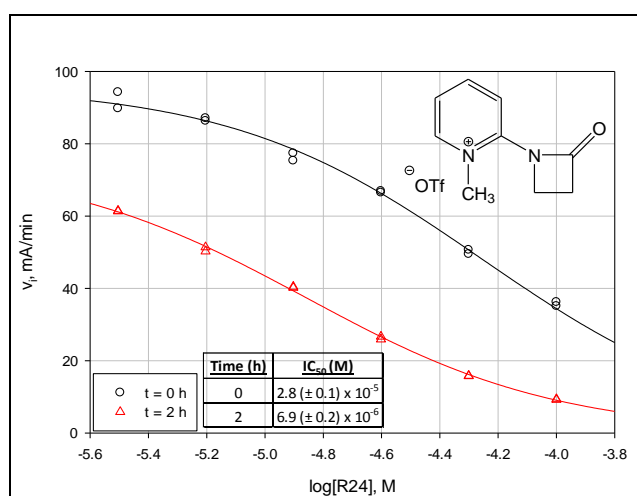
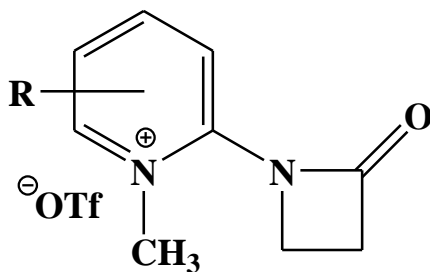
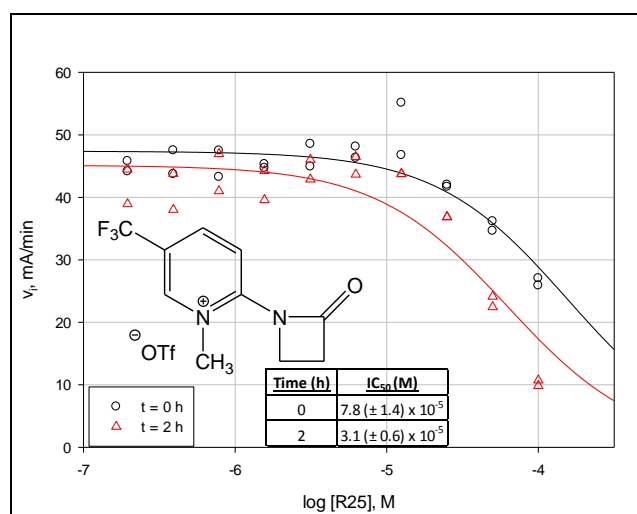
**Figure B20:** Dose Response plot for **R20** (3-100  $\mu\text{M}$ )



**Figure B21:** Dose Response plot for **R21** (0.2-100  $\mu\text{M}$ )



**Figure B22:** Dose Response plot **R22** (2  $\mu$ M-1 mM)

Pyridinium  $\beta$ -LactamsFigure B23: Dose Response plot for R24 (3-100  $\mu$ M)Figure B24: Dose Response plot for R25 (0.2-100  $\mu$ M)



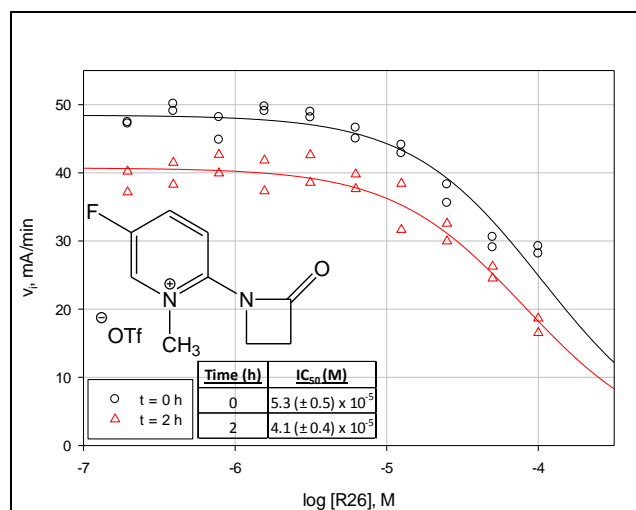


**Figure B25:** Dose Response plot for **R26** (0.2-100  $\mu$ M)

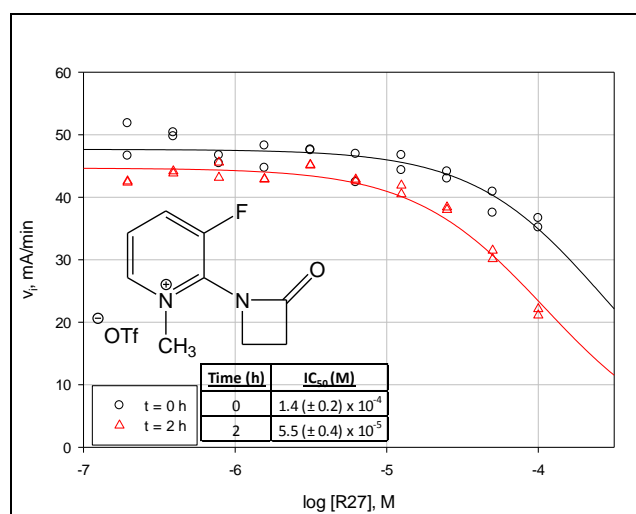


**Figure B26:** Dose Response plot for **R27** (0.2-100  $\mu$ M)

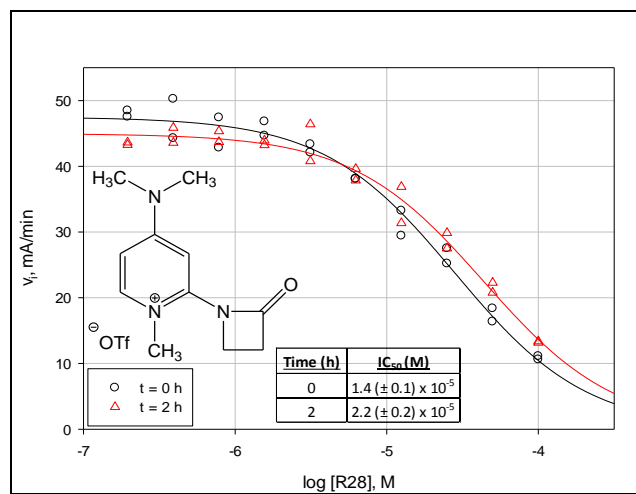


Figure B27: Dose Response plot for R28 (0.2-100  $\mu$ M)

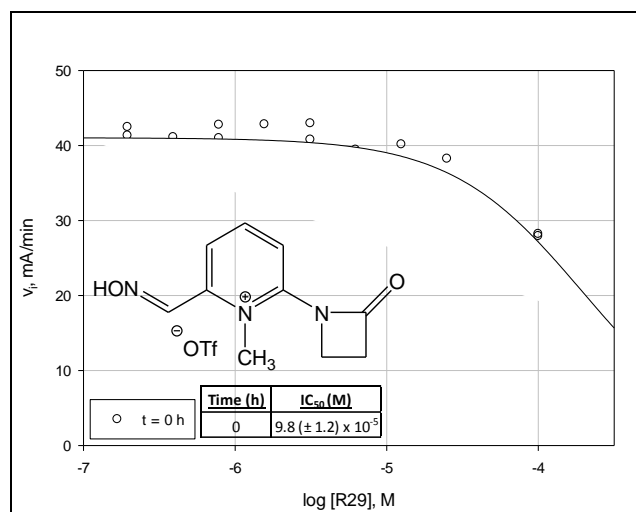
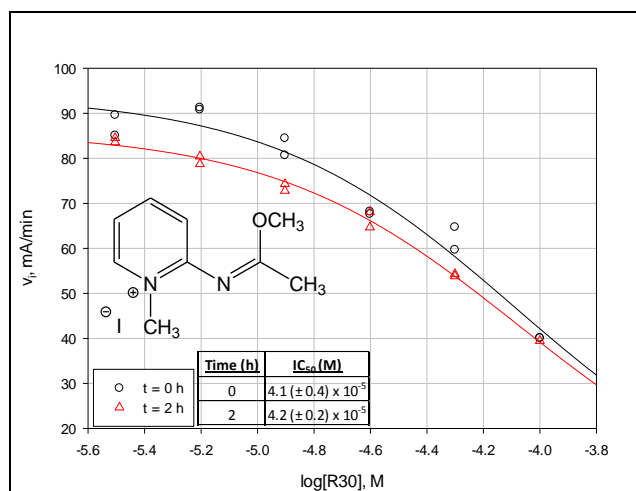


Figure B28: Dose Response plot for R29 (0.2-100 $\mu$ M)

*Additional Aromatic Alkylating Compounds*

IC<sub>50</sub> values for compounds R33-R35 were determined by S. Nilanthi Yasapala of the Quinn research group at the University of Iowa-Department of Chemistry.



**Figure B29:** Dose Response plot for **R30** (3-100  $\mu$ M)

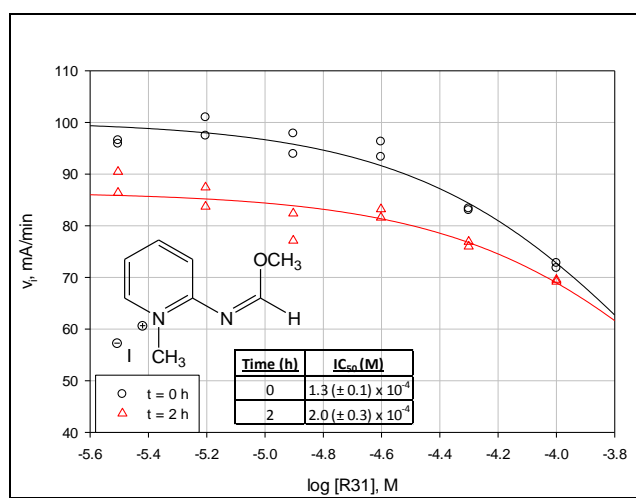


**Figure B30:** Dose Response plot for **R31** (3-100  $\mu$ M)

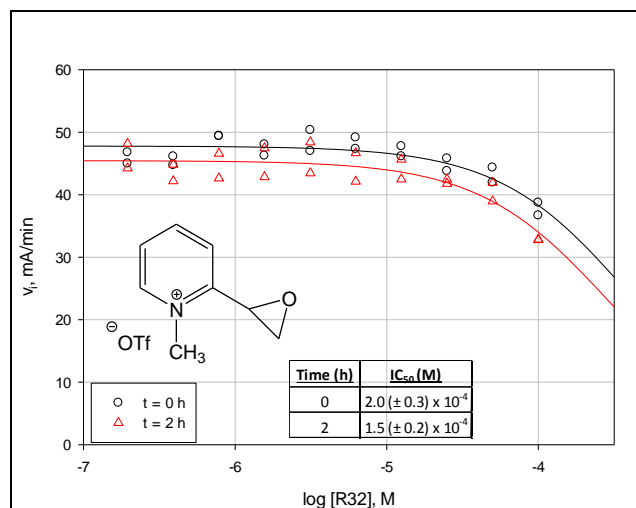
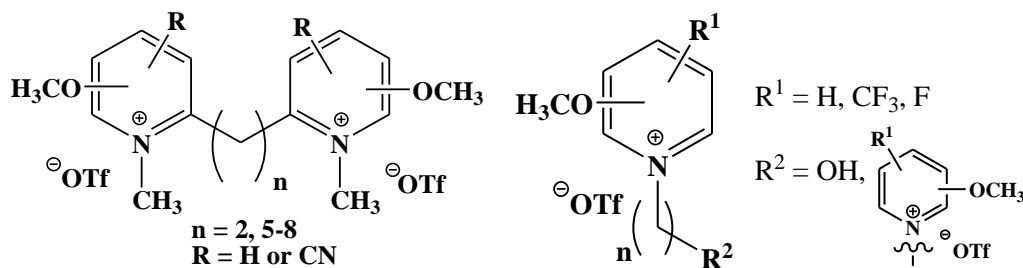


**Figure B31:** Dose Response plot for **R32** (0.2-100  $\mu$ M)

### *Mono/Bis-pyridinium Gorge-Spanning Compounds*

Class I compounds are methyl pyridinium gorge-spanning compounds tethered by an aliphatic linker covalently bound ortho to the heterocyclic nitrogen. Class II compounds are gorge-spanning pyridiniums tethered by an aliphatic linker covalently bound to the heterocyclic nitrogen. IC<sub>50</sub> values for compounds R36-R40 and R46 determined by Joseph J. Topczewski, Maurice K. Payne, or S. Nilanthi Yasapala of theQuinn research group at the University of Iowa-Department of Chemistry.



**Class I**

**Class II**

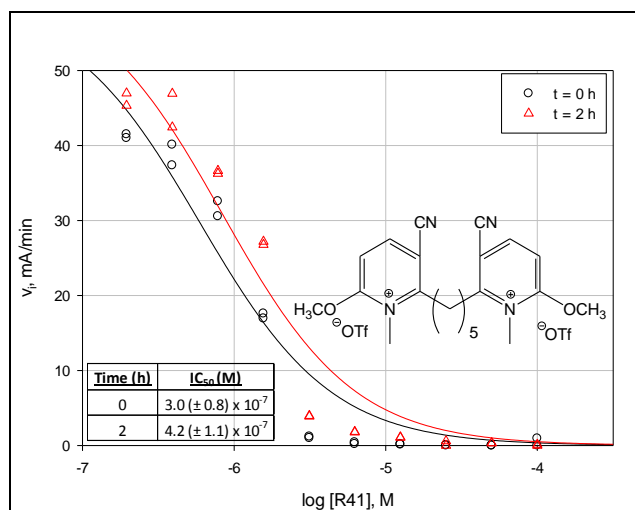


Figure B32: Dose Response plot for **R41** (0.2-100  $\mu$ M)

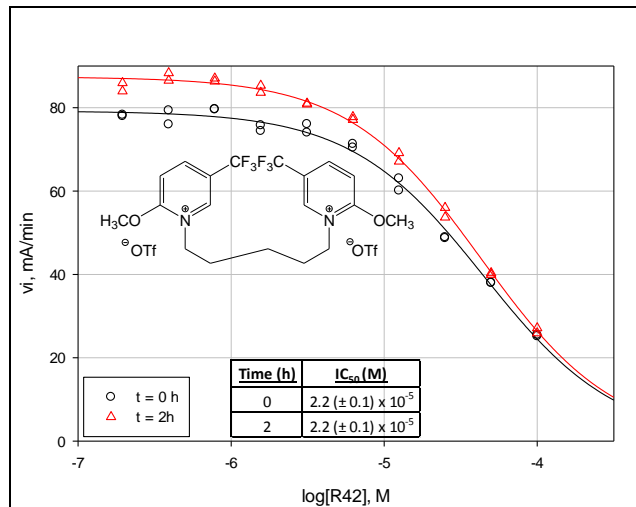


Figure B33: Dose Response plot for **R42** (0.2-100  $\mu$ M)

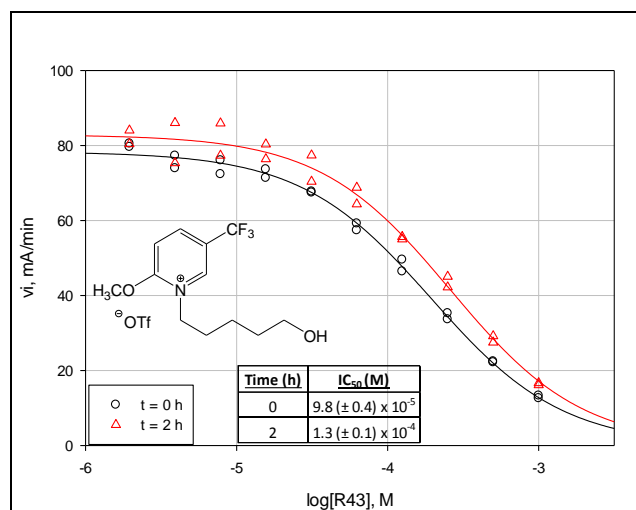


Figure B34: Dose Response plot for R43 (2  $\mu$ M-1 mM)

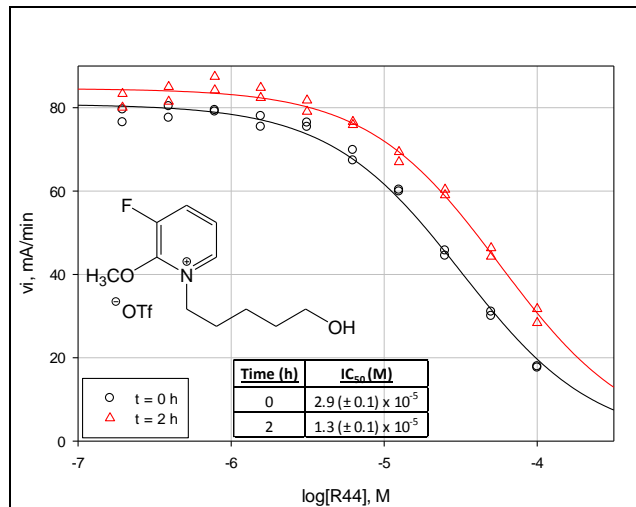
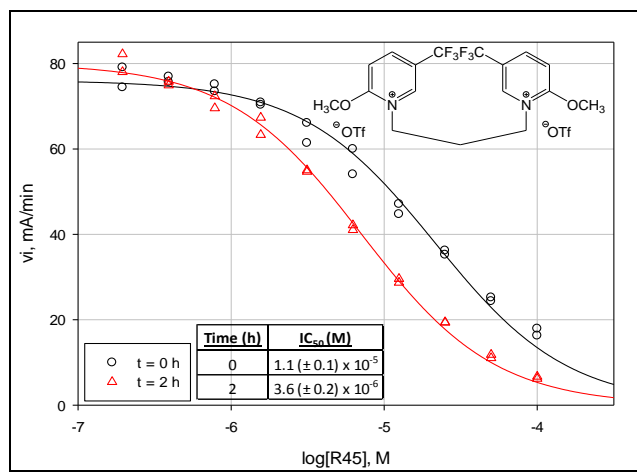


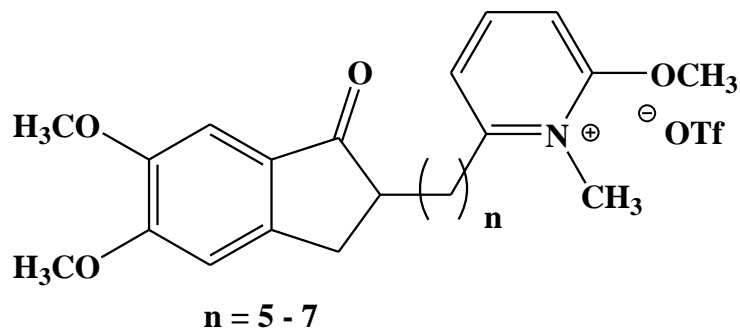
Figure B35: Dose Response plot for R44(0.2-100  $\mu$ M)



**Figure B36:** Dose Response plot for **R45** (0.2-100  $\mu$ M)

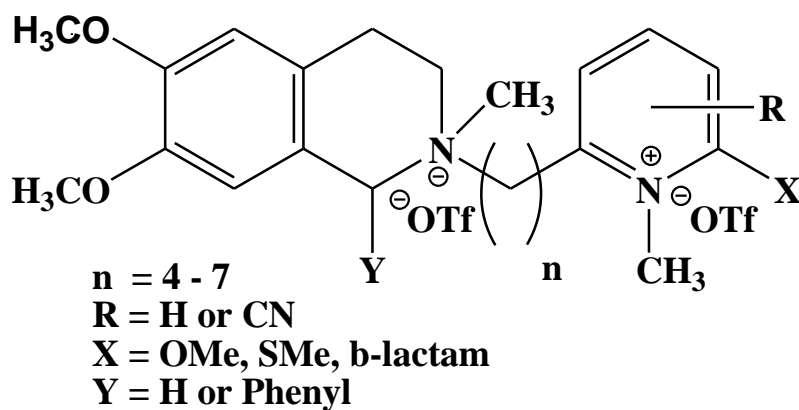
*Aricept Core/ Pyridinium Gorge-Spanning Compounds*

IC<sub>50</sub> values for compounds R47-R50 were determined by Joseph J. Topczewski of the Quinn research group at the University of Iowa-Department of Chemistry.



*Sharpless Core-Pyridinium Gorge Spanning Compounds*

IC<sub>50</sub> values for compounds R52 and R57-R59 were determined by Joseph J. Topczewski of the Quinn research group at the University of Iowa-Department of Chemistry. This family of compounds also consists of un-quaternized and mono-quaternary structures.





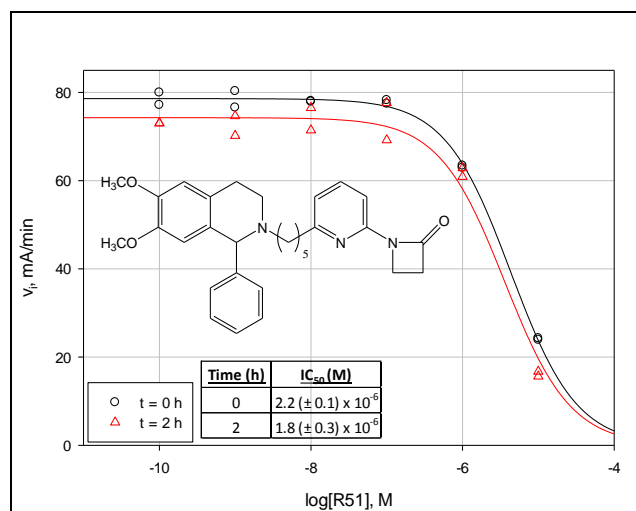


**Figure B37:** Dose Response plot for **R51** (1 nM-10  $\mu$ M)

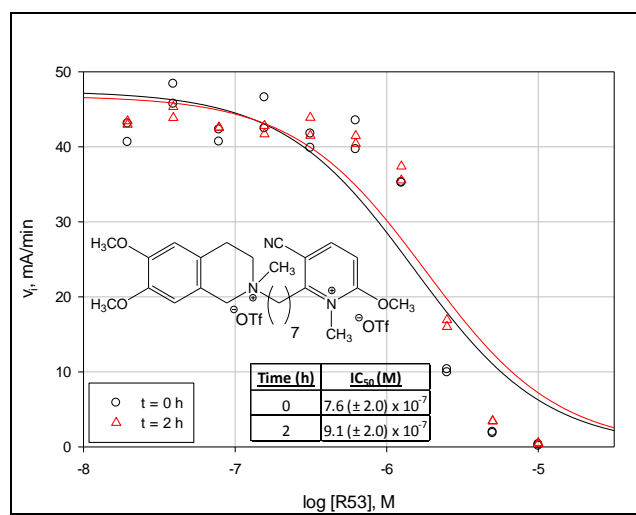


**Figure B38:** Dose Response plot for **R53** (20 nM-10  $\mu$ M)

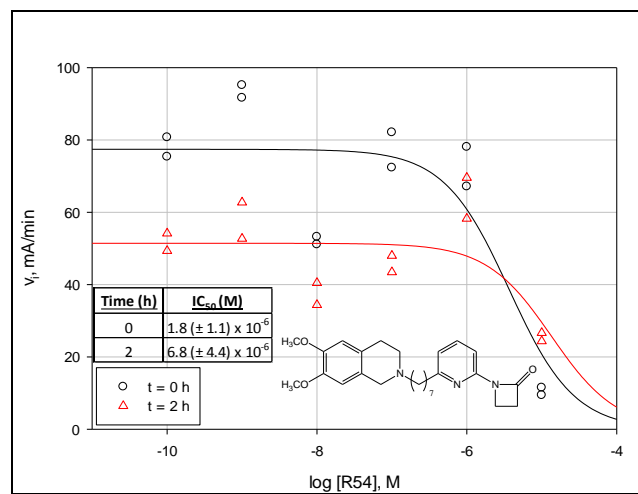


Figure B39: Dose Response plot for R54 (100 pM-10  $\mu$ M)

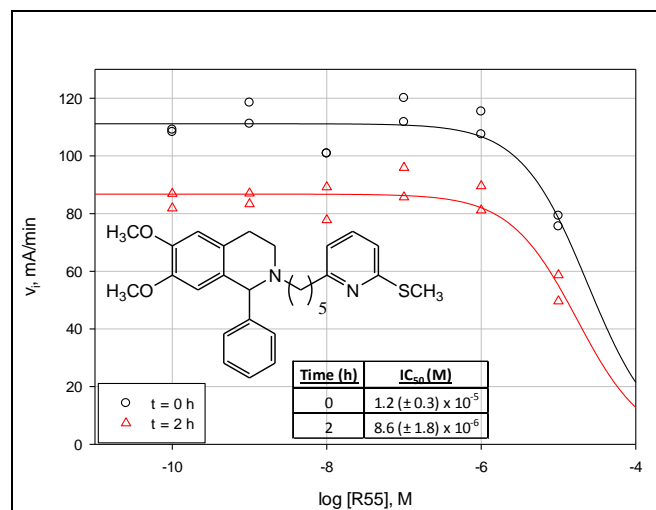
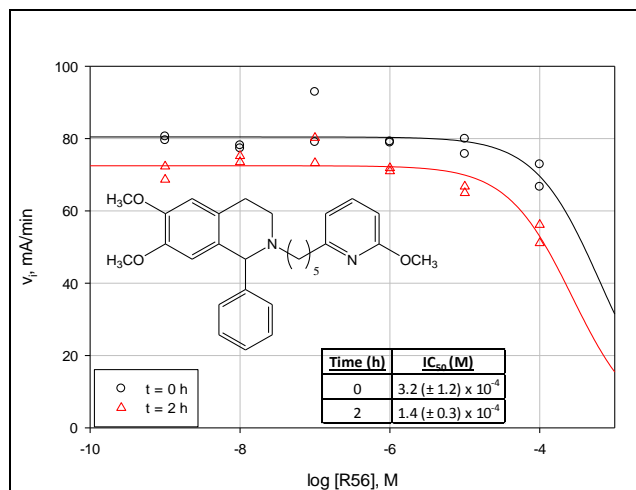


Figure B40: Dose Response plot for R55 (100 pM-10  $\mu$ M)

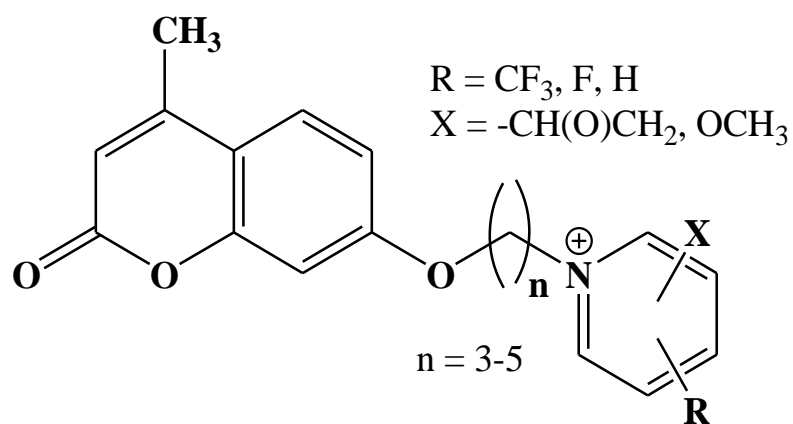


**Figure B41:** Dose Response plot for **R56** (1 nM-100 μM)

*4-methylumbelliferyl-pyridinium Gorge-Spanning Compounds*

IC<sub>50</sub> values for compounds R60-R66 were determined by S. Nilanthi

Yasapala of the Quinn research group at the University of Iowa-Department of Chemistry.



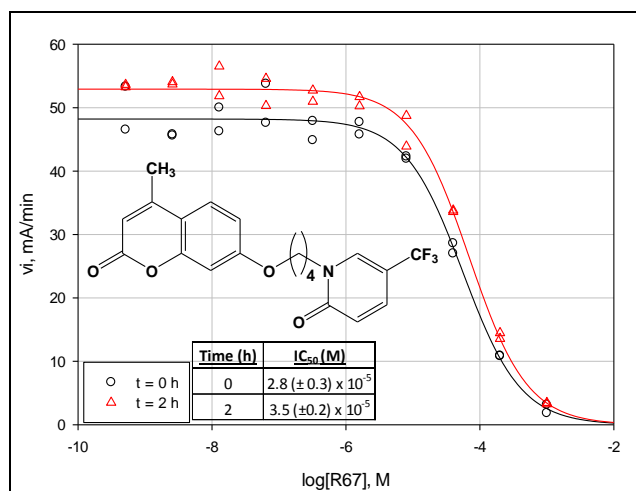


Figure B42: Dose Response plot for R67 (51 nM-1 mM)

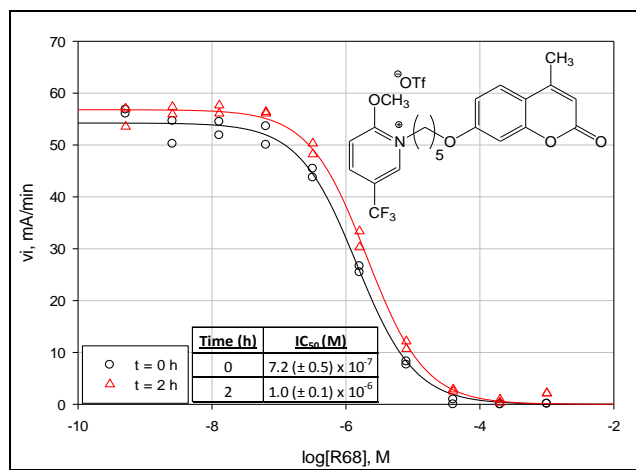
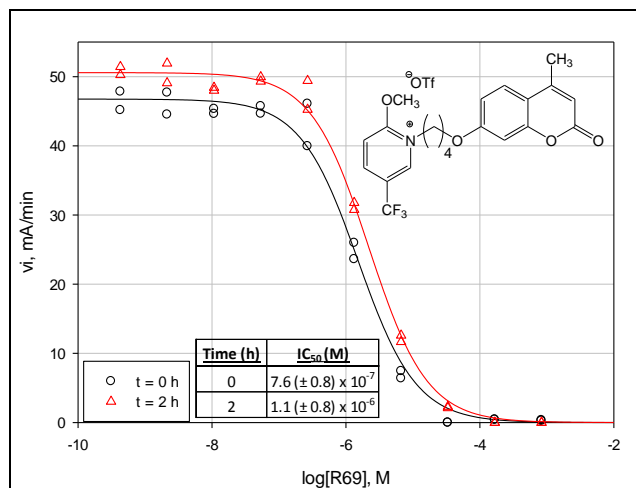
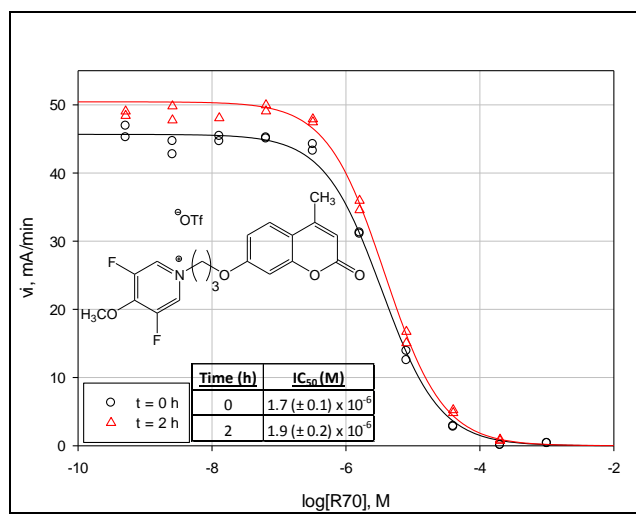


Figure B43: Dose Response plot for R68 (51 nM-1 mM)



**Figure B44:** Dose Response plot for **R69** (51 nM-1 mM)



**Figure B45:** Dose Response plot for **R70** (51 nM-1 mM)

### Dimethyl Sulfonium Compounds

Dimethyl sulfonium compounds are substituted aromatic/heterocyclic compounds or are in moieties tethered to gorge-spanning parent compounds (Aricept core or methyl umbelliferyl).

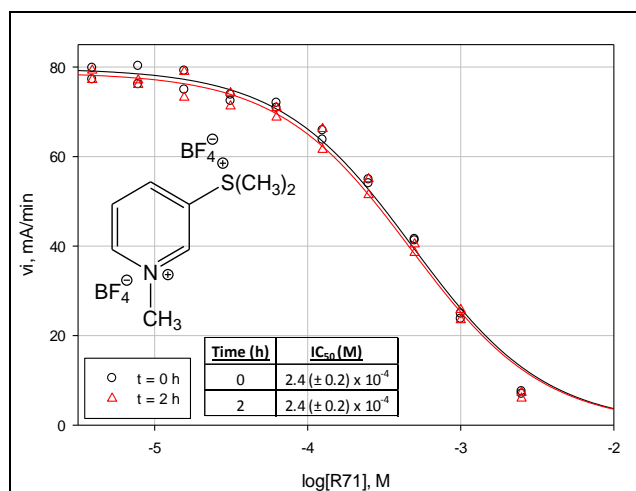


**Figure B46:** Dose Response plot for **R71** (4  $\mu$ M-2.5 mM)

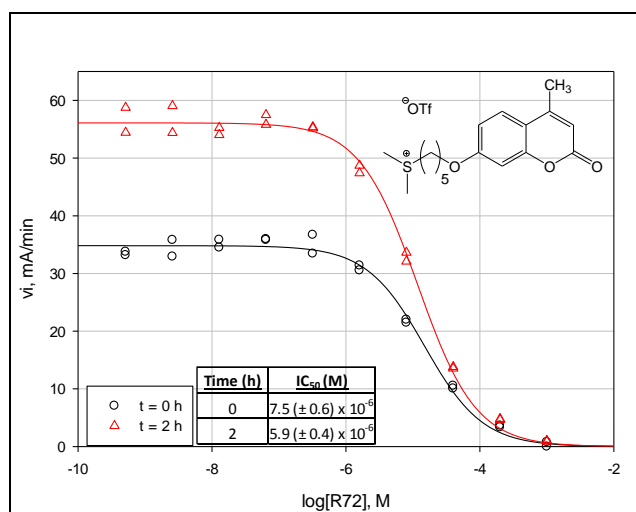


**Figure B47:** Dose Response plot for **R72** (51 nM-1 mM)

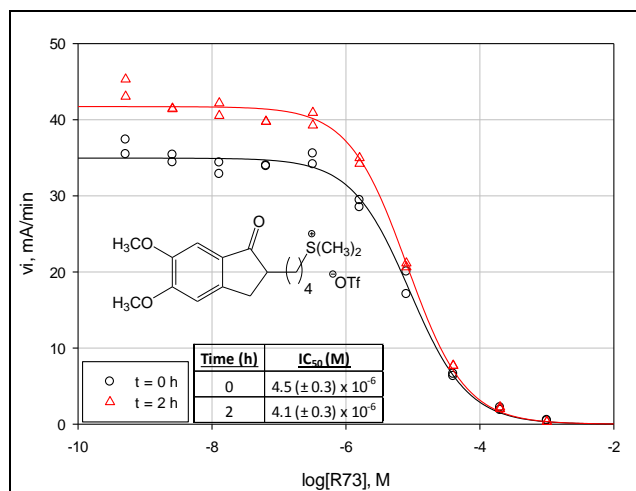


Figure B48: Dose Response plot R73 (51 nM-1 mM)

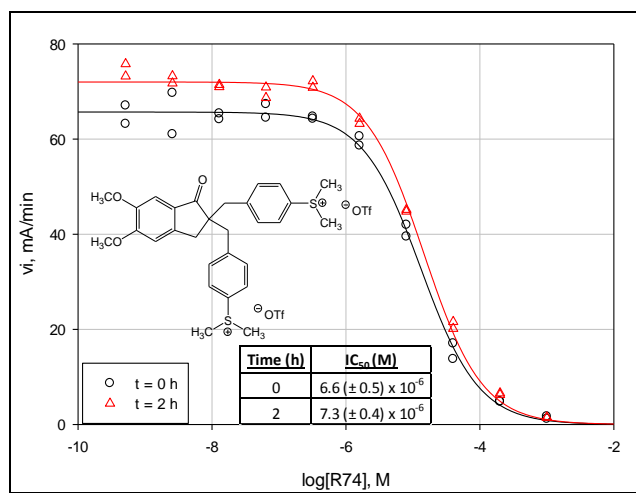
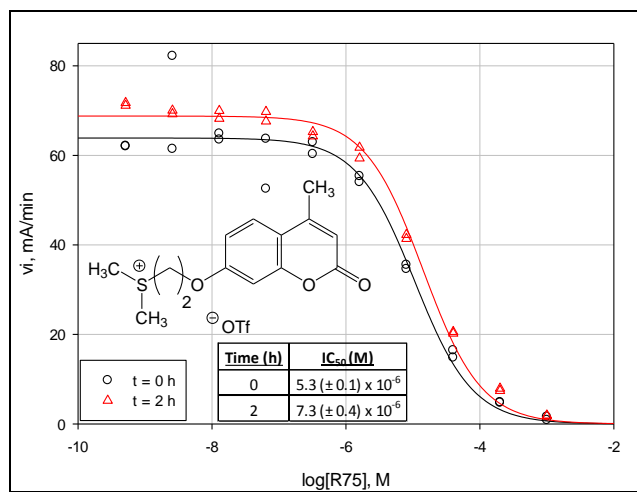
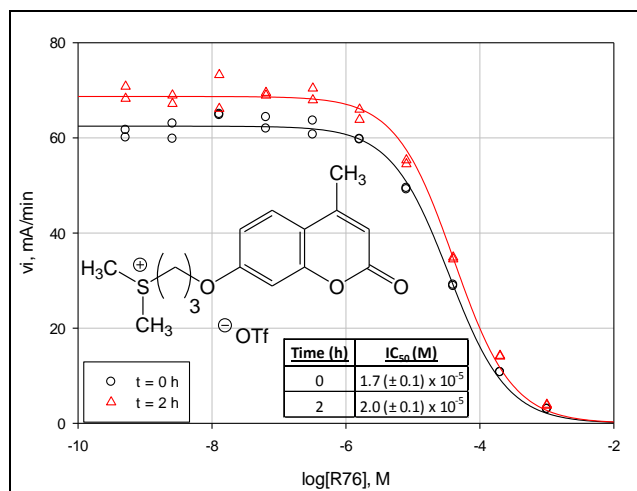


Figure B49: Dose Response plot R74 (51 nM-1 mM)



**Figure B50:** Dose Response plot for **R75** (51 nM-1 mM)



**Figure B51:** Dose Response plot for **R76** (51 nM-1 mM)



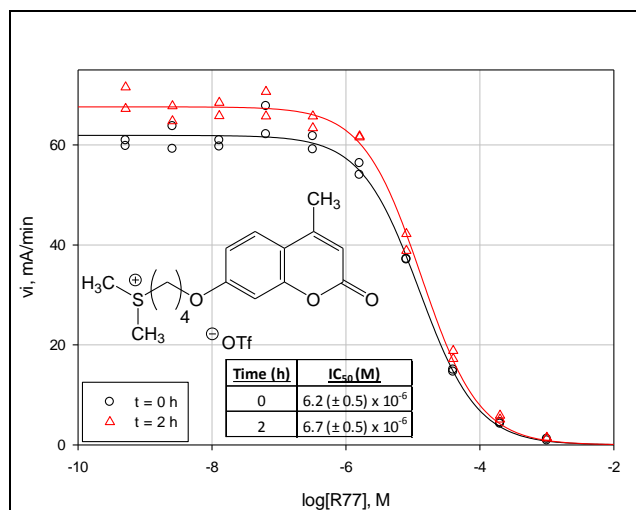


**Figure B52:** Dose Response plot for **R77** (51 nM-1 mM)

### 2-PAM, R13, and R15 “Resurrection” Assay Procedure

57 nM *hAChE* was inactivated with **2A** and in the general methods of Appendix B. Inactivated *hAChE* was allowed to “age” by incubating for 48 hours at 27°C. Control *hAChE* was prepared in the absence of inhibitor using an acetonitrile blank. Residual *hAChE* activity was assayed following Ellman conditions described in the general procedure after a 30 minute incubation at 27 °C with 100 μM 2-PAM. Aliquots of “aged” *hAChE* (*hAChE*<sub>aged</sub>) were dosed with varied concentrations of 2-PAM, **R13**, and **R15** then incubated at 27 °C before treatment with 100 μM 2-PAM for 30 minutes. The percent of reactivated *hAChE*<sub>aged</sub> was followed over a 24-72 hour period by the Ellman method. Percent of recovered *hAChE* activity by 2-PAM was calculated using Eq. 3.5, which is the ratio of the initial rates of *hAChE*<sub>aged</sub> and *hAChE*<sub>free</sub> catalyzed hydrolysis of ATCh assayed following each incubation with 2-PAM, **R13**, and **R15**.

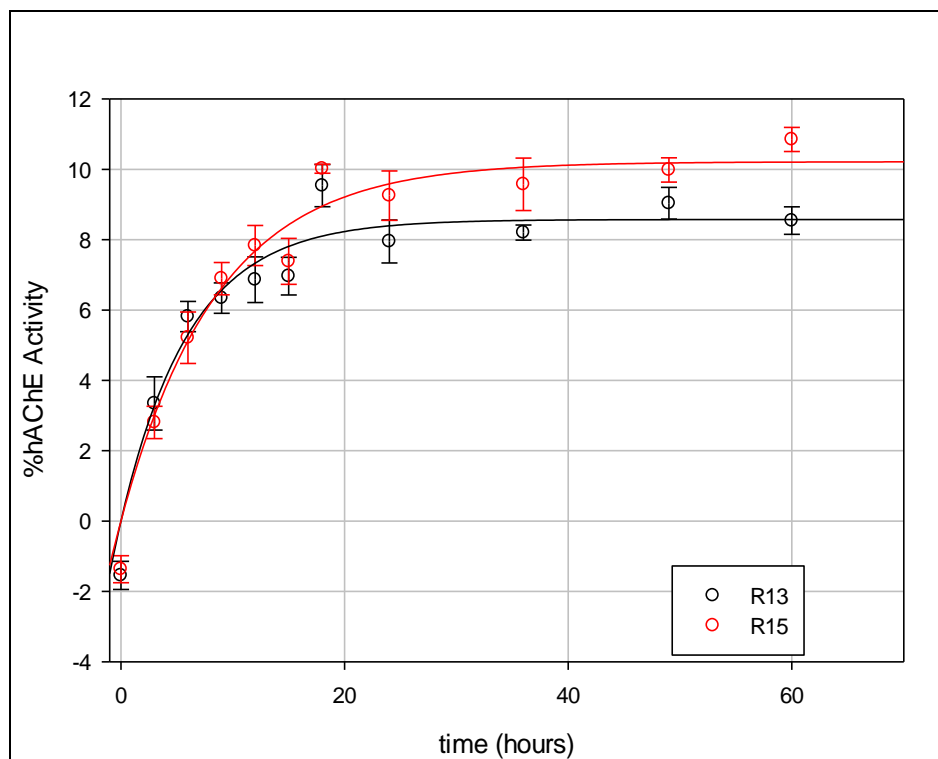


**Figure B53:** Plot of apparent recovered aged-*hAChE* activity by oxime substituted resurrecting agents **R13** and **R15** as a function time (h).

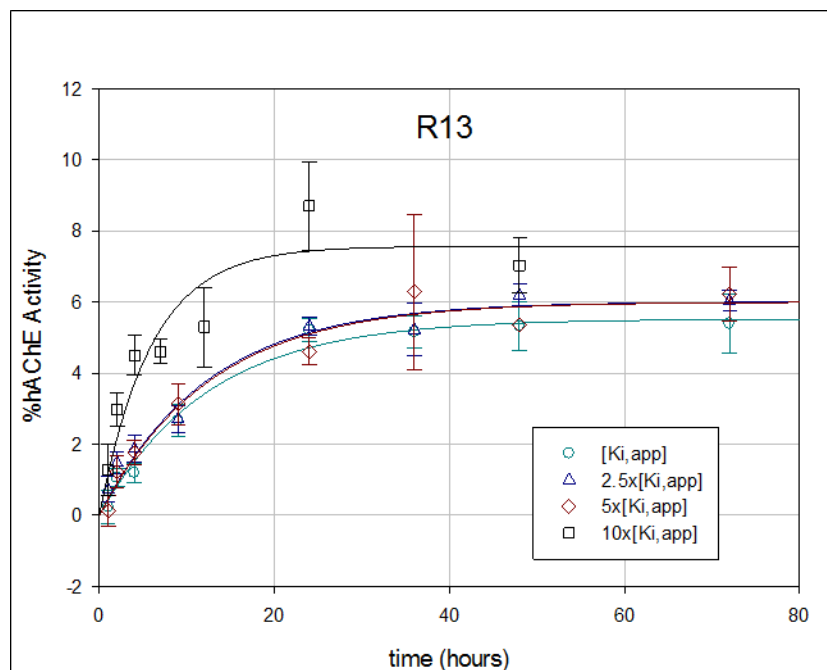


**Figure B54:** Plot of apparent recovered aged-*hAChE* activity as a function of time for resurrecting agent **R13** at varied concentrations (177  $\mu$ M-1.8 mM)

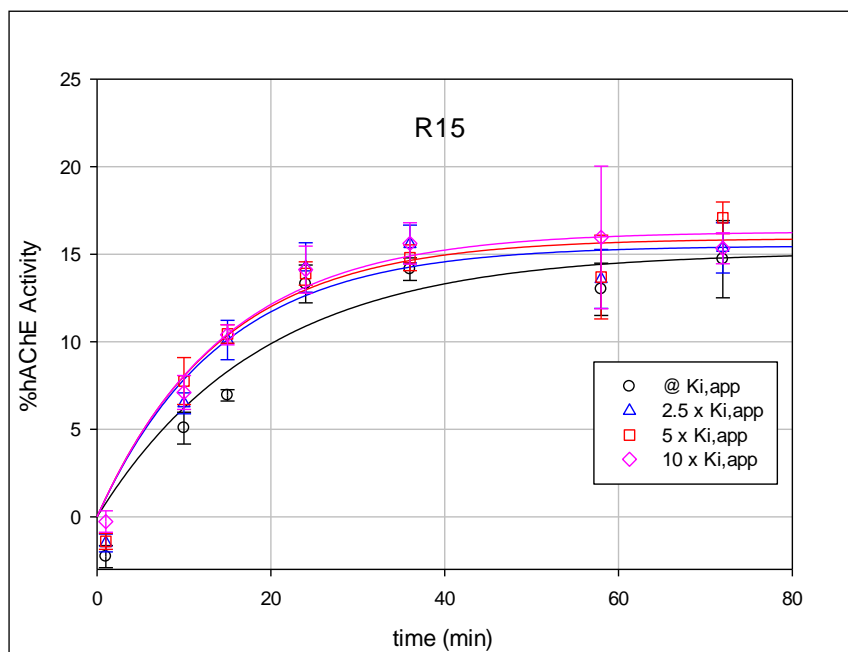


**Figure B55:** Plot of apparent recovered aged-*hAChE* activity as a function of time for resurrecting agent **R15** at varied concentrations (110  $\mu$ M-1.1 mM)

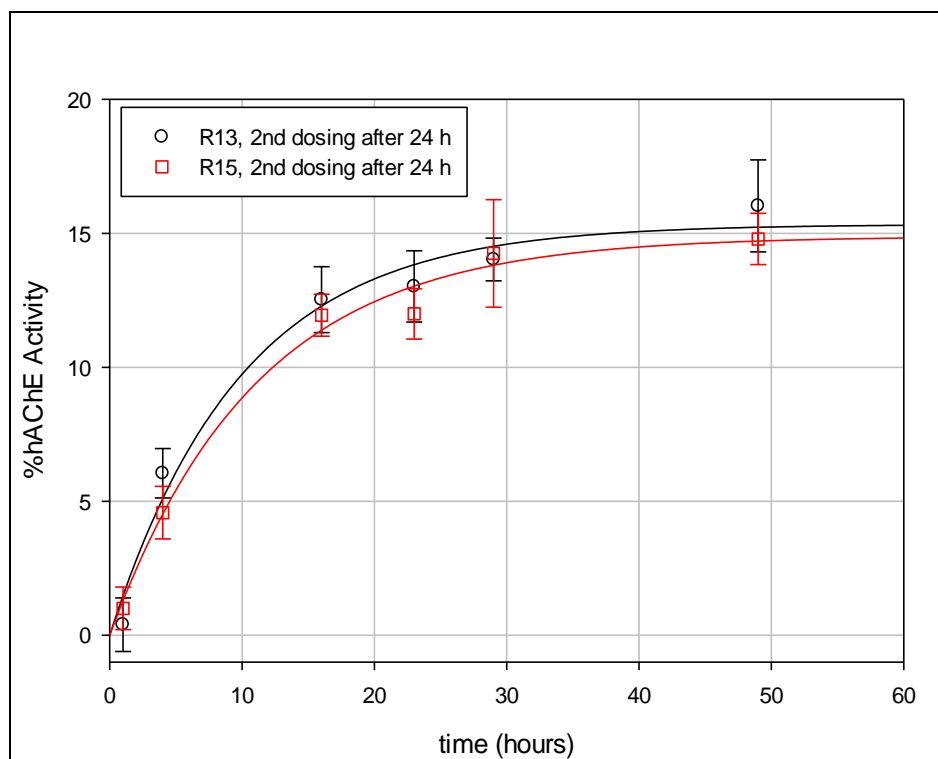


**Figure B56:** Plot of apparent recovered aged-*hAChE* activity with second dosing of resurrector agents **R13** (885  $\mu\text{M}$ ) and **R15** (550  $\mu\text{M}$ ).

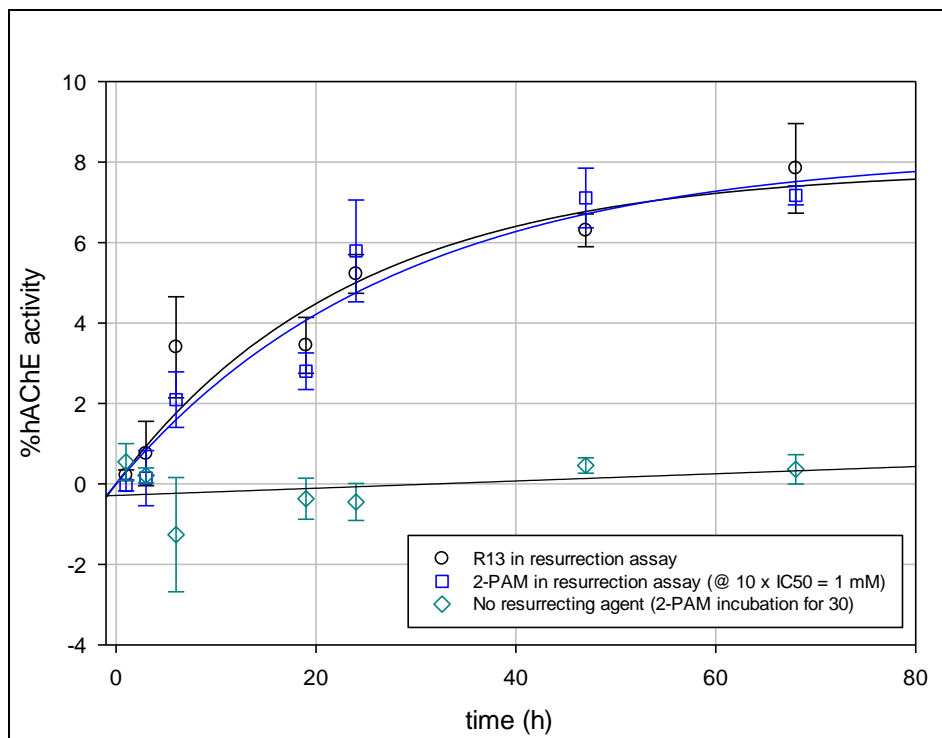


**Figure B57:** Plot of apparent recovered aged-*hAChE* activity of resurrecting agent **R13** with parallel assay of 2-PAM (in the resurrection assay Fig. 3.7) and no resurrecting agent (only 30 min pre-assay incubation with 100  $\mu$ M 2-PAM)

Additionally,  $hAChE_{aged}$  was exposed to a second dosing of the resurrecting oximes **R13** and **R15** after the first 24 hours of incubation and followed to determine the extent of recovered aged- $hAChE$  activity. Rates of “resurrection” ( $k_{res}$ ) were calculated using non-linear regression analysis for each resurrecting oxime. From Eq. 3.6, we determine the amount of recovered  $hAChE$  ( $\%hAChE_{Res.}$ ). Concentration dependence on the apparent recovery of  $hAChE$  activity was followed for 72 hours. Rates of “resurrection” ( $k_{res}$ ) were calculated using non-linear regression analysis for each resurrecting oxime. Figs. B53-B57 show the resurrection assay results and apparent recovery of aged- $hAChE$  activity, which has been attributed to the reactivation of the  $R_P$  OP analogue of **2A**.

## APPENDIX C:

SUPPORTING MATERIALS FOR  $\beta$ -LACTAM INHIBITORSMaterials and General Methods

All reagents were purchased from a commercial vendor in the highest purity available and were used without further purification unless otherwise stated. Lyophilized recombinant *human* acetylcholinesterase (*hAChE*), acetylthiocholine iodide (ATCh), 5,5'-dithiobis(2-nitro benzoic acid) (DTNB), and 2-PAM were obtained from Sigma-Aldrich. Inhibitors **R24-R28** were synthesized by Dr. Joseph J. Topczewski, post-doctoral associate in the Quinn research group at the University of Iowa. Solvents were either used as received or dried over molecular sieves where noted.

Deionized distilled water (DD-H<sub>2</sub>O) was used to prepare all assay solutions and filtered through a Barnstead International hose nipple organic removal ion exchange cartridge. Phosphate buffer (PB) at 50 mM concentration was prepared in bulk at pH ranging from 7.2-7.3. The pH was determined by an ion selective pH electrode that was calibrated prior to each measurement. All stock solutions were prepared from solid material and stored in polypropylene containers at 4 °C as follows: 0.1% (w/v) BSA solution in PB, 45 mM ATCh in DD-H<sub>2</sub>O, 20 mM DTNB in PB, 14 nM *hAChE* in 0.1% (w/v) BSA solution, and 1.4 nM *hAChE* in 0.1% (w/v) BSA solution. Working solutions were prepared using calibrated micropipettes and solvents matching the parent stock. To ensure sample integrity, all  $\beta$ -lactam inhibitors were prepared from solid and used immediately after preparation.

Assays were conducted on a Molecular Devices SpectraMaxM2 micro-plate reader and on polystyrene 96-well plates (Costar, round bottom). Activity of *hAChE* was



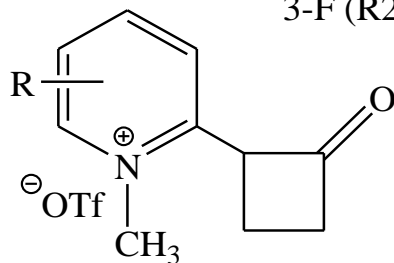
measured spectrophotometrically at 412 nm and 27 °C following the Ellman assay method (26). Time point readings were obtained at the minimum possible interval over a 10 min duration. Incubation was performed in duplicate for each inhibitor concentration. Initial rates ( $v_i$ , mA/min) were calculated by least-squares analysis of the time courses at less than 10% turnover of the initial substrate concentration. Non-linear regression analysis was performed using SigmaPlot 12.0 to obtain inhibition parameters. Rates were corrected for background (nonenzymic) hydrolysis of ATCh. Plots for the bimolecular rate constants for inhibitors **R24-R27** and described by equation C1:

$$k_{obs} = \frac{k_i[I]}{K_I + [I]}; k_{obs} = \frac{k_i}{K_I} [I] \text{ at } [I] \ll K_I$$

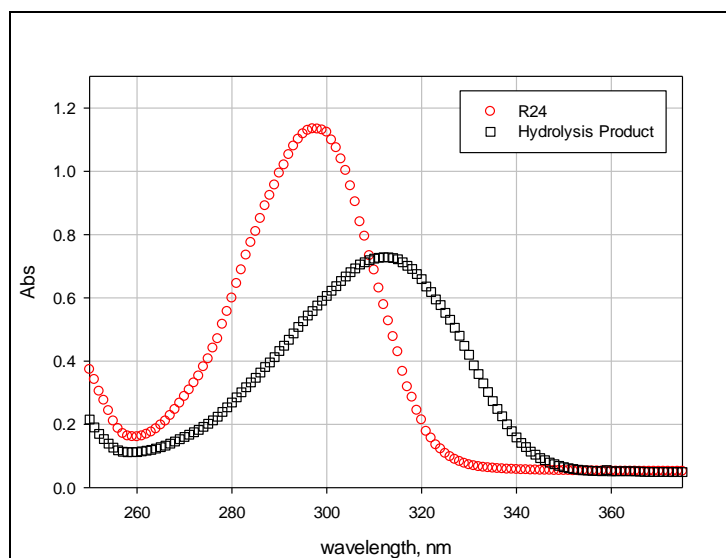
**Equation C1:** Equation defining the observed pseudo first-order rate constant,  $k_{obs}$ ; where  $[I] \equiv$  inhibitor concentration (**R24-R27**);  $k_i \equiv$  first-order inhibition rate constant;  $K_I \equiv$  inhibitor dissociation constant;

#### Inhibitor Structure

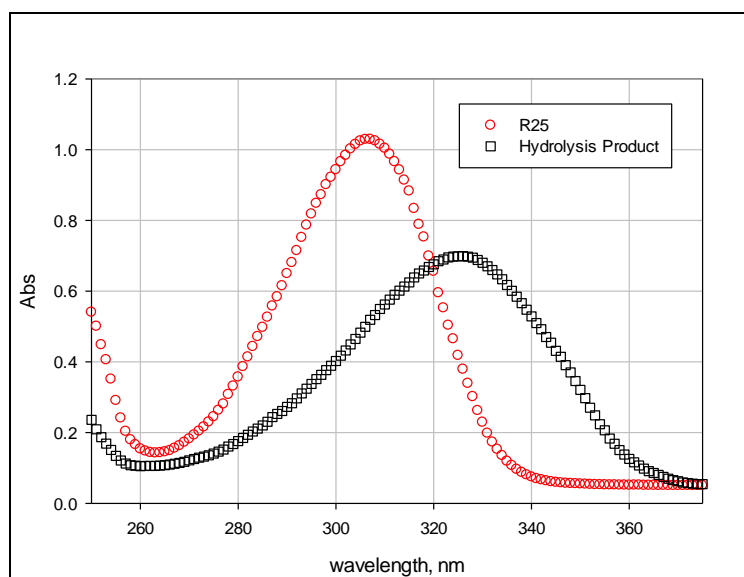
R = H (R24), 5-CF<sub>3</sub> (R25), 5-F(R26),  
3-F (R27), 4-N(Me)<sub>2</sub> (R28)



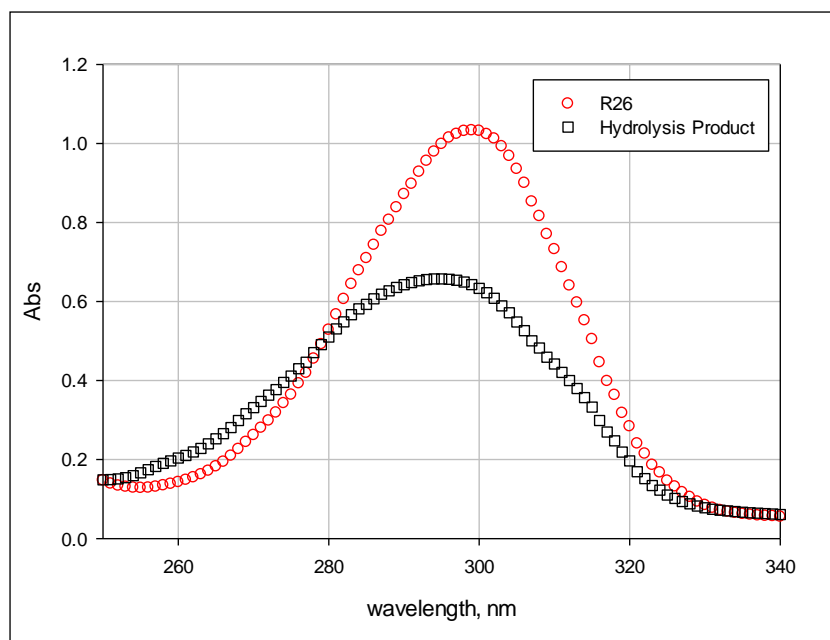
### Supporting Information for Hydrolytic Stability Assay



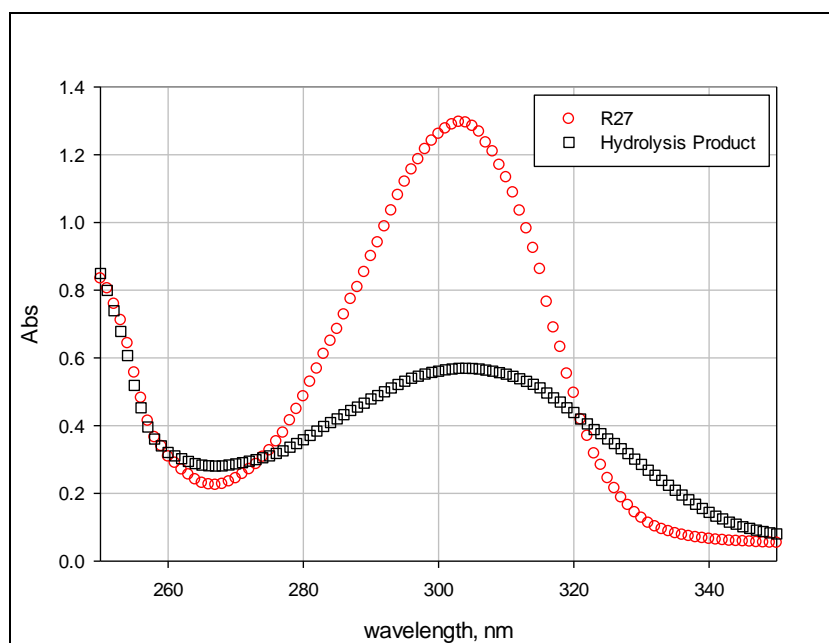
**Figure C1:** UV spectrum (250 nm-380 nm) for inhibitor **R24**



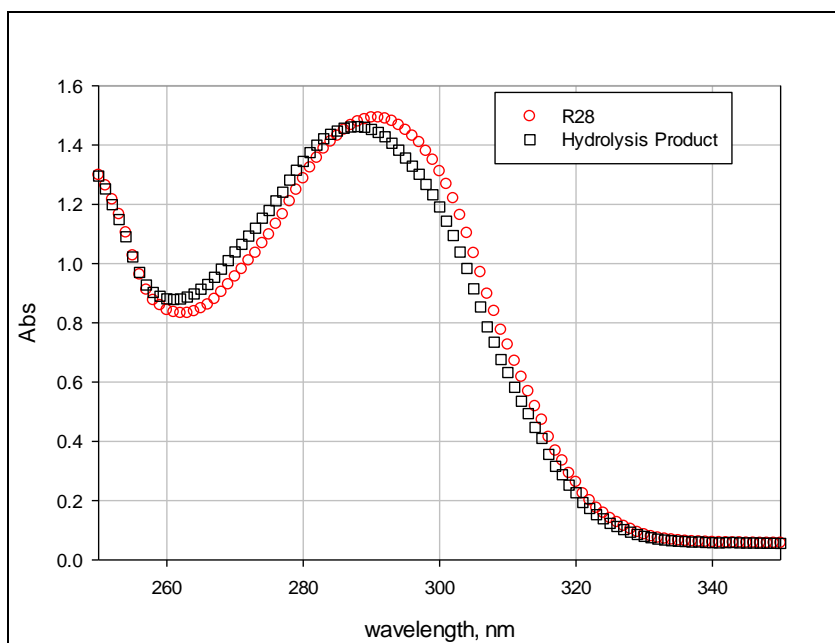
**Figure C2:** UV spectrum (250 nm-380 nm) for inhibitor **R25**



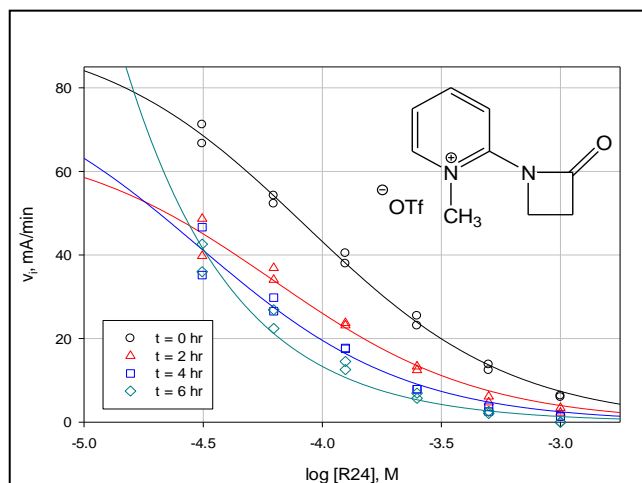
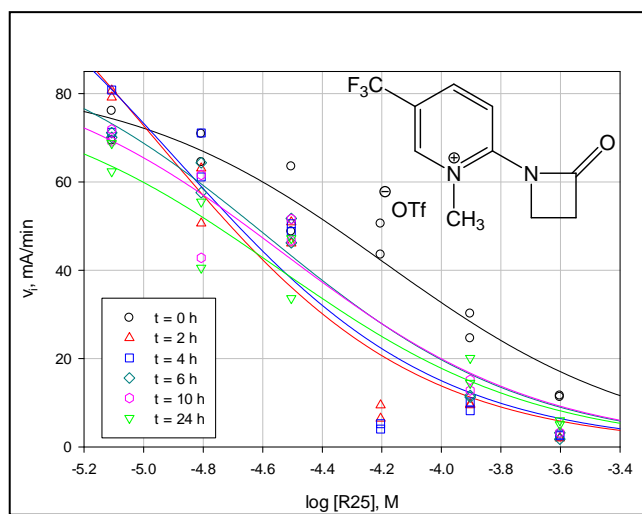
**Figure C3:** UV spectrum (250 nm-340 nm) for inhibitor **R26**



**Figure C4:** UV spectrum (250 nm-350 nm) for inhibitor **R27**



**Figure C5:** UV spectrum (250 nm-350 nm) for inhibitor **R28**

Supporting Information for IC<sub>50</sub> DeterminationFigure C6: Dose Response plots for R24 (30  $\mu$ M-1 mM)Figure C7: Dose Response plots for R25 (8-250  $\mu$ M)

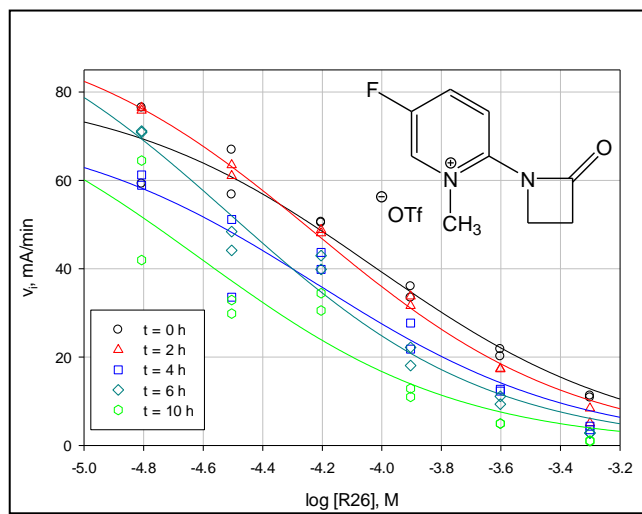


Figure C8: Dose Response plots for R26 (30  $\mu\text{M}$ -1 mM)

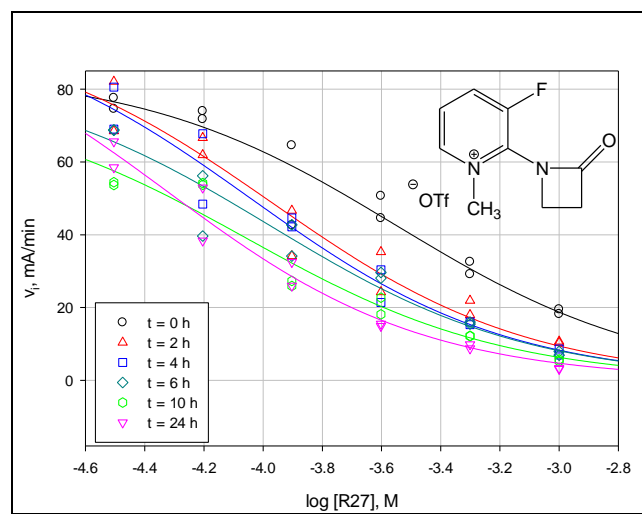
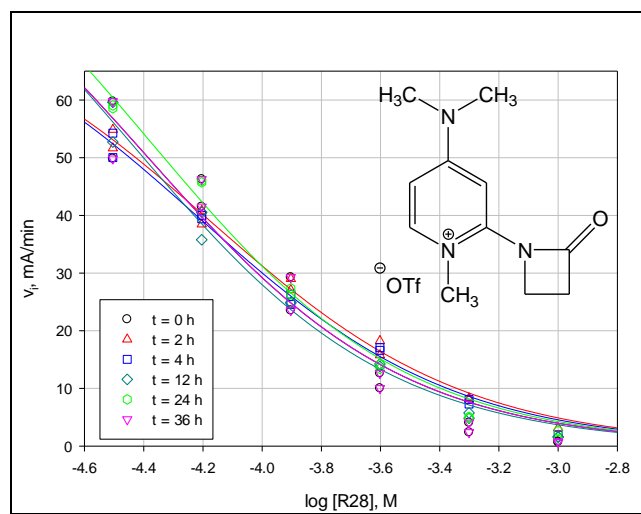
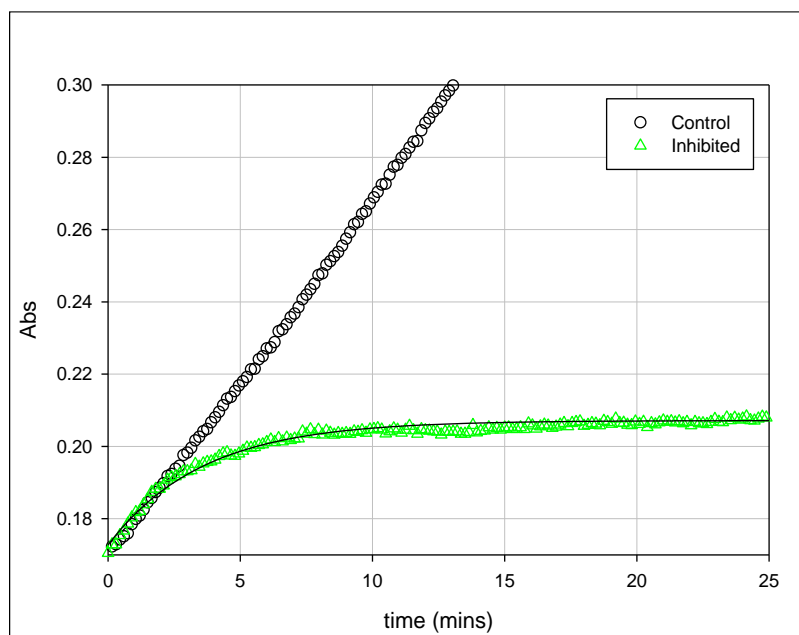


Figure C9: Dose Response plots for R27 (30  $\mu\text{M}$ -1 mM)



**Figure C10:** Dose Response plots for **R28** (30  $\mu$ M-1 mM)

### Supporting Information for Continuous Assays



**Figure C11:** Truncated continuous assay time course for  $\beta$ -lactam inhibitor **R25** (200  $\mu$ M) fit to Eq. 4.7.

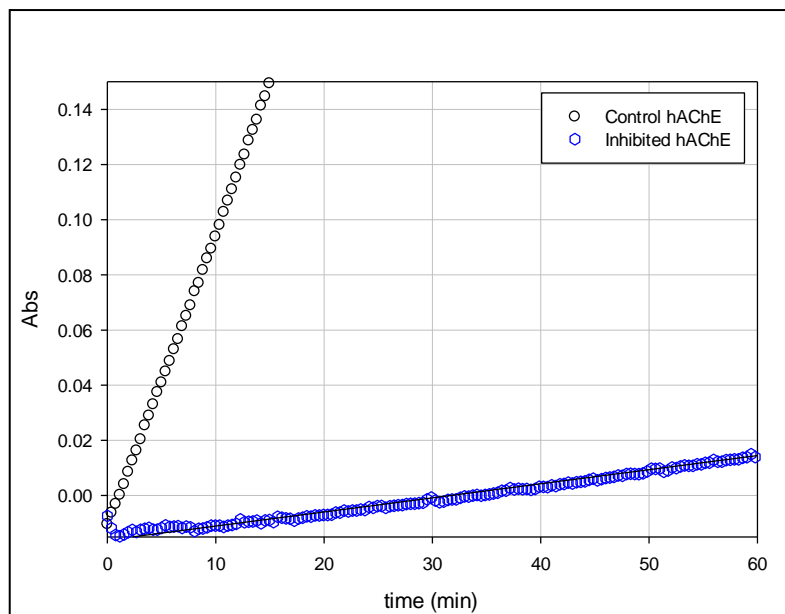


**Figure C12:** Continuous assay time course for  $\beta$ -lactam inhibitor **R28** fit to Eq. 4.8



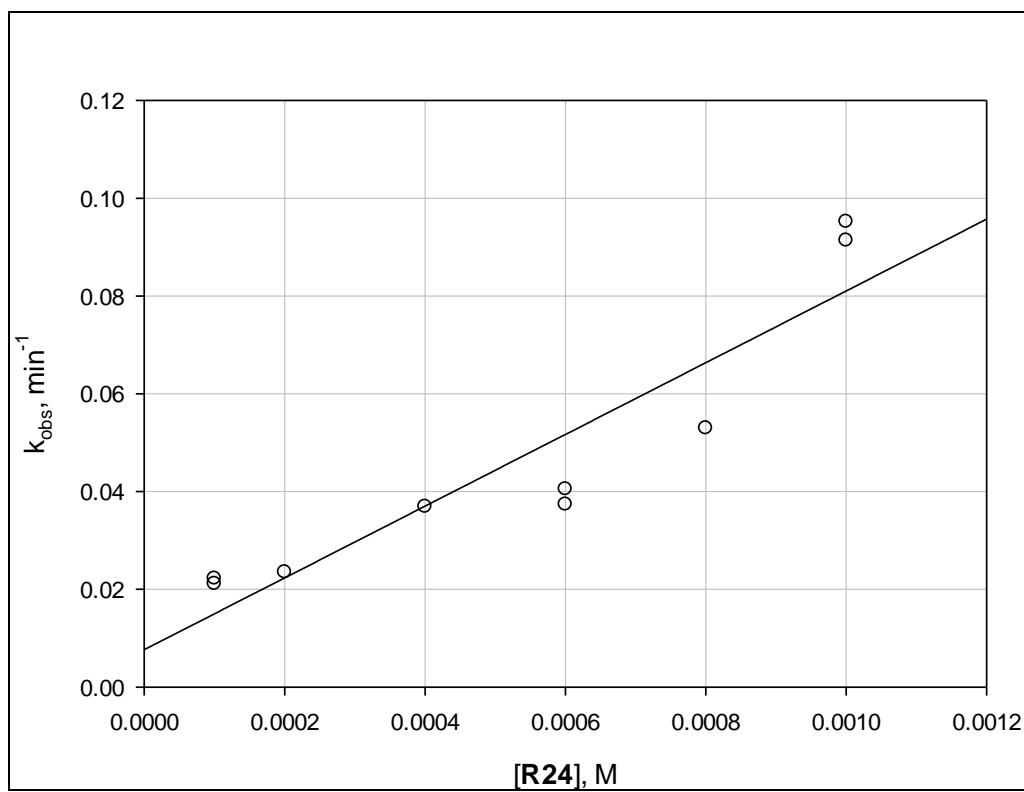


**Figure C13:** Second-order rate constant plot of  $k_{\text{obs}}$  ( $\text{min}^{-1}$ ) versus **R24** concentration, Eq. C1

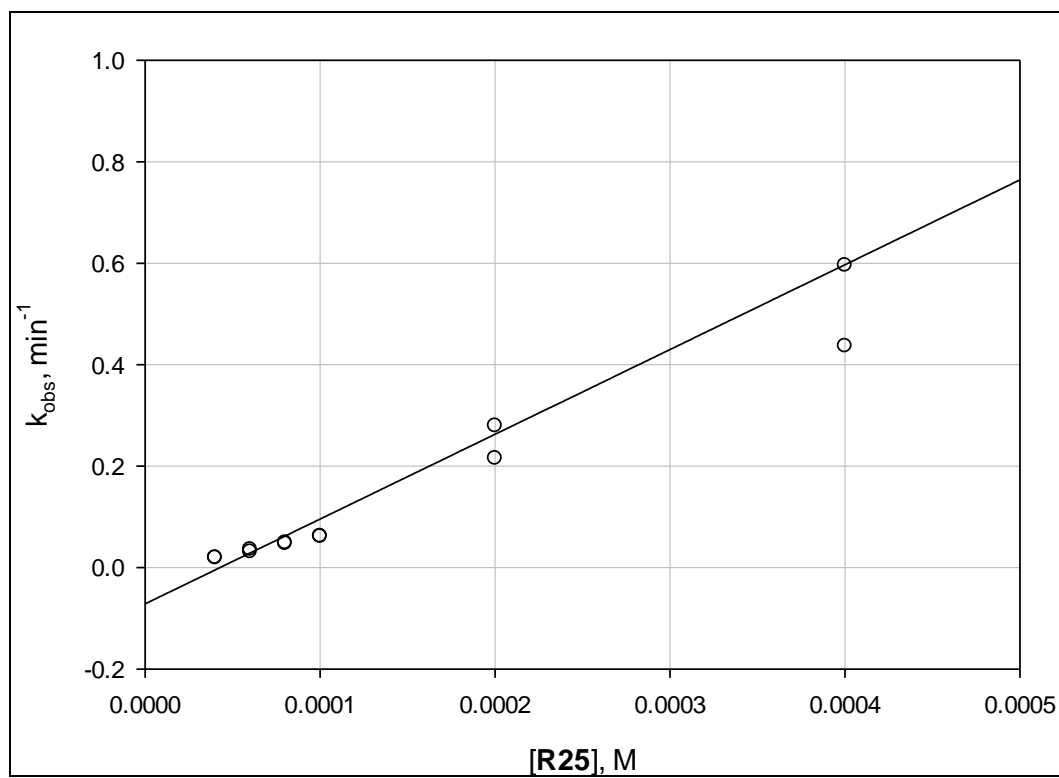


**Figure C14:** Second-order rate constant plot of  $k_{\text{obs}}$  ( $\text{min}^{-1}$ ) versus **R25** concentration, Eq. C1

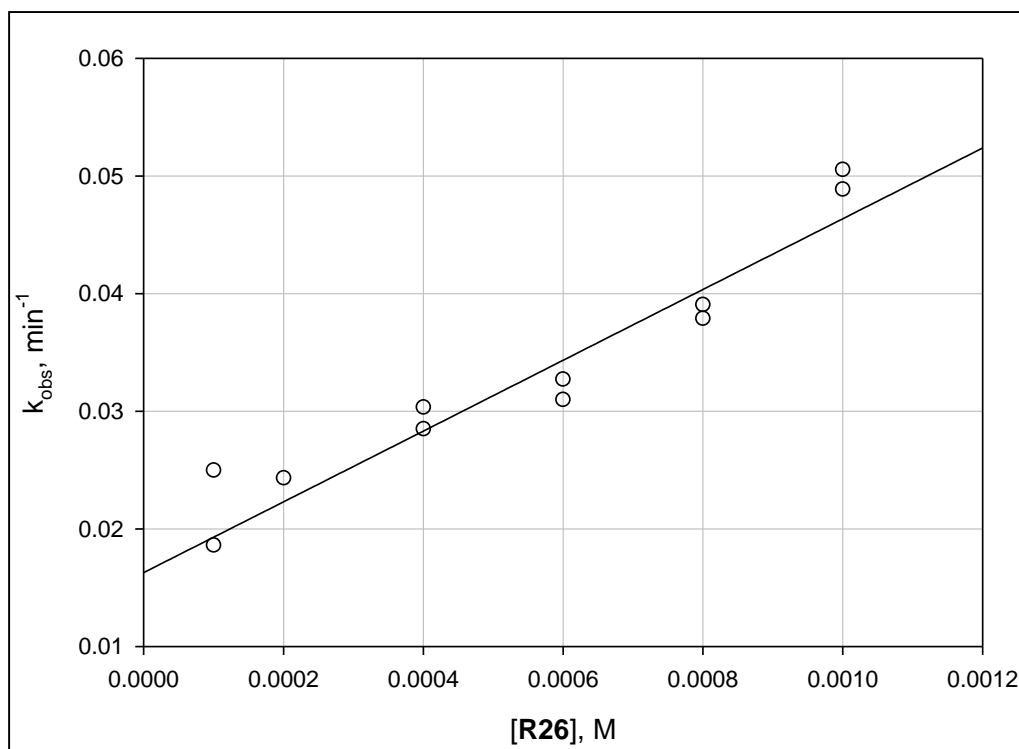


**Figure C15:** Plot for second-order rate constant of  $k_{\text{obs}}$  ( $\text{min}^{-1}$ ) versus **R26** concentration, Eq. C1

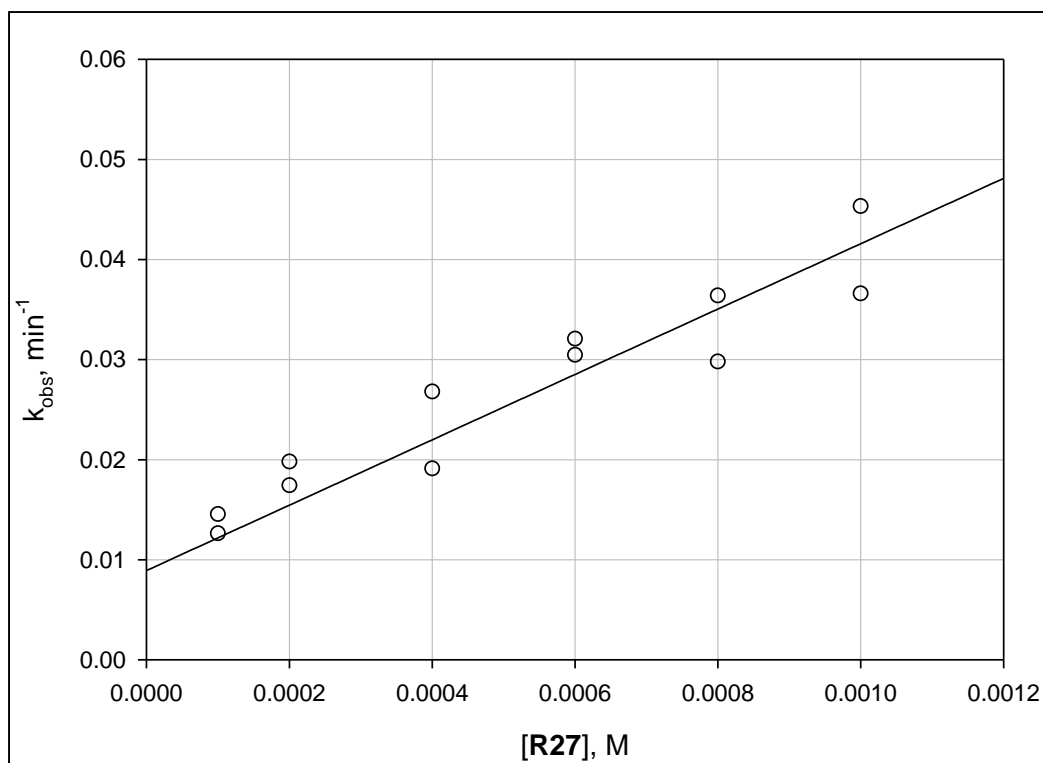


**Figure C16:** Second-order rate constant plot of  $k_{\text{obs}}$  ( $\text{min}^{-1}$ ) versus **R27** concentration, Eq. C1

**Table C1:** Bimolecular rate constants for inhibitors **R24**, **R26-27** from biphasic fit to equation Eq. 4.6 and inhibitor **R25** from Eq. 4.7

Inhibitors <b>R24-27</b>		
Entry	R =	<u><math>k_i/K_i, \text{min}^{-1} \text{M}^{-1}</math></u>
<b>R24</b>	H	$7 (\pm 1) \times 10^1$
<b>R26</b>	5-F	$2.9(\pm 0.3) \times 10^1$
<b>R27</b>	3-F	$2.9(\pm 0.2) \times 10^1$
<b>R25</b>	5-CF <sub>3</sub>	$1.2 (\pm 0.1) \times 10^3$

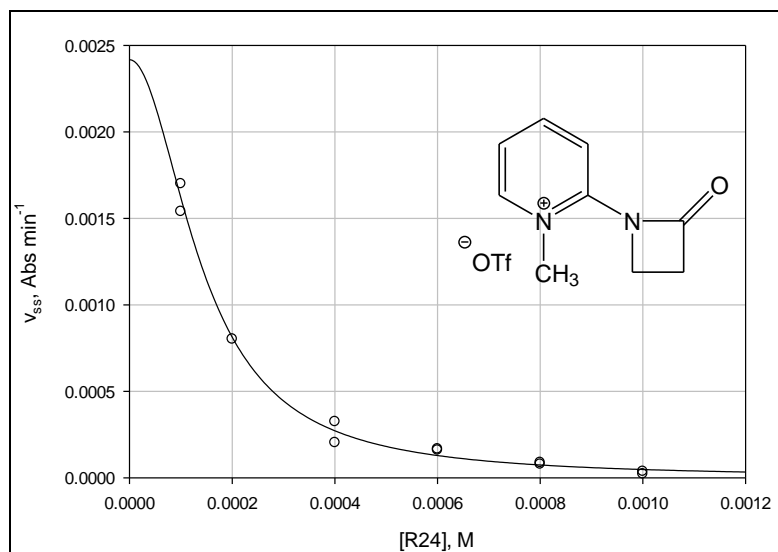


**Figure C17:** Dixon plot of  $v$  (Abs/min) versus inhibitor **R24** concentration (100  $\mu$ M-1 mM) fit to Eq. 4.9

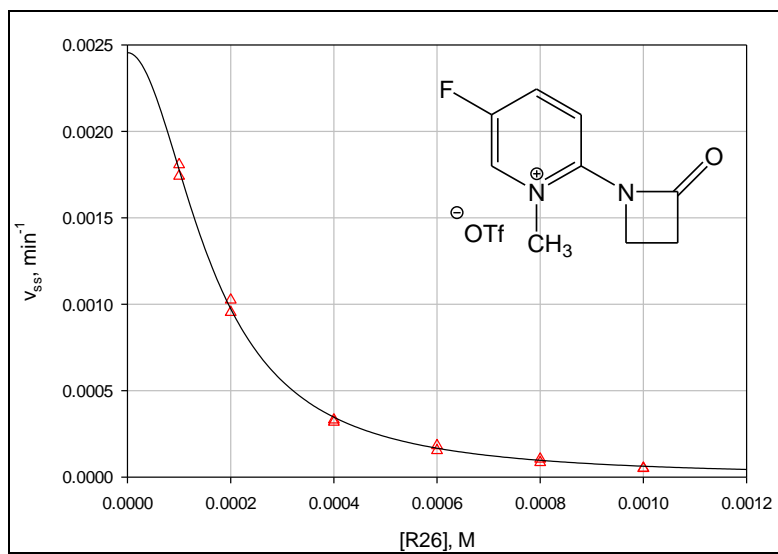


**Figure C18:** Dixon plot of  $v$  (Abs/min) versus inhibitor **R26** concentration (100  $\mu$ M-1 mM) fit to Eq. 4.9

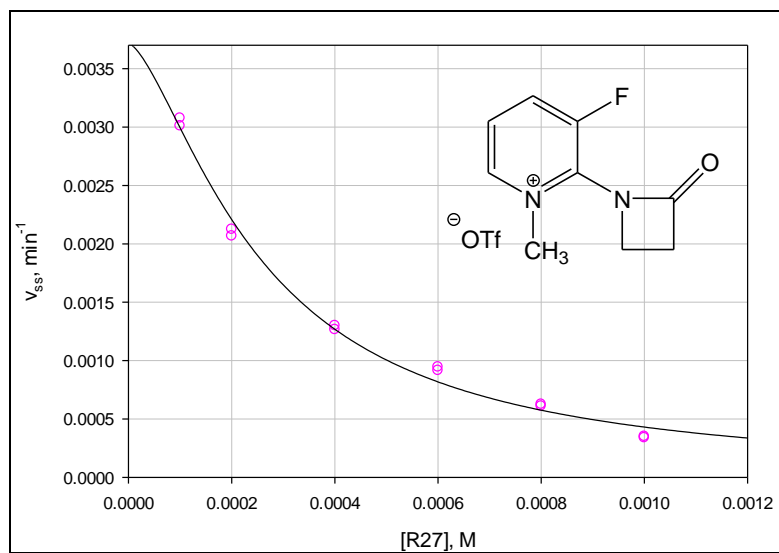


**Figure C19:** Dixon plot of  $v$  (Abs/min) versus inhibitor **R27** concentration (100  $\mu$ M-1 mM) fit to Eq. 4.9

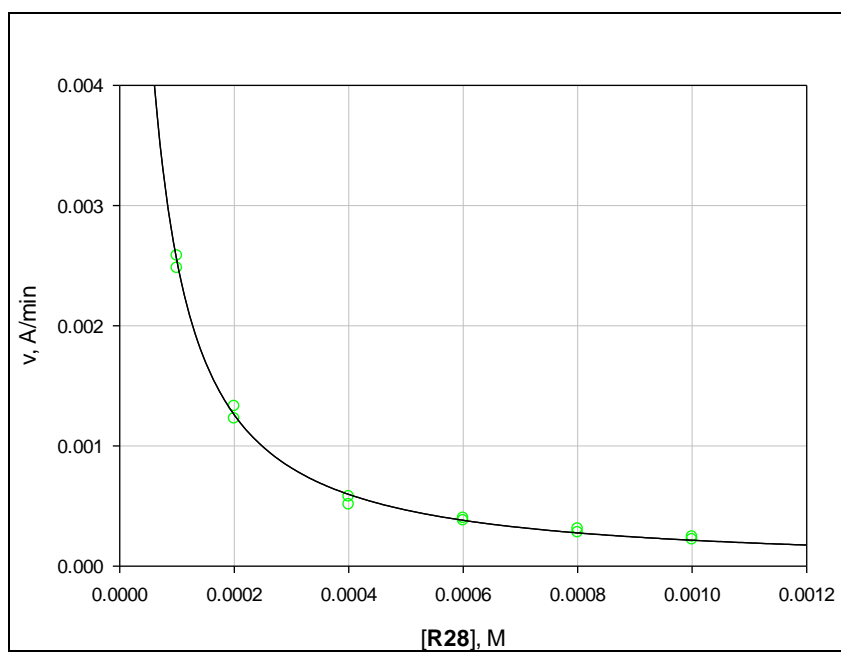


**Figure C20:** Dixon plot of  $v$  (Abs/min) versus inhibitor **R28** concentration (100  $\mu$ M-1 mM) fit to Eq. 4.9

Supporting Information for reactivation assay

Inhibitor **R24** (R = H) was selected to inhibit *hAChE* and assay the spontaneous recovery of enzyme activity. This experiment was conducted by preparing a solution containing 227  $\mu\text{L}$  of 140 nM *hAChE* with either 23  $\mu\text{L}$  of 11.3 mM or 1.13 mM inhibitor **R24**. A control solution was prepared with a 23  $\mu\text{L}$  blank of DD- $\text{H}_2\text{O}$ . Upon preparation, both the inhibited and control *hAChE* solutions were diluted 100-fold in 0.1% (w/v) BSA in 50 mM PB (pH 7.33) such that the *hAChE* concentration was 1.4 nM and inhibitor **R24** concentrations were 10  $\mu\text{M}$  and 1  $\mu\text{M}$  respectively. The 100-fold diluted solutions of both inhibited and control *hAChE* were assayed at various time points over a 17 hour period under Ellman assay conditions described in the general methods section of Appendix C. Assay wells were prepared as follows: 10  $\mu\text{L}$  of inhibited /control 1.4 nM *hAChE*, 10  $\mu\text{L}$  of 20 mM DTNB, 10  $\mu\text{L}$  of 4.5 mM ATCh, and 270  $\mu\text{L}$  of 50 mM PB (pH 7.3). Inhibitor concentrations in the assay wells were diluted to 333 nM and 33 nM respectively. Initial rates ( $v_i$ , mA/min) were calculated by least-squares analysis of the time courses at less than 10% turnover of the initial substrate concentration. All values were corrected for background (nonenzymic) hydrolysis of ATCh and performed in duplicate. The overall percent activity was determined by equation C1:

$$\%hAChE \text{ Activity} = \left( \frac{v_{i,inhibited}}{v_{i,control}} \right) \times 100$$

**Equation C1:** Ratio of the initial rates ( $v_i$ , mA/min) for the inhibited and control *hAChE* reactions with inhibitor **R24**



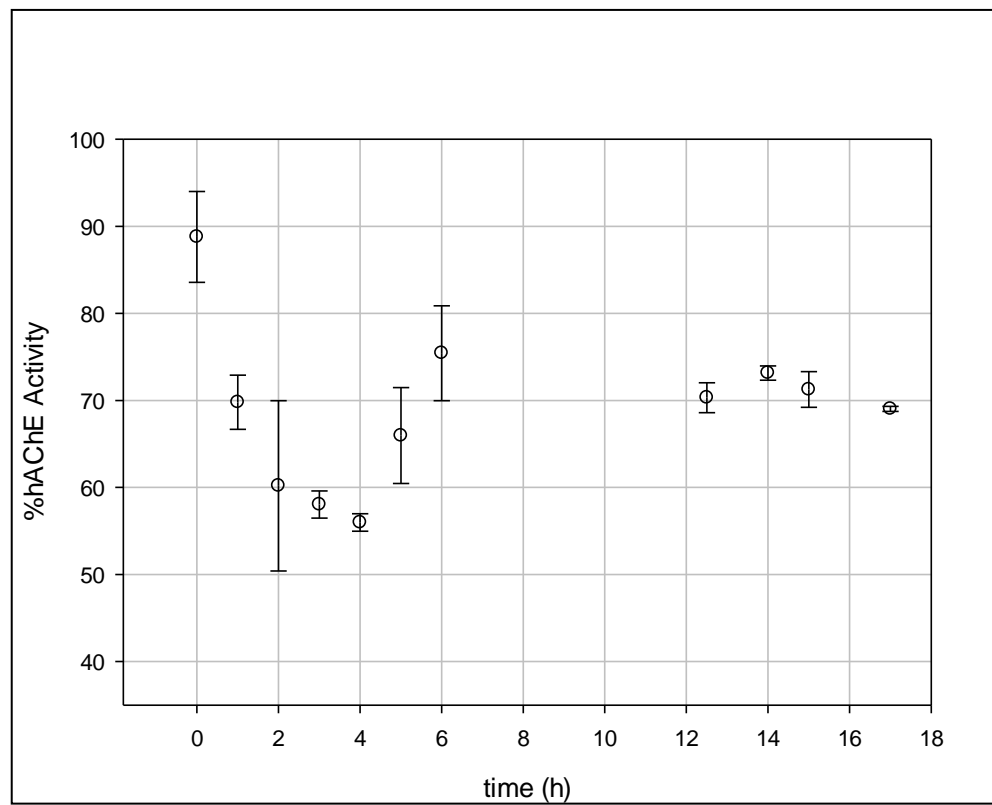


**Figure C21:** Percent of spontaneously recovered *hAChE* activity after inhibition with inhibitor **R24**

Fig. C21 shows the %*hAChE* Activity at each time point measured following inhibition by inhibitor **R24** and subsequent dilution. There was an observed recovery of *hAChE* activity after 17 h incubation following initial exposure to inhibitor **R24**.

#### Computational Docking and Molecular Modeling Procedure

All computational work reported was performed by Dr. Jason A. Morrill of William Jewell College-Department of Chemistry and is reported here as supporting information to compliment kinetic studies for  $\beta$ -lactam inhibitors **R24-R28**. To investigate the likely mode of binding of the  $\beta$ -lactams in the active site of *hAChE*, and the extent to which docking pre-aligned the lactam ring for acylation of Ser203, docking simulations were carried out using Autodock Vina (77). The results of the docking simulations are available in Table C2. The computed binding affinities correlate well with  $-\ln(K_i)$  as indicated by a coefficient of determination of  $R^2 = 0.6138$  (entry **R25** was left out of the correlation due to lack of experimental  $K_i$  value). Specifically, in the docking analysis we were looking for a ligand alignment with the Ser203 oxygen that would support a Bürgi-Dunitz trajectory (87). As indicated in Fig. C22 the lowest energy binding mode for nearly all of the ligands are aligned in a similar manner, with the carbonyl group of the lactam in close proximity of the oxygen of Ser203. Although the carbonyl of the lactam is docked in close proximity to the oxygen of Ser203, the Bürgi-Dunitz alignment is missed by over  $50^\circ$  in the docked poses. Apparently the binding mode is the result of a hydrogen bonding interaction between these ligands and the N-H groups of Gly 121 and Gly 122.

To investigate the extent to which acetylcholinesterase inhibition is a function of the intrinsic reactivity of the ligands we also modeled their acylation of Ser 203.

Reactions were modeled using the SAM1 semiempirical quantum mechanical method as implemented in AMPAC *with graphical user interface*. The reactions were modeled beginning with the lowest energy binding mode geometry and correspond to simultaneous nucleophilic acyl substitution of Ser203 at the lactam carbonyl group, with double proton transfer from Ser203 to His447 and from His447 to Glu334. In the modeled reactions the imidazole of His447 was in the neutral ionization state. (see Scheme 4.2) Reaction modeling was achieved by adjusting the distance between the oxygen of Ser 203 and the carbonyl carbon the lactam until a product geometry was achieved. The geometry approximating the transition state was then fully optimized without constraints. Following characterization by means of normal mode analysis the transition state geometry was found to exhibit a single negative eigenvalue corresponding to the transition vector for the reaction. All critical points along the reaction pathway were characterized by means of normal mode analysis.

**Table C2:** Comparison of the computed ligand docking results and experimental inhibitor dissociation constants.

Inhibitors <b>R24-28</b>					
Entry	R =	<u>IC<sub>50</sub>, <math>\mu</math>M</u>	<u>Computed Binding Affinity (kcal/mol)</u>	<u>Burgi-Dunitz Angle (Ser203OC=O) (Docked Pose)</u>	<u>Burgi-Dunitz Angle (Ser203OC=O) (Transition State)</u>
<b>R24</b>	H	43 $\pm$ 3	-6.5	45°	103°
<b>R26</b>	5-F	47 $\pm$ 8	-6.8	35°	101°
<b>R27</b>	3-F	140 $\pm$ 30	-6.7	44°	103°
<b>R25</b>	5-CF <sub>3</sub>	33 $\pm$ 6	-6.2	34°	102°
<b>R28</b>	4-N(Me) <sub>2</sub>	25 $\pm$ 2	-6.1	33°	105°

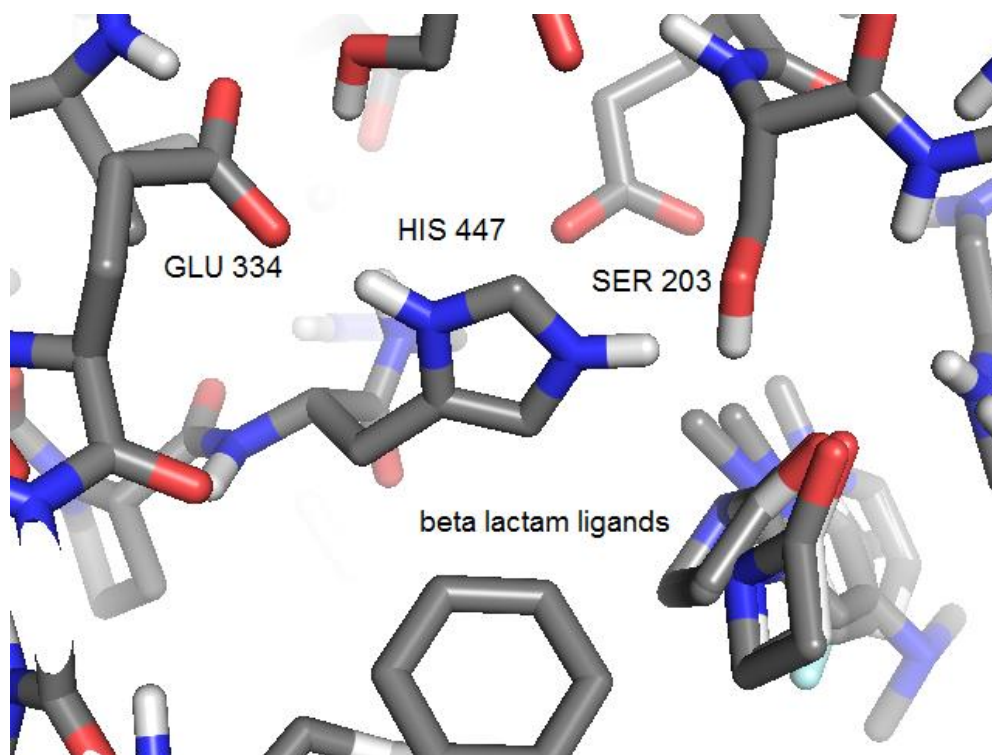


**Figure C22:** Docking poses for each of the  $\beta$ -lactam ligands under investigation in their respective lowest energy pose in the docking analysis. Courtesy of Dr. Jason A. Morrill (William Jewell College, Department of Chemistry)

## REFERENCES

1. Taylor, P. and Radić, Z. *Annu. Rev. Pharmacol. Toxicol.*, **1994**, 34, 281-320
2. Nicolet, Y.; Lockridge, O.; Masson, P.; Fontecilla-Camps, J.C.; and Nachon, F. *J. Biol. Chem.*, **2003**, 278, 41141-41147
3. Quinn, D.M. *Chem. Rev.*, **1987**, 87, 956-979
4. Ofek, K.; and Soreq, H. *Chem. Biol. Interact.*, **2013**, 203, 113-119
5. Martyn, J.A.J.; Fagerlund, M.J.; and Eriksson, L.I. *Anaesthesia*, **2009**, 64, 1-9
6. Schumacher, M.; Camp, S.; Maulet, Y.; Newton, M.; MacPhee-Quigley, K.; Taylor, S.S.; Friedmann, T.; and Taylor, P. *Nature*, **1986**, 319, 407-409
7. Sussman, J.L.; Harel, M.; Frolov, F.; Oefner, C.; Goldman, A.; Toker, L.; and Silman, I. *Science*, **1991**, 253, 872-879
8. Kryger, G.; Harel, M.; Giles, K.; Toker, L.; Velan, B.; Lazar, A.; Kronman, C.; Barak, D.; Ariel, N.; Shafferman, A.; Silman, I.; and Sussman, J.L. *Acta Cryst. D.*, **2000**, 56, 1385-1394
9. Dvir, H.; Silman, I.; Harel, M.; Rosenberry, T.L.; and Sussman, J.L. *Chem. Biol. Interact.*, **2010**, 187, 10-22
10. Dougherty, D.A.; and Stauffer, D.A. *Science*, **1990**, 250, 1558-1560
11. Bourne, Y.; Taylor, P.; Radić, Z.; and Marchot, P. *EMBO*, **2003**, 22, 1-12
12. Bourne, Y.; Radić, Z.; Sulzenbacher, G.; Kim, E.; Taylor, P.; and Marchot, P. *J. Biol. Chem.*, **2006**, 281, 29256-29267
13. Shafferman, A.; Kronman, C.; Flashner, Y.; Leitner, M.; Grosfeld, H.; Ordentlich, A.; Gozes, Y.; Cohen, S.; Ariel, N.; Barak, D.; Harel, M.; Silman, I.; Sussman, J.L.; and Velan, B. *J. Biol. Chem.*, **1992**, 267, 17640-17648
14. Barak, D.; Kronman, C.; Ordentlich, A.; Ariel, N.; Bromberg, A.; Marcus, D.; Lazar, A.; Velan, B.; and Shafferman, A. *J. Biol. Chem.*, **1994**, 264, 6296-6305
15. Changeux, J.P. *Mol. Pharm.*, **1966**, 2, 369-392
16. Shafferman, A.; Velan, B.; Ordentlich, A.; Kronman, C.; Grosfeld, H.; Leitner, M.; Flashner, Y.; Cohen, S.; Barak, D.; and Ariel, N. *EMBO*, **1992**, 11, 3561-3568

17. Radić, Z.; Reiner, E.; and Taylor, P. *Mol. Pharm.*, **1991**, 39, 98-104
18. Small, D.H. *TIBS*, **1990**, 213-216
19. Massoulié, J.; and Bon, S. *Ann. Rev. Neurosci.*, **1982**, 5, 57-106
20. Small, D.H.; and Simpson, R.J. *Neurosci. Lett.*, **1988**, 89, 223-228
21. Johnson, G.; and Moore, S.W. *Biochem. Biophys. Res. Comm.*, **1999**, 258, 758-762
22. Mercey, G.; Renou, J.; Verdet, T.; Kliachyna, M.; Baati, R.; Gillon, E.; Arboléas, M.; Liodice, M.; Nachon, F.; Jean, L.; and Renard, P.Y. *J. Med. Chem.*, **2012**,
23. Malany, S.; Sawai, M.; Sikorski, R.S.; Servalli, J.; Quinn, D.M.; Radić, Z.; Taylor, P.; Kronman, C.; Velan, B.; and Shafferman, A. *J. Am. Chem. Soc.*, **2000**, 122, 2981-2987
24. Tormos, J.R.; Wiley, K.L.; Wang, Y.; Fournier, D.; Masson, P.; Nachon, F.; and Quinn, D.M. *J. Am. Chem. Soc.*, **2010**, 132, 17751-17759
25. Selwood, T.; Feaster, S.R.; States, M.J.; Pryor, A.N.; and Quinn, D.M. *J. Am. Chem. Soc.*, **1993**, 115, 10477-10482
26. Ellman, G.L.; Courtney, K.D.; Andres, V.; and Featherstone, R.M. *Biochem. Pharm.*, **1961**, 88-95
27. Szegletes, T.; Mallender, W.D.; Thomas, P.J.; and Rosenberry, T.L. *Biochemistry*, **1999**, 38, 122-133
28. Radić, Z.; Quinn, D.M.; Vellom, D.C.; Camp, S.; and Taylor, P. *J. Biol. Chem.*, **1995**, 270, 20391-20399
29. Stojan, J.; Brochier, L.; Alies, C.; Colletier, J.P.; and Fournier, D. *Eur. J. Biochem.*, **2004**, 271, 1364-1371
30. Houghton, P.J.; Ren, Y.; and Howes, M-J. *Nat. Prod. Rep.* **2006**, 23, 181-199
31. Conti-Fine, B.M.; Milani, M.; and Kaminski, H.J. *J. Clin. Invest.* **2006**, 2843-2854
32. Alzheimer's Association, Alzheimer's Disease Facts and Figures 2013.  
[http://www.alz.org/downloads/facts\\_figures\\_2013.pdf](http://www.alz.org/downloads/facts_figures_2013.pdf)

33. Simoni, E.; Daniele, S.; Bottegoni, G.; Pizzirani, D.; Trincavelli, M.L.; Goldoni, L.; Tarozzo, G.; Reggiani, A.; Martini, C.; Piomelli, D.; Melchiorre, C.; Rosini, M.; and Cavalli, A. *J. Med. Chem.* **2012**, 55, 9708-9721
34. Wolfe, M.S. *Sci. Am.* **2006**, 72-79
35. Vanlaer, S.; De Borggraeve, W.M.; Voet, A.; Gielens, C.; De Maeyer, M.; Compernelle, F. *Eur. J. Org. Chem.*, **2008**, 2571-2581
36. Inestrosa, N.C.; Alvarez, A.; Pérez, C.A.; Moreno, R.D.; Vincente, M.; Linker, C.; Casanueva, O.I.; Soto, C.; and Garrido, J. *Neuron*, **1996**, 16, 881-891
37. Håkansson, L. *Acta. Neurol. Scand.*, **1993**, 149, 7-9
38. Gottwald, M.D.; and Rozanski, R.I. *Exp. Opin. Invest. Drugs*, **1999**, 8, 1673-1682
39. Kawakami, Y.; Inoue, A.; Kawai, T.; Wakita, M.; Sugimoto, H.; and Hopfinger, A.J. *Bioorg. Med. Chem.*, **1996**, 4, 1429-1446
40. Committee on Alternative Chemical Demilitarization Technologies, National Research Council, *Alternative Technologies for the Destruction of Chemical Agents and Munitions*. National Academies Press, **1993**.
41. Mercey, G.; Verdelet, T.; Renou, J.; Kliachyna, M.; Baati, R.; Nachon, F.; Jean, L.; and Renard, P-Y. *Acct. Chem. Res.* **2012**, 45, 756-766
42. Kim, K.; Tsay, O.G.; Atwood, D.A.; and Churchill, D.G. *Chem. Rev.*, **2011**, 111, 5345-5403
43. Mazur, A.; and Bodansky, O. *J. Biol. Chem.*, **1946**, 163, 261-276
44. Wilson, I.B.; and Ginsburg, S.A. *Biochim. Biophys. Acta*, **1955**, 18, 168-170
45. Poziomek, E.J.; Hackley, B.E.; and Steinburg, G.M. *J. Org. Chem.*, **1958**, 23, 714-717
46. Wandhammer, M.; de Koning, M.; van Grol, M.; Liodice, M.; Saurel, L.; Noort, D.; Goeldner, M.; and Nachon, F. *Chem. Biol. Interact.*, **2013**, 203, 19-23
47. Worek, F.; Thiermann, H.; Szinicz, L.; and Eyer, P. *Biochem. Pharm.*, **2004**, 68, 2237-2248
48. Harris, L.W.; Heyl, W.C.; Stitcher, D.L.; and Broomfield, C.A. *Biochem. Pharm.*, **1978**, 27, 757-761
49. Gupta, R.C. *Handbook of Toxicology of Chemical Warfare Agents*, **2009**, 1<sup>st</sup> ed.



50. Millard, C.B.; Kryger, G.; Ordentlich, A.; Greenblatt, H.M.; Harel, M.; Raves, M.L.; Segall, Y.; Barak, D.; Shafferman, A.; Silman, I.; and Sussman, J.L. *Biochemistry*, **1999**, 38, 7032-7039
51. Millard, C.B.; Koellner, G.; Ordentlich, A.; Shafferman, A.; Silman, I.; and Sussman, J.L. *J. Am. Chem. Soc.*, **1999**, 121, 9883-9884
52. Wilson, I.B. *J. Biol. Chem.*, **1951**, 190, 111-117
53. Albanus, L.; Järplid, B.; and Sundwall, A. *Br. J. Exp. Pathol.*, **1964**, 45, 120-127
54. Mounter, L.A.; and Ellin, R.I. *Mol. Pharm.*, **1968**, 4, 452-456
55. Sun, M.; Chang, Z.; Shau, M.; Huang, R.; and Chou, T. *Eur. J. Biochem.*, **1979**, 100, 527-530
56. Saxena, A.; Viragh, C.; Frazier, D.S.; Kovach, I.M.; Maxwell, D.M.; Lockridge, O.; and Doctor, B.P. *Biochemistry*, **1998**, 37, 15086-15096
57. Kovach, I.M.; Akhmetshin, R.; Enyedy, I.J.; and Viragh, C. *Biochem. J. Lett.*, **1997**, 324, 995-996
58. Shafferman, A.; Ordentlich, A.; Barak, D.; Stein, D.; Ariel, N.; and Velan, B. *Biochem. J.*, **1996**, 318, 833-840
59. Shafferman, A.; Ordentlich, A.; Barak, D.; Stein, D.; Ariel, N.; and Velan, B. *Biochem. J.*, **1997**, 324, 996-998
60. Sanson, B.; Nachon, F.; Colletier, J.P.; Froment, M.T.; Toker, L.; Greenblatt, H.M.; Sussman, J.L.; Ashani, Y.; Masson, P.; Silman, I.; and Weik, M. *J. Med. Chem.*, **2009**, 52, 7593-7603
61. Antonijevic, B.; and Stojiljkovic, M.P. *Clin. Med. Res.*, **2007**, 5, 71-82
62. Timperley, C.M.; Casey, K.E.; Notman, S.; Sellers, D.J.; Williams, N.E.; Williams, N.H.; Williams, G.R. *J. Fluor. Chem.*, 2006, 127, 1554-1563
63. Wong, L.; Radić, Z.; Brüggemann, R.J.M.; Hosea, N.; Berman, H.A.; and Taylor, P. *Biochemistry*, **2000**, 39, 5750-5757
64. Taylor, P.; Kovarik, Z.; Reiner, E.; and Radić, Z. *Toxicology*, **2007**, 233, 70-78
65. Berends, F.; Posthumus, C.H.; Sluys, I.V.D.; and Deierkauf, F.A. *Biochem. Biophys. Acta*, **1959**, 34, 576-578

66. Michel, H.O.; Hackley, B.E.; Berkowitz, L.; List, G.; Hackley, E.B.; Gillian, W.; and Pankau, M. *Arch. Biochem. Biophys.*, **1967**, 121, 29-34
67. Harris, L.W.; Fleisher, J.H.; Clark, J.; and Cliff, W.J. *Science*, **1966**, 154, 404-407
68. Holten, K.B. and Onusko, E.M. *Am. Fam. Phys.* **2000**, 62, 611-620
69. Nikaido, H. *Science* **1994**, 264-380
70. Hamilton-Miller, J.M.T *J. Antimicrob. Chemo.* **1999**, 44, 729-734
71. Page, M.I *Acc. Chem. Res.* **2004**, 297-303
72. Frère, J-M; Joris, B.; Varetto, L.; and Crine, M. *Biochem. Pharmacol.* **1988**, 37, 125-132
73. Matagne, A.; Dubus, A.; Galleni, M.; and Frère, J-M. *Nat. Prod. Rep.* **1999**, 16, 1-19
74. Imming, P.; Klar, B.; and Dix, D. *J. Med. Chem.* **2000**, 43, 4328-4331
75. Potashman, M.H. and Duggan, M.E. *J. Med. Chem.* **2009**, 52, 1231-1246
76. Cheung, J.; Rudolph, M.J.; Burshteyn, F.; Cassidy, M.S.; Gary, E.N.; Love, J.; Franklin, M.C.; Height, J.J. *J. Med. Chem.* **2012**, 55, 10282-10286
77. Trott, O. and Olson, A.J. *J. Comp. Chem.* **2009**, 31, 455-461).
78. Markmee, S.; Ruchirawat, S.; Prachyawarakorn, V.; Ingkaninan, K.; and Khorana, N. *Bioorg. Med. Chem. Lett.*, 2006, 16, 2170-2172
79. Radić, Z.; Kirchhoff, P.D.; Quinn, D.M.; McCammon, J.A.; Taylor, P. *J. Biol. Chem.*, 1997, 23265-23277
80. Elacqua, E.; Frišćić, T.; MacGillivray, L.R. *Isr. J. Chem.*, 2012, 52, 53-59
81. Elacqua, E.; MacGillivray, L.R. *Eur. J. Org. Chem.*, 2010, 6883-6894
82. Elacqua, E.; Bučar, D.K.; Skvortsova, Y.; Baltrusaitis, J.; Geng, M.L.; MacGillivray, L.R. *Org. Lett.*, 2009, 11, 5106-5109
83. Sokolov, A.N.; Bučar, D.K.; Baltrusaitis, J.; Gu, S.X.; MacGillivray, L.R. *Angew. Chem. Int. Ed.*, 2010, 49, 4273-4277
84. Stojaković, J.; Farris, B.S.; MacGillivray, L.R. *Chem. Commun.*, 2012, 48, 7958-7960

85. Auletta, J.T.; Johnson, J.L.; Rosenberry, T.L. *Chem. Biol. Int.*, 2010, 187, 135-141
86. Lineweaver, H.; Bur, D.J. *J. Am. Chem. Soc.*, 1934, 56, 658
87. Jakobsche, C.E.; Choudhary, A; Miller, S.J.; Raines, R.T. *J. Am. Chem. Soc.* **2010**, 132(19), 6651-6653
88. Topczewski, J.J.; and Quinn, D.M. *Org. Lett.*, **2013**, 15, 1084-1087
89. Bourne, Y.; Sharpless, K.B.; et al. *Chem. Biol. Inter.*, **2005**, 157, 159-164
90. Kryger, G.; Silman, I.; and Sussman, J.L. *Structure*, **1999**, 7, 297-307
91. Hörnberg, A.; Tunemalm, A.K.; and Ekström, F. *Biochemistry*, **2007**, 46, 4815-4825
92. Hosea, N.A.; Berman, H.A.; and Taylor, P. *Biochemistry*, **1995**, 34, 11528-11536